

DOCTORAL THESIS

**Concentration and homogenization in evolving,  
complex, and multiphase microstructures:  
theory and application to NMR- and  
humidity-monitored cementitious materials**

submitted in satisfaction of the requirements for the degree  
Doctor of Science in Civil Engineering  
of the Vienna University of Technology, Department of Civil Engineering

DISSERTATION

**Konzentration und Homogenisierung in  
komplexen und mehrphasigen Mikrostrukturen:  
Theorie und Anwendung auf NMR- und  
feuchtigkeitsüberwachte Zementmaterialien**

ausgeführt zum Zwecke der Erlangung des akademischen Grades eines  
Doktors der technischen Wissenschaften  
eingereicht an der Technischen Universität Wien, Fakultät für Bauingenieurwesen

von

Mag. Inz. **Nabor Jiménez Segura**  
Matrikelnr.: 11806395

Betreuer:

Univ. Prof. Dipl.-Ing. Dr. techn. **Bernhard L.A. Pichler**  
Institut für Mechanik der Werkstoffe und Strukturen  
Technische Universität Wien

Ko-Betreuer:

Univ. Prof. Dipl.-Ing. Dr. techn. **Christian Hellmich**  
Institut für Mechanik der Werkstoffe und Strukturen  
Technische Universität Wien

Gutachter:

Prof. **Albert Giraud**  
GeoResources Laboratory  
University of Lorraine

Univ. Prof. **Agathe Robisson**  
Institut für Werkstofftechnologie, Bauphysik und Bauökologie  
Technische Universität Wien

Wien, im August 2022

.....

# Acknowledgements

The path traveled until the completion of this thesis has been long and not always easy. I feel very lucky for the support and company received from many people around, for which I am immensely grateful.

First of all, I would like to thank the supervisors of my research, Bernhard Pichler and Christian Hellmich. Thank you for introducing me into the fascinating world of micromechanics. It has been a great opportunity to learn from you. This document is the result of endless hours of interesting discussions; thanks for your dedication. Your passion for science is truly inspiring.

To one of the pillars of my life: my parents and my family. Despite the distance, you were always there for me. I am very happy that I can count on you for anything. In this happy moment I want to remember and thank the ones who unfortunately are not here anymore. I miss you. In particular, to Pacho, for his interest on my research during our last talk.

Huge credit to the woman who stayed by my side, day by day, during the tough moments. That is no simple task. I am sincerely grateful for your support and understanding. This thesis would not be possible without your contribution. Many thanks and please keep helping me, Zuza.

To all the people involved in the ERICA project. It was a pleasure to be part of this project. I have learned from every person, and the discussions emerging in our catch-up meetings certainly improved the quality of my work. I want to thank the colleagues at HTC for their hospitality during my stay – very unexpectedly shortened.

Of course, I do not forget about every person that contributed to make Vienna a new home during all these years. Thomas, Walter, and the rest of MV Leobendorf. Klaus, Johann, and the SK Austria. Rodrigo, Petr, Luis, and all my colleagues from the Institute of Mechanics of Materials and Structures, not only for the great atmosphere in the office, but also for the informal scientific discussions. I take your friendship as a gift and memory. Martina Pöll, Astrid Schuh, and Gabriele Ostrowski, many thanks for helping me navigate through the administrative challenges. To David Kaufmann and Jan Vales for their readiness to solve the technical problems.

Prof. Kapusta, Dr. Utke, Prof. Rustichelli, thank you for your guidance during the Masters degree.

Lastly, I would like to acknowledge the financial support in the framework of the European Union's Horizon 2020 research and innovation programme under the Marie Skłodowska-Curie grant agreement No. 764691.

# Abstract

Many heterogeneous materials have microstructures which are hierarchically organized across several orders of magnitude. It is of fundamental scientific interest in engineering mechanics to establish quantitative links between microstructural properties and the macroscopic behavior of such materials. This is setting the scene for the theoretical part of the present thesis. It is methodically rooted in continuum micromechanics and focused on innovative approaches to the “stress average rule” and “strain concentration tensors”. The latter render scale transitions possible, e.g. they enable (i) downscaling of the macrostrains imposed on representative volume elements of microheterogeneous materials to the strains experienced by the microstructural constituents, as well as (ii) upscaling of the elastic stiffness and the eigentress of the microstructural constituents to their macroscopic counterparts.

Cementitious materials are particularly challenging when it comes to multiscale modeling. They exhibit evolving microstructures at early material ages, because of the chemical reaction between the water and the binder. The finally formed microstructures consist of solid constituents and pores with characteristic sizes ranging across four orders of magnitude: from a few tens of micrometers to a few single nanometers. Many macroscopic properties of cementitious materials result from physico-chemical processes occurring at nanometric scales. This is setting the scene for the application part of the present thesis. It is focused on two challenging topics regarding multiscale modeling of cement pastes: the evolution of the volume fractions of the microstructural constituents at early material ages and sorption-induced macroscopic volume changes at mature material ages.

The present thesis strives for establishing a synthesis between fundamental developments and challenging applications in the field of multiscale mechanics. To this end, the core of the thesis is organized in five chapters. Following an overall Introduction, three of the core chapters are devoted to theoretical advances. The remaining two core chapters are devoted to the practical applications, followed by overall Conclusions.

Chapter 2 is dedicated to the revision of the foundations of one of the central pillars of continuum micromechanics: the derivation of the stress and strain average rules. Traditionally, these rules are derived from equilibrium and compatibility conditions, together with microdisplacement *and* microtraction boundary conditions associated with homogeneous macrostrains and macrostresses, respectively. However, only displacements *or* tractions can be prescribed at the boundary of bodies, such that the remaining average rule turns out as a mere definition. The present thesis suggests a way to do without such a definition, resorting to the principle of virtual power as a vehicle to guarantee mechanical equilibrium. The strain average rule is traditionally derived from homogeneous strain boundary conditions. Then, arbitrary differentiable, so-called virtual microvelocities are prescribed at the boundary of a representative volume element. They are linked to corresponding homogeneous virtual macrovelocities and macrostrain rates. The latter are related multilinearly to the microscopic virtual strain rate fields inside the representative volume element. Under this setting, the equivalence of the macroscopic and the microscopic expressions for the virtual power densities yields the well-known stress average rule and, in case of microscopically uniform force fields, a volume force average rule.

Chapter 3 refers to homogenization over a representative volume element of *complex* material microstructures which cannot be satisfactorily represented by an assemblage of homogeneous subdomains called phases. The contribution of the present thesis complements existing methods which depend on the boundary conditions applied to the representative volume element, and which do not provide direct access to the macro-micro-relations in terms

of concentration tensors. As a remedy, a Green's function-based homogenization method for complex microstructures is introduced. The new method rests on mapping, through the strain average rule, the microscopic strain fields associated with an auxiliary problem to the macroscopic strains subjected to the representative volume element. Thereby, the auxiliary problem is defined on a homogeneous infinite matrix subjected to homogeneous auxiliary strains and to inhomogeneous polarization stresses representing the fluctuations of the microscopic stiffness field of the complex microstructure within the representative volume element. The corresponding microscopic strains appear as the solution of a Fredholm integral equation. It delivers a multilinear operator linking the homogeneous auxiliary strains to the microscopic strains. This operator, together with the aforementioned mapping, eventually allows for completing the model in terms of concentration tensor and homogenized stiffness quantification. As for illustration, a microstructure with harmonically fluctuating stiffness is exemplarily homogenized. The corresponding singular convolution integrals are evaluated from the solution of the Poisson's equation. This evaluation strategy is then verified through a Cauchy principal value analysis.

Chapter 4 refers to micromechanics of composites with multiple phases of different shapes embedded into a matrix phase. Homogenization of such materials by means the classical Mori-Tanaka scheme yields non-symmetric homogenized stiffness tensor. For energetic reasons, the latter need to be explicitly symmetrized. In the present thesis, the implications of such symmetrization techniques on the concentration tensors are explored, i.e. implications on the relations between macroscopic strains imposed onto a representative volume element of a microheterogeneous material, and the microscopic phase strains developing across the material microstructure. Thereby, the important idea of Mori and Tanaka to approximate the phase strains by the homogeneous strains inside an Eshelbian inhomogeneity embedded into an infinite matrix, together with the phase strains fulfilling the strain average rule, is adopted. However, the proposed approach refrains from the identification of the strain in the matrix phase as the auxiliary strain imposed remotely at the infinite matrix of Eshelby's matrix-inhomogeneity problem. Instead, a conversion tensor is introduced, in order to provide a multilinear relation between the auxiliary strains, on the one hand, and the macroscopic strains imposed onto a representative volume element of a microheterogeneous material, on the other hand. The homogenized stiffness is expressed as (i) a function of the conversion tensor quantifying the aforementioned multilinear relation, and (ii) as the symmetrized Mori-Tanaka estimate. In this way, the conversion tensor and all phase concentrations tensors can be determined in a way which allows the overall elastic stiffness to remain symmetric.

Chapter 5 is devoted to the hydration-driven evolution of the volume fractions of microstructural constituents of Portland cement pastes at early material ages. The analysis is based on results from proton nuclear magnetic resonance relaxometry ( $^1\text{H}$  NMR) tests taken from the literature. These data provide access to the evolution of the amounts of hydrogen in calcium hydroxide, calcium-silicate-hydrates, water in capillary pores, and water in gel pores. The presented developments suggest a change of the variable used for parametrization of formulae describing the early-age evolution of phase volume fractions. Traditional approaches use the hydration degree. The latter is equal to the percentage of cement clinker which has dissolved in water. Herein, the precipitation degree is introduced. It is equal to the fraction of hydrogen bound into solid constituents divided by the total amount of hydrogen in the material. Mix-, storage-, and temperature-invariant precipitation characteristics are found when illustrating the  $^1\text{H}$  NMR signal fractions as a function of the precipitation degree. This allows for developing a set of formulae describing the early-age evolution of the volume fractions of the constituent of cement pastes, as a function of the initial composition (ini-

tial water-to-cement mass ratio), the storage conditions (either sealed curing or underwater storage), and the curing temperature.

Chapter 6 is devoted to modeling of wetting-induced macroscopic swelling of mature cement paste by means of a multiscale poromechanical approach accounting for eigenstrains. Cement paste is represented by means of four scale-separated matrix-inclusion composites consisting of residual cement clinker, calcium hydroxide, capillary pores, gel pores, and calcium silicate hydrates. Experimental data include adsorption isotherms and macroscopic swelling measurements taken from the literature. The radii of spherical gel and capillary pore populations are assumed to follow exponential distributions. The latter are identified by means of adsorption porosimetry. This is the basis for a poromechanical analysis. Wetting-induced changes of effective pore pressures of gel and capillary pores are quantified and upscaled to the macroscale of cement paste. This explains the measured macroscopic swelling only partially. Thus, the modeling approach is enriched by including an additional nanoscopic process: adsorption-induced swelling of nanoscopic calcium-silicate-hydrates, modeled by means of a function linking nanoscopic eigenstrains and relative humidity. This function is identified from experimental data referring to mature cement paste with an initial water-to-cement mass ratio amounting to 0.40. The validity of this humidity-eigenstrain function is then tested through prediction of the macroscopic swelling of mature cement paste with an initial water-to-cement mass ratio amounting to 0.55. The results are satisfactory and underline that sorption-induced nanoscopic volume changes of calcium-silicate-hydrates contribute significantly to corresponding macroscopic volume changes of mature cement paste.

# Kurzfassung

Viele heterogene Materialien weisen Mikrostrukturen auf, die über mehrere Größenordnungen hierarchisch organisiert sind. Es ist von grundlegendem wissenschaftlichem Interesse in der Ingenieurmechanik, quantitative Zusammenhänge zwischen mikrostrukturellen Eigenschaften und dem makroskopischen Verhalten solcher Verbundwerkstoffe herzustellen. Diesem Interesse widmet sich der theoretische Teil der vorliegenden Arbeit. Er ist methodisch in der Kontinuumsmechanik verwurzelt und innovativen Zugängen zur „Spannungsmittelungsregel“ und den „Verzerrungs-Konzentrationsensoren“ gewidmet. Letztere machen Skalenübergänge möglich, z.B. ermöglichen sie (i) das Herunterskalieren von Makroverzerrungen, die repräsentativen Volumenelementen von mikroheterogenen Materialien eingepreßt werden, zu den Verzerrungen der mikrostrukturellen Bestandteile, sowie (ii) das Hochskalieren der elastischen Steifigkeiten und der Eigenspannungen der mikrostrukturellen Bestandteile auf ihre makroskopischen Gegenstücke.

Zementgebundene Materialien stellen eine besondere Herausforderung für die Mehrskalenmodellierung dar. Aufgrund der chemischen Reaktion zwischen dem Wasser und dem Bindemittel weisen sie im frühen Materialalter sich entwickelnde Mikrostrukturen auf. Die schlussendlich geformten Mikrostrukturen bestehen aus Festkörperbestandteilen und Poren mit charakteristischen Größen, die sich über vier Größenordnungen erstrecken: von einigen Duzend Mikrometern bis zu einigen wenigen Nanometern. Viele makroskopische Eigenschaften zementgebundener Materialien resultieren aus physikalisch-chemischen Prozessen, die auf der Nanoskala ablaufen. Diesen Aspekten widmet sich der Anwendungsteil der vorliegenden Arbeit. Er bezieht sich auf zwei herausfordernde Themen der Mehrskalenmodellierung von Zementsteinen: die Entwicklung der Volumenanteile der mikrostrukturellen Bestandteile im frühen Materialalter und sorptionsinduzierte makroskopische Volumenänderungen im ausgehärteten Zustand.

Die vorliegende Arbeit stellt eine Synthese zwischen grundlegenden Entwicklungen und anspruchsvollen Anwendungen auf dem Gebiet der Mehrskalenmechanik dar. Nach einer allgemeinen Einführung widmen sich drei Kernkapitel den theoretischen Arbeiten. Die verbleibenden zwei Hauptkapitel sind den praktischen Anwendungen gewidmet, gefolgt von allgemeinen Schlussfolgerungen.

Kapitel 2 widmet sich der Überarbeitung des Fundaments für eine der zentralen Säulen der Kontinuumsmechanik: der Herleitung der Spannungs- und Verzerrungs-Mittelungsregeln. Traditionell werden diese Regeln aus Gleichgewichts- und Kompatibilitätsbedingungen abgeleitet, zusammen mit Randbedingungen in den mikroskopischen Verschiebungen *und* den mikroskopischen Spannungen, die mit homogenen makroskopischen Verzerrungen bzw. homogenen makroskopischen Spannungen verbunden sind. An der Oberfläche von Körpern können jedoch streng genommen nur Verschiebungen *oder* Spannungen vorgeschrieben werden, so dass sich die verbleibende Mittelungsregel als bloße Definition herausstellt. Die vorliegende Arbeit schlägt einen Weg vor, auf eine solche Definition zu verzichten, und greift dabei auf das Prinzip der virtuellen Leistungen als Konzept zur Gewährleistung des mechanischen Gleichgewichts zurück. Die Verzerrungs-Mittelungsregel wird traditionell hergeleitet: ausgehend von homogenen Verzerrungsrandbedingungen. Dann werden beliebige, differenzierbare, so genannte virtuelle Mikrogeschwindigkeiten an der Berandung eines repräsentativen Volumenelements vorgegeben, die mit beliebigen homogenen virtuellen Makrogeschwindigkeiten und Makroverzerrungsraten verknüpft sind. Letztere sind multilinear mit den mikroskopischen virtuellen Verzerrungsratenfeldern innerhalb des repräsentativen Volumenelements verknüpft. In diesem Setting führt die Äquivalenz der makroskopischen und der mikroskopischen Ausdrücke für die virtuellen



Leistungsdichten auf die bekannte Spannungsmittelungsregel und im Falle mikroskopisch gleichförmiger Volumenkraftfelder auf eine Volumenkraftmittelungsregel.

Kapitel 3 bezieht sich auf die Homogenisierung von repräsentativen Volumenelementen *komplexer* Materialmikrostrukturen, die nicht zufriedenstellend durch endliche Anzahl homogener Teilbereiche dargestellt werden können. Der Beitrag der vorliegenden Arbeit ergänzt bestehende Methoden, die von den Randbedingungen des repräsentativen Volumenelements abhängen und keinen direkten Zugang zu den Makro-Mikro-Beziehungen im Sinne von Konzentrationstensoren bieten. Als Abhilfe wird ein Homogenisierungsverfahren vorgestellt, das auf Greenschen Funktionen fußt. Beim neuen Verfahren werden aus Hilfsproblemen gewonnene mikroskopische Verzerrungen kraft Mittelungsregel über das repräsentative Volumenelement den makroskopischen Verzerrungen zugeordnet. Dabei wird das Hilfsproblem auf einer homogenen unendlichen Matrix definiert. Letztere ist homogenen Hilfsdehnungen und inhomogenen Polarisationsspannungen unterworfen, wobei die Polarisationsspannungen die Fluktuationen des mikroskopischen Steifigkeitsfeldes der komplexen Mikrostruktur innerhalb des repräsentativen Volumenelements abbilden. Die entsprechenden mikroskopischen Dehnungen ergeben sich als Lösung einer Fredholm-Integralgleichung. Sie liefert einen multilinearen Operator, der die homogenen Hilfsdehnungen mit den mikroskopischen Dehnungen verknüpft. Dieser Operator und die zuvor genannte Verknüpfung erlauben schließlich die Vervollständigung des Modells in Bezug auf den Konzentrationstensor und die Quantifizierung der homogenisierten Steifigkeit. Beispielhaft wird eine Mikrostruktur mit harmonisch fluktuierender Steifigkeit homogenisiert. Mit Hilfe der Lösung der Poisson-Gleichung werden die entsprechenden singulären Faltungsintegrale ausgewertet. Diese Auswertungsstrategie wird abschließend durch eine Cauchy-Hauptwertanalyse verifiziert.

Kapitel 4 bezieht sich auf die Mikromechanik von Verbundwerkstoffen mit mehreren Phasen unterschiedlicher Form, die in eine Matrixphase eingebettet sind. Das populäre Mori-Tanaka-Schema liefert bei Homogenisierung solcher Materialien unsymmetrische homogenisierte Steifigkeitstensoren. Letztere müssen explizit symmetrisiert werden. In der vorliegenden Dissertation werden die Auswirkungen solcher Symmetrisierungstechniken auf die Konzentrationstensoren untersucht, d.h. Auswirkungen auf die Beziehungen zwischen makroskopischen Verzerrungen, die einem repräsentativen Volumenelement eines mikroheterogenen Materials eingeprägt werden, und den mikroskopischen Phasenverzerrungen, die sich innerhalb der Materialmikrostruktur einstellen. Dabei wird die wichtige Idee von Mori und Tanaka übernommen, die Phasenverzerrungen durch die homogenen Dehnungen innerhalb Eshelbischer Inhomogenitäten zu approximieren, die jeweils in eine unendliche Matrix eingebettet sind, wobei die Phasenverzerrungen die Verzerrungsmittelungsregel erfüllen. Der vorgeschlagene Ansatz sieht jedoch davon ab, die Verzerrung in der Matrixphase als jene Hilfsverzerrung zu identifizieren, die im Unendlichen der Matrix der Eshelbischen Matrix-Inhomogenitätsprobleme auferlegt ist. Stattdessen wird ein Umwandlungstensor eingeführt, um einen multilinearen Zusammenhang zwischen den Hilfsdehnungen und den makroskopischen Verzerrungen, die einem repräsentativen Volumenelement eines mikroheterogenen Materials eingeprägt sind, herzustellen. Die homogenisierte Steifigkeit wird ausgedrückt als (i) eine Funktion des Umwandlungstensors, der die oben erwähnte multilineare Beziehung quantifiziert, und (ii) als die symmetrisierte Mori-Tanaka-Abschätzung. Auf diese Weise können der Umwandlungstensor und alle Phasenkonzentrationstensoren so bestimmt werden, dass die elastische Gesamtsteifigkeit symmetrisch bleibt.

Kapitel 5 widmet sich der hydrationsgetriebenen Entwicklung der Volumenanteile der mikrostrukturellen Bestandteile von Portlandzementsteinen im frühen Materialalter. Die Studie basiert auf Ergebnissen von Protonen-Kernmagnetresonanz-Relaxometrie ( $^1\text{H}$  NMR)-

Tests aus der Literatur. Diese Daten bieten quantitativen Einblick in die Entwicklung der Wasserstoffmengen, die in Kalziumhydroxid, in Kalzium-Silikat-Hydraten, sowie in Kapillar- und Gelwasser gebunden sind. Dieser Einblick motiviert einen Paradigmenwechsel hinsichtlich der Variable, mittels der die Entwicklung von Phasenvolumenanteilen im frühen Materialalter beschrieben wird. Einschlägige Entwicklungsansätze basieren auf dem Hydratationsgrad. Letzterer entspricht dem Prozentsatz an Zementklinker, der sich in Wasser aufgelöst hat. In der vorliegenden Arbeit wird der Ausfallgrad eingeführt. Er ist gleich dem Anteil des in Festkörperbestandteilen gebundenen Wasserstoffs dividiert durch die Gesamtmenge an Wasserstoff im Material. Mischungs-, lagerungs- und temperaturinvariante Ausfallcharakteristiken finden sich bei der Darstellung der  $^1\text{H}$  NMR-Signalanteile als Funktion des Ausfallgrades. Letzterer erscheint als die Zementsteinentwicklung quantifizierendes Argument in Funktionen für die Volumsfraktionen seiner Bestandteile. Diese Funktionen hängen auch von der Ausgangszusammensetzung (anfängliches Wasser-zu-Zement-Massenverhältnis), den Lagerbedingungen (entweder versiegelte Aushärtung oder Unterwasserlagerung) und der Aushärtungstemperatur ab.

Kapitel 6 widmet sich der Modellierung des befeuchtungsinduzierten makroskopischen Schwellens von ausgehärtetem Zementstein mittels eines mehrskaligen poromechanischen Ansatzes unter Berücksichtigung von Eigendehnungen. Zementstein wird durch Matrix-Inklusions-Komposite auf vier verschiedenen Maßstäben dargestellt. Diese Komposite bestehen aus übrig gebliebenem Zementklinker, Kalziumhydroxid, Kapillarporen, Gelporen und Kalzium-Silikat-Hydraten. Zugehörige experimentelle Daten umfassen Adsorptionsisotherme und makroskopische Schwellmessungen aus der Literatur. Im Rahmen der Modellierung wird angenommen, dass die Radien der kugelförmigen Gel- und Kapillarporenpopulationen durch Exponentialverteilungen beschrieben werden können. Letztere werden mittels Adsorptionsporosimetrie identifiziert. Dies ist die Grundlage für eine poromechanische Analyse. Die durch Befeuchtung induzierte Änderungen des effektiven Porendrucks von Gel- und Kapillarporen werden quantifiziert und auf die Makroskala von Zementstein hochskaliert. Dies erklärt die gemessene makroskopische Schwellung nur teilweise. Daher wird der Modellierungsansatz durch die Einbeziehung eines weiteren nanoskopischen Prozesses bereichert: Adsorptionsinduzierte Quellung von nanoskopischen Kalzium-Silikat-Hydraten, modelliert in Form von Eigenspannungen die sich als Funktion der relativen Feuchtigkeit entwickeln. Diese Beziehung wird mittels experimenteller Daten identifiziert, die sich auf ausgereiften Zementstein mit einem anfänglichen Wasser-zu-Zement-Massenverhältnis von 0,40 beziehen. Die identifizierte Beziehung wird sodann getestet, in dem sie zur mikromechanischen Vorhersage der makroskopischen Quellung von reifem Zementstein mit einem anfänglichen Wasser-zu-Zement-Massenverhältnis von 0,55 herangezogen wird. Die Ergebnisse sind zufriedenstellend und unterstreichen, dass sorptionsinduzierte nanoskopische Volumenänderungen von Kalzium-Silikat-Hydraten signifikant zu entsprechenden makroskopischen Volumenänderungen von reifem Zementstein beitragen.



# Contents

<b>1</b>	<b>Introduction</b>	<b>1</b>
1.1	Introduction to micromechanics: concentration tensors and homogenization . . . . .	1
1.1.1	Homogenization of linear elastic media . . . . .	1
1.1.2	Extension towards eigenstressed media . . . . .	4
1.2	Introduction to cementitious materials . . . . .	5
1.2.1	Nuclear magnetic resonance relaxometry in cementitious materials . . . . .	6
1.2.2	Volume changes of cement pastes induced by changes in the relative humidity . . . . .	7
1.3	Outline of the thesis . . . . .	8
<b>2</b>	<b>Stress average rule derived through the principle of virtual power</b>	<b>10</b>
2.1	Introduction – Motivation and Scope . . . . .	11
2.2	Principle of Virtual Power applied to a continuum mechanics system and its microstructurally representative volume elements . . . . .	13
2.3	Equivalence of macroscopic and microscopic expressions for internal and external power densities – stress and volume force averaging rules . . . . .	15
2.4	Implications for computational homogenization: internal virial stresses of atomistic systems, and continuum RVEs undergoing large deformations . . . . .	17
2.5	Discussion and Conclusion . . . . .	19
<b>3</b>	<b>A Green’s function-based approach to the concentration tensor fields in complex elastic microstructures</b>	<b>21</b>
3.1	Introduction – Motivation and Scope . . . . .	22
3.2	An auxiliary problem on an infinite domain, and its relation to the RVE . . . . .	24
3.3	Green’s function-based solution to the auxiliary problem of the infinite matrix with a complex microstructure . . . . .	26
3.4	Illustrative example: microstructure with harmonically fluctuating bulk moduli	29
3.4.1	Complex microstructure with harmonically fluctuating microscopic bulk modulus . . . . .	29
3.4.2	Normal strain-related components of $\mathbb{A}^0(\boldsymbol{x})$ . . . . .	30
3.4.3	Shear strain-related components of $\mathbb{A}^0(\boldsymbol{x})$ . . . . .	34
3.4.4	Tensorial link between auxiliary and real macrostrains . . . . .	37
3.4.5	Homogenized stiffness of harmonically fluctuating microstructure . . . . .	39
3.5	Discussion . . . . .	39
3.5.1	Singular convolution integrals - alternative evaluation by means of Cauchy principal value . . . . .	40

3.5.2	Use of the Lippmann-Schwinger equation: auxiliary problems, integration domains, and macroscopic strains associated with the RVE . . . .	41
3.5.3	Range of validity of Lippmann-Schwinger equation . . . . .	43
3.5.4	Practical note concerning non-harmonic microstiffness fluctuations . .	43
3.6	Conclusions . . . . .	44
<b>4</b>	<b>Concentration tensors preserving elastic symmetry of multiphase composites</b>	<b>45</b>
4.1	Introduction . . . . .	46
4.2	Mathematical derivation of elastic symmetry-preserving concentration tensors	47
4.3	Benchmark example . . . . .	50
4.4	Conclusions . . . . .	53
<b>5</b>	<b>Mix-, storage- and temperature-invariant precipitation characteristics in white cement paste, expressed through an NMR-based analytical model</b>	<b>55</b>
5.1	Introduction . . . . .	56
5.2	Temperature-, storage-, and mix-invariant relations between molar fractions of differently mobile hydrogen portions and the precipitation degree $\eta$ . . . . .	60
5.2.1	Normalized NMR signals, molar fractions of differently mobile hydrogen portions, and the precipitation degree . . . . .	60
5.2.2	Identification of mix-invariant relations between hydrogen molar fractions and precipitation degree; obtained from NMR data of samples cured under sealed conditions . . . . .	61
5.2.3	Testing temperature- and storage-invariance of the relations between hydrogen molar fractions and the precipitation degree: evaluation of NMR data from samples cured under water at six different temperatures	63
5.2.4	Water and hydrogen uptake characteristics of cement pastes cured under water . . . . .	65
5.3	Precipitation kinetics . . . . .	66
5.3.1	Precipitation evolutions governed by curing temperature, derived from NMR data . . . . .	66
5.3.2	Identification of Arrhenius-type precipitation kinetics law . . . . .	68
5.4	Precipitation-driven constituent masses in the cement paste system, and corresponding degree of hydration . . . . .	70
5.5	Precipitation-driven constituent volumes of the cement paste system, and corresponding mass density of solid C-S-H . . . . .	72
5.5.1	Volumes of invariably dense material constituents and of overall cement paste . . . . .	72
5.5.2	Determination of mass density of solid C-S-H, from under water cured samples . . . . .	74
5.5.3	Volume fractions in cement paste precipitating under sealed conditions	75
5.6	Conclusions . . . . .	76
<b>6</b>	<b>Swelling of nanoscopic solid C-S-H governs macroscopic expansion of mature cement paste during isothermal adsorption</b>	<b>79</b>
6.1	Introduction . . . . .	80
6.2	Model development . . . . .	82
6.2.1	Experimental measurements: water content and uniaxial swelling during isothermal adsorption . . . . .	82

6.2.2	Hierarchical organization of mature cement paste . . . . .	84
6.2.3	Status of individual pores of partially saturated cement paste . . . . .	85
6.2.4	Characterization of porosity: identification of characteristic radii $R_{gpor}$ and $R_{cpor}$ . . . . .	86
6.3	Multiscale homogenization of mature cement paste . . . . .	88
6.3.1	Microscopic input . . . . .	88
6.3.2	Bottom-up homogenization of pore pressures . . . . .	89
6.3.3	Top-down identification of eigenstrain of solid C-S-H . . . . .	91
6.3.4	Bottom-up prediction of macroscopic swelling . . . . .	91
6.4	Conclusions . . . . .	93
Appendix 6.A	Young's equation . . . . .	93
Appendix 6.B	The equation of state through Berthelot rule . . . . .	93
<b>7</b>	<b>Summary, conclusions, and outlook</b>	<b>95</b>
7.1	Summary of the micromechanics modeling . . . . .	95
7.2	Summary of their application to cementitious materials . . . . .	96
7.2.1	Conclusions drawn from the study of precipitation in cement paste . .	96
7.2.2	Conclusions drawn from the study of swelling C-S-H . . . . .	98
7.3	Perspectives . . . . .	98
	<b>Bibliography</b>	<b>100</b>
	<b>A Numerical computation of strain concentration and homogenized stiffness tensor of multiphase matrix-inclusion composites</b>	<b>113</b>
	<b>Personal information</b>	<b>117</b>
	Curriculum Vitae . . . . .	117
	Scientific Dissemination . . . . .	118

# List of Figures

1.1	Illustrative sketch of a microheterogeneous material. . . . .	2
1.2	Sketch illustrating Eshelby’s matrix-inhomogeneity problem. . . . .	4
1.3	Microstructure of cement paste at the scale of observation of several tens of microns. . . . .	6
1.4	Experimentally measured water content and deformation mature cement pastes during isothermal desorption and adsorption. . . . .	8
2.1	Different characteristics of the representative volume element. . . . .	12
3.1	Illustration of elements making up the new homogenization scheme. . . . .	24
3.2	Numerical value of integral expression $I$ for several values of elastic moduli. . . . .	38
4.1	Two-dimensional sketch illustrating Eshelby’s three-dimensional matrix-inhomogeneity problem. . . . .	47
4.2	Benchmark material: matrix-inclusion composite with two types of inclusions. . . . .	51
5.1	Proton NMR signal fraction as function of material age, obtained from white cement paste samples cured under sealed conditions. . . . .	58
5.2	Proton NMR signal fraction as function of material age, obtained from white cement paste samples cured under water. . . . .	59
5.3	Molar fraction of hydrogen in solid C-S-H as function of the precipitation degree. . . . .	62
5.4	Trends of gel and capillary pore fractions, with the precipitation degree. . . . .	62
5.5	Cumulative molar fractions of hydrogen as functions of the precipitation degree. . . . .	63
5.6	Exemplary model validation: cumulative molar fractions of hydrogen as function of the precipitation degree. . . . .	64
5.7	Relative increase of the total NMR intensity. . . . .	65
5.8	Temporal evolution of the precipitation degree of cement pastes cured at different temperatures. . . . .	66
5.9	“Eventually” reached “maximum” precipitation degree of cement pastes. . . . .	67
5.10	Water-to-silica ratio of solid C-S-H. . . . .	68
5.11	Modeled temporal evolution of the precipitation degree of cement pastes cured at different temperatures. . . . .	69
5.12	Evolution of precipitation degree as a function of curing temperature. . . . .	70
5.13	Hydration degree as function of the precipitation degree. . . . .	73
5.14	Density of solid C-S-H as a function of precipitation degree and curing temperature. . . . .	75
5.15	Evolution of phase assemblage of cement pastes as functions of the precipitation degree. . . . .	77

6.1	Experimentally measured water content during isothermal adsorption of partially-dried mature cement pastes. . . . .	83
6.2	Experimentally measured isothermal swelling of partially-dried mature cement pastes. . . . .	83
6.3	Hierarchical representation of mature cement pastes. . . . .	84
6.4	Representation of pore status under partial saturation. . . . .	85
6.5	Representation of a spherical meniscus in a cylinder. . . . .	86
6.6	Kelvin radius and thickness of adsorbed layer for different values of internal relative humidity. . . . .	87
6.7	Experimentally measured water content and modeled water content during isothermal adsorption of partially-dried mature cement pastes. . . . .	88
6.8	Modeled volume deformation in mature cement pastes produced due to changes in effective pore pressures. . . . .	91
6.9	Top-down identified eigenstrain of the solid C-S-H as a function of relative humidity. . . . .	92
6.10	Prediction of macroscopic expansion of mature cement paste produced due to changes in effective pore pressures <i>and</i> microscopic swelling of solid C-S-H. . . . .	92
6.11	Representation of a liquid droplet wetting a plain surface. . . . .	93

# List of Tables

4.1	Volume fractions and isotropic elastic stiffness constants of the three material phases of the benchmark material, illustrated in Fig. 4.2. . . . .	50
5.1	Factorial, exponential, and proportionality constants quantifying mix-, storage-, and temperature-independent precipitation characteristics, identified from the NMR data of Fig. 5.1. . . . .	61
5.2	Temperature-independent binary variable $\pi_4$ distinguishing between two types of curing conditions: (i) sealed storage (= closed system), and (ii) underwater storage (= open system), leading to the increase of the total amount of hydrogen resulting from uptake of water driven by chemical shrinkage. . . . .	65
5.3	Constants quantifying the influence of temperature on the precipitation kinetics.	67
5.4	Root-mean-square errors according to Eq. (5.32), referring to the differences between experimental data points and Arrhenius-type kinetics model predictions of Fig. 5.11. . . . .	70
5.5	Physical properties of water, calcium-silicate in C-S-H, and calcium hydroxide (Allen et al., 2007; Muller et al., 2013a; Gallucci et al., 2013). . . . .	71
5.6	Mass densities of water, calcium hydroxide, and clinker (Muller et al., 2013a).	73
6.1	Densities and water contents of saturated mature cement pastes (Maruyama, 2010). . . . .	82
6.2	Volume fractions of material phases relative to cement paste derived from precipitation model (for $\xi = 0.86$ ). . . . .	85
6.3	Elastic constants of solid constituents of mature cement paste (Ulm et al., 2004).	89
6.4	Step-by-step homogenization of mature cement paste from the smallest scale to the macroscopic application scale (cement paste). . . . .	90



## Introduction

### 1.1 Introduction to micromechanics: concentration tensors and homogenization

The field of continuum micromechanics is devoted to establishing a link between the microscopic mechanical properties of a microheterogeneous material and the effective mechanical properties that this material exhibits at the macroscopic scale (Zaoui, 2002). Thus, in continuum micromechanics, a macroscopic point of the studied material is conceptually set equivalent to a microscopic representative volume elements (RVEs) of the material, see Fig. 1.1. For this equivalence to be mathematically sound, the principle of separation of scales must be fulfilled. The principle of separation of scales states that, on the one hand, the characteristic size of the RVE,  $\ell$ , must be much smaller than the structural length,  $\mathcal{L}$ , and, on the other hand, the characteristic size  $\ell$  must be much larger than the characteristic size of the inhomogeneities in the RVE,  $d$ . Mathematically, the principle of separation of scales reads as

$$d \ll \ell \ll \mathcal{L}. \quad (1.1)$$

The first  $\ll$ -sign admits factor on the order of 2 to 3 (Drugan and Willis, 1996), with the resulting uncertainties below 5%. The second  $\ll$ -sign, in turn, refers to a factor of 5 to 10 (Kohlhauser and Hellmich, 2013).

After the macro- and microscopic scales have been clearly defined, the RVE must be described in detail. First, the microscopic constituents (also called phases) must be identified. Each material phase has associated mechanical properties, as well as geometric properties such as shape, orientation and volume. The phases are *statistical* representations of the inhomogeneities of the RVE. Thus, every (microscopic) point in the RVE,  $\underline{x} \in V_{\text{RVE}}$  is inside of a phase. For this reason, it is important to note that the results of these homogenization techniques are approximations or estimates of the real properties.

#### 1.1.1 Homogenization of linear elastic media

In the context of linear elasticity, a physically realistic RVE must fulfill a set of mechanical laws (Zaoui, 2002):

- linearized symmetric strain  $\boldsymbol{\varepsilon}$  as the symmetric gradient of the displacement  $\underline{u}$

$$\boldsymbol{\varepsilon}(\underline{x}) = \text{grad}^S \underline{u}(\underline{x}); \quad (1.2)$$

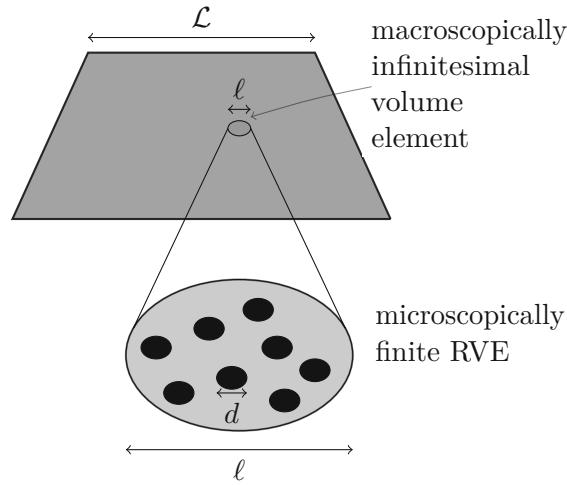


**Fig. 1.1.** Illustrative sketch of a microheterogeneous material. At the microscale (below), the first inequality in (1.1) is represented, with the characteristic size of the inhomogeneities,  $d$ , being much smaller than the characteristic size of the RVE,  $\ell$ . At the macroscale (above), the second inequality in (1.1) is represented, with the characteristic size of the RVE,  $\ell$ , being much smaller than the structural length,  $\mathcal{L}$ .

- geometrical boundary conditions prescribed at the boundary of the RVE, which yields the so-called strain average rule, stating that the macroscopic strain  $\mathbf{E}$  is equal to the average of the microscopic strain  $\boldsymbol{\varepsilon}$  over the entire RVE (Hashin, 1963, 1965, 1983)

$$\mathbf{E} = \frac{1}{V_{\text{RVE}}} \int_{V_{\text{RVE}}} \boldsymbol{\varepsilon}(\underline{x}) \, dV(\underline{x}); \quad (1.3)$$

- the microscopic elastic law relates the microscopic strain and stress  $\boldsymbol{\sigma}$  by means of the microscopic stiffness tensor  $\mathfrak{c}$

$$\boldsymbol{\sigma}(\underline{x}) = \mathfrak{c}(\underline{x}) : \boldsymbol{\varepsilon}(\underline{x}); \quad (1.4)$$

- equilibrium conditions

$$\nabla_x \cdot \boldsymbol{\sigma}(\underline{x}) + \underline{f}(\underline{x}) = 0, \quad \forall \underline{x} \in V_{\text{RVE}}, \quad (1.5)$$

where  $\nabla_x$  stands for the nabla operator and  $\underline{f}$  denotes the volume forces;

- the stress average rule as (Hill, 1963; Zaoui, 2002)

$$\boldsymbol{\Sigma} = \frac{1}{V_{\text{RVE}}} \int_{V_{\text{RVE}}} \boldsymbol{\sigma}(\underline{x}) \, dV(\underline{x}). \quad (1.6)$$

Moreover, due to the linearity of the field equations, the microscopic strains are related to the macroscopic strain in a multilinear manner. Therefore, it is possible to introduce a strain concentration (or downscaling) relation that reads as (Zaoui, 2002; Hill, 1963)

$$\boldsymbol{\varepsilon}(\underline{x}) = \mathbb{A}(\underline{x}) : \mathbf{E}, \quad (1.7)$$

where  $\mathbb{A}$  is the concentration (or downscaling) tensor. The concentration tensor is characteristic of the microstructure, i.e. it is independent of the loading scenario. Consequently, combining (1.4), (1.6), and (1.7), the macroscopic elastic law is derived as

$$\boldsymbol{\Sigma} = \mathbb{C}^{hom} : \mathbf{E}, \quad (1.8)$$

with the homogenized stiffness tensor reading as (Zaoui, 2002; Hill, 1963)

$$\mathbb{C}^{hom} = \frac{1}{V_{RVE}} \int_{V_{RVE}} \mathbb{c}(\underline{x}) : \mathbb{A}(\underline{x}) \, dV(\underline{x}). \quad (1.9)$$

Thus, the identification of a suitable estimate for the concentration tensors  $\mathbb{A}$  is the key to a successful homogenization scheme.

A classical way to simplify the complexity of the RVE is to identify a finite number of material phases,  $N_r$ , such that

$$\sum_{i=1}^{N_r} V_r = V_{RVE}. \quad (1.10)$$

Therefore, volume fractions associated to the phases are defined as

$$f_r = \frac{V_r}{V_{RVE}}. \quad (1.11)$$

This simplification allows to rewrite (1.3), (1.6), (1.4), (1.7), and (1.9) as (Hill, 1963; Laws, 1973; Zaoui, 2002)

$$\mathbf{E} = \sum_{r=1}^{N_r} f_r \boldsymbol{\varepsilon}_r, \quad (1.12)$$

$$\boldsymbol{\Sigma} = \sum_{r=1}^{N_r} f_r \boldsymbol{\sigma}_r, \quad (1.13)$$

$$\boldsymbol{\sigma}_r = \mathbb{c}_r : \boldsymbol{\varepsilon}_r, \quad (1.14)$$

$$\boldsymbol{\varepsilon}_r = \mathbb{A}_r : \mathbf{E}, \quad \forall r = 1, \dots, N_r, \quad (1.15)$$

$$\mathbb{C}_{hom} = \sum_{r=1}^{N_r} f_r \mathbb{c}_r : \mathbb{A}_r, \quad (1.16)$$

respectively; with  $\boldsymbol{\varepsilon}_r$ ,  $\boldsymbol{\sigma}_r$ , and  $\mathbb{A}_r$  as the average strain, stress, and concentration tensor, respectively, associated to phase  $r$ , and with  $\mathbb{c}_r$  as the stiffness of that phase.

Thus, after this simplification, the task of a homogenization scheme is to provide estimates for the  $N_r$  concentration tensors associated with the phases. To this end, the famous Eshelby's inhomogeneity problem (Eshelby, 1957) is used, consisting of an ellipsoidal domain of stiffness  $\mathbb{c}_i$  (the inhomogeneity), which is embedded into an infinite matrix with stiffness  $\mathbb{c}_m$ , see Fig. 1.2. The latter matrix is subjected to uniform strains  $\mathbf{E}_\infty$  at infinity. For this problem, classical analytical solutions (Eshelby, 1957; Laws, 1977) link  $\mathbf{E}_\infty$  to the uniform strains in the inhomogeneity. These solutions, together with the strain average rule, are used to establish a link between the auxiliary strain  $\mathbf{E}_\infty$  and the real macroscopic strain of the RVE  $\mathbf{E}$ . Then, the estimates for the microscopic average strains in the phases, and therefore the concentration tensors, are calculated.

On the one hand, in the case of a microstructure which consists of inclusions embedded in a matrix phase, the Mori-Tanaka scheme (Mori and Tanaka, 1973; Benveniste, 1987) is a

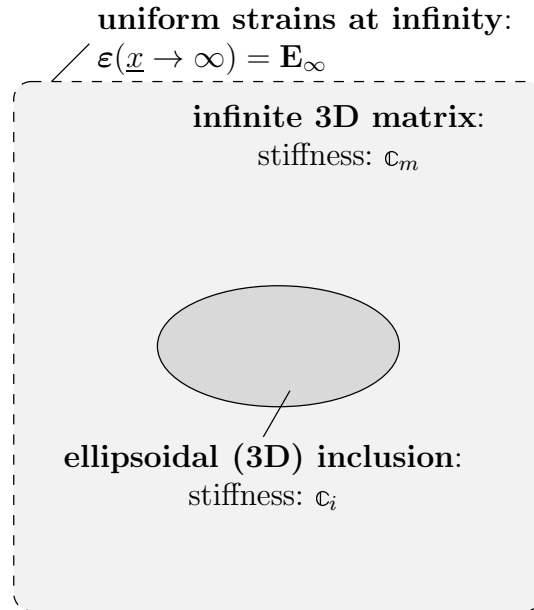


**Fig. 1.2.** Two-dimensional sketch illustrating Eshelby's three-dimensional matrix-inhomogeneity problem:  $\mathbf{E}_\infty$  denotes the remote strain,  $\underline{x}$  is the position vector, while  $\mathfrak{c}_m$  and  $\mathfrak{c}_i$ ,  $i \in 1, \dots, N_r$ , respectively, are the stiffness tensors of the matrix, and of the ellipsoidal inhomogeneity. The stiffness of the matrix depends on the chosen scheme: in the Mori-Tanaka scheme, this stiffness is equal to the stiffness of the matrix phase in the RVE (Mori and Tanaka, 1973; Benveniste, 1987); in the self-consistent scheme, the stiffness of the infinite matrix is equal to the homogenized stiffness (Kröner, 1958).

suitable choice. In this scheme, the stiffness of the auxiliary infinite matrix is set equal to the stiffness of the real matrix phase of the RVE, see Fig. 1.2. This scheme provides explicit formulae for the concentration and homogenized stiffness tensors. However, one must be careful in the case of complex, multiphase microstructures, since it may lead to unsymmetric homogenized stiffness tensors (Ferrari, 1991; Sevostianov and Kachanov, 2014).

On the other hand, in the case of a polycrystalline microstructure, the self-consistent scheme (Kröner, 1958) represents a more suitable choice. In this scheme, the stiffness of the infinite matrix is set equal to the resulting homogenized stiffness, see Fig. 1.2. Therefore, this scheme provides implicit expressions for the homogenized stiffness tensors. Then, the homogenized stiffness tensor can be computed by means of an iteration process.

### 1.1.2 Extension towards eigenstressed media

Extending simple linear elasticity towards eigenstressed media, a larger number of physical phenomena can be studied. Eigenstresses  $\boldsymbol{\sigma}^E$  are stresses arising from non-elastic origins. In order to account for these eigenstresses, the microscopic and macroscopic elastic laws must be rewritten as (Zaoui, 2002)

$$\boldsymbol{\sigma}_r = \mathfrak{c}_r : \boldsymbol{\varepsilon}_r + \boldsymbol{\sigma}_r^E, \quad (1.17)$$

and

$$\boldsymbol{\Sigma} = \mathbb{C}^{hom} : \mathbf{E} + \boldsymbol{\Sigma}^E, \quad (1.18)$$

where  $\Sigma^E$  is the homogenized macroscopic eigenstress, defined by Levin's theorem as (Levin, 1967)

$$\Sigma^E = \sum_{r=1}^{N_r} f_r \sigma_r^E : \mathbb{A}_r. \quad (1.19)$$

Since the concentration tensors are characteristics of the microstructure, they are independent of the presence of eigenstresses.

The presented homogenization schemes can be applied in hierarchical material systems, such as wood (Bader et al., 2010), shale (Gruescu et al., 2007), fired clay (Kiefer et al., 2020), bituminous mixes (Somé et al., 2022), fiber-reinforced composites including soft biological tissues (Guilleminot et al., 2008; Morin et al., 2018, 2021), nanoclay composites (Cauvin et al., 2007), or cement pastes (Ulm et al., 2004; Pichler et al., 2008; Koichi et al., 2009; Pichler and Dormieux, 2010; Pichler and Hellmich, 2011). The latter are discussed in more detail in the following section.

## 1.2 Introduction to cementitious materials

Cement, mainly used to form concrete, is one of the most consumed materials in the world. The reason why cement and concrete are the most valued construction materials is their strength, durability, and versatility.

Concrete consists of sand, aggregates, and cement paste, as well as other minor components. In concrete, cement paste acts as a binding matrix. For this reason, the properties of concrete greatly depend on those of the cement paste which forms it.

Cement paste, in turn, consists of clinker grains, water, and the reaction products of the mix of these two components, of which the most important is calcium-silicate-hydroxide (C-S-H). The production of clinker emits CO<sub>2</sub> and, due to the massive consumption of cement and concrete worldwide, it translates into a considerable effect on global warming.

Therefore, a better understanding of the properties of cement, its hydration, and its role in concrete is crucial, since it allows to optimize the obtained product, reducing the production of clinker and, subsequently, the CO<sub>2</sub> emissions.

Concrete is a composite material. At the macroscopic scale, i.e. few centimeters and larger, concrete behaves as a homogeneous material. However, at smaller scales, the different constituents of concrete present different properties, which result in a heterogeneous microstructure.

The same holds true for cement paste, but at smaller scales. In the order of magnitude of several millimeters, cement paste presents homogeneous material properties. At the smaller scales, a heterogeneous microstructure can be resolved, see Fig. 1.3. The microstructure of cement paste is truly complex, with connected pores ranging from few nanometers to several microns. Such complexity throughout several orders of magnitude becomes a real challenge when it comes to modeling the properties of cement paste. Well-known modeling techniques such as the Finite Element Method (Zienkiewicz et al., 2005) or molecular dynamics (Hansson et al., 2002) are not suitable to approach multiscale materials such as cement paste (from nano- to milli- meters) because the needed computation power would be just boundless. For this reason, the homogenization techniques described in the previous section are employed to study the mechanical properties of cement pastes. One of the essential inputs required to use the homogenization schemes is the phase assemblage of the material, i.e. the volume fractions of the different constituents of the material. In order to quantify these volume fractions, nuclear magnetic resonance relaxometry (NMR) is an ideal technique.

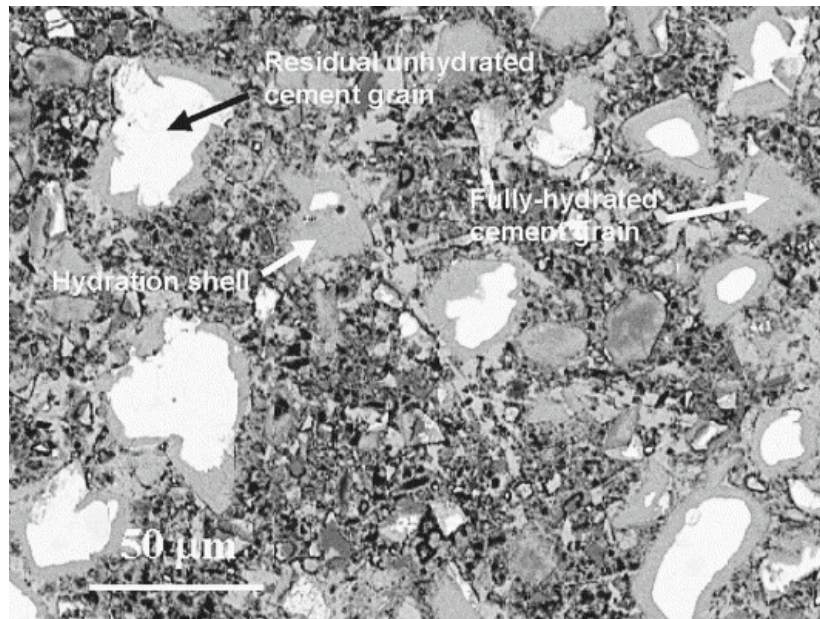


**Fig. 1.3.** Microstructure of cement paste at the scale of observation of several tens of microns (Diamond, 2004): unhydrated clinker grains in white, and embedded in a “foam” consisting of different hydrates and capillary pores.

### 1.2.1 Nuclear magnetic resonance relaxometry in cementitious materials

Proton nuclear magnetic resonance (NMR) relaxometry is a powerful technique to quantify amounts of bound water in a sample. NMR is a non-destructive, non-invasive technique, which means that the sample does not require drying or damage during the preparation process. In the case of cementitious materials, NMR probes hydrogen atoms chemically bound in the reaction products, i.e. solid C-S-H and calcium hydroxide (CH), and in the water present in the porosity of the sample. The mobility of the hydrogen atoms depends on its surroundings.

Thus, NMR identifies populations of hydrogen atoms with similar surroundings. NMR relaxometry quantifies the amounts of these populations, since these amounts are proportional to the amplitude of the signal intensity associated to each group. Each group is characterized by its relaxation time  $T_2$ . The relaxation time  $T_2$  is the smaller the more confined environment. For example, strongly bound hydrogen in reaction products exhibits smaller relaxation time  $T_2$  than weakly bound hydrogen in bulk water.

In more detail, NMR identifies four different populations of hydrogen atoms in cement paste, with different relaxation times (McDonald et al., 2010; Valori et al., 2013; Muller et al., 2013a): (i) stronger chemical bonding in crystals such as calcium hydroxide, (ii) weaker chemical bonding in calcium-silicate-hydrate building blocks (solid C-S-H), (iii) stronger confinement in gel pores, and (iv) weaker confinement in capillary pores. Thus, one proton NMR test provides four signal intensities associated with these populations.

The hydrogen-containing phases of cement pastes are the reaction products (CH and solid C-S-H), and the water in its porosity. Moreover, focusing on C-S-H, its water content is not constant. Curing temperature of cement paste is a crucial factor, since the water-to-silica ratio which is the larger of the precipitated solid C-S-H depends on it (Bahafid et al., 2017). Moreover, the water content in the solid C-S-H present in mature cement paste varies as well. Both temperature and relative humidity ( $RH$ ) changes results in a release/uptake of water by solid C-S-H. In the case of temperature changes, molecular dynamics simulations coupled with



a Grand Canonical Monte-Carlo approach suggests that an increase of temperature results in a release of water by solid C-S-H (Bonnaud et al., 2013), which was proved experimentally by proton nuclear magnetic resonance relaxometry (Wyrzykowski et al., 2017). Thus, the water content of solid C-S-H decreases upon heating and increases upon cooling in a quasi instantaneous and reversible manner. The water released/adsorbed by the solid C-S-H water migrates to the gel (or capillary) porosity, which results in changes of the internal relative humidity, as well as the effective porewater underpressures acting on the solid skeleton. These changes of effective pore pressures provide a microporomechanical explanation for the anomalous macroscopic thermal expansion of mature cement paste (Wang et al., 2018). Regarding changes of relative humidity, the water content of solid C-S-H is altered when the internal relative humidity drops below 20% (Feldman, 1968; Muller et al., 2013b; Pinson et al., 2015). Reduction of internal relative humidity below this level results in progressive drying of the solid C-S-H. After such a decrease of the water content of solid C-S-H has taken place, a subsequent increase in relative humidity results in re-adsorption of water into the solid C-S-H (Feldman, 1968; Muller et al., 2013b; Pinson et al., 2015). Thus, isothermal drying and re-wetting of cementitious materials may also change the water content of solid C-S-H. This process presents a hysteresis, since the water released by solid C-S-H while drying below 20% is progressively re-adsorbed during adsorption in the entire  $RH$ -range.

However, cement pastes also consist of phases with no hydrogen, such as the unhydrated clinker and, in the case of sealed samples, vapor-filled voids. In order to compute the phase assemblage of the studied cement from the NMR data correctly, the data must be processed taking under consideration the characteristics of the material, e.g. initial composition, age of the material, curing conditions, etc.

Once the phase assemblage of the material is known, the mechanical properties of the constituents must be identified. Then, homogenization techniques can be applied. In the present work, these multiscale models will be applied to the study of volume changes of cement pastes induced by changes in the relative humidity.

### 1.2.2 Volume changes of cement pastes induced by changes in the relative humidity

The volume changes that take place when cement pastes are exposed to an unsaturated medium are typically referred to as drying shrinkage (Feldman and Sereda, 1964a,b). Drying shrinkage may result in cracking which, in turn, reduces the mechanical properties and constitutes a durability issue since it accelerates, for instance, the corrosion of the reinforcements in concrete.

The mechanisms behind drying shrinkage are not yet fully understood. It is generally accepted that, when a sample is dried for the first time, irreversible changes occur. There are several mechanisms which can be the cause of this deformation:

- Changes in the capillary pressure, based on the Kelvin-Laplace theory (Powers, 1968; Grasley et al., 2006; Wang et al., 2018).
- Movement of interlayer water (Feldman, 1968; Pinson et al., 2015).
- Disjoining pressure (Bažant, 1972; Maruyama, 2010).

It seems likely that a combination of these mechanisms is responsible for the shrinkage.

A hysteresis exists both in the content of water in the sample and in the induced deformation, see Fig. 1.4.

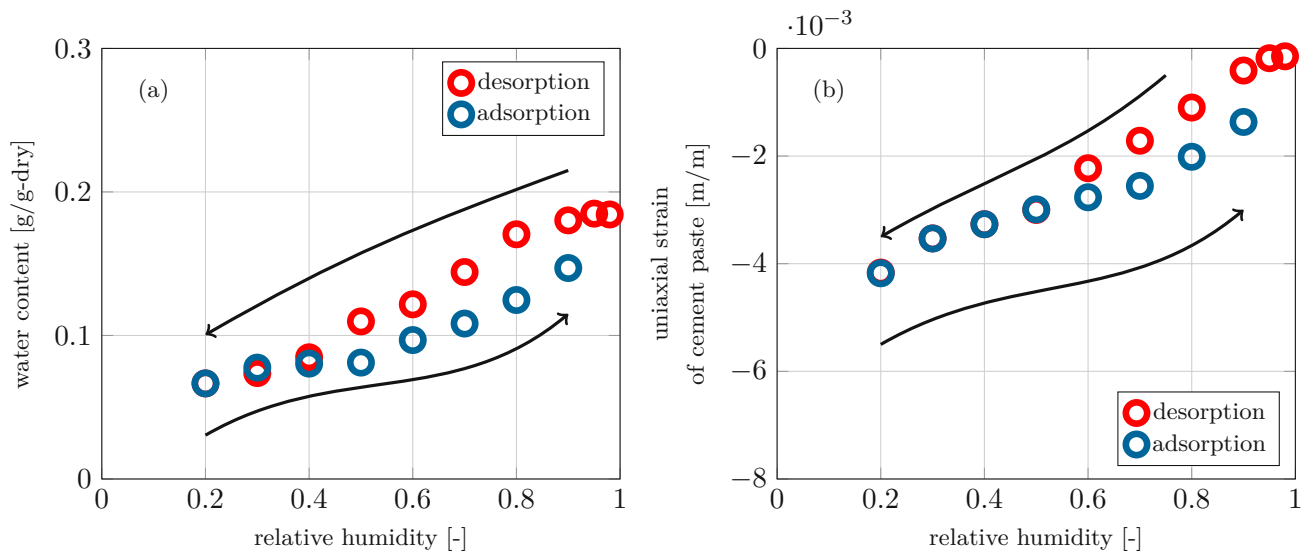


**Fig. 1.4.** Experimentally measured (a) water content and (b) deformation mature cement pastes during isothermal desorption and adsorption (Maruyama, 2010).

After the first drying and its irreversible changes, the following drying-wetting cycles appear to be reversible (Pinson et al., 2015). Therefore, before probing the irreversible phenomena taking place during the first drying, it seems reasonable to investigate the reversible cycle. Thus, in the present work, multiscale homogenization techniques will be used to study the swelling of cement paste during isothermal adsorption.

### 1.3 Outline of the thesis

The thesis is organized into several chapters, starting with the very fundamentals of continuum micromechanics, spanning all the way from both re-examination and extension of the fundamentals of continuum micromechanics, via the chemical physics-based hydration modeling of cementitious materials, to the multiscale micromechanics-enabled quantification of swelling - one of the most challenging, still fairly open topics in cement and concrete research. All these chapters are written in the format of scientific papers, being published, under revision, under review, or in preparation for publication in peer-reviewed scientific journals. In more detail,

- Chapter 2 deals with most fundamental pillars of the field of continuum micromechanics: the stress and strain average rules. Accordingly, it is generally accepted that the so-called microscopic stress and strain fields inside a representative volume element characterizing a piece of matter can be spatially averaged in order to come up with so-called macroscopic stresses and strains associated with the macroscopic material point describing the very same piece of matter. The rationale for these averaging processes, however, is much less clear than it seems on a first glance. In fact, it is current standard to derive only one of the aforementioned average rules (either on geometrical or on statical grounds), and then introduce the other merely as a definition. A remedy is given in Chapter 2, by adopting classical reasonings for the strain average rule, and then re-deriving the stress average rule from the principle of virtual power.
- While averaging provides a way from “micro” to “macro”, the opposite way, from “macro” to “micro” is standardly called concentration, localization, or downscaling,

with corresponding tensorial operators linking macroscopic strains (and stresses) to corresponding microscopic strain (and stress) fields. Again, the existence and the format of these operators are often kind of postulated, from the “structure of the underlying differential equations”, and moreover, they are simply unknown for various types of more or less complex microstructures. Remedies are formulated in Chapters 3 and 4, both giving new expressions for concentrations tensors, in two fundamentally different settings: on the one hand, for continuously fluctuating microstructures on the basis of a Green’s functions approach associated with an auxiliary problem of the Lippmann-Schwinger type (with mathematical structures known from quantum mechanics), and on the other hand, for phase-based composite-type microstructures where classical approaches such as the Mori-Tanaka estimate do not properly perform, and hence need to be complemented by stiffness tensor symmetrization techniques.

- Phase identification (in terms of occupied space and physico-mechanical behavior) is one of the most challenging tasks in applied micromechanics, where a bridge between physical chemistry/chemical physics and engineering needs to be established. In cementitious materials, phases (such as clinker, hydrates, and different types of pores) are driven through the hydration process, and corresponding hydration-dependent phase volume fractions are normally challenging to be rigorously derived, because of dependencies on temperature, mix proportions, and storage conditions. Chapter 4 presents an interesting way out of this dilemma, by introducing a new variable into the world of cement chemistry: the precipitation degree, accessible through NMR measurements quantifying water contained in different phases at different mobilities. As concerns, the physico-mechanical behavior of cementitious materials, one of the most unexplored aspects concerns nanoscopic hydrate swelling: combining theoretical aspects of Chapters 2, 3, and 4, with physical aspects of Chapter 5, Chapter 6 presents the micromechanics-guided re-evaluation of macroscopic isothermal adsorption and swelling tests, so as to quantify humidity-driven eigenstrains in the solid C-S-H.

Finally, Chapter 7 provides a summary, conclusions, and an outlook to further research avenues having been opened by the novel results achieved in the present thesis.

# Chapter 2

---

## Stress average rule derived through the principle of virtual power

**Authored by:** Nabor Jiménez Segura, Bernhard L.A. Pichler, Christian Hellmich

**Published in:** *ZAMM: Journal of Applied Mathematics and Mechanics / Zeitschrift für Angewandte Mathematik und Mechanik.*

The final publication is available at:  
<https://doi.org/10.1002/zamm.202200091>.

**Abstract:** Stress and strain average rules are the key conceptual pillars of the wide field of continuum micromechanics of materials. The aforementioned rules express that the spatial average of (micro-)stress and (micro-)strain fields throughout a microscopically finite representative volume element (RVE) are equal to the (macro-)stress and (macro-)strain values associated with the corresponding macroscopically infinitesimal volume element (macroscopic material point). According to the famous contribution of Hashin, stress and strain average rules are derived from equilibrium and compatibility conditions, together with (micro-)displacement and (micro-)traction boundary conditions associated with homogeneous (macro-)strains and (macro-)stresses, respectively. However, as, strictly speaking, only displacements *or* tractions can be described at the boundary, the remaining average rule turns out as a mere definition. We here suggest a way to do without such a definition, by resorting to the principle of virtual power as a means to guarantee mechanical equilibrium: At the boundary of the RVE, we prescribe virtual (micro-)velocities which are linked to arbitrary, but homogeneous virtual (macro-)velocities and (macro-)strain rates, while the latter are also linked, in a multilinear fashion, with the microscopic virtual strain rate fields inside the RVE. Considering, under these conditions, equivalence of the macroscopic and the microscopic expressions for the virtual power densities of the internal and the external forces yields the well-known stress average rule and, in case of microscopically uniform force fields, a volume force average rule. The same strategy applied to an RVE hosting single forces between atomistic mass points, readily yields the macroscopic “internal virial stress tensor”.

**Contribution:** Nabor Jiménez Segura: Investigation, Methodology, Formal analysis, Visualization, Writing – original draft, review & editing. Bernhard L.A. Pichler: Supervision, Conceptualization, Funding acquisition, Methodology, Formal analysis, Writing – original draft,

Writing – review & editing. Christian Hellmich: Supervision, Conceptualization, Funding acquisition, Methodology, Formal analysis, Supervision, Writing – review & editing.

**Keywords:** Continuum micromechanics of materials; Stress average rule; Strain average rule; Principle of virtual power.

## 2.1 Introduction – Motivation and Scope

Composite material mechanics (Hill, 1965b; Hashin, 1983), also referred to as continuum micromechanics (Zaoui, 2002), is a very successful and versatile branch of continuum mechanics. It describes the mechanical behavior of a representative volume element (RVE) of matter, coinciding with the infinitesimal volume of classical continuum mechanics, but being considered, at the same time, as a finite volume at the microscopic scale, see Fig. 2.1(a). Stresses and strains are introduced both at the microscopic and at the macroscopic level, and their relation is governed by average rules. Hashin (Hashin, 1963, 1965) considered fields of microstrains and microstresses depending on a microscopic location variable  $\underline{x}$ , so that the strain and stress average rules read as

$$\mathbf{E} = \frac{1}{V_{\text{RVE}}} \int_{V_{\text{RVE}}} \boldsymbol{\varepsilon}(\underline{x}) \, dV(\underline{x}), \quad (2.1)$$

$$\boldsymbol{\Sigma} = \frac{1}{V_{\text{RVE}}} \int_{V_{\text{RVE}}} \boldsymbol{\sigma}(\underline{x}) \, dV(\underline{x}), \quad (2.2)$$

with  $\boldsymbol{\varepsilon}$  standing for the microscopic linearized strain tensor,  $\boldsymbol{\sigma}$  standing for the microscopic Cauchy stress tensor,  $\mathbf{E}$  denoting the macroscopic linearized strain,  $\boldsymbol{\Sigma}$  denoting the macroscopic Cauchy stress tensor, and  $V_{\text{RVE}}$  denoting the volume of the RVE. Hashin (Hashin, 1963, 1965) showed that - in case of kinematically compatible microstrains, and of equilibrated microstresses in the absence of body forces, respectively - the relations (2.1) and (2.2) imply the following boundary conditions for the RVE:

$$\underline{\xi}(\underline{x}) = \mathbf{E} \cdot \underline{x}, \quad \forall \underline{x} \in S_{\text{RVE}}, \quad (2.3)$$

$$\underline{t}(\underline{x}) = \boldsymbol{\Sigma} \cdot \underline{n}(\underline{x}), \quad \forall \underline{x} \in S_{\text{RVE}}, \quad (2.4)$$

with  $\underline{\xi}$  as microdisplacements,  $\underline{t}$  as micro-tractions,  $\underline{n}$  as outward-oriented unit normal vector, and  $S_{\text{RVE}}$  as the surface of the RVE. Accordingly, Eqs. (2.3) and (2.4) are standardly referred to as the "Hashin boundary conditions" (Hashin, 1983). It should be noted that the rules (2.1) and (2.2) are normally applied simultaneously, and since the boundary conditions (2.3) and (2.4) cannot be applied simultaneously to one and the same RVE, the "Hashin boundary conditions" are less convincing than they might appear on first sight. In other words, one of the rules (2.1) and (2.2) needs to remain a definition, whenever the other one has been formulated on the basis of equilibrium or compatibility considerations. A very pragmatic way out of this somewhat unsatisfactory solution was proposed by Hori and Nemat-Nasser (Hori and Nemat-Nasser, 1999) by considering the RVE as a (presumably cuboidal or cylindrical) macroscopic sample undergoing a mechanical test, see Fig. 2.1(b). Hori and Nemat-Nasser consider the surface integrals over micro-tractions and micro-displacements as "natural quantities" arising from such a mechanical test. By means of micro-stress equilibrium and micro-strain compatibility, respectively, the aforementioned surface integrals are then transformed into volume integrals over stress and strain, giving way to the average rules (2.1) and (2.2). However, there are cases where the tested sample does not coincide with the RVE: In the context of ultrasonic test with different frequencies (Fritsch and Hellmich, 2007; Kohlhauser and Hellmich, 2013),

the size  $\ell$  of the RVE is governed by the wavelength  $\lambda$ , i.e. (Zaoui, 2002):  $\ell \ll \lambda$ , see Fig. 2.1(c). This situation goes beyond the reasoning of Hori and Nemat-Nasser (Hori and Nemat-Nasser, 1999).

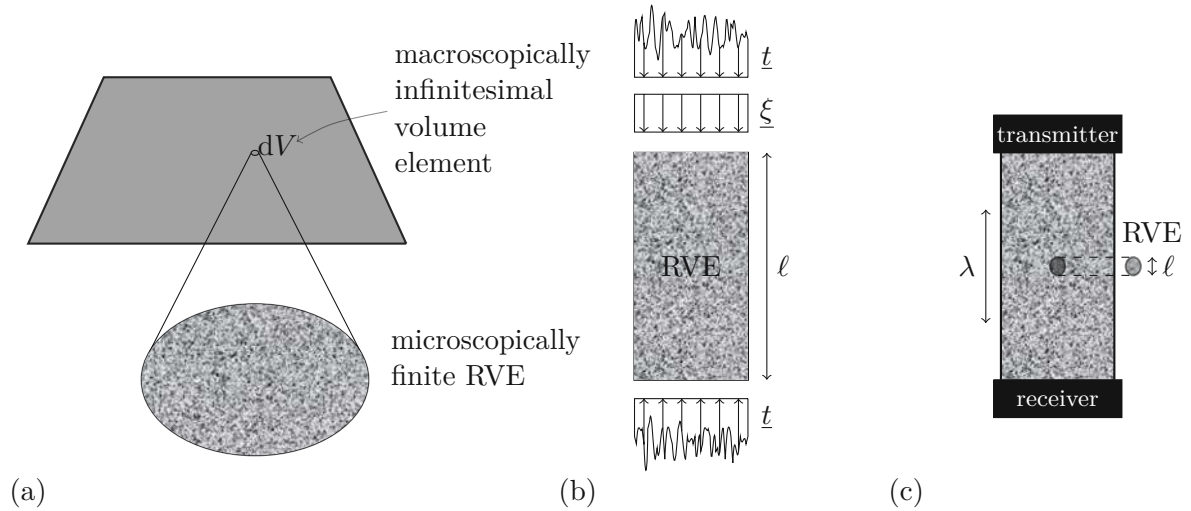


**Fig. 2.1.** Different characteristics of the representative volume element (RVE): (a) scale separation between structural scale and material scale; (b) RVE coinciding with samples undergoing a classical mechanical test (Hori and Nemat-Nasser, 1999); (c) RVE not coinciding with a sample undergoing an ultrasonic test with wavelength  $\lambda$  (Zaoui, 2002; Fritsch and Hellmich, 2007; Kohlhauser and Hellmich, 2013).

Hence, we consider the derivation of strain and stress average rules governing simultaneously the behavior of an RVE as a topic of on-going interest. In this context, we here aim at preserving the conceptual beauty of Hashin's geometrical boundary conditions leading to Eq. (2.1), while looking for a simultaneously open rigorous way to derive Eq. (2.2) from a fundamental principle of continuum mechanics. In more detail, we employ the principle of virtual power as stated by Germain (Germain, 1973) in 1973: a mechanical system is in equilibrium if the power performed by the external and internal forces on any virtual velocity field characterizing the aforementioned system vanishes. After recalling this principle for a standard macroscopic continuum mechanical system, we employ it for a microscopically finite representative volume element playing the role of an infinitesimal volume element at the macroscopic level (see Section 2.2). Thereafter, we link the microscopic virtual velocity field to the virtual quantities governing the macroscopically infinitesimal volume element, i.e. velocity and strain rate tensor (see Section 2.3). Next, the implications for computational homogenization in atomistic systems and continuum RVEs undergoing large deformations are discussed (see Section 2.4). The paper is concluded by setting our derivation in context to somehow related deliberations in the rich field of micromechanics (Section 2.5).



## 2.2 Principle of Virtual Power applied to a continuum mechanics system and its microstructurally representative volume elements

The Principle of Virtual Power (PVP) states that a mechanical system is in equilibrium if, under any virtual motion  $\check{\underline{V}}$  defining the type of mechanical system considered, the virtual power of forces associated with the mechanical system vanishes (Germain, 1972, 1973),

$$\mathcal{P}(\check{\underline{V}}) = 0, \quad (2.5)$$

with the virtual power  $\mathcal{P}$  being a multilinear form on  $\check{\underline{V}}$ . In the case of classical continuum mechanics under quasistatic conditions, the principle (2.5) takes the form (Germain, 1972, 1973),

$$\mathcal{P}^{ext}[\check{\underline{V}}(\underline{X})] + \mathcal{P}^{int}[\check{\underline{D}}(\underline{X})] = 0, \quad (2.6)$$

with the virtual power of external forces  $\mathcal{P}^{ext}$ , the virtual power of internal forces  $\mathcal{P}^{int}$ , with  $\check{\underline{V}}(\underline{X})$  being any three-dimensional continuous vector field across all (macroscopic) points  $\underline{X}$  of the continuum with volume  $V$  and surface  $S$ , and with  $\check{\underline{D}}(\underline{X})$  as the (macroscopic) virtual Eulerian strain rate tensor, mathematically reading as

$$\begin{aligned} \check{\underline{D}}(\underline{X}) &= \frac{1}{2} \left\{ \frac{\partial \check{\underline{V}}}{\partial \underline{X}}(\underline{X}) + \left[ \frac{\partial \check{\underline{V}}}{\partial \underline{X}}(\underline{X}) \right]^T \right\} \\ &= \frac{1}{2} \left\{ \text{GRAD}_X \check{\underline{V}}(\underline{X}) + [\text{GRAD}_X \check{\underline{V}}(\underline{X})]^T \right\} = \text{GRAD}_X^S \check{\underline{V}}(\underline{X}), \end{aligned} \quad (2.7)$$

whereby  $\text{GRAD}_X$  is the (macroscopic) gradient operator with respect to variable  $\underline{X}$ , and  $\text{GRAD}_X^S$  is its symmetrized counterpart.  $\mathcal{P}^{ext}$  and  $\mathcal{P}^{int}$  are linear forms on  $\check{\underline{V}}$  and  $\check{\underline{D}}$ , respectively

$$\mathcal{P}^{ext} = \int_V \underline{F}(\underline{X}) \cdot \check{\underline{V}}(\underline{X}) \, dV(\underline{X}) + \int_S \underline{T}(\underline{X}) \cdot \check{\underline{V}}(\underline{X}) \, dS(\underline{X}), \quad (2.8)$$

$$\mathcal{P}^{int} = - \int_V \underline{\Sigma}(\underline{X}) : \check{\underline{D}}(\underline{X}) \, dV(\underline{X}), \quad (2.9)$$

with  $\underline{F}$  as the (macroscopic) volume forces and  $\underline{T}$  as the (macroscopic) surface forces.

In continuum micromechanics (Zaoui, 2002), any infinitesimal volume element  $dV$  around any *macroscopic* material point  $\underline{X}$  is represented by a *microscopically* finite representative volume element (RVE) with a characteristic size  $\ell$ ; such an RVE carrying all features of a classical continuum mechanics system at the microscopic scale. In order to maintain the physical relevance of the infinitesimally small macroscopic volume elements  $dV$ , the corresponding RVEs need to be much smaller than the structural length  $\mathcal{L}$ , i.e. (Zaoui, 2002; Auriault et al., 2010):

$$\ell \ll \mathcal{L} = \frac{\|\underline{\Sigma}(\underline{X})\|}{\|[\text{GRAD}_X \underline{\Sigma}(\underline{X})]\|}. \quad (2.10)$$

Thereby, the  $\ll$ -sign typically refers to a factor (Kohlhauser and Hellmich, 2013) of 5 to 10. Applying the PVP to such an RVE yields

$$\mathcal{P}_{\text{RVE}}^{ext} = \int_{V_{\text{RVE}}} \underline{f}(\underline{x}) \cdot \check{\underline{v}}(\underline{x}) \, dV(\underline{x}) + \int_{S_{\text{RVE}}} \underline{t}(\underline{x}) \cdot \check{\underline{v}}(\underline{x}) \, dS(\underline{x}), \quad (2.11)$$

$$\mathcal{P}_{\text{RVE}}^{int} = - \int_{V_{\text{RVE}}} \underline{\sigma}(\underline{x}) : \check{\underline{d}}(\underline{x}) \, dV(\underline{x}), \quad (2.12)$$

so that

$$\int_{V_{\text{RVE}}} \underline{f}(\underline{x}) \cdot \check{\underline{v}}(\underline{x}) \, dV(\underline{x}) + \int_{S_{\text{RVE}}} \underline{t}(\underline{x}) \cdot \check{\underline{v}}(\underline{x}) \, dS(\underline{x}) - \int_{V_{\text{RVE}}} \boldsymbol{\sigma}(\underline{x}) : \check{\underline{\mathbf{d}}}(\underline{x}) \, dV(\underline{x}) = 0, \quad (2.13)$$

with  $\check{\underline{v}}$  as the microscopic virtual velocities,  $\underline{f}$  and  $\underline{t}$  as the microscopic volume and surface forces, and  $\check{\underline{\mathbf{d}}}$  as the microscopic virtual strain rates, the latter reading as

$$\begin{aligned} \check{\underline{\mathbf{d}}}(\underline{x}) &= \frac{1}{2} \left\{ \frac{\partial \check{\underline{v}}}{\partial \underline{x}}(\underline{x}) + \left[ \frac{\partial \check{\underline{v}}}{\partial \underline{x}}(\underline{x}) \right]^T \right\} \\ &= \frac{1}{2} \left\{ \text{grad}_x \check{\underline{v}}(\underline{x}) + [\text{grad}_x \check{\underline{v}}(\underline{x})]^T \right\} = \text{grad}_x^S \check{\underline{v}}(\underline{x}). \end{aligned} \quad (2.14)$$

In (2.14),  $\text{grad}_x$  denotes the microscopic gradient operator, and  $\text{grad}_x^S$  denotes its symmetrized counterpart. This operator induces the microheterogeneity size  $d$  as

$$d = \frac{\|\boldsymbol{\sigma}(\underline{X})\|}{\|[\text{grad}_x \boldsymbol{\sigma}(\underline{X})]\|} \ll \ell. \quad (2.15)$$

Thereby, the  $\ll$ -sign refers to a factor of 2 to 3 for spherical or parallel cylindrical inclusions embedded in a continuous matrix phase (Drugan and Willis, 1996; Gusev, 1997; Grimal et al., 2011). Integration by parts of the power of internal forces of the RVE according to (2.12) yields

$$\mathcal{P}_{\text{RVE}}^{\text{int}} = - \int_{V_{\text{RVE}}} \text{div}_x [\boldsymbol{\sigma}(\underline{x}) \cdot \check{\underline{v}}(\underline{x})] \, dV(\underline{x}) + \int_{V_{\text{RVE}}} \text{div}_x \boldsymbol{\sigma}(\underline{x}) \cdot \check{\underline{v}}(\underline{x}) \, dV(\underline{x}). \quad (2.16)$$

with the divergence operator standing for

$$\text{div}_x(\bullet) = \nabla_x \cdot (\bullet) \quad \text{with} \quad \nabla_x = \sum_{i=1}^3 \frac{\partial}{\partial x_i} \underline{e}_i, \quad (2.17)$$

whereby  $\underline{e}_1$ ,  $\underline{e}_2$ , and  $\underline{e}_3$  are orthonormal base vectors. Application of the divergence theorem to the first term of the right-hand side in (2.16) yields

$$- \int_{V_{\text{RVE}}} \text{div}_x [\boldsymbol{\sigma}(\underline{x}) \cdot \check{\underline{v}}(\underline{x})] \, dV(\underline{x}) = - \int_{S_{\text{RVE}}} \underline{n}(\underline{x}) \cdot \boldsymbol{\sigma}(\underline{x}) \cdot \check{\underline{v}}(\underline{x}) \, dS(\underline{x}). \quad (2.18)$$

Insertion of (2.18) into (2.16), and of the respective result into (2.13), yields, after rearrangement of the terms integrated over volumes and surfaces, respectively, the following expression:

$$\int_{V_{\text{RVE}}} \left[ \underline{f}(\underline{x}) + \text{div}_x \boldsymbol{\sigma}(\underline{x}) \right] \cdot \check{\underline{v}}(\underline{x}) \, dV(\underline{x}) + \int_{S_{\text{RVE}}} \left[ \underline{t}(\underline{x}) - \boldsymbol{\sigma}(\underline{x}) \cdot \underline{n}(\underline{x}) \right] \cdot \check{\underline{v}}(\underline{x}) \, dS(\underline{x}) = 0. \quad (2.19)$$

As (2.19) needs to hold for any virtual microscopic velocity field  $\check{\underline{v}}$ , it readily delivers equilibrium conditions for all microscopic points inside the RVE,

$$\text{div}_x \boldsymbol{\sigma}(\underline{x}) + \underline{f}(\underline{x}) = 0, \quad \forall \underline{x} \in V_{\text{RVE}}, \quad (2.20)$$

and Cauchy's fundamental theorem for the microscopic points at the surface of the RVE,

$$\underline{t}(\underline{x}) = \boldsymbol{\sigma}(\underline{x}) \cdot \underline{n}(\underline{x}), \quad \forall \underline{x} \in S_{\text{RVE}}. \quad (2.21)$$

## 2.3 Equivalence of macroscopic and microscopic expressions for internal and external power densities – stress and volume force averaging rules

Still, the RVE-related virtual powers need to be fully governed by the virtual kinematical properties of the infinitesimal volume elements  $dV(\underline{X})$  at the *macroscopic* scale, i.e. being proportional to the macroscopic location-dependent macroscopic virtual velocities and strain rates,  $\check{V}(\underline{X})$  and  $\check{D}(\underline{X})$ . Accordingly, we impose the latter two macroscopic quantities onto the RVE, in terms of the following microscopic virtual velocity fields prescribed at the boundary of the RVE,

$$\forall \underline{x} \in S_{\text{RVE}} : \quad \check{v}(\underline{x}, \underline{X}) = \check{V}(\underline{X}) + \check{D}(\underline{X}) \cdot \underline{x}, \quad (2.22)$$

noting that Eq. (2.22) can be seen as a modification and extension of the so-called ‘‘Hashin boundary conditions’’ (Hashin, 1983). Expressions (2.22) and (2.14) imply an average rule for the virtual strain rates, reading as

$$\check{D}(\underline{X}) = \frac{1}{V_{\text{RVE}}(\underline{X})} \int_{V_{\text{RVE}}(\underline{X})} \check{d}(\underline{x}, \underline{X}) \, dV(\underline{x}, \underline{X}), \quad (2.23)$$

which appears as the rate form of the well-known strain average rule, see Eq. (2.1). Note that  $dV(\underline{x}, \underline{X})$  refers to integration over the microscopic variables  $\underline{x}$ , at the macroscopic position  $\underline{X}$ . Within the RVE, the microscopic virtual strain rate needs to be proportional to the macroscopic strain rate, which we express by a multilinear downscaling relation of the form

$$\check{d}(\underline{x}, \underline{X}) = \mathbb{A}_d(\underline{x}, \underline{X}) : \check{D}(\underline{X}), \quad (2.24)$$

with a yet-to-be-determined continuous downscaling tensor field  $\mathbb{A}_d(\underline{x}, \underline{X})$ .

Identification of the RVE-related and macroscopic volume element-related expressions for the power densities of internal forces, as derived from (2.9), (2.12), and (2.24), yields

$$\pi^{\text{int}}(\underline{X}) = -\Sigma(\underline{X}) : \check{D}(\underline{X}) \stackrel{!}{=} \pi_{\text{RVE}}^{\text{int}}(\underline{X}) = -\frac{1}{V_{\text{RVE}}(\underline{X})} \int_{V_{\text{RVE}}(\underline{X})} \boldsymbol{\sigma}(\underline{x}, \underline{X}) : \mathbb{A}_d(\underline{x}, \underline{X}) \, dV(\underline{x}, \underline{X}) : \check{D}(\underline{X}), \quad (2.25)$$

where  $\stackrel{!}{=}$  indicates the bridging of scales. Namely, the internal and external power densities remain the very same physical quantities, regardless of whether they are expressed in terms of macroscopic or microscopic virtual velocities or strain rates. An alternative expression for the internal power density as a function of the macroscopic virtual strain rate is obtained from insertion of (2.18) into the first integral on the right-hand side of (2.16), followed by specifying the corresponding result for the boundary conditions (2.22) and the equilibrium conditions (2.20). Accordingly, this alternative power density expression reads as

$$\begin{aligned} \pi^{\text{int}}(\underline{X}) &= -\frac{1}{V_{\text{RVE}}(\underline{X})} \int_{S_{\text{RVE}}(\underline{X})} \left[ \check{V}(\underline{X}) + \underline{x} \cdot \check{D}(\underline{X}) \right] \cdot \boldsymbol{\sigma}(\underline{x}, \underline{X}) \cdot \underline{n}(\underline{x}, \underline{X}) \, dS(\underline{x}, \underline{X}) \\ &\quad - \frac{1}{V_{\text{RVE}}(\underline{X})} \int_{V_{\text{RVE}}(\underline{X})} \left[ \underline{f}(\underline{x}, \underline{X}) \right] \cdot \check{v}(\underline{x}, \underline{X}) \, dV(\underline{x}, \underline{X}). \end{aligned} \quad (2.26)$$

Taking the macroscopic virtual strain rate out of the first integral of (2.26), and applying the

divergence theorem to this first integral, while considering equilibrium condition (2.20), yields

$$\begin{aligned} \pi^{int}(\underline{X}) &= - \left[ \frac{1}{V_{RVE}(\underline{X})} \int_{V_{RVE}(\underline{X})} \boldsymbol{\sigma}(\underline{x}, \underline{X}) \, dV(\underline{x}, \underline{X}) \right] : \check{\mathbf{D}}(\underline{X}) \\ &\quad - \frac{1}{V_{RVE}(\underline{X})} \int_{V_{RVE}(\underline{X})} \underline{f}(\underline{x}, \underline{X}) \cdot \left[ \underline{v}(\underline{x}, \underline{X}) - \check{\mathbf{V}}(\underline{X}) - \check{\mathbf{D}}(\underline{X}) \cdot \underline{x} \right] \, dV(\underline{x}, \underline{X}) \end{aligned} \quad (2.27)$$

Identity of (2.27) and (2.25) requires the concentration tensor  $\mathbb{A}_d$  to be equal to the identity tensor

$$\mathbb{A}_d(\underline{x}, \underline{X}) = \mathbb{1} \quad \rightarrow \quad \check{\mathbf{d}}(\underline{x}, \underline{X}) = \check{\mathbf{D}}(\underline{X}), \quad \forall \underline{x} \in V_{RVE}(\underline{X}), \quad (2.28)$$

and the expression (2.22) to be not only valid at the boundary, but also throughout the entire volume of the RVE,

$$\check{\underline{v}}(\underline{x}, \underline{X}) = \check{\mathbf{V}}(\underline{X}) + \check{\mathbf{D}}(\underline{X}) \cdot \underline{x}, \quad \forall \underline{x} \in V_{RVE}(\underline{X}). \quad (2.29)$$

Requirement (2.28), together with (2.25), yields the classical stress average rule, reading as

$$\underline{\Sigma}(\underline{X}) = \frac{1}{V_{RVE}(\underline{X})} \int_{V_{RVE}(\underline{X})} \boldsymbol{\sigma}(\underline{x}, \underline{X}) \, dV(\underline{x}, \underline{X}). \quad (2.30)$$

We note that the derivation of Eq. (2.30), different from the classical derivations (Hashin, 1983; Zaoui, 2002), did without the requirement of vanishing volume forces  $\underline{f}$ .

As regards the latter, the equivalence of the macroscopic and microscopic expressions for the external power density, i.e. of (2.8) and (2.11), mathematically reads as

$$\pi^{ext}(\underline{X}) = \underline{F}(\underline{X}) \cdot \check{\mathbf{V}}(\underline{X}) \stackrel{!}{=} \pi_{RVE}^{ext}(\underline{X}) = \frac{1}{V_{RVE}(\underline{X})} \int_{V_{RVE}(\underline{X})} \underline{f}(\underline{x}, \underline{X}) \cdot \check{\underline{v}}(\underline{x}, \underline{X}) \, dV(\underline{x}, \underline{X}). \quad (2.31)$$

Inserting (2.29) into (2.31) results in

$$\begin{aligned} \underline{F}(\underline{X}) \cdot \check{\mathbf{V}}(\underline{X}) &= \left[ \frac{1}{V_{RVE}(\underline{X})} \int_{V_{RVE}(\underline{X})} \underline{f}(\underline{x}, \underline{X}) \, dV(\underline{x}, \underline{X}) \right] \cdot \check{\mathbf{V}}(\underline{X}) \\ &\quad + \left[ \frac{1}{V_{RVE}(\underline{X})} \int_{V_{RVE}(\underline{X})} \underline{f}(\underline{x}, \underline{X}) \otimes \underline{x} \, dV(\underline{x}, \underline{X}) \right] : \check{\mathbf{D}}(\underline{X}). \end{aligned} \quad (2.32)$$

We will show in the following that the term in the second pair of square brackets will vanish if (i) the microscopic volume forces arise from a microscopically uniform field (such as the gravitational field), and if (ii) the microscopic location is measured from the center of gravity of the RVE. As a microscopically parallel force field, i.e. as a microscopic field of uniform direction, we choose the gravitational field, which reads mathematically as

$$\underline{f}(\underline{x}, \underline{X}) = \underline{g}(\underline{X}) \rho(\underline{x}, \underline{X}), \quad (2.33)$$

with the gravitational acceleration  $\underline{g}$  and the microscopic mass density  $\rho$ . Specifying the term in the second pair of square brackets in (2.32), for the parallel force field (2.33), yields

$$\underline{g}(\underline{X}) \otimes \left[ \frac{1}{V_{RVE}(\underline{X})} \int_{V_{RVE}(\underline{X})} \rho(\underline{x}, \underline{X}) \underline{x} \, dV(\underline{x}, \underline{X}) \right]. \quad (2.34)$$

We are left with showing that the integral in Eq. (2.34) vanishes if  $\underline{x}$  is measured from the center of gravity of the RVE. Therefore, we adopt a location vector  $\tilde{\underline{x}}$  measured from an arbitrary origin, locating the center of gravity at  $\tilde{\underline{x}}_{CG}$ . According to the very definition of the center of gravity,  $\tilde{\underline{x}}_{CG}$  needs to fulfill

$$\int_{V_{\text{RVE}}(\underline{X})} \rho(\tilde{\underline{x}}, \underline{X}) \tilde{\underline{x}} \, dV(\tilde{\underline{x}}, \underline{X}) = \tilde{\underline{x}}_{CG} \int_{V_{\text{RVE}}(\underline{X})} \rho(\tilde{\underline{x}}, \underline{X}) \, dV(\tilde{\underline{x}}, \underline{X}), \quad (2.35)$$

and since  $\underline{x}$  is measured from the center of gravity, it is related to  $\tilde{\underline{x}}$  and  $\tilde{\underline{x}}_{CG}$  through

$$\underline{x} = \tilde{\underline{x}} - \tilde{\underline{x}}_{CG}. \quad (2.36)$$

Use of Eqs. (2.36) and (2.35) in Eq. (2.34) yields

$$\int_{V_{\text{RVE}}} \rho(\underline{x}, \underline{X}) \underline{x} \, dV(\underline{x}, \underline{X}) = \int_{V_{\text{RVE}}} \rho(\tilde{\underline{x}}, \underline{X}) (\tilde{\underline{x}} - \tilde{\underline{x}}_{CG}) \, dV(\tilde{\underline{x}}, \underline{X}) = (\tilde{\underline{x}}_{CG} - \tilde{\underline{x}}_{CG}) \int_{V_{\text{RVE}}} \rho(\tilde{\underline{x}}, \underline{X}) \, dV(\tilde{\underline{x}}, \underline{X}) = 0. \quad (2.37)$$

Accordingly, a microscopically parallel force field (i.e. one with a uniform direction at the microscale) delivers the following volume force average rule

$$\underline{F}(\underline{X}) = \frac{1}{V_{\text{RVE}}(\underline{X})} \int_{V_{\text{RVE}}(\underline{X})} \underline{f}(\underline{x}, \underline{X}) \, dV(\underline{x}, \underline{X}). \quad (2.38)$$

## 2.4 Implications for computational homogenization: internal virial stresses of atomistic systems, and continuum RVEs undergoing large deformations

Our derivation of the stress average rule also has interesting implications with respect to computational homogenization. The latter is definitely required when it comes to homogenization over discrete mechanical systems, such as atoms represented by mass points in a molecular dynamics setting (Chen and Fish, 2006). In such a system, hosted within an RVE, the resultant internal force acting on the  $i$ -th atom of the assembly is the sum of all interaction forces  $\underline{f}_{ij}$  between this atom and all the other atoms in the RVE. This reads mathematically as

$$\underline{f}_i^{\text{int}} = \sum_{j(\neq i)} \underline{f}_{ij}^{\text{int}}, \quad (2.39)$$

with the law of action and reaction (Newton's third law) requiring that (Salençon, 2018; Newton, 1687)

$$\underline{f}_{ij}^{\text{int}} = -\underline{f}_{ji}^{\text{int}}, \quad \text{with} \quad \underline{f}_{ij} \times \underline{x}_{ij} = 0, \quad (2.40)$$

whereby

$$\underline{x}_{ij} = \underline{x}_j - \underline{x}_i \quad (2.41)$$

denotes the vector pointing from position  $\underline{x}_i$  to  $\underline{x}_j$ .

The virtual power density of internal forces acting on the atomic mass points hosted inside an RVE of volume  $V_{\text{RVE}}$  reads as

$$\pi_{\text{RVE}}^{\text{int}} = \frac{1}{V_{\text{RVE}}} \sum_i \underline{f}_i^{\text{int}} \cdot \check{\underline{v}}(\underline{x}_i) = \frac{1}{V_{\text{RVE}}} \sum_i \left( \sum_{j(\neq i)} \underline{f}_{ij}^{\text{int}} \right) \cdot \check{\underline{v}}(\underline{x}_i), \quad (2.42)$$

where the virtual velocity  $\check{\underline{v}}$ , following Eq. (2.29), appears as the mathematical tool for homogenizing the discrete mechanical systems made of mass points representing single atoms. Accordingly, specification of Eq. (2.29) for  $\underline{x} = \underline{x}_i$ , and insertion of the result into Eq. (2.42) yields

$$\pi_{\text{RVE}}^{\text{int}} = \frac{1}{V_{\text{RVE}}} \sum_i \left( \sum_{j(\neq i)} \underline{f}_{ij}^{\text{int}} \right) \cdot (\check{\underline{V}} + \check{\underline{D}} \cdot \underline{x}_i) = \frac{1}{V_{\text{RVE}}} \left[ \sum_i \left( \sum_{j(\neq i)} \underline{f}_{ij}^{\text{int}} \right) \otimes \underline{x}_i \right] : \check{\underline{D}}. \quad (2.43)$$

Setting equal Eq. (2.43) with the macroscopic ‘‘homogenized’’ continuum mechanics expression for the power density of internal forces, see the left portion of Eq. (25), yields the macroscopic Cauchy stress as

$$\underline{\Sigma} = -\frac{1}{V_{\text{RVE}}} \left[ \sum_i \left( \sum_{j(\neq i)} \underline{f}_{ij}^{\text{int}} \right) \otimes \underline{x}_i \right], \quad (2.44)$$

which is fully equivalent with the expressions which were quite recently provided by Zhou (Zhou, 2003) and Chen and Fish (Chen and Fish, 2006). Actually, an only slight formalistic difference in the latter references arises from the use of Eq. (2.41) in (2.44), leading to the following alternative format for the macroscopic stresses

$$\underline{\Sigma} = \frac{1}{2V_{\text{RVE}}} \left[ \sum_i \left( \sum_{j(\neq i)} \underline{x}_{ij} \otimes \underline{f}_{ij}^{\text{int}} \right) \right], \quad (2.45)$$

whereby we have made use of Eq. (2.40) and, consequently, of  $\underline{f}_{ij} \otimes \underline{x}_{ij} = \underline{f}_{ji} \otimes \underline{x}_{ji}$ .

We note the brevity and elegance of our approach to the homogenized stresses of Eq. (2.45), when compared to the more expensive derivations of Zhou (Zhou, 2003) and Chen and Fish (Chen and Fish, 2006). In fact, Chen and Fish (Chen and Fish, 2006) applied an asymptotic expansion-based homogenization approach to a periodic discrete system of atomic mass points, while Zhou (Zhou, 2003) started with formulating the balance of linear momentum in terms of the macroscopic spatial gradient of the homogenized stress, on the one hand, and of a discrete system of mass points, on the other hand. Subsequent Fourier transformation of the aforementioned formulation, followed by a particular inversion technique (Cormier et al., 2001), yields an explicit formula for the macroscopic stress, which eventually turns out to be fully equivalent to Eq. (2.45). In this context, Zhou (Zhou, 2003) particularly emphasizes that the macroscopic Cauchy stresses according to Eq. (2.45) are only related to the interaction forces between atomic mass points, and do not depend on an additional kinetics energy term which is often motivated by the famous 1870 paper of Clausius (Clausius, 1870). Zhou’s reasoning is fully consistent with our derivation of Eq. (2.45); and we may also note that, already as early as 1897, Finger (Finger, 1897) pointed out that mechanical stresses are only associated with the internal virial, i.e. the interaction forces between point forces, and not with additional kinetic energy terms. In this sense, the macroscopic stresses Eq. (2.45) may be appropriately called ‘‘internal virial stresses’’ or ‘‘interatomic virial stresses’’.

Computational homogenization in the classical narrower sense relates to continuous systems undergoing large deformations; and the average rule for the Cauchy stress according to Eq. (2.30) is indeed valid, regardless of whether the system has undergone small or large deformations leading to its current configuration. Still, for the study of actual material behavior, the stress average rule needs to be complemented by relations pertaining to geometric compatibility and (micro-)constitutive behavior. As regards the former, the virtual strain rate average rule (2.23) naturally motivates to introduce an actual strain rate average rule of

the format (Morin et al., 2018, 2021)

$$\mathbf{D}(\underline{X}) = \frac{1}{V_{\text{RVE}}} \int_{V_{\text{RVE}}} \mathbf{d}(\underline{x}, \underline{X}) \, dV(\underline{x}, \underline{X}), \quad (2.46)$$

and temporal integration over an arbitrary succession of such strain rates allows for the representation of any large strain deformation (Morin et al., 2018, 2021). As regards constitutive modeling, Eq. (2.46) can be complemented by thermodynamically consistent, microscopic hypoelasticity, where microscopic strain rates arise from the action of objective micro-stress rates (Morin et al., 2018, 2021; Truesdell, 1955; Rajagopal and Srinivasa, 2009)

$$\mathbf{d} = \rho \frac{\partial^2 G_\rho}{\partial \boldsymbol{\sigma} \partial \boldsymbol{\sigma}} : (\dot{\boldsymbol{\sigma}} + \boldsymbol{\sigma} \cdot \boldsymbol{\omega} - \boldsymbol{\omega} \cdot \boldsymbol{\sigma}), \quad (2.47)$$

with the spin tensor  $\boldsymbol{\omega}$ , the microscopic Gibbs potential per unit mass,  $G_\rho$ , and the partial temporal derivative of the stress tensor,  $\dot{\boldsymbol{\sigma}}$ . Based on the stress average rule (2.30), as well as on kinematic compatibility (2.46) and (micro-)constitutive behavior (2.47), a complete formalism for up and downscaling of stresses, strain rates, and spins can be derived (Morin et al., 2018, 2021, 2015). This formalism allows for rigid body motions of microstructural entities, which may evolve independently of the overall macroscopic deformation state. The latter phenomenon is called non-affine microstructural deformation, and such deformation patterns are repeatedly encountered, typically so in biological materials (Krasny et al., 2017). In the more particular case of affine deformations where the overall elastic energy is fully governed by the deformation gradient (linking the current to the reference configuration), the Cauchy stresses can be transformed into Piola-Kirchhoff stresses, along with the very popular hyperelastic formulations linking Piola-Kirchhoff stresses to Green-Lagrange-strains. For this case, there exists a very rich scientific literature on stress and strain averaging rules, as collected in pertinent review papers, such as the one provided by Saeb et al. (Saeb et al., 2016).

## 2.5 Discussion and Conclusion

Widening the perspective on the classical stress average rule in micromechanics, beyond Hashin's idea (Hashin, 1983; Zaoui, 2002; Hashin, 1963, 1965) of an equilibrated RVE subjected to homogeneous stress boundary conditions (so that the strain average rule becomes a mere definition) and also beyond the straightforward identification of an RVE with a mechanically tested sample on which average traction forces are measured (Hori and Nemat-Nasser, 1999), we here derived the stress average rule from the principle of virtual power. In this context, we note that we applied the PVP not only to the microscopically finite RVE itself, but also to the macroscopic system consisting of infinitely many such RVEs seen as infinitesimal volume elements. This way, our derivation does without prescribing (micro-)tractions at the boundary of the RVE, be they related to homogeneous (macroscopic) stresses or to experimental measurements. The main theoretical tool enabling this independence are the relations (2.22) and (2.23), linking macroscopic and microscopic virtual velocities and their symmetric gradients. In this sense, our derivation obviously extends the application range of the stress average rule beyond the confines resulting from its classical derivation, and our new derivation also upgrades the stress average rule from a "useful definition" to a theoretically sound result arising from the most fundamental principle in continuum mechanics. This gives further conceptual credibility concerning the use of this rule for many material systems



described by classical Mori-Tanaka (Mori and Tanaka, 1973; Benveniste, 1987) or self-consistent (Kröner, 1958; Zaoui, 2002) homogenization schemes. These schemes are based on the stress average rule, and they are applied all the way from construction materials, such as concrete or wood (Bernard et al., 2003; Pichler and Hellmich, 2011; Hofstetter et al., 2005), to biological and biomedical materials, such as bone or ceramic tissue engineering scaffolds (Hellmich and Ulm, 2002; Fritsch and Hellmich, 2007; Fritsch et al., 2009).

We are aware that both the stress average rule (2.30), and even the less classical volume force relation (2.32) have been reported in the open literature, often in the context of the so-called Hill's lemma (Hill, 1963), and most clearly so by Nicot et al. (Nicot et al., 2017). However, the key aspect of the present contribution is to not take the stress average rule as granted (Nicot et al. (Nicot et al., 2017) introduce it as a *definition*), but to employ the PVP as a theoretical means for exploring the (micro-)equilibrium of an RVE the virtual kinematics of which is fully governed by two macroscopic quantities: the macroscopic virtual velocity and its symmetric gradient (i.e. the macroscopic virtual Eulerian strain rate tensor). Then, the stress average rule and the volume force average rule for a microscopically parallel volume force field arise as *results*.

This use of the PVP to explore equilibrium conditions (or in the dynamic case, motion rules) is the target already of the original paper of Germain (Germain, 1973), where he covered classical and second-order continua. This example has been followed by very many examples from different branches of the rich field of mechanics and beyond, such as second-order fluid-solid interaction or poromechanics (Eremeyev and Altenbach, 2014; Sciarra et al., 2007), structural mechanics (Touratier, 1991; Höller et al., 2019; Zhang et al., 2017), bio-macromolecule homogenization (Kalliauer et al., 2020), or elastic parameter homogenization (Grédiac et al., 2006).

# Chapter 3

---

## A Green's function-based approach to the concentration tensor fields in complex elastic microstructures

**Authored by:** Nabor Jiménez Segura, Bernhard L.A. Pichler, Christian Hellmich

**Publication outlook:** At the time of finalizing the thesis, this has been submitted to *European Journal of Mechanics - A/Solids*, currently under revision.

**Abstract:** Computational homogenization based on FEM or FFT models are the gold standard when it comes to homogenization over a representative volume element (RVE), of so-called complex material microstructures, i.e. such which cannot be satisfactorily represented by an assemblage of homogeneous subdomains called phases. As a complement to the aforementioned methods, which depend on the boundary conditions applied to the RVE and which, as a rule, do not give direct access to the macro-micro-relations in terms of concentration tensors, we here introduce a Green's function-based homogenization method for complex microstructures: Inspired by the ideas underlying traditional phase-based homogenization schemes, such as the Mori-Tanaka or the self-consistent model, the new method rests on mapping, through the strain average rule, the microscopic strain fields associated with an auxiliary problem to the macroscopic strains subjected to the RVE. Thereby, the auxiliary problem is defined on a homogeneous infinite matrix subjected to homogeneous auxiliary strains and to inhomogeneous (fluctuating) polarization stresses representing the fluctuations of the microstiffness field, i.e. the complex microstructure within the RVE. The corresponding microscopic strains appear as the solution of a Fredholm integral equation, delivering a multilinear operator linking the homogeneous auxiliary strains to the microscopic strains. This operator, together with the aforementioned mapping, eventually allows for completing the model in terms of concentration tensor and homogenized stiffness quantification. This is illustrated by example of a harmonically fluctuating microstructure, whereby the corresponding singular convolution integrals are evaluated from the solution of the Poisson's equation, and this evaluation strategy is then verified through a Cauchy principal value analysis.

**Contribution:** Nabor Jiménez Segura: Investigation, Methodology, Formal analysis, Computation, Visualization, Writing – original draft, review & editing. Bernhard L.A. Pichler:

Supervision, Conceptualization, Funding acquisition, Methodology, Formal analysis, Writing – original draft, Writing – review & editing. Christian Hellmich: Supervision, Conceptualization, Funding acquisition, Methodology, Formal analysis, Supervision, Writing – review & editing.

**Keywords:** Complex microstructure; Green's function; Concentration tensor; Homogenized stiffness; Fredholm integral equation of the second kind; Harmonically fluctuating micro elasticity.

### 3.1 Introduction – Motivation and Scope

The main problem in the wide field of micromechanics of materials (Hill, 1963; Zaoui, 2002) is to quantify the effect of mechanical property distribution throughout the microstructures filling a so-called representative volume element (RVE), on the overall mechanical properties of this RVE, i.e. the properties linking the macroscopic strains (being the average over the microscopic strains inside the RVE) to the macroscopic stresses (being the average over the microscopic stresses inside the RVE). Restricting the present contribution to the case of linear elasticity, the problem comprises the following mathematical relations (Zaoui, 2002):

- geometrical boundary conditions prescribed at the boundary of the RVE,  $S_{\text{RVE}}$ , in the form proposed by Hashin (1983)

$$\underline{u}(\underline{x}) = \mathbf{E} \cdot \underline{x}, \quad \forall \underline{x} \in S_{\text{RVE}}, \quad (3.1)$$

with  $\underline{x}$  denoting the microscopic location vector, with  $\underline{u}$  denoting the microscopic displacement vector, and with  $\mathbf{E}$  denoting the macroscopic strain tensor, which is independent of the location  $\underline{x}$ . Boundary conditions (3.1) imply the validity of the strain average rule (Hashin, 1963, 1965, 1983)

$$\mathbf{E} = \frac{1}{V_{\text{RVE}}} \int_{V_{\text{RVE}}} \boldsymbol{\varepsilon}(\underline{x}) \, dV(\underline{x}) = \langle \boldsymbol{\varepsilon} \rangle, \quad (3.2)$$

where  $\boldsymbol{\varepsilon}$  denotes the microscopic linearized strain tensors, defined as the symmetric part of the microscopic gradient of the displacement field  $u(\underline{x})$ , i.e.

$$\boldsymbol{\varepsilon}(\underline{x}) = \frac{1}{2} \left\{ \text{grad}_{\underline{x}} \underline{u}(\underline{x}) + [\text{grad}_{\underline{x}} \underline{u}(\underline{x})]^T \right\} = \text{grad}_{\underline{x}}^S \underline{u}(\underline{x}); \quad (3.3)$$

- the microscopic elastic law being a function of the microstructural position vector  $\underline{x}$

$$\boldsymbol{\sigma}(\underline{x}) = \mathfrak{c}(\underline{x}) : \boldsymbol{\varepsilon}(\underline{x}), \quad (3.4)$$

with the microscopic stress tensor  $\boldsymbol{\sigma}$  and the microscopic stiffness tensor  $\mathfrak{c}$ ;

- equilibrium conditions

$$\nabla_{\underline{x}} \cdot \boldsymbol{\sigma}(\underline{x}) + \underline{f}(\underline{x}) = 0, \quad \forall \underline{x} \in V_{\text{RVE}}, \quad (3.5)$$

where  $\nabla_{\underline{x}}$  stands for the nabla operator and  $\underline{f}$  denotes the volume forces;

- the equivalence of macroscopic and microscopic expressions for virtual power densities of internal forces (Jiménez Segura et al., 2022b), which, together with (3.5), yields the well-known stress average rule as (Hill, 1963; Zaoui, 2002)

$$\boldsymbol{\Sigma} = \frac{1}{V_{\text{RVE}}} \int_{V_{\text{RVE}}} \boldsymbol{\sigma}(\underline{x}) \, dV(\underline{x}) = \langle \boldsymbol{\sigma} \rangle; \quad (3.6)$$

- the strain concentration (or downscaling) relation linking, in a multilinear way, the macroscopic to the microscopic strain field (Zaoui, 2002; Hill, 1963)

$$\boldsymbol{\varepsilon}(\underline{x}) = \mathbb{A}(\underline{x}) : \mathbf{E}, \quad (3.7)$$

where  $\mathbb{A}$  is the concentration (or downscaling) tensor;

- the macroscopic elastic law, which follows from (3.4), (3.6), and (3.7) as

$$\boldsymbol{\Sigma} = \mathbb{C}^{hom} : \mathbf{E}, \quad (3.8)$$

with the homogenized stiffness tensor reading as (Zaoui, 2002; Hill, 1963)

$$\mathbb{C}^{hom} = \frac{1}{V_{RVE}} \int_{V_{RVE}} \mathbb{c}(\underline{x}) : \mathbb{A}(\underline{x}) \, dV(\underline{x}). \quad (3.9)$$

The classical approach for making the problem (3.1)–(3.9) tractable is to restrict the discussion to  $N_r$  homogeneous subdomains or phases within the RVE. Accordingly, the general microstiffness distribution  $\mathbb{c}(\underline{x})$  is replaced by a finite number of microstiffness tensors  $\mathbb{c}_r$ ,  $r = 1, \dots, N_r$ , which characterize phases of different shapes, typically represented by means of ellipsoids. The strains in the latter are approximated from the solutions of Eshelby's matrix-inhomogeneity problem (Eshelby, 1957), and combination of these solutions with the strain average rule specified for a finite number of phases leads to the well-known Mori-Tabaka or self-consistent models (Kröner, 1958; Mori and Tanaka, 1973; Benveniste, 1987; Benveniste et al., 1991), with many applications in a variety of disciplines, including construction and biomedical engineering (Hofstetter et al., 2005; Bernard et al., 2003; Pichler and Hellmich, 2011; Hellmich et al., 2004; Fritsch and Hellmich, 2007).

Still, there is interest in homogenizing over non-uniform stiffness distributions  $\mathbb{c}(\underline{x})$ ; or in other words, over micro-heterogeneous materials with complex microstructures, i.e. such microstructures which cannot be satisfactorily represented by an assemblage of phases as mentioned before. In this context, the most popular approach is based on the Finite Element Method - FEM (Zienkiewicz et al., 2005). It involves discretizing the RVE into very many finite elements, and subjecting it to suitable boundary conditions (Moës et al., 2003; Pahr and Zysset, 2008; Scheiner et al., 2009; Grimal et al., 2011). The latter may be homogeneous, as in (3.1), or periodic. The results of this type of so-called computational homogenization depend on both the discretization level and the chosen boundary conditions, which requires careful sensitivity analyses to be carried out when aiming at quantitatively reliable results. Also, the computational effort increases with the square of the degrees of freedom, rendering a detailed representation of the microstructure as computationally very expensive. As a remedy to both the discretization and the CPU challenges, FFT-based homogenization schemes based on the Lippmann-Schwinger equation (Lippmann and Schwinger, 1950) have emerged as an interesting alternative to the FEM, in particular so when it comes to image-based computational homogenization (Moulinec and Suquet, 1998; Brisard and Dormieux, 2010; Cai et al., 2019). Such FFT methods are based on a voxel representation of the microstructure, with the elastic properties being constant over one voxel.

Yet, directing our attention back to (3.1)–(3.9), we observe that both FEM and FFT-based homogenization techniques primarily focus on the homogenized stiffness tensor  $\mathbb{C}^{hom}$ , somewhat neglecting the concentration tensor field  $\mathbb{A}$ . However, the latter quantity, giving access to microscopic stress and strain fields, is of great interest as well, in particular so as concerns upscaling of elasto-brittle material behavior (Fritsch et al., 2009; Sanahuja et al.,

2010; Fritsch et al., 2013; Königsberger et al., 2018; Wolfram et al., 2022), or of eigenstrains and eigenstresses (Levin, 1967; Rosen and Hashin, 1970; Wang et al., 2018).

This motivates the present paper, presenting a novel way to derive strain concentration tensor fields  $\mathbb{A}(\underline{x})$ , from a given microstiffness distribution  $\mathbb{c}(\underline{x})$  characterizing a complex microstructure. For this purpose, we adopt a key idea underlying the classical phase-based homogenization approaches such as the Mori-Tanaka or the self-consistent scheme, namely the introduction of an auxiliary problem defined on an infinite elastic domain, and the suitable combination of such an auxiliary problem with the strain average rule (3.2). In this way, we can resort to fundamental elastic solutions in the form of Green's functions, while also circumventing the rather awkward dependence of homogenization results on the chosen boundary conditions, as encountered with FEM- and FFT-based computational homogenization approaches. Accordingly, the paper is organized as follows: Section 2 introduces an auxiliary problem on an infinite elastic domain, and its relation to the strain average rule reflecting the geometrical compatibility throughout the microscopically finite RVE. Section 3 covers a Green's function-based solution to the auxiliary problem of Section 2. After an illustrative example for a microstructure with harmonically fluctuating bulk moduli, given in Section 4, the paper is concluded in Section 5.

### 3.2 An auxiliary problem on an infinite domain, and its relation to the RVE

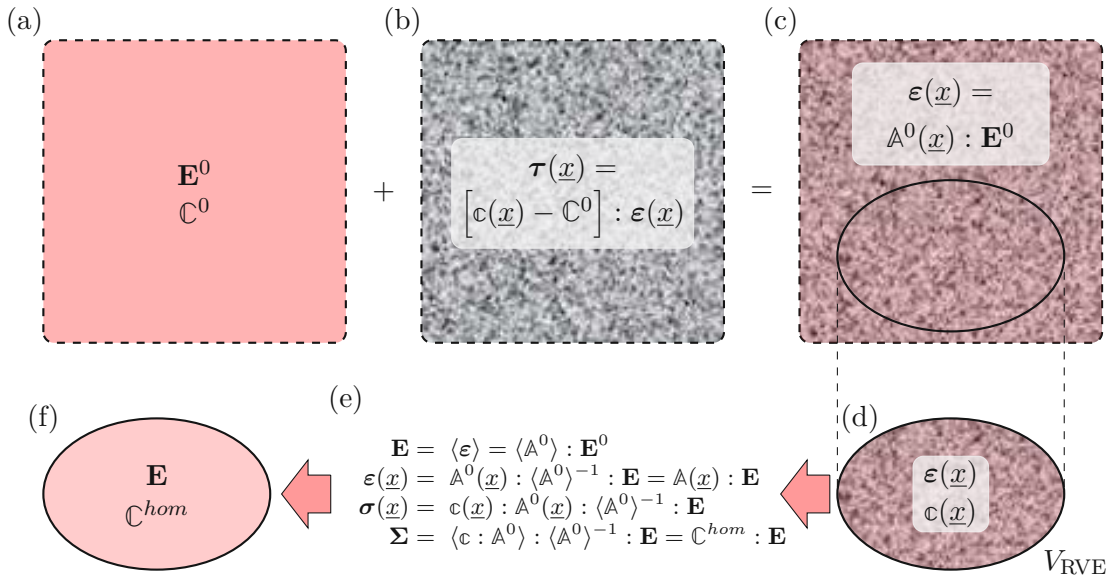


**Fig. 3.1.** Illustration of elements making up the new homogenization scheme: (a) infinite homogeneous elastic matrix of stiffness  $\mathbb{C}^0$  subjected to background (auxiliary) strains  $\mathbf{E}^0$ ; (b) same matrix undergoing equilibrated (polarization) stresses which are equivalent to the effect of fluctuations  $(\mathbb{c}(\underline{x}) - \mathbb{C}^0)$  in microstiffness,  $\mathbb{c}(\underline{x})$ , around the homogeneous stiffness  $\mathbb{C}^0$ , (c) sum of load cases (a) and (b); (d) selection of corresponding microstrains and microstiffnesses within a finite domain (RVE) characterizing the microheterogeneous material; (e) strain averaging over RVE, with  $\langle \bullet \rangle = \frac{1}{V_{RVE}} \int_{V_{RVE}} \bullet(\underline{x}) dV(\underline{x})$ , and corresponding concentration and homogenization formulae; (f) macroscopic elastic representation of RVE.

Traditional phase-based micromechanical approaches, such as the Mori-Tanaka or the

self-consistent estimates, are built on the solution of Eshelby's matrix-inhomogeneity problem, where an ellipsoidal inhomogeneity of a specific stiffness is embedded into an infinite matrix of yet another stiffness. The latter matrix is remotely subjected to some auxiliary strains  $\mathbf{E}^0$ . The solution of Eshelby (1957) then relates the auxiliary strains to the homogeneous strains  $\boldsymbol{\varepsilon}^I$  in the inhomogeneity, according to

$$\boldsymbol{\varepsilon}^I = \mathbb{A}^{0,I} : \mathbf{E}^0, \quad (3.10)$$

with  $\mathbb{A}^{0,I}$  as the concentration tensor associated with inhomogeneity  $I$  embedded in an infinite matrix subjected to  $\mathbf{E}^0$ .  $\mathbb{A}^{0,I}$  depends on the stiffness contrast between inhomogeneity and matrix, as well as on the shape of the inhomogeneity and its orientation with respect to the material directions of the matrix. In the traditional approach,  $\boldsymbol{\varepsilon}^I$  is then associated to strains in an ellipsoidal phase inside the RVE, and different inhomogeneities which are all embedded in the same type of matrix are introduced so as to consider different phases within the RVE.

However, as we presently wish to go beyond phase assemblages, we need to extend the auxiliary problem (3.10) beyond homogeneous ellipsoidal domain-related strain  $\boldsymbol{\varepsilon}^I$  and, instead, introduce a general strain field of the form

$$\boldsymbol{\varepsilon}(\underline{x}) = \mathbb{A}^0(\underline{x}) : \mathbf{E}^0, \quad (3.11)$$

with  $\mathbb{A}^0$  as a concentration tensor field associated with a complex microstructure represented by a stiffness distribution  $\mathbf{c}(\underline{x})$ , spreading throughout an infinite domain, see Fig. 1(c). The stiffness distribution is considered as fluctuation around a homogeneous stiffness  $\mathbb{C}^0$ . The strains  $\boldsymbol{\varepsilon}(\underline{x})$  then consist of two portions: (i) auxiliary strains  $\mathbf{E}^0$  prevailing in the homogeneous infinite domain of stiffness  $\mathbb{C}^0$ , see Fig. 1(a), and (ii) fluctuations around  $\mathbf{E}^0$  which arise from the fluctuations in the stiffness field,  $[\mathbf{c}(\underline{x}) - \mathbb{C}^0]$ , see Fig. 1(b). These strains can be derived from the Green's functions known for elastic matrices, together with the concept of polarization stresses introduced by Eshelby, as will be detailed in Section 3. We are left with relating the new auxiliary problem (3.11) to the RVE. Therefore, we consider a finite domain of  $\mathbf{c}(\underline{x})$  which is statistically representative of the microstructure within the RVE, we identify the volume of this domain with the volume of the RVE, see Fig. 1(d), and we then apply the strain average rule (3.2), which yields in combination with (3.11) that

$$\mathbf{E} = \left[ \frac{1}{V_{\text{RVE}}} \int_{V_{\text{RVE}}} \mathbb{A}^0(\underline{x}) \, dV(\underline{x}) \right] : \mathbf{E}^0 = \mathbb{M}^{-1} : \mathbf{E}^0 \quad \Longrightarrow \quad \mathbb{M} = \left[ \frac{1}{V_{\text{RVE}}} \int_{V_{\text{RVE}}} \mathbb{A}^0(\underline{x}) \, dV(\underline{x}) \right]^{-1}, \quad (3.12)$$

with  $\mathbb{M}$  as the auxiliary-to-macroscopic strain conversion tensor. Multiplication from the left, of (3.12) with  $\mathbb{M}$ , and insertion of the corresponding result into (3.11), yields

$$\boldsymbol{\varepsilon}(\underline{x}) = \mathbb{A}^0(\underline{x}) : \left[ \frac{1}{V_{\text{RVE}}} \int_{V_{\text{RVE}}} \mathbb{A}^0(\underline{x}) \, dV(\underline{x}) \right]^{-1} : \mathbf{E}, \quad (3.13)$$

and comparison of (3.13) with (3.7) yields the strain concentration tensor as

$$\mathbb{A}(\underline{x}) = \mathbb{A}^0(\underline{x}) : \left[ \frac{1}{V_{\text{RVE}}} \int_{V_{\text{RVE}}} \mathbb{A}^0(\underline{x}) \, dV(\underline{x}) \right]^{-1}, \quad (3.14)$$



and when considering, in addition, (3.9), the homogenized stiffness tensor is eventually retrieved as

$$\mathbb{C}^{hom} = \left[ \frac{1}{V_{RVE}} \int_{V_{RVE}} \mathbf{c}(\underline{x}) : \mathbb{A}^0(\underline{x}) \, dV(\underline{x}) \right] : \left[ \frac{1}{V_{RVE}} \int_{V_{RVE}} \mathbb{A}^0(\underline{x}) \, dV(\underline{x}) \right]^{-1}, \quad (3.15)$$

see Fig. 1(f). Reformulation of  $\mathbf{c}(\underline{x}) = \mathbb{C}^0 + [\mathbf{c}(\underline{x}) - \mathbb{C}^0]$  yields

$$\mathbb{C}^{hom} = \mathbb{C}^0 + \left[ \frac{1}{V_{RVE}} \int_{V_{RVE}} [\mathbf{c}(\underline{x}) - \mathbb{C}^0] : \mathbb{A}^0(\underline{x}) \, dV(\underline{x}) \right] : \left[ \frac{1}{V_{RVE}} \int_{V_{RVE}} \mathbb{A}^0(\underline{x}) \, dV(\underline{x}) \right]^{-1}. \quad (3.16)$$

We are left with the determination of  $\mathbb{A}^0(\underline{x})$ . Therefore, we will first link this property to the elastic Green's function (Section 3), before giving an illustrative example (Section 4).

### 3.3 Green's function-based solution to the auxiliary problem of the infinite matrix with a complex microstructure

In order to determine the concentration tensor field  $\mathbb{A}^0(\underline{x})$  of our new auxiliary problem, we employ the method of Green's functions (Fredholm, 1900; Ting and Lee, 1997). This method is only applicable for *homogeneous* elastic spaces, which motivates us to adapt a famous idea of Eshelby (1957), which concerns the equivalence of an inhomogeneous elasticity distribution to a homogeneous elastic space subjected to inhomogeneous polarization stresses  $\boldsymbol{\tau}$ . Mathematically speaking, the constitutive law (3.4) is re-cast into the format (Willis, 1977)

$$\boldsymbol{\sigma}(\underline{x}) = \mathbb{C}^0 : \boldsymbol{\varepsilon}(\underline{x}) + \boldsymbol{\tau}(\underline{x}). \quad (3.17)$$

Equating (3.17) with (3.4) yields

$$\boldsymbol{\tau}(\underline{x}) = [\mathbf{c}(\underline{x}) - \mathbb{C}^0] : \boldsymbol{\varepsilon}(\underline{x}), \quad (3.18)$$

see Fig. 1(b). Insertion of the displacement-to-strain conversion relation (3.3) into the equivalent constitutive law (3.17), and of the corresponding result into the equilibrium condition (3.5) yields

$$\nabla_x \cdot [\mathbb{C}^0 : \text{grad}_x^S \underline{u}(\underline{x})] = -[f(\underline{x}) + \nabla_x \cdot \boldsymbol{\tau}(\underline{x})]. \quad (3.19)$$

The solution of the linear partial differential equation (3.19),  $\underline{u}(\underline{x})$ , is the sum of the homogeneous solution  $\underline{u}_h$  and the particular solution  $\underline{u}_p$ ,

$$\underline{u}(\underline{x}) = \underline{u}_h(\underline{x}) + \underline{u}_p(\underline{x}), \quad (3.20)$$

whereby

- the homogeneous solution  $\underline{u}_h(\underline{x})$  satisfies the homogeneous linear partial differential equation

$$\nabla_x \cdot [\mathbb{C}^0 : \text{grad}_x^S \underline{u}_h(\underline{x})] = 0, \quad (3.21)$$

with the inhomogeneous boundary conditions

$$\underline{u}_h(\underline{x}) = \mathbf{E}^0(\underline{X}) \cdot \underline{x}, \quad \forall |\underline{x}| \rightarrow \infty; \quad (3.22)$$



- and the particular solution  $\underline{u}_p(\underline{x})$  satisfies the inhomogeneous linear partial differential equation

$$\underline{\nabla}_x \cdot [\mathbb{C}^0 : \text{grad}^S \underline{u}_p(\underline{x})] = -[\underline{f}(\underline{x}) + \underline{\nabla}_x \cdot \underline{\tau}(\underline{x})], \quad (3.23)$$

with homogeneous boundary conditions

$$\underline{u}_p(\underline{x}) = 0, \quad \forall |\underline{x}| \rightarrow \infty. \quad (3.24)$$

The homogeneous solution reads as

$$\underline{u}_h(\underline{x}) = \mathbf{E}^0(\underline{X}) \cdot \underline{x}, \quad \forall \underline{x} \in \mathbb{R}^3. \quad (3.25)$$

The particular solution can be given in the form

$$\underline{u}_p(\underline{x}) = \int_{\mathbb{R}^3} \mathbf{G}(\underline{x} - \underline{y}) \cdot \left\{ \underline{f}(\underline{y}) + \underline{\nabla}_y \cdot \underline{\tau}(\underline{y}) \right\} dV(\underline{y}), \quad (3.26)$$

where  $\mathbf{G}(\underline{x} - \underline{y})$  denotes the displacement-related Green's function tensor, satisfying the differential equation

$$\underline{\nabla}_x \cdot [\mathbb{C}^0 : \text{grad}_x^S \mathbf{G}(\underline{x} - \underline{y})] = -\underline{\delta}(\underline{x} - \underline{y}), \quad (3.27)$$

with boundary conditions

$$\mathbf{G}(\underline{x} - \underline{y}) = 0, \quad \forall |\underline{x}| \rightarrow \infty, \quad (3.28)$$

In (3.27),  $\underline{\delta}$  denotes the second-order Dirac function tensor, with the following properties

$$\underline{\delta}(\underline{x}) = 0 \text{ for } \underline{x} \neq 0, \quad (3.29)$$

$$\underline{\delta}(\underline{x}) = 0 \text{ for } \underline{x} = 0, \quad (3.30)$$

$$\int_{\mathbb{R}^3} \underline{\delta}(\underline{x}) dV(\underline{x}) = \mathbf{1}, \quad (3.31)$$

with  $\mathbf{1}$  denoting the second-order identity tensor. The last term in (3.26) can be transformed by means of the chain rule, the divergence theorem, and boundary condition (3.28), yielding

$$\int_{\mathbb{R}^3} \mathbf{G}(\underline{x} - \underline{y}) \cdot \underline{\nabla}_y \cdot \underline{\tau}(\underline{y}) dV(\underline{y}) = - \int_{\mathbb{R}^3} [\text{grad}_y \mathbf{G}(\underline{x} - \underline{y})] : \underline{\tau}(\underline{y}) dV(\underline{y}). \quad (3.32)$$

Insertion of (3.32) into (3.26), adding the respective result to (3.25), and using the obtained expression  $\underline{u}(\underline{x})$  in (3.3) yield the microscopic strain field throughout the RVE as

$$\underline{\varepsilon}(\underline{x}) = \mathbf{E}^0 + \int_{\mathbb{R}^3} \mathcal{G}(\underline{x} - \underline{y}) \cdot \underline{f}(\underline{y}) dV(\underline{y}) - \int_{\mathbb{R}^3} \mathbb{G}(\underline{x} - \underline{y}) : \underline{\tau}(\underline{y}) dV(\underline{y}). \quad (3.33)$$

In (3.33), the following gradients of the Green's functions were explicitly introduced

$$\mathcal{G}(\underline{x} - \underline{y}) = \text{grad}_x^S \mathbf{G}(\underline{x} - \underline{y}), \quad (3.34)$$

$$\mathbb{G}(\underline{x} - \underline{y}) = \text{grad}_x^S \text{grad}_y \mathbf{G}(\underline{x} - \underline{y}). \quad (3.35)$$

Considering cases where, in (3.33), the effect of polarization stresses clearly outweighs that of volume forces, and insertion of the polarization stress expression (3.18) into (3.33) yields

$$\boldsymbol{\varepsilon}(\underline{x}) = \mathbf{E}^0 - \int_{\mathbb{R}^3} \mathbb{G}(\underline{x} - \underline{y}) : [\mathbf{c}(\underline{y}) - \mathbb{C}^0] : \boldsymbol{\varepsilon}(\underline{y}) \, dV(\underline{y}). \quad (3.36)$$

(3.36) is an implicit integral equation for the microscopic strain field, as the latter appears both as a separate term and part of an integrand in a volume integral over the infinite elastic domain. More precisely, the microstrains are the solution of a Fredholm equation of the second kind (Fredholm, 1900). The solution of (3.36) is found by means of an infinitely often repeated substitution process concerning  $\boldsymbol{\varepsilon}(\underline{y})$  in the last integral of (3.36). Accordingly, the term  $\boldsymbol{\varepsilon}(\underline{y})$  in the last integral of (3.36) is numbered in a way reflecting these insertion processes, namely by  $\boldsymbol{\varepsilon}(\underline{y}^{(i)})$ ,  $i = 1, 2, \dots, \infty$ .

As a starting point, (3.36) is specified for  $\underline{y} = \underline{y}^{(1)}$  in the last integral of (3.36), yielding

$$\boldsymbol{\varepsilon}(\underline{x}) = \mathbf{E}^0 - \int_{\mathbb{R}^3} \mathbb{G}(\underline{x} - \underline{y}^{(1)}) : [\mathbf{c}(\underline{y}^{(1)}) - \mathbb{C}^0] : \boldsymbol{\varepsilon}(\underline{y}^{(1)}) \, dV(\underline{y}^{(1)}). \quad (3.37)$$

In order to come up with an expression for  $\boldsymbol{\varepsilon}(\underline{y}^{(1)})$  to be inserted into the last integral in (3.37), we specify (3.37) for  $\underline{y}^{(1)} = \underline{y}^{(2)}$  and for  $\underline{x} = \underline{y}^{(1)}$ , yielding

$$\boldsymbol{\varepsilon}(\underline{y}^{(1)}) = \mathbf{E}^0 - \int_{\mathbb{R}^3} \mathbb{G}(\underline{y}^{(1)} - \underline{y}^{(2)}) : [\mathbf{c}(\underline{y}^{(2)}) - \mathbb{C}^0] : \boldsymbol{\varepsilon}(\underline{y}^{(2)}) \, dV(\underline{y}^{(2)}). \quad (3.38)$$

Insertion of (3.38) into (3.37) yields

$$\begin{aligned} \boldsymbol{\varepsilon}(\underline{x}) = & \left\{ \mathbb{I} - \int_{\mathbb{R}^3} \mathbb{G}(\underline{x} - \underline{y}^{(1)}) : [\mathbf{c}(\underline{y}^{(1)}) - \mathbb{C}^0] \, dV(\underline{y}^{(1)}) \right\} : \mathbf{E}^0 \\ & + \int_{\mathbb{R}^3} \mathbb{G}(\underline{x} - \underline{y}^{(1)}) : [\mathbf{c}(\underline{y}^{(1)}) - \mathbb{C}^0] : \int_{\mathbb{R}^3} \mathbb{G}(\underline{y}^{(1)} - \underline{y}^{(2)}) : [\mathbf{c}(\underline{y}^{(2)}) - \mathbb{C}^0] : \boldsymbol{\varepsilon}(\underline{y}^{(2)}) \, dV(\underline{y}^{(2)}) \, dV(\underline{y}^{(1)}), \end{aligned} \quad (3.39)$$

where  $\mathbb{I}$  is the symmetric fourth-order identity tensor. We now generalize this idea, in order to come up with the strain field for the  $(\alpha)$ -th step of the substitution process,  $\boldsymbol{\varepsilon}(\underline{y}^{(\alpha)})$ . For this purpose, we specify (3.37) for  $\underline{x} = \underline{y}^{(\alpha)}$  and  $\underline{y}^{(1)} = \underline{y}^{(\alpha+1)}$ . Repeating this process over and over again gives access to a relation involving an auxiliary macrostrain concentration tensor field  $\mathbb{A}^0(\underline{x})$  and a residual term comprising the implicit strain field  $\mathbf{R}[\underline{x}, \boldsymbol{\varepsilon}(\underline{y}^{(N)})]$ , reading as

$$\boldsymbol{\varepsilon}(\underline{x}) = \mathbb{A}^0(\underline{x}) : \mathbf{E}^0 + \mathbf{R}[\underline{x}, \boldsymbol{\varepsilon}(\underline{y}^{(N)})]. \quad (3.40)$$

In more detail, the concentration tensor field reads as

$$\mathbb{A}^0(\underline{x}) = \mathbb{I} + \sum_{n=1}^N (-1)^n \mathbb{A}_n^0(\underline{x}), \quad (3.41)$$

where

$$\mathbb{A}_1^0(\underline{x}) = \int_{\mathbb{R}^3} \mathbb{G}(\underline{x} - \underline{y}) : [\mathbf{c}(\underline{y}) - \mathbb{C}^0] \, dV(\underline{y}), \quad (3.42)$$

and, for  $n > 1$ ,

$$\begin{aligned} \mathbb{A}_n^0(\underline{x}) &= \int_{\mathbb{R}^3} \dots \int_{\mathbb{R}^3} \mathbb{G}(\underline{x} - \underline{y}^{(1)}) : \prod_{i=2}^n \left\{ [\mathbb{c}(\underline{y}^{(i-1)}) - \mathbb{C}^0] : \mathbb{G}(\underline{y}^{(i-1)} - \underline{y}^{(i)}) \right\} \\ &\quad : [\mathbb{c}(\underline{y}^{(n)}) - \mathbb{C}^0] \, dV(\underline{y}^{(n)}) \dots dV(\underline{y}^{(1)}), \quad \forall n \in [2, \infty). \end{aligned} \quad (3.43)$$

The residual term after  $N$  iterations reads as

$$\begin{aligned} \mathbf{R}[\underline{x}, \boldsymbol{\varepsilon}(\underline{y}^{(N)})] &= \int_{\mathbb{R}^3} \dots \int_{\mathbb{R}^3} \mathbb{G}(\underline{x} - \underline{y}^{(1)}) : \prod_{i=2}^N \left\{ [\mathbb{c}(\underline{y}^{(i-1)}) - \mathbb{C}^0] : \mathbb{G}(\underline{y}^{(i-1)} - \underline{y}^{(i)}) \right\} : [\mathbb{c}(\underline{y}^{(N)}) - \mathbb{C}^0] \\ &\quad : \boldsymbol{\varepsilon}(\underline{y}^{(N)}) \, dV(\underline{y}^{(N)}) \dots dV(\underline{y}^{(1)}). \end{aligned} \quad (3.44)$$

Note that for  $N \rightarrow \infty$ ,  $\mathbf{R}[\underline{x}, \boldsymbol{\varepsilon}(\underline{y}^{(N)})] \rightarrow 0$ , provided the following requirement is met:

$$\int_{\mathbb{R}^3} G_{ijkl}(\underline{y}^{(\alpha-1)} - \underline{y}^{(\alpha)}) [c_{klmn}(\underline{y}^{(\alpha)}) - C_{klmn}^0] G_{mnpq}(\underline{y}^{(\alpha)} - \underline{y}^{(\alpha+1)}) \, dV(\underline{y}^{(\alpha)}) < 1, \quad \forall \underline{y}^{(\alpha-1)}, \underline{y}^{(\alpha+1)} \in V_{\text{RVE}}, \quad (3.45)$$

for an arbitrary  $\alpha$ .

### 3.4 Illustrative example: microstructure with harmonically fluctuating bulk moduli

#### 3.4.1 Complex microstructure with harmonically fluctuating microscopic bulk modulus

In order to illustrate the applicability of the novel integral expressions (3.41)–(3.43), we resort to the Green's function for an infinitely extended isotropic elastic body with bulk modulus  $k_0$  and Poisson's ratio  $\nu_0$ ; it reads as (Dvorak, 2012)

$$\mathbf{G}(\underline{x} - \underline{y}) = \frac{(1 + \nu_0)}{6\pi k_0 (1 - 2\nu_0)} \mathbf{1} \frac{1}{|\underline{x} - \underline{y}|} - \frac{(1 + \nu_0)}{24\pi k_0 (1 - \nu_0) (1 - 2\nu_0)} \left( \text{grad}_x \text{grad}_x |\underline{x} - \underline{y}| \right), \quad (3.46)$$

where, with respect to the actual formula (4.5.12) given on page 107 of (Dvorak, 2012), we consider  $k_0 = \frac{2\mu_0(1+\nu_0)}{3(1-2\nu_0)}$ , being  $\mu_0$  the shear modulus. Moreover, we consider a harmonic stiffness distribution across this infinitely extended body, according to

$$\mathbb{c}(\underline{x}) = \mathbb{C}^0 + 3\Delta k \sin\left(\frac{2\pi}{\lambda_1} x_1\right) \sin\left(\frac{2\pi}{\lambda_2} x_2\right) \sin\left(\frac{2\pi}{\lambda_3} x_3\right) \mathbb{I}^{\text{vol}}, \quad (3.47)$$

where  $x_1$ ,  $x_2$ , and  $x_3$  are the components of location vector  $\underline{x}$  with respect to an orthonormal base frame  $\underline{e}_1$ ,  $\underline{e}_2$ ,  $\underline{e}_3$ , such that  $\underline{x} = x_1 \underline{e}_1 + x_2 \underline{e}_2 + x_3 \underline{e}_3$ , and  $\mathbb{I}^{\text{vol}}$  stands for the volumetric part of the symmetric fourth-order unity tensor  $\mathbb{I}$  ( $I_{ijrs} = 1/2 (\delta_{ir}\delta_{js} + \delta_{is}\delta_{jr})$ ), reading as  $\mathbb{I}^{\text{vol}} = 1/3 (\mathbf{1} \otimes \mathbf{1})$ , with components  $I_{ijkl}^{\text{vol}} = 1/3 (\delta_{ij} \delta_{kl})$ , where  $\mathbf{1}$  is the second-order unity tensor with the Kronecker delta  $\delta_{ij}$  as its components.  $\Delta k$  is a parameter which scales the stiffness variance and  $\lambda_i$  sets the size of one fluctuation in direction  $i$ .

### 3.4.2 Normal strain-related components of $\mathbb{A}^0(\underline{x})$

The auxiliary strain downscaling tensor  $\mathbb{A}^0(\underline{x})$  is the result of the sum of an infinite series, see (3.41). The first term of this series,  $\mathbb{A}_1^0(\underline{x})$ , is defined through (3.42), so that consideration of (3.47) yields the component 1111 of  $\mathbb{A}_1^0$  as

$$\begin{aligned} A_{1,1111}^0(\underline{x}) &= \sum_{h=1}^3 \sum_{\ell=1}^3 \int_{\mathbb{R}^3} G_{11h\ell}(\underline{x} - \underline{y}) \left[ 3\Delta k \sin\left(\frac{2\pi}{\lambda_1} y_1\right) \sin\left(\frac{2\pi}{\lambda_2} y_2\right) \sin\left(\frac{2\pi}{\lambda_3} y_3\right) I_{h\ell 11}^{vol} \right] dV(\underline{y}) \\ &= \Delta k \sum_{\ell=1}^3 \int_{\mathbb{R}^3} G_{11\ell\ell}(\underline{x} - \underline{y}) \sin\left(\frac{2\pi}{\lambda_1} y_1\right) \sin\left(\frac{2\pi}{\lambda_2} y_2\right) \sin\left(\frac{2\pi}{\lambda_3} y_3\right) dV(\underline{y}). \end{aligned} \quad (3.48)$$

In order to retrieve the components  $G_{1111}$ ,  $G_{1122}$ , and  $G_{1133}$ , we start with the general expression for the components of the Green's function (3.46), reading as

$$G_{ij} = \frac{(1 + \nu_0)}{6\pi k_0 (1 - 2\nu_0)} \frac{\delta_{ij}}{|\underline{x} - \underline{y}|} - \frac{(1 + \nu_0)}{24\pi k_0 (1 - \nu_0) (1 - 2\nu_0)} \left( \frac{\partial^2}{\partial x_i \partial x_j} |\underline{x} - \underline{y}| \right). \quad (3.49)$$

The fourth-order Green's function gradient (3.35) exhibits the following components

$$\begin{aligned} G_{ijkl} &= \frac{(1 + \nu_0)}{12\pi k_0 (1 - 2\nu_0)} \left( \frac{\partial^2}{\partial x_j \partial y_\ell} \frac{\delta_{ik}}{|\underline{x} - \underline{y}|} + \frac{\partial^2}{\partial x_i \partial y_\ell} \frac{\delta_{jk}}{|\underline{x} - \underline{y}|} \right) - \\ &\quad \frac{(1 + \nu_0)}{24\pi k_0 (1 - \nu_0) (1 - 2\nu_0)} \left( \frac{\partial^4}{\partial x_i \partial x_j \partial x_k \partial y_\ell} |\underline{x} - \underline{y}| \right). \end{aligned} \quad (3.50)$$

In order to evaluate (3.50), it is useful to recall the following properties of the spatial derivatives of the norm  $|\underline{x} - \underline{y}|$ . The first-order derivative of the aforementioned norm reads as

$$\frac{\partial}{\partial x_i} |\underline{x} - \underline{y}| = \frac{x_i - y_i}{|\underline{x} - \underline{y}|}, \quad (3.51)$$

revealing the interesting property

$$\frac{\partial}{\partial x_i} |\underline{x} - \underline{y}| = -\frac{\partial}{\partial y_i} |\underline{x} - \underline{y}|. \quad (3.52)$$

The first derivative of the inverse of the norm  $|\underline{x} - \underline{y}|$  reads as

$$\frac{\partial}{\partial x_i} \left( \frac{1}{|\underline{x} - \underline{y}|} \right) = -\frac{x_i - y_i}{|\underline{x} - \underline{y}|^3}, \quad (3.53)$$

revealing the interesting property

$$\frac{\partial}{\partial x_i} \frac{1}{|\underline{x} - \underline{y}|} = -\frac{\partial}{\partial y_i} \frac{1}{|\underline{x} - \underline{y}|}. \quad (3.54)$$

(3.52) and (3.54) allow for re-writing (3.50) as

$$\begin{aligned} G_{ijkl} &= -\frac{(1 + \nu_0)}{12\pi k_0 (1 - 2\nu_0)} \left( \frac{\partial^2}{\partial x_j \partial x_\ell} \frac{\delta_{ik}}{|\underline{x} - \underline{y}|} + \frac{\partial^2}{\partial x_i \partial x_\ell} \frac{\delta_{jk}}{|\underline{x} - \underline{y}|} \right) + \\ &\quad \frac{(1 + \nu_0)}{24\pi k_0 (1 - \nu_0) (1 - 2\nu_0)} \left( \frac{\partial^4}{\partial x_i \partial x_j \partial x_k \partial x_\ell} |\underline{x} - \underline{y}| \right), \end{aligned} \quad (3.55)$$

so that the components occurring in (3.48) read as

$$G_{1111} = -\frac{(1 + \nu_0)}{6\pi k_0 (1 - 2\nu_0)} \left( \frac{\partial^2}{\partial x_1^2} \frac{1}{|\underline{x} - \underline{y}|} \right) + \frac{(1 + \nu_0)}{24\pi k_0 (1 - \nu_0) (1 - 2\nu_0)} \left( \frac{\partial^4}{\partial x_1^4} |\underline{x} - \underline{y}| \right), \quad (3.56)$$

$$G_{1122} = \frac{(1 + \nu_0)}{24\pi k_0 (1 - \nu_0) (1 - 2\nu_0)} \left( \frac{\partial^4}{\partial x_1^2 \partial x_2^2} |\underline{x} - \underline{y}| \right), \quad (3.57)$$

$$G_{1133} = \frac{(1 + \nu_0)}{24\pi k_0 (1 - \nu_0) (1 - 2\nu_0)} \left( \frac{\partial^4}{\partial x_1^2 \partial x_3^2} |\underline{x} - \underline{y}| \right). \quad (3.58)$$

The sum of (3.56) to (3.58), to be calculated in (3.48), can be further simplified through an identity which follows from deriving (3.51) with respect to the components of the location vector,

$$\frac{\partial^2}{\partial x_i^2} |\underline{x} - \underline{y}| = \frac{\sum_{k \neq i} (x_k - y_k)^2}{|\underline{x} - \underline{y}|^3}. \quad (3.59)$$

Namely, (3.59) entails the following identity

$$\frac{\partial^2}{\partial x_1^2} |\underline{x} - \underline{y}| + \frac{\partial^2}{\partial x_2^2} |\underline{x} - \underline{y}| + \frac{\partial^2}{\partial x_3^2} |\underline{x} - \underline{y}| = 2 \frac{1}{|\underline{x} - \underline{y}|}, \quad (3.60)$$

twofold derivation of which yields an identity comprising the derivatives of the norm  $|\underline{x} - \underline{y}|$  occurring in (3.56) to (3.58) reading as

$$\frac{\partial^4}{\partial x_1^4} |\underline{x} - \underline{y}| + \frac{\partial^4}{\partial x_1^2 \partial x_2^2} |\underline{x} - \underline{y}| + \frac{\partial^4}{\partial x_1^2 \partial x_3^2} |\underline{x} - \underline{y}| = 2 \frac{\partial^2}{\partial x_1^2} \frac{1}{|\underline{x} - \underline{y}|}. \quad (3.61)$$

Insertion of (3.56)–(3.58) into (3.48), while considering (3.61), yields

$$A_{1,1111}^0(\underline{x}) = \frac{-\Delta k (1 + \nu_0)}{12\pi k_0 (1 - \nu_0)} \int_{\mathbb{R}^3} \left( \frac{\partial^2}{\partial x_1^2} \frac{1}{|\underline{x} - \underline{y}|} \right) \sin\left(\frac{2\pi}{\lambda_1} y_1\right) \sin\left(\frac{2\pi}{\lambda_2} y_2\right) \sin\left(\frac{2\pi}{\lambda_3} y_3\right) dV(\underline{y}). \quad (3.62)$$

A change of variable to  $\underline{z} = \underline{y} - \underline{x}$  results in

$$A_{1,1111}^0(\underline{x}) = \frac{-\Delta k (1 + \nu_0)}{12\pi k_0 (1 - \nu_0)} \int_{\mathbb{R}^3} \left( \frac{\partial^2}{\partial z_1^2} \frac{1}{|\underline{-z}|} \right) \sin\left[\frac{2\pi}{\lambda_1} (x_1 + z_1)\right] \sin\left[\frac{2\pi}{\lambda_2} (x_2 + z_2)\right] \sin\left[\frac{2\pi}{\lambda_3} (x_3 + z_3)\right] dV(\underline{z}). \quad (3.63)$$

Transforming (3.63) by means of

$$\sin(a + b) = \sin(a) \cos(b) + \cos(a) \sin(b), \quad (3.64)$$

and considering the second derivative of the inverse of the norm of  $-\underline{z}$  as

$$\frac{\partial^2}{\partial z_1^2} \left( \frac{1}{|\underline{-z}|} \right) = \frac{2(-z_1)^2 - (-z_2)^2 - (-z_3)^2}{|\underline{-z}|^5}, \quad (3.65)$$

as well as that the even and odd functions appearing as factors in the integral expression of (3.63) imply

$$\int_{-a}^a \left( \frac{\partial^2}{\partial z_1^2} \frac{1}{|\underline{-z}|} \right) \sin\left(\frac{2\pi}{\lambda_i} z_i\right) dz_i = 0, \quad \forall a \in \mathbb{R}, i \in [1, 2, 3], \quad (3.66)$$

we arrive at

$$A_{1,1111}^0(\underline{x}) = \frac{-\Delta k (1 + \nu_0)}{12\pi k_0 (1 - \nu_0)} \sin\left(\frac{2\pi}{\lambda_1} x_1\right) \sin\left(\frac{2\pi}{\lambda_2} x_2\right) \sin\left(\frac{2\pi}{\lambda_3} x_3\right) \quad (3.67)$$

$$\int_{\mathbb{R}^3} \left(\frac{\partial^2}{\partial z_1^2} \frac{1}{|\underline{z}' - \underline{z}|}\right) \cos\left(\frac{2\pi}{\lambda_1} z_1\right) \cos\left(\frac{2\pi}{\lambda_2} z_2\right) \cos\left(\frac{2\pi}{\lambda_3} z_3\right) dV(\underline{z}).$$

Noting that  $\frac{\partial}{\partial z_1} \frac{1}{|\underline{z}' - \underline{z}|} = -\frac{\partial}{\partial z_1'} \frac{1}{|\underline{z}' - \underline{z}|}$  and  $\frac{\partial^2}{\partial z_1^2} \frac{1}{|\underline{z}' - \underline{z}|} = \frac{\partial^2}{\partial z_1'^2} \frac{1}{|\underline{z}' - \underline{z}|}$ , the integral in (3.67) can be expressed by means of an auxiliary function in  $\underline{z}'$ , according to

$$\int_{\mathbb{R}^3} \left(\frac{\partial^2}{\partial z_1^2} \frac{1}{|\underline{z}' - \underline{z}|}\right) \cos\left(\frac{2\pi}{\lambda_1} z_1\right) \cos\left(\frac{2\pi}{\lambda_2} z_2\right) \cos\left(\frac{2\pi}{\lambda_3} z_3\right) dV(\underline{z}) = \frac{\partial^2 \phi}{\partial z_1'^2}(\underline{z}' = 0), \quad (3.68)$$

where the auxiliary function  $\phi(\underline{z}')$  stands for

$$\phi(\underline{z}') = \int_{\mathbb{R}^3} \frac{1}{|\underline{z}' - \underline{z}|} \cos\left(\frac{2\pi}{\lambda_1} z_1\right) \cos\left(\frac{2\pi}{\lambda_2} z_2\right) \cos\left(\frac{2\pi}{\lambda_3} z_3\right) dV(\underline{z}). \quad (3.69)$$

(3.69) exhibits two remarkable properties. Firstly, its format

$$\phi(\underline{z}') = \int_{\mathbb{R}^3} \frac{1}{|\underline{z}' - \underline{z}|} f(\underline{z}) dV(\underline{z}) \quad (3.70)$$

is the solution of the Poisson's equation

$$\nabla^2 \phi(\underline{z}') = -4\pi f(\underline{z}'). \quad (3.71)$$

Secondly, (3.69) is symmetric in the sense of

$$\begin{aligned} \phi(z'_1, z'_2, z'_3) &= \phi(z'_1, z'_3, z'_2) = \phi(z'_2, z'_3, z'_1) = \phi(z'_2, z'_1, z'_3) = \phi(z'_3, z'_1, z'_2) = \phi(z'_3, z'_2, z'_1) \\ &\rightarrow \frac{\partial \phi}{\partial z'_1} = \frac{\partial \phi}{\partial z'_2} = \frac{\partial \phi}{\partial z'_3} \quad \rightarrow \quad \frac{\partial^2 \phi}{\partial z_1'^2} = \frac{\partial^2 \phi}{\partial z_2'^2} = \frac{\partial^2 \phi}{\partial z_3'^2}. \end{aligned} \quad (3.72)$$

Use of the latter relations in (3.71), while accounting for the structure of  $f$  according to (3.69) and (3.70), yields

$$\nabla^2 \phi(\underline{z}') = 3 \frac{\partial^2 \phi}{\partial z_1'^2} = -4\pi \cos\left(\frac{2\pi}{\lambda_1} z'_1\right) \cos\left(\frac{2\pi}{\lambda_2} z'_2\right) \cos\left(\frac{2\pi}{\lambda_3} z'_3\right), \quad (3.73)$$

where we made use of (3.72). Solving the equation for  $\frac{\partial^2 \phi}{\partial z_1'^2}(\underline{z}' = 0)$  and inserting the corresponding result into (3.67) yield

$$A_{1,1111}^0(\underline{x}) = \frac{1}{3} \left[ \frac{\Delta k (1 + \nu_0)}{3 k_0 (1 - \nu_0)} \right] \sin\left(\frac{2\pi}{\lambda_1} x_1\right) \sin\left(\frac{2\pi}{\lambda_2} x_2\right) \sin\left(\frac{2\pi}{\lambda_3} x_3\right). \quad (3.74)$$

The second term of the series for the auxiliary concentration tensor for the considered harmonic isotropic micro-stiffness distribution follows from insertion of (3.47) into (3.43), so that its component 1111 is obtained as

$$A_{2,1111}^0(\underline{x}) = \sum_{h=1}^3 \sum_{\ell=1}^3 \sum_{i=1}^3 \sum_{j=1}^3 \int \int_{\mathbb{R}^3} G_{11h\ell}(\underline{x} - \underline{y}) \left[ 3\Delta k \sin\left(\frac{2\pi}{\lambda_1} y_1\right) \sin\left(\frac{2\pi}{\lambda_2} y_2\right) \sin\left(\frac{2\pi}{\lambda_3} y_3\right) I_{hlij}^{vol} \right]$$

$$\sum_{m=1}^3 \sum_{n=1}^3 G_{ijmn}(\underline{y} - \underline{y}') \left[ 3\Delta k \sin\left(\frac{2\pi}{\lambda_1} y'_1\right) \sin\left(\frac{2\pi}{\lambda_2} y'_2\right) \sin\left(\frac{2\pi}{\lambda_3} y'_3\right) I_{mn11}^{vol} \right] dV(\underline{y}') dV(\underline{y}). \quad (3.75)$$

Specification of (3.75) for (3.55), while considering identity (3.61), yields

$$A_{2,1111}^0(\underline{x}) = \left[ \frac{-\Delta k (1 + \nu_0)}{12\pi k_0 (1 - \nu_0)} \right]^2 \int_{\mathbb{R}^3} \left( \frac{\partial^2}{\partial x_1^2} \frac{1}{|\underline{x} - \underline{y}|} \right) \sin\left(\frac{2\pi}{\lambda_1} y_1\right) \sin\left(\frac{2\pi}{\lambda_2} y_2\right) \sin\left(\frac{2\pi}{\lambda_3} y_3\right) \\ \nabla^2 \left[ \int_{\mathbb{R}^3} \left( \frac{1}{|\underline{y} - \underline{y}'|} \right) \sin\left(\frac{2\pi}{\lambda_1} y'_1\right) \sin\left(\frac{2\pi}{\lambda_2} y'_2\right) \sin\left(\frac{2\pi}{\lambda_3} y'_3\right) dV(\underline{y}') \right] dV(\underline{y}). \quad (3.76)$$

Considering the last integral in (3.76) as the Green's function solving the Poisson's equation

$$\nabla^2 \phi(\underline{y}) = -4\pi \sin\left(\frac{2\pi}{\lambda_1} y_1\right) \sin\left(\frac{2\pi}{\lambda_2} y_2\right) \sin\left(\frac{2\pi}{\lambda_3} y_3\right) \quad (3.77)$$

yields

$$A_{2,1111}^0(\underline{x}) = (-4\pi) \left[ \frac{-\Delta k (1 + \nu_0)}{12\pi k_0 (1 - \nu_0)} \right]^2 \int_{\mathbb{R}^3} \left( \frac{\partial^2}{\partial x_1^2} \frac{1}{|\underline{x} - \underline{y}|} \right) \sin^2\left(\frac{2\pi}{\lambda_1} y_1\right) \sin^2\left(\frac{2\pi}{\lambda_2} y_2\right) \sin^2\left(\frac{2\pi}{\lambda_3} y_3\right) dV(\underline{y}). \quad (3.78)$$

Recalling from (3.62) and (3.74) that

$$\int_{\mathbb{R}^3} \left( \frac{\partial^2}{\partial x_1^2} \frac{1}{|\underline{x} - \underline{y}|} \right) f(\underline{y}) dV(\underline{y}) = -\frac{4\pi}{3} f(\underline{x}), \quad (3.79)$$

for any  $f(\underline{y})$  with the symmetry properties of (3.72), the integral in (3.78) can be solved, yielding

$$A_{2,1111}^0(\underline{x}) = \frac{1}{3} \left[ \frac{\Delta k (1 + \nu_0)}{3 k_0 (1 - \nu_0)} \right]^2 \sin^2\left(\frac{2\pi}{\lambda_1} x_1\right) \sin^2\left(\frac{2\pi}{\lambda_2} x_2\right) \sin^2\left(\frac{2\pi}{\lambda_3} x_3\right). \quad (3.80)$$

Repeating this derivation for the 1111-component of any other member of the series, i.e. for  $A_{n,1111}^0$  with  $n > 2$ , one notices that

$$A_{n,1111}^0(\underline{x}) = (-1)^n \frac{1}{3} \left[ -\frac{\Delta k (1 + \nu_0)}{3 k_0 (1 - \nu_0)} \sin\left(\frac{2\pi}{\lambda_1} x_1\right) \sin\left(\frac{2\pi}{\lambda_2} x_2\right) \sin\left(\frac{2\pi}{\lambda_3} x_3\right) \right]^n. \quad (3.81)$$

Moreover, because of the symmetry of the considered micro-stiffness distribution,  $A_{n,1111}^0(\underline{x}) = A_{n,2222}^0(\underline{x}) = A_{n,3333}^0(\underline{x})$  are equal and given by (3.81). Furthermore, it can be straightforwardly proved that (3.81) is the result of any component of the type  $A_{n,ii\ell\ell}^0$ .

The components of the auxiliary strain downscaling tensor  $\mathbb{A}^0(\underline{x})$  are calculated as an infinite sum, see (3.41). Therefore, the explicit expression for the sum of an infinite geometric series, reading as

$$\sum_{i=0}^{\infty} \alpha^i = \frac{1}{1 - \alpha}, \quad \text{for } |\alpha| < 1, \quad (3.82)$$

is applied to  $\alpha = -\frac{\Delta k (1 + \nu_0)}{3 k_0 (1 - \nu_0)} \sin\left(\frac{2\pi}{\lambda_1} x_1\right) \sin\left(\frac{2\pi}{\lambda_2} x_2\right) \sin\left(\frac{2\pi}{\lambda_3} x_3\right)$ . This yields the normal strain concentration tensor components as

$$A_{iii}^0(\underline{x}) = \frac{2}{3} + \frac{1}{1 + \frac{\Delta k (1 + \nu_0)}{3 k_0 (1 - \nu_0)} \sin\left(\frac{2\pi}{\lambda_1} x_1\right) \sin\left(\frac{2\pi}{\lambda_2} x_2\right) \sin\left(\frac{2\pi}{\lambda_3} x_3\right)}, \quad (3.83)$$

$$A_{ijj}^0(\underline{x}) = -\frac{1}{3} + \frac{1}{1 + \frac{\Delta k (1 + \nu_0)}{3 k_0 (1 - \nu_0)} \sin\left(\frac{2\pi}{\lambda_1} x_1\right) \sin\left(\frac{2\pi}{\lambda_2} x_2\right) \sin\left(\frac{2\pi}{\lambda_3} x_3\right)}. \quad (3.84)$$



### 3.4.3 Shear strain-related components of $\mathbb{A}^0(\underline{x})$

Next, we turn to the shear-related components of the concentration tensor, i.e. to  $A_{ijkl}$  with  $i \neq j$  or  $k \neq \ell$ . The concentration tensor is driven by the micro-stiffness fluctuation around the base stiffness  $\mathbb{C}^0$ , see the expressions (3.41)–(3.43), so that the chosen harmonic micro-stiffness distribution (3.47), where the shear stiffness does not fluctuate around the basic contribution, implies that

$$A_{n,ijkl}^0(\underline{x}) = 0, \quad \forall n \in \mathbb{N}, \quad \underline{x} \in V_{\text{RVE}}, \quad k \neq \ell. \quad (3.85)$$

Combining (3.85) with (3.41) implies that

$$A_{ijij}^0(\underline{x}) = 1, \quad \forall \underline{x} \in V_{\text{RVE}}, \quad i \neq j, \quad (3.86)$$

and

$$A_{ijk\ell}^0(\underline{x}) = 0, \quad \forall \underline{x} \in V_{\text{RVE}}, \quad i \neq j, \quad k \neq \ell, \quad i \neq k, \quad j \neq \ell. \quad (3.87)$$

Let us now turn to the remaining non-vanishing shear-related components of the concentration tensor, i.e. to  $A_{1,ij\ell\ell}^0(\underline{x})$ , with  $i \neq j$ . For the microstiffness distribution (3.47), the respective first term in the series of (3.41), defined by (3.42), reads as

$$\begin{aligned} A_{1,ij\ell\ell}^0(\underline{x}) &= \sum_{h=1}^3 \sum_{k=1}^3 \int_{\mathbb{R}^3} G_{11hk}(\underline{x} - \underline{y}) \left[ 3\Delta k \sin\left(\frac{2\pi}{\lambda_1} y_1\right) \sin\left(\frac{2\pi}{\lambda_2} y_2\right) \sin\left(\frac{2\pi}{\lambda_3} y_3\right) I_{hk\ell\ell}^{\text{vol}} \right] dV(\underline{y}) \\ &= \Delta k \sum_{h=1}^3 \int_{\mathbb{R}^3} G_{11hh}(\underline{x} - \underline{y}) \sin\left(\frac{2\pi}{\lambda_1} y_1\right) \sin\left(\frac{2\pi}{\lambda_2} y_2\right) \sin\left(\frac{2\pi}{\lambda_3} y_3\right) dV(\underline{y}). \end{aligned} \quad (3.88)$$

Insertion of (3.55) into (3.88), while considering the identity resulting from derivation of (3.60) with respect to  $x_i$  and  $x_j$ , reading as

$$\frac{\partial^4}{\partial x_i \partial x_j \partial x_1^2} |\underline{x} - \underline{y}| + \frac{\partial^4}{\partial x_i \partial x_j \partial x_2^2} |\underline{x} - \underline{y}| + \frac{\partial^4}{\partial x_i \partial x_j \partial x_3^2} |\underline{x} - \underline{y}| = 2 \frac{\partial^2}{\partial x_i \partial x_j} \frac{1}{|\underline{x} - \underline{y}|}, \quad (3.89)$$

yields

$$A_{1,ij\ell\ell}^0(\underline{x}) = \left[ \frac{-\Delta k (1 + \nu_0)}{12\pi k_0 (1 - \nu_0)} \right] \int_{\mathbb{R}^3} \left( \frac{\partial^2}{\partial x_i \partial x_j} \frac{1}{|\underline{x} - \underline{y}|} \right) \sin\left(\frac{2\pi}{\lambda_1} y_1\right) \sin\left(\frac{2\pi}{\lambda_2} y_2\right) \sin\left(\frac{2\pi}{\lambda_3} y_3\right) dV(\underline{y}). \quad (3.90)$$

Introducing the variable  $\underline{z} = \underline{y} - \underline{x}$ , using the relation (3.64), and considering

$$\frac{\partial}{\partial z_j} \left[ \frac{\partial}{\partial z_{i \neq j}} \left( \frac{1}{|\underline{z}|} \right) \right] = 3 \frac{(-z_i)(-z_j)}{|\underline{z}|^5}, \quad (3.91)$$

and the corresponding consequence of even and odd functions

$$\int_{-a}^a \left( \frac{\partial}{\partial z_i} \frac{1}{|\underline{z}|} \right) \cos\left(\frac{2\pi}{\lambda_i} z_i\right) dz_i = 0, \quad \forall a \in \mathbb{R}, \quad (3.92)$$

(3.90) can be transformed to

$$\begin{aligned} A_{1,ij\ell\ell}^0(\underline{x}) &= \left[ \frac{-\Delta k (1 + \nu_0)}{12\pi k_0 (1 - \nu_0)} \right] \cos\left(\frac{2\pi}{\lambda_i} x_i\right) \cos\left(\frac{2\pi}{\lambda_j} x_j\right) \sin\left(\frac{2\pi}{\lambda_k} x_{k \neq i,j}\right) \\ &\int_{\mathbb{R}^3} \left( \frac{3 z_i z_j}{|\underline{z}|^5} \right) \sin\left(\frac{2\pi}{\lambda_i} z_i\right) \sin\left(\frac{2\pi}{\lambda_j} z_j\right) \cos\left(\frac{2\pi}{\lambda_k} z_k\right) dV(\underline{z}). \end{aligned} \quad (3.93)$$

Introducing the microstructure-related variable change  $\underline{z}' = \left(\frac{2\pi}{\lambda_1} z_1, \frac{2\pi}{\lambda_2} z_2, \frac{2\pi}{\lambda_3} z_3\right)$  into (3.93) yields

$$A_{1,ij\ell\ell}^0(\underline{x}) = \left[ \frac{-\Delta k (1 + \nu_0)}{12\pi k_0 (1 - \nu_0)} \right] \cos\left(\frac{2\pi}{\lambda_i} x_i\right) \cos\left(\frac{2\pi}{\lambda_j} x_j\right) \sin\left(\frac{2\pi}{\lambda_k} x_k\right) \int_{\mathbb{R}^3} \left( \frac{3 z'_i z'_j}{|-\underline{z}'|^5} \right) \sin(z'_i) \sin(z'_j) \cos(z'_k) dV(\underline{z}'). \quad (3.94)$$

Considering

$$\int_{-\infty}^{\infty} \frac{z'_i}{[(-z'_i)^2 + (-z'_j)^2 + (-z'_k)^2]^{5/2}} \sin(z'_i) dz'_i = \frac{2 K_1(\sqrt{(-z'_j)^2 + (-z'_k)^2})}{3 \sqrt{(-z'_j)^2 + (-z'_k)^2}}, \quad (3.95)$$

with  $K_1$  being the modified Bessel function of the second kind, (3.94) can be re-written as

$$A_{1,ij\ell\ell}^0(\underline{x}) = \left[ \frac{-\Delta k (1 + \nu_0)}{12\pi k_0 (1 - \nu_0)} \right] \cos\left(\frac{2\pi}{\lambda_i} x_i\right) \cos\left(\frac{2\pi}{\lambda_j} x_j\right) \sin\left(\frac{2\pi}{\lambda_k} x_k\right) \int_{-\infty}^{\infty} \int_{-\infty}^{\infty} \left[ \frac{2 z'_j}{\sqrt{(-z'_j)^2 + (-z'_k)^2}} \right] K_1(\sqrt{(-z'_j)^2 + (-z'_k)^2}) \sin(z'_j) \cos(z'_k) dz'_j dz'_k. \quad (3.96)$$

Applying a transformation towards polar coordinates,  $z'_j = \rho \cos \theta$  and  $z'_k = \rho \sin \theta$ , yields

$$A_{1,ij\ell\ell}^0(\underline{x}) = \left[ \frac{-\Delta k (1 + \nu_0)}{12\pi k_0 (1 - \nu_0)} \right] \cos\left(\frac{2\pi}{\lambda_i} x_i\right) \cos\left(\frac{2\pi}{\lambda_j} x_j\right) \sin\left(\frac{2\pi}{\lambda_k} x_k\right) \int_0^{2\pi} \int_0^{\infty} 2 \rho \cos \theta K_1(\rho) \sin(\rho \cos \theta) \cos(\rho \sin \theta) d\rho d\theta. \quad (3.97)$$

Thanks to the trigonometric identity  $\sin(a) \cos(b) = \frac{1}{2}[\sin(a+b) + \sin(a-b)]$ , (3.97) can be reformulated as

$$A_{1,ij\ell\ell}^0(\underline{x}) = \left[ \frac{-\Delta k (1 + \nu_0)}{12\pi k_0 (1 - \nu_0)} \right] \cos\left(\frac{2\pi}{\lambda_i} x_i\right) \cos\left(\frac{2\pi}{\lambda_j} x_j\right) \sin\left(\frac{2\pi}{\lambda_k} x_k\right) \int_0^{2\pi} \cos \theta \int_0^{\infty} \rho K_1(\rho) \left[ \sin((\cos \theta + \sin \theta) \rho) + \sin((\cos \theta - \sin \theta) \rho) \right] d\rho d\theta. \quad (3.98)$$

Thus, integrating over  $\rho$  yields

$$A_{1,ij\ell\ell}^0(\underline{x}) = \left[ \frac{-\Delta k (1 + \nu_0)}{12\pi k_0 (1 - \nu_0)} \right] \cos\left(\frac{2\pi}{\lambda_i} x_i\right) \cos\left(\frac{2\pi}{\lambda_j} x_j\right) \sin\left(\frac{2\pi}{\lambda_k} x_k\right) \int_0^{2\pi} \cos \theta \left[ \frac{\cos \theta + \sin \theta}{2 + 2 \cos \theta \sin \theta} + \frac{\cos \theta - \sin \theta}{2 - 2 \cos \theta \sin \theta} + \frac{\sinh^{-1}(\cos \theta + \sin \theta)}{(2 + 2 \cos \theta \sin \theta)^{3/2}} + \frac{\sinh^{-1}(\cos \theta - \sin \theta)}{(2 - 2 \cos \theta \sin \theta)^{3/2}} \right] d\theta. \quad (3.99)$$

The integral remaining in (3.99) amounts to 4.188784. Thus, the first element of the series is

$$A_{1,ij\ell\ell}^0(\underline{x}) = 4.1888 \left[ \frac{-\Delta k (1 + \nu_0)}{12\pi k_0 (1 - \nu_0)} \right] \cos\left(\frac{2\pi}{\lambda_i} x_i\right) \cos\left(\frac{2\pi}{\lambda_j} x_j\right) \sin\left(\frac{2\pi}{\lambda_k} x_k\right). \quad (3.100)$$

The following element of the series  $A_{2,ij\ell}^0(\underline{x})$  reads, after the introduction of the corresponding Green's functions from (3.55), as

$$A_{2,ij\ell}^0(\underline{x}) = \left[ \frac{-\Delta k (1 + \nu_0)}{12\pi k_0 (1 - \nu_0)} \right]^2 \int_{\mathbb{R}^3} \left( \frac{\partial^2}{\partial x_i \partial x_j} \frac{1}{|\underline{x} - \underline{y}|} \right) \sin\left(\frac{2\pi}{\lambda_1} y_1\right) \sin\left(\frac{2\pi}{\lambda_2} y_2\right) \sin\left(\frac{2\pi}{\lambda_3} y_3\right) \\ \nabla^2 \left[ \int_{\mathbb{R}^3} \left( \frac{1}{|\underline{y} - \underline{y}'|} \right) \sin\left(\frac{2\pi}{\lambda_1} y'_1\right) \sin\left(\frac{2\pi}{\lambda_2} y'_2\right) \sin\left(\frac{2\pi}{\lambda_3} y'_3\right) dV(\underline{y}') \right] dV(\underline{y}). \quad (3.101)$$

After application of Poisson's equation (3.71), (3.101) can be expressed as follows, when using  $\sin^2(a) = \frac{1}{2}[1 - \cos(2a)]$

$$A_{2,ij\ell}^0(\underline{x}) = \left[ \frac{-\Delta k (1 + \nu_0)}{12\pi k_0 (1 - \nu_0)} \right]^2 \int_{\mathbb{R}^3} \left( \frac{\partial^2}{\partial x_i \partial x_j} \frac{1}{|\underline{x} - \underline{y}|} \right) \\ \left[ 1 - \cos\left(2\frac{2\pi}{\lambda_1} y_1\right) \right] \left[ 1 - \cos\left(2\frac{2\pi}{\lambda_2} y_2\right) \right] \left[ 1 - \cos\left(2\frac{2\pi}{\lambda_3} y_3\right) \right] dV(\underline{y}). \quad (3.102)$$

Proceeding with an analogous process to the one carried out to obtain  $A_{1,ij\ell}^0(\underline{x})$ , i.e. variable change to  $\underline{z} = \underline{y} - \underline{x}$ , partial derivation with respect to  $z_i$  and  $z_j$ , change of the variable  $\underline{z}' = \left(\frac{2\pi}{\lambda_1} z_1, \frac{2\pi}{\lambda_2} z_2, \frac{2\pi}{\lambda_3} z_3\right)$ , integration over  $z'_i$ , change towards polar coordinate system ( $z'_j = \rho \cos \theta$  and  $z'_k = \rho \sin \theta$ ), integration over  $r$  and, lastly, integration over  $\theta$  yield

$$A_{2,ij\ell}^0(\underline{x}) = \left[ \frac{-\Delta k (1 + \nu_0)}{12\pi k_0 (1 - \nu_0)} \right]^2 \sin\left(2\frac{2\pi}{\lambda_i} x_i\right) \sin\left(2\frac{2\pi}{\lambda_j} x_j\right) \left[ 0.7854 - 0.5236 \cos\left(2\frac{2\pi}{\lambda_k} x_k\right) \right]. \quad (3.103)$$

Similarly, the third element was computed as

$$A_{3,ij\ell}^0(\underline{x}) = \left[ \frac{-\Delta k (1 + \nu_0)}{12\pi k_0 (1 - \nu_0)} \right]^3 \left[ 1.767 \sin\left(\frac{2\pi}{\lambda_i} x_i\right) \sin\left(\frac{2\pi}{\lambda_j} x_j\right) \cos\left(\frac{2\pi}{\lambda_k} x_k\right) - \right. \\ 0.482 \sin\left(3\frac{2\pi}{\lambda_i} x_i\right) \sin\left(\frac{2\pi}{\lambda_j} x_j\right) \cos\left(\frac{2\pi}{\lambda_k} x_k\right) - 0.482 \sin\left(\frac{2\pi}{\lambda_i} x_i\right) \sin\left(3\frac{2\pi}{\lambda_j} x_j\right) \cos\left(\frac{2\pi}{\lambda_k} x_k\right) - \\ 0.161 \sin\left(\frac{2\pi}{\lambda_i} x_i\right) \sin\left(\frac{2\pi}{\lambda_j} x_j\right) \cos\left(3\frac{2\pi}{\lambda_k} x_k\right) + 0.279 \sin\left(3\frac{2\pi}{\lambda_i} x_i\right) \sin\left(3\frac{2\pi}{\lambda_j} x_j\right) \cos\left(\frac{2\pi}{\lambda_k} x_k\right) + \\ 0.093 \sin\left(3\frac{2\pi}{\lambda_i} x_i\right) \sin\left(\frac{2\pi}{\lambda_j} x_j\right) \cos\left(3\frac{2\pi}{\lambda_k} x_k\right) + 0.093 \sin\left(\frac{2\pi}{\lambda_i} x_i\right) \sin\left(3\frac{2\pi}{\lambda_j} x_j\right) \cos\left(3\frac{2\pi}{\lambda_k} x_k\right) \\ \left. - 0.065 \sin\left(3\frac{2\pi}{\lambda_i} x_i\right) \sin\left(3\frac{2\pi}{\lambda_j} x_j\right) \cos\left(3\frac{2\pi}{\lambda_k} x_k\right) \right]. \quad (3.104)$$

For the following terms  $A_{n,ij\ell}^0(\underline{x})$ , corresponding substitution of Green's functions (3.55) and reiterated application of Poisson's equation (3.71) yield

$$A_{n,ij\ell}^0(\underline{x}) = \left[ \frac{-\Delta k (1 + \nu_0)}{12\pi k_0 (1 - \nu_0)} \right]^n \int_{\mathbb{R}^3} \left( \frac{\partial^2}{\partial x_i \partial x_j} \frac{1}{|\underline{x} - \underline{y}|} \right) \sin^n\left(\frac{2\pi}{\lambda_1} y_1\right) \sin^n\left(\frac{2\pi}{\lambda_2} y_2\right) \sin^n\left(\frac{2\pi}{\lambda_3} y_3\right) dV(\underline{y}). \quad (3.105)$$

These terms can be computed in the same manner as the previous ones, converging rapidly due to the factor  $\left[ \frac{-\Delta k (1 + \nu_0)}{12\pi k_0 (1 - \nu_0)} \right]^n$ .

### 3.4.4 Tensorial link between auxiliary and real macrostrains

For the present case, the RVE is regarded as any assembly of a finite number of fluctuations which are periodically repeated, i.e.

$$\underline{x} \in V_{\text{RVE}} = n_\lambda^3 \lambda_1 \lambda_2 \lambda_3 \iff \begin{cases} n_\lambda (-\lambda_1/2) \leq x_1 \leq n_\lambda (\lambda_1/2), \\ n_\lambda (-\lambda_2/2) \leq x_2 \leq n_\lambda (\lambda_2/2), \\ n_\lambda (-\lambda_3/2) \leq x_3 \leq n_\lambda (\lambda_3/2). \end{cases} \quad (3.106)$$

The real concentration tensor associated with this microstructure,  $\mathbb{A}(\underline{x})$ , is related to the auxiliary concentration tensor calculated in the previous sections,  $\mathbb{A}^0(\underline{x})$ , according to (3.14). Thus, this section is devoted to the derivation of the tensorial link  $\mathbb{M}$ , see (3.12). For the sake of simplicity, the inverse of  $\mathbb{M}$ ,  $\mathbb{M}^{-1}$ , will be calculated first, and in order to obtain the auxiliary-to-RVE tensor as

$$\mathbb{M} = (\mathbb{M}^{-1})^{-1}. \quad (3.107)$$

Like in the previous sections, the components of tensor  $\mathbb{M}^{-1}$  will be obtained individually. The first components studied are  $M_{iiii}^{-1}$ . Insertion of (3.83) into the inverse of (3.12) yields

$$M_{iiii}^{-1} = \frac{2}{3} \left[ \frac{1}{V_{\text{RVE}}} \int_{V_{\text{RVE}}} dV(\underline{x}) \right] + \frac{1}{V_{\text{RVE}}} \int_{V_{\text{RVE}}} \frac{1}{1 + \frac{\Delta k(1+\nu_0)}{3k_0(1-\nu_0)} \sin\left(\frac{2\pi}{\lambda_1}x_1\right) \sin\left(\frac{2\pi}{\lambda_2}x_2\right) \sin\left(\frac{2\pi}{\lambda_3}x_3\right)} dV(\underline{x}). \quad (3.108)$$

Clearly, the term in square brackets is equal to 1, while we must focus on the other integral expression

$$\begin{aligned} I &= \frac{1}{V_{\text{RVE}}} \int_{n_\lambda(-\lambda_1/2)}^{n_\lambda(\lambda_1/2)} \int_{n_\lambda(-\lambda_2/2)}^{n_\lambda(\lambda_2/2)} \int_{n_\lambda(-\lambda_3/2)}^{n_\lambda(\lambda_3/2)} \frac{1}{1 + \frac{\Delta k(1+\nu_0)}{3k_0(1-\nu_0)} \sin\left(\frac{2\pi}{\lambda_1}x_1\right) \sin\left(\frac{2\pi}{\lambda_2}x_2\right) \sin\left(\frac{2\pi}{\lambda_3}x_3\right)} dx_1 dx_2 dx_3 \\ &= \frac{1}{\lambda_1 \lambda_2 \lambda_3} \int_{-\lambda_1/2}^{\lambda_1/2} \int_{-\lambda_2/2}^{\lambda_2/2} \int_{-\lambda_3/2}^{\lambda_3/2} \frac{1}{1 + \frac{\Delta k(1+\nu_0)}{3k_0(1-\nu_0)} \sin\left(\frac{2\pi}{\lambda_1}x_1\right) \sin\left(\frac{2\pi}{\lambda_2}x_2\right) \sin\left(\frac{2\pi}{\lambda_3}x_3\right)} dx_1 dx_2 dx_3. \end{aligned} \quad (3.109)$$

Proceeding with a change of variable  $\underline{x}' = \left(\frac{2\pi}{\lambda_1}x_1, \frac{2\pi}{\lambda_2}x_2, \frac{2\pi}{\lambda_3}x_3\right)$  yields

$$I = \left(\frac{1}{2\pi}\right)^3 \int_{-\pi}^{\pi} \int_{-\pi}^{\pi} \int_{-\pi}^{\pi} \frac{1}{1 + \frac{\Delta k(1+\nu_0)}{3k_0(1-\nu_0)} \sin(x'_1) \sin(x'_2) \sin(x'_3)} dx'_1 dx'_2 dx'_3. \quad (3.110)$$

Solving the integral for  $x'_1$  yields

$$\begin{aligned} I &= \left(\frac{1}{2\pi}\right)^3 \int_{-\pi}^{\pi} \int_{-\pi}^{\pi} \frac{2 \tan^{-1}\left(\frac{\psi(x'_2, x'_3) + \tan(\pi/2)}{\sqrt{1-\psi^2(x'_2, x'_3)}}\right)}{\sqrt{1-\psi^2(x'_2, x'_3)}} dx'_2 dx'_3 - \left(\frac{1}{2\pi}\right)^3 \int_{-\pi}^{\pi} \int_{-\pi}^{\pi} \frac{2 \tan^{-1}\left(\frac{\psi(x'_2, x'_3) + \tan(-\pi/2)}{\sqrt{1-\psi^2(x'_2, x'_3)}}\right)}{\sqrt{1-\psi^2(x'_2, x'_3)}} dx'_2 dx'_3 \\ &= \left(\frac{1}{2\pi}\right)^3 \int_{-\pi}^{\pi} \int_{-\pi}^{\pi} \frac{2\pi}{\sqrt{1-\psi^2(x'_2, x'_3)}} dx'_2 dx'_3, \end{aligned} \quad (3.111)$$

where  $\psi(x'_2, x'_3) = \frac{\Delta k (1 + \nu_0)}{3 k_0 (1 - \nu_0)} \sin(x'_2) \sin(x'_3)$ . Integrating  $I$  with respect to  $x'_2$  yields

$$I = 4\pi \left(\frac{1}{2\pi}\right)^3 \int_{-\pi}^{\pi} \left[ K \left( \left[ \frac{\Delta k (1 + \nu_0)}{3 k_0 (1 - \nu_0)} \right]^2 \sin^2(x'_3) \right) + \frac{1}{\sqrt{1 - \left[ \frac{\Delta k (1 + \nu_0)}{3 k_0 (1 - \nu_0)} \right]^2 \sin^2(x'_3)}} K \left( \frac{\left[ \frac{\Delta k (1 + \nu_0)}{3 k_0 (1 - \nu_0)} \right]^2 \sin^2(x'_3)}{1 - \left[ \frac{\Delta k (1 + \nu_0)}{3 k_0 (1 - \nu_0)} \right]^2 \sin^2(x'_3)} \right) \right] dx'_3, \quad (3.112)$$

where  $K(a)$  is the complete elliptic integral of the first kind with parameter  $a$ . The value of  $I$ , see (3.112), has been obtained numerically by means of different integration methods, including the trapezoidal or Simpson's rule (Horwitz, 2001; Whittaker and Robinson, 1967), for several values of  $\mathcal{K} = \left[ \frac{\Delta k (1 + \nu_0)}{3 k_0 (1 - \nu_0)} \right]$ . The value of  $I$  is equal to 1 for  $\mathcal{K} = 0$ , and increases non-linearly with increasing  $\mathcal{K}$ , see Fig. 3.2. Thus, from (3.108),

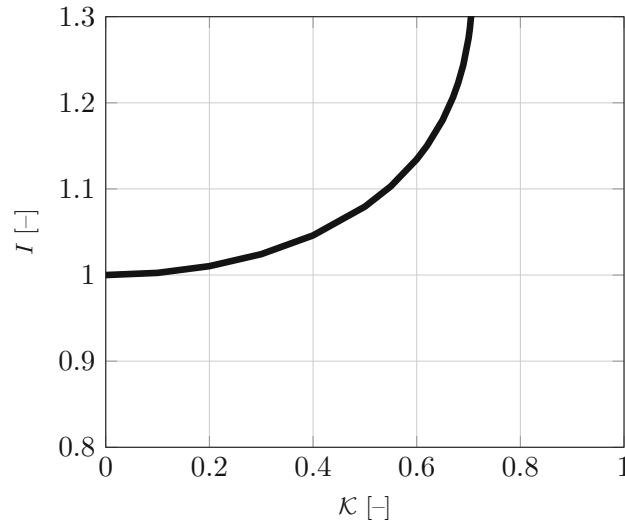


**Fig. 3.2.** Numerical value of  $I$ , see (3.112), obtained for several values of  $\mathcal{K} = \left[ \frac{\Delta k (1 + \nu_0)}{3 k_0 (1 - \nu_0)} \right]$ .

$$M_{iii}^{-1} = \frac{2}{3} + I(\mathcal{K}). \quad (3.113)$$

The next components to be considered are  $M_{iij}^{-1}$ , with  $i \neq j$ . They read, from (3.84) and (3.112), as

$$M_{iij}^{-1} = -\frac{1}{3} + I(\mathcal{K}), \quad \forall i \neq j. \quad (3.114)$$

The shear components read as

$$M_{ijj}^{-1} = 1, \quad \forall i \neq j, \quad (3.115)$$

and

$$M_{ijkl}^{-1} = 0, \quad \forall i \neq j, \quad k \neq \ell, \quad i \neq k, \quad j \neq \ell. \quad (3.116)$$

### 3.4.5 Homogenized stiffness of harmonically fluctuating microstructure

From (3.16), the difference between the homogenized stiffness and the background stiffness  $\mathbb{C}^0$  reads as

$$\Delta\mathbb{C}^{hom} = \mathbb{C}^{hom} - \mathbb{C}^0 = \left[ \frac{1}{V_{RVE}} \int_{V_{RVE}} [\mathbb{c}(\underline{x}) - \mathbb{C}^0] : \mathbb{A}^0(\underline{x}) dV(\underline{x}) \right] : \mathbb{M}. \quad (3.117)$$

One more time, the components of this tensor will be obtained individually. The only non-vanishing components  $\Delta C_{hom,ijkl}$  are those with  $i = j$ , due to

$$[c_{ijkl}(\underline{x}) - C_{ijkl}^0] = \Delta k \sin\left(\frac{2\pi}{\lambda_1}x_1\right) \sin\left(\frac{2\pi}{\lambda_2}x_2\right) \sin\left(\frac{2\pi}{\lambda_3}x_3\right) \delta_{ij} \delta_{kl}. \quad (3.118)$$

Moreover, noting (3.87), the components  $\Delta C_{hom,iikl}$  read as

$$\Delta C_{hom,iikl} = \sum_{p=1}^3 \sum_{q=1}^3 \left[ \frac{1}{V_{RVE}} \int_{V_{RVE}} \Delta k \sin\left(\frac{2\pi}{\lambda_1}x_1\right) \sin\left(\frac{2\pi}{\lambda_2}x_2\right) \sin\left(\frac{2\pi}{\lambda_3}x_3\right) A_{ppqq}^0(\underline{x}) dV(\underline{x}) \right] M_{qqkl}. \quad (3.119)$$

Thus, inserting (3.83) and (3.84) into (3.119) and applying  $\underline{x}' = \frac{2\pi}{\lambda}\underline{x}$  yields

$$\Delta C_{hom,iikl} = \left[ \frac{9\Delta k}{(2\pi)^3} \int_{V'_{RVE}} \frac{\sin(x'_1) \sin(x'_2) \sin(x'_3)}{1 + \frac{\Delta k(1+\nu_0)}{3k_0(1-\nu_0)} \sin(x'_1) \sin(x'_2) \sin(x'_3)} dV(\underline{x}') \right] \sum_{q=1}^3 M_{qqkl}. \quad (3.120)$$

Integrating (3.120) with respect to  $x'_1$  from  $-\pi$  to  $\pi$  yields

$$\begin{aligned} \Delta C_{hom,iikl} &= \frac{27k_0(1-\nu_0)}{(1+\nu_0)(2\pi)^3} \left[ \int_{-\pi}^{\pi} \int_{-\pi}^{\pi} 2\pi dx'_2 dx'_3 - \int_{-\pi}^{\pi} \int_{-\pi}^{\pi} \frac{2\pi}{\sqrt{1-\psi^2(x'_2, x'_3)}} dx'_2 dx'_3 \right] \sum_{q=1}^3 M_{qqkl} \\ &= \frac{27k_0(1-\nu_0)}{(1+\nu_0)} [1 - I(\mathcal{K})] \sum_{q=1}^3 M_{qqkl}, \end{aligned} \quad (3.121)$$

whereby we have made use of (3.111). Clearly, for the stiffness field (3.47), the following components vanish

$$\Delta C_{hom,ijkl} = 0, \quad \forall i \neq j. \quad (3.122)$$

Moreover, components

$$\Delta C_{hom,ijkl} = 0, \quad \forall k \neq \ell, \quad (3.123)$$

since  $M_{iikl} = 0, \forall k \neq \ell$ , see (3.107) and (3.116).

## 3.5 Discussion

It is worthwhile to discuss key characteristics of the convolution integral-type mathematical relations for the concentration tensor fields introduced in the present paper. As it is well known that the Green kernel occurring in this integral expressions is singular at the point  $\underline{x} = \underline{y}$ , the corresponding convolutions need to be carried out with care, and it is therefore interesting to compare the solution strategy based on the Poisson's equation, as applied throughout Section 3.4, with the more traditional way of evaluating such integrals, namely by

introducing an infinitesimally small sphere around the singularity, and by transforming the volume integral within that sphere to a surface integral across the sphere's surface. This will be covered in the first subsection of the present Discussion section.

It is also instructive to compare our approach to earlier suggestions for the use of a Fredholm integral equation similar to (3.36), often referred to as the Lippmann-Schwinger equation; in particular so concerning the domain over which the convolution integral is evaluated, the type of polarization field considered, and the relation of the Fredholm integral equation to the macroscopic strain associated with the RVE. This is topic of the second subsection of the present Discussion section.

Finally, we discuss the range of validity of the Fredholm integral equation (3.36), and the practical evaluation of the concentration tensor expressions in the case of microstructures which are more general than that with the harmonically fluctuating microscopic bulk moduli covered in Section 3.4. Corresponding deliberations conclude the present Discussion section.

### 3.5.1 Singular convolution integrals - alternative evaluation by means of Cauchy principal value

All integral expressions defining concentration tensor fields, such as (3.14), (3.41)–(3.43), (3.48), (3.62), and (3.67), exhibit singularities at  $\underline{x} = \underline{y}$ , i.e. at  $\underline{x} - \underline{y} = -\underline{z} = 0$ . In Section 3.4, we circumvented a direct treatment of this singularity, when evaluating (3.67) from the solution of the Poisson's equation, in combination with an auxiliary function in  $\underline{z}'$ , which allowed for “taking” the singularity “out of the integration domain”. In order to check the relevance of this strategy, we here evaluate the integral in (3.67) by an alternative approach, sometimes referred to as the Cauchy principal value analysis. Therefore, the integral in (3.67) is split into two portions associated with two integration domains: The first one is a sphere around the singular point (with a variable radius  $\epsilon$ , eventually tending towards zero), and the second one is the remaining (unbounded) three-dimensional space.

Denoting the small spherical domain as  $V^\epsilon$ , the integral in (3.67) can be recast as, see e.g. Buryachenko (2007), p. 54,

$$\int_{V^\epsilon} \frac{\partial^2}{\partial z_1^2} \left( \frac{1}{|\underline{z}|} \right) f(\underline{z}) \, dV(\underline{z}) = \int_{V^\epsilon} \frac{\partial^2}{\partial z_1^2} \left( \frac{1}{|\underline{z}|} \right) [f(\underline{z}) - f(0)] \, dV(\underline{z}) + \left[ \int_{V^\epsilon} \frac{\partial^2}{\partial z_1^2} \left( \frac{1}{|\underline{z}|} \right) \, dV(\underline{z}) \right] f(0), \quad (3.124)$$

whereby

$$f(\underline{z}) = \cos \left( \frac{2\pi}{\lambda} z_1 \right) \cos \left( \frac{2\pi}{\lambda} z_2 \right) \cos \left( \frac{2\pi}{\lambda} z_3 \right), \quad (3.125)$$

is fully in line with the developments of (3.69) and (3.70).

As stated before, we are interested in the limit case of  $\epsilon \rightarrow 0$

$$\lim_{\epsilon \rightarrow 0} \int_{V^\epsilon} \frac{\partial^2}{\partial z_1^2} \left( \frac{1}{|\underline{z}|} \right) [f(\underline{z}) - f(0)] \, dV(\underline{z}) = 0, \quad (3.126)$$

so that

$$\lim_{\epsilon \rightarrow 0} \int_{V^\epsilon} \frac{\partial^2}{\partial z_1^2} \left( \frac{1}{|\underline{z}|} \right) f(\underline{z}) \, dV(\underline{z}) = \lim_{\epsilon \rightarrow 0} \left[ \int_{V^\epsilon} \frac{\partial^2}{\partial z_1^2} \left( \frac{1}{|\underline{z}|} \right) \, dV(\underline{z}) \right] f(0) = \lim_{\epsilon \rightarrow 0} \left[ \int_{S^\epsilon} \frac{\partial}{\partial z_1} \left( \frac{1}{|\underline{z}|} \right) n_1 \, dS(\underline{z}) \right] f(0), \quad (3.127)$$

whereby we made use of the divergence theorem, with underline  $\underline{n}$  standing for the outward normal onto the spherical surface. Notably, the surface integral in (3.127) does not exhibit



any singularity any more, since the radius  $\epsilon$ , however small it may become, never actually reaches zero, so that the integrand in the last integral of (3.127) always stays finite. Let us evaluate the latter in more detail: Realizing that

$$\epsilon = |\underline{x} - \underline{y}| = |-\underline{z}| = |\underline{z}| = (z_1^2 + z_2^2 + z_3^2)^{1/2}, \quad (3.128)$$

the integrand in the surface integral of (3.127) can be transformed to

$$\frac{\partial}{\partial z_1} \left[ (z_1^2 + z_2^2 + z_3^2)^{-1/2} \right] = -z_1 (z_1^2 + z_2^2 + z_3^2)^{-3/2} = -\frac{z_1}{\epsilon^3}. \quad (3.129)$$

Then, the surface integral in (3.127) is preferably evaluated in spherical coordinates, where

$$z_1 = \epsilon \cos \phi \sin \theta, \quad (3.130)$$

$$n_1 = \cos \phi \sin \theta, \quad (3.131)$$

$$dS = \epsilon^2 \sin \theta \, d\phi \, d\theta. \quad (3.132)$$

so that use of (3.129)–(3.132) in the surface integral of (3.127) yields an expression which becomes independent of  $\epsilon$ , and hence, of the limiting process. In mathematical detail, we have

$$\lim_{\epsilon \rightarrow 0} \left[ \int_{S^\epsilon} \frac{\partial}{\partial z_1} \left( \frac{1}{|\underline{z}|} \right) n_1 \, dS(\underline{z}) \right] f(0) = \left[ - \int_{\theta=0}^{\pi} \sin^3 \theta \, d\theta \int_{\phi=0}^{2\pi} \cos^2 \phi \, d\phi \right] f(0) = -\frac{4\pi}{3}. \quad (3.133)$$

which proves the result obtained in (3.73) and (3.67); the latter turning out to be the Cauchy principal value of the singular surface integral of (3.127).

Accordingly, the small spherical integration domain yields the solution of the entire volume integral (spanning also the entire three-dimensional space outside the small spherical domain); hence, the integral of (3.60), when evaluated over the three-dimensional space except for the small sphere enclosing the singularity at the origin  $\underline{z} = 0$ , vanishes. This last statement can also be found in the book of Buryachenko (2007), namely as the last equation of (3.29) in the aforementioned reference.

The situation is totally different when it comes to the shear-related concentration tensor components according to (3.90): there, the Cauchy principal value needed to be multiplied by  $\sin(0) = 0$  so that the integration over the small sphere delivers zero, and it is the domain outside the small sphere, which solely contributes to the integral in (3.90). A procedure for solving this regular integral was presented, see (3.91)–(3.100).

### 3.5.2 Use of the Lippmann-Schwinger equation: auxiliary problems, integration domains, and macroscopic strains associated with the RVE

From a terminological viewpoint, we note that equations of the format (3.36), irrespective of the chosen integration domains or the format of the polarization stresses, are often referred to as the Lippmann-Schwinger equation, as a similar equation has been proposed by Lippmann and Schwinger (1950) in the field of quantum mechanics. In this context, it is interesting to compare our present contribution to earlier micromechanical applications of the Lippmann-Schwinger equation: A form which is virtually identical to (3.36) appears as Equation (9) in (Molinari and El Mouden, 1996); except for a sign change stemming from the definition of the

fourth-order Green operator as the twofold gradient with respect to  $\underline{x}$  (which is differing from our definition (3.35)). Mathematically speaking, the aforementioned sign change is due to

$$\text{grad}_x \text{grad}_x \mathbf{G}(\underline{x} - \underline{y}) = -\text{grad}_x^S \text{grad}_y \mathbf{G}(\underline{x} - \underline{y}). \quad (3.134)$$

However, the actual use of Equation (9) in (Molinari and El Mouden, 1996) is quite different from our present use of (3.36), as Molinari and El Mouden (1996) introduce an infinite number of uniform subfields of microscopic stiffnesses, representing strongly interacting “elastic inclusions” within an RVE of a composite material. At the same time, as a certain commonality of the approach of Molinari and El Mouden (1996) and our present contribution, we note that the latter authors’ strain  $\boldsymbol{\varepsilon}^0$  plays exactly the role of our auxiliary strain  $\mathbf{E}^0$ : it is the strain applied to the auxiliary homogeneous, infinite matrix which undergoes polarization stresses. However, different from our approach to solve this auxiliary problem so as to provide the microscopic strains as a function of the auxiliary strains, Molinari and El Mouden (1996) apply the strain average rule directly to the Fredholm integral equation, i.e. to their Equation (9), and they discuss explicit solutions for finite numbers of inclusions within a periodically repeating cubic cell. In this context, Molinari and El Mouden (1996) apply the strain average rule to an infinite domain, as can be seen from their Equation (15), while our Eq. (3.12) is clearly related to the (finite) RVE, and hence to the Hashin displacement boundary conditions imposed onto the latter according to (3.1). We also note that neither Equation (9) nor Equation (16) in (Molinari and El Mouden, 1996) give access to the concentration tensor fields - so that the expression (3.14), together with (3.41)–(3.43), turn out as an interesting original aspect of the present paper.

(3.36) of the present paper is also reminiscent of Equation (2.28) in (Torquato, 1997). However, different from our approach, Torquato (1997) restricts a non-vanishing polarization field to a *finite* domain within his infinitely large auxiliary problem subjected to some auxiliary strain  $\boldsymbol{\varepsilon}^0$ , the role of which is comparable to our auxiliary strain  $\mathbf{E}^0$ . In this context, he notes that the result of the corresponding convolution integral depends on the shape of the aforementioned finite domain, a situation which does not occur in our analysis in which the convolution integrals are evaluated throughout the unbounded auxiliary matrix. Eventually, Torquato (1997) lets his finite polarization domain coincide with the RVE of an anisotropic two-phase composite, for which he identifies stiffness series expansions in powers of “elastic polarizabilities”.

A further difference appears between (3.36) of the present contribution and the formally similar Equation (4) of the famous paper of Moulinec and Suquet (1994), see also (Moulinec and Suquet, 1998). The latter authors introduce the convolution integral directly on the (finite) RVE, noting that a corresponding explicit Green’s function can only be given in the case of periodic displacement boundary conditions imposed onto the RVE, and of corresponding microscopic strains which fluctuate periodically around their average (i.e., around the macroscopic strain). Namely, it is under this periodicity condition, that an explicit solution for the convolution problem exists in the Fourier space, which, in turn, allows for the development of a very efficient algorithm for the mechanical treatment of images made up of pixels or voxels, with the polarization stress being constant throughout one pixel or voxel, respectively.

Green’s operators in convolution integrals over a finite volume (i.e. differing from our present integration over an infinite auxiliary domain) have been already introduced in the 1970s: In this context, Zeller and Dederichs (1973) noted that the corresponding Green’s functions read as  $\mathbf{G}(\underline{x}, \underline{y}) = \mathbf{G}(\underline{y}, \underline{x})$ , rather than  $\mathbf{G}(\underline{x} - \underline{y}) = \mathbf{G}(\underline{y} - \underline{x})$ , an aspect which was overlooked by Kórringa (1973). However, explicit expressions for the aforementioned Green’s functions are not available, so that Zeller and Dederichs (1973) restricted their analysis to

series expansions for small stiffness fluctuations, while Kröner (1977) uses convolution integrals over finite volumes for the derivation of bounds for the effective elastic moduli of disordered materials.

Our iterative scheme for solving the Fredholm integral equation (3.36) also bears some similarities with earlier contributions in the field: Kröner (1977) presents an iterative solution for the Lippmann-Schwinger equation formulated directly on the RVE, and Torquato (1997) proposes an iterative scheme which finally delivers the polarization stress as a function of the homogeneous auxiliary strain  $\boldsymbol{\varepsilon}^0$ .

### 3.5.3 Range of validity of Lippmann-Schwinger equation

The practical relevance of the case where the polarization stresses in (33) outweigh the effect microscopic volume forces, which is the prerequisite for the Lippmann-Schwinger equation (3.36) to hold, deserves further discussion: Within the representative volume element (RVE), the microscopic stresses  $\boldsymbol{\sigma}$  fluctuate around their spatial average, which is the macroscopic stress  $\boldsymbol{\Sigma}$ , and the characteristic length scale  $d$  of this fluctuation is scale-separated from the length of the RVE,  $\ell_{RVE}$ , which reads mathematically as

$$\frac{\partial(\boldsymbol{\sigma} - \boldsymbol{\Sigma})}{\partial x} = \frac{\partial \boldsymbol{\sigma}}{\partial x}, \quad \text{with} \quad \frac{\|\boldsymbol{\sigma}\|}{\|\frac{\partial \boldsymbol{\sigma}}{\partial x}\|} = d. \quad (3.135)$$

Due to the mathematical structure (5) of the microscopic equilibrium conditions, any microscopic volume forces leading to microscopic stress fluctuation are required to change their sign, i.e. their direction, over distances as small as  $d$ . Practically speaking, this is an exceptional case: Even if in composites with high contrast in mass density, the corresponding gravitational forces of varying magnitude would always share the same direction; or in other words, practically relevant force fields are often parallel within the RVE. We note in passing, that such micro-parallel force field, directly implying the validity of (36), even fulfill a force field average rule (Jiménez Segura et al., 2022b).

### 3.5.4 Practical note concerning non-harmonic microstiffness fluctuations

Finally, we discuss which aspects of Section 3.4 hold beyond the restriction to harmonically fluctuating microstiffnesses, and how the semi-analytical solutions presented in this section may be generalized to non-harmonic microstiffness fluctuations. In this context, the key generalization step would be the representation of any, arbitrarily general continuous microstiffness distribution across a finite RVE by a three-dimensional Fourier series. Generalizing, in this way, the example distribution of (3.47) to an arbitrarily inhomogeneous bulk modulus distribution  $\Delta k(x_1, x_2, x_3)$  yields

$$\mathfrak{c}(\underline{x}) = \mathbb{C}^0 + 3 \sum_k \sum_l \sum_m c_{klm} \exp\left(2\pi i \left[\frac{kx_1}{\lambda_1} + \frac{lx_2}{\lambda_2} + \frac{mx_3}{\lambda_3}\right]\right), \quad (3.136)$$

with  $i$  now standing for the imaginary unit, and with the Fourier coefficients  $c_{klm}$  being obtained from

$$c_{klm} = \int_{-a}^a \int_{-a}^a \int_{-a}^a \exp\left(-2\pi i \left[\frac{kx_1}{\lambda_1} + \frac{lx_2}{\lambda_2} + \frac{mx_3}{\lambda_3}\right]\right) \Delta k(x_1, x_2, x_3) dx_1 dx_2 dx_3 \quad (3.137)$$

In other words, sums of products of any three trigonometric functions, be they sine or cosine, – rather than the product of three sine or three cosine terms – would occur throughout the

convolution integrals. However, the effect on the corresponding modifications of Eq.(3.63) and (3.90) are only minor: Thanks to (3.64) and

$$\cos(a + b) = \cos(a)\cos(b) - \sin(a)\sin(b), \quad (3.138)$$

the structure of the integrals in (3.67) and (3.93) stay unaffected. This shows the considerable potential of our method for material investigation based on Fourier-representation of images - as an interesting complement to the popular voxel-based FFT schemes.

### 3.6 Conclusions

The effects of elastic behavior at the microscale are represented by means of the Green's function formalism, leading to Fredholm integral equations which provide novel, series-type integral expressions for the concentration tensor field. The latter may be analytically solved in special cases, providing an unprecedented direct access to macro-to-micro scale transition relations, as expressed by the concentration tensor expressions (3.14), (3.41)–(3.43), (3.83), (3.84), and (3.105). This opens new avenues for exploring the mechanical effect of eigenstrains in hierarchical material systems with complex morphologies, as an interesting alternative to classical computational homogenization. The new approach also provides semi-analytical access to the homogenized stiffness, such as the calculated for a microstructure with harmonically fluctuating bulk moduli, see (3.16) and (3.121). Since  $I(\mathcal{K}) \geq 1$ , see Fig. 3.2, the resulting homogenized stiffness,  $\mathbb{C}^{hom}$ , is smaller than or equal to the average stiffness,  $\mathbb{C}^0$ . This is fully consistent with the famous result of Voigt (1889) that average over the microstiffness is larger the homogenized stiffness, in the sense that (Zaoui, 2002)

$$\mathbf{E} : \left( \langle \mathbb{A}^T : \mathbb{c} : \mathbb{A} \rangle - \mathbb{C}^{hom} \right) : \mathbf{E} \geq 0, \quad \forall \mathbf{E}. \quad (3.139)$$

# Chapter 4

---

## Concentration tensors preserving elastic symmetry of multiphase composites

**Authored by:** Nabor Jiménez Segura, Bernhard L.A. Pichler, Christian Hellmich

**Publication outlook:** At the time of finalizing the thesis, this has been submitted to *Mechanics of Materials*, currently under revision.

**Abstract:** The micromechanics of composites with multiple phases of different shapes embedded into a matrix phase, typically requires symmetrization strategies for their homogenized elasticity tensors, in particular so if the popular Mori-Tanaka estimate is employed. We here explore the implications of such symmetrization techniques, on the concentrations tensors, i.e. on the relations between macroscopic strains imposed onto a representative volume element of microelastic matter, and the microscopic phase strains developing across the materials' microstructure. Thereby, we adopt the important idea of Mori and Tanaka to approximate the phase strains by the homogeneous strains inside an Eshelbian inhomogeneity embedded into an infinite matrix, together with the phase strains fulfilling the strain average rule; while we refrain from the identification of the strain in the matrix phase as the auxiliary strain imposed remotely at the infinite matrix of Eshelby's matrix-inhomogeneity problem. Instead of this identification, we allow for a general multilinear relation between auxiliary strains and RVE-related macroscopic strains, and we express the homogenized stiffness as (i) a function of the conversion tensor quantifying the aforementioned multilinear relation, and (ii) as the symmetrized Mori-Tanaka estimate. In this way, the conversion tensor and all phase concentrations tensors can be determined in a way which allows the overall elastic stiffness to remain symmetric.

**Contribution:** Nabor Jiménez Segura: Investigation, Methodology, Formal analysis, Computation, Visualization, Writing – original draft, review & editing. Bernhard L.A. Pichler: Supervision, Conceptualization, Funding acquisition, Methodology, Formal analysis, Writing – original draft, Writing – review & editing. Christian Hellmich: Supervision, Conceptualization, Funding acquisition, Methodology, Formal analysis, Supervision, Writing – review & editing.

**Keywords:** Composite mechanics; Symmetry; Matrix-inclusion; Elasticity.

## 4.1 Introduction

The strain concentration tensor, coined in a landmark paper of Hill (Hill, 1963), is a central notion in the wide field of composite mechanics or continuum micromechanics (Zaoui, 2002). In linear elastic media, it assigns the macroscopic strains  $\mathbf{E}$  associated with the classical macroscopically infinitesimal volume element of continuum mechanics, to the microscopic strains  $\boldsymbol{\varepsilon}_r$ ,  $r = 1, \dots, N_r$ , associated to  $N_r$  subdomains or phases inside a microscopically finite representative volume element (RVE) which coincides with the aforementioned macroscopic volume element. Mathematically, this macro-to-micro linking is expressed as

$$\boldsymbol{\varepsilon}_r = \mathbb{A}_r : \mathbf{E}, \quad \forall r = 1, \dots, N_r, \quad (4.1)$$

with  $\mathbb{A}_r$  as the fourth-order strain concentration tensor of phase  $r$ , and  $N_r$  denoting the number of phases. Equivalently, a stress concentration tensor links macroscopic and microscopic stresses. The significance of these concentration tensors extends beyond the narrower field of elasticity homogenization; as it also allows for upscaling of non-elastic properties, such as eigenstrains/eigenstresses (Levin, 1967; Rosen and Hashin, 1970; Wang et al., 2018) or strength properties of elasto-brittle materials (Fritsch et al., 2009; Sanahuja et al., 2010; Fritsch et al., 2013; Königsberger et al., 2018).

A particularly popular and versatile method for estimating the strain concentration tensors  $\mathbb{A}_r$  of composites consisting of one matrix phase and one or several inclusion phases is the so-called Mori-Tanaka homogenization scheme (Mori and Tanaka, 1973; Benveniste, 1987; Benveniste et al., 1991; Zaoui, 2002), where the phase strains are approximated by the strains in one Eshelbian inhomogeneity (Eshelby, 1957) embedded into an infinite matrix (with the elastic properties of the matrix phase). This infinite matrix is subjected to remote (auxiliary) strains, with the latter arising from the fulfillment of the strain average rule (Hashin, 1983)

$$\sum_{r=1}^{N_r} f_r \boldsymbol{\varepsilon}_r = \mathbf{E}, \quad (4.2)$$

whereby  $f_r$  stands for the volume fraction of phase  $r$ .

However, depending on the chosen shapes and elastic properties of the inclusion phases, the Mori-Tanaka estimates of the homogenized stiffness may violate the symmetry requirements for elasticity tensors, so that the Mori-Tanaka scheme is only physically relevant if at least one of the following three conditions is met:

1. all phases and the overall composite behave isotropically (Sevostianov and Kachanov, 2014; Ferrari, 1991);
2. all inclusion phases have the same stiffness (Benveniste et al., 1991; Sevostianov and Kachanov, 2014);
3. all inclusion phases have the same shape and the same orientation (Benveniste et al., 1989, 1991; Sevostianov and Kachanov, 2014).

While these limitations have been classically deplored, Sevostianov and Kachanov (2014) took a radically different perspective on the topic, by actively symmetrizing the Mori-Tanaka-derived non-symmetric elastic stiffness tensors. This interesting approach motivates the present

paper; proposing a scheme which is still based on Eshelby's inhomogeneity problem as a good tool for the approximation of inclusion phase strains, while overcoming the aforementioned limitations. In more detail, we will show that the source of these limitations is the classical assumption of the matrix phase strains to coincide with the auxiliary remote strains of Eshelby's inhomogeneity problem. As a remedy, we will not require this coincidence, and instead, we will explicitly introduce a multilinear relation between macroscopic strains and Eshelby problem-related auxiliary strains, defined through a newly introduced fourth-order RVE-to-remote strain conversion tensor whose form will be derived from the actively symmetrized form of the multiphase Mori-Tanaka estimate. The corresponding mathematical derivations are found in Section 2 of the present paper, and complemented by a numerical benchmark example, see Section 3, followed by Conclusions, see Section 4.

## 4.2 Mathematical derivation of elastic symmetry-preserving concentration tensors

Our starting point is the famous idea of Mori and Tanaka (Mori and Tanaka, 1973; Benveniste, 1987) to relate the macroscopic strains  $\mathbf{E}$  imposed onto the boundary of the RVE to strains  $\mathbf{E}_\infty$  associated with Eshelby's inhomogeneity problem (Eshelby, 1957), consisting of an ellipsoidal domain of stiffness  $\mathbb{c}_i$  (the inhomogeneity), which is embedded into an infinite matrix with stiffness  $\mathbb{c}_m$ , see Fig. 4.1. The latter matrix is subjected to uniform strains  $\mathbf{E}_\infty$  at infinity. For this problem, classical analytical solutions (Eshelby, 1957; Laws, 1977) link  $\mathbf{E}_\infty$  to the

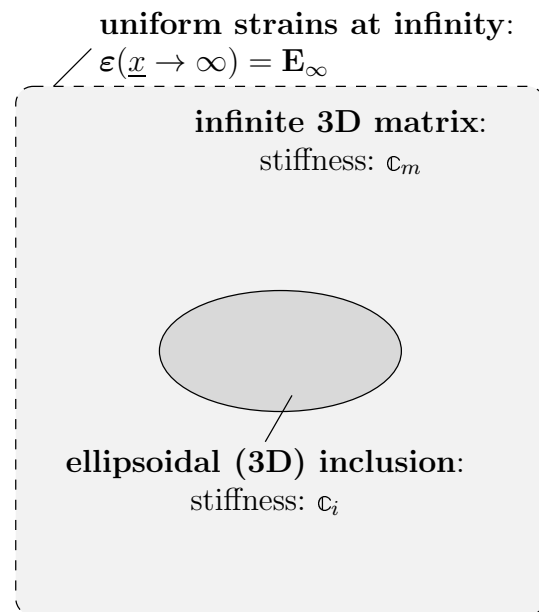


**Fig. 4.1.** Two-dimensional sketch illustrating Eshelby's three-dimensional matrix-inhomogeneity problem:  $\mathbf{E}_\infty$  denotes the remote strain,  $\underline{x}$  is the position vector, while  $\mathbb{c}_m$  and  $\mathbb{c}_i$ , respectively, are the stiffness tensors of the matrix, and of the ellipsoidal inhomogeneity.

uniform strains in the inhomogeneity; and these solutions are repeatedly used for estimating the microscopic strains within the RVE, in particular so the strains in  $N_i = (N_r - 1)$  inclusion



phases which are all surrounded by a matrix phase, according to

$$\boldsymbol{\varepsilon}_i = \mathbb{A}_i^\infty : \mathbf{E}_\infty, \quad \forall i = 1, \dots, N_i, \quad (4.3)$$

where

$$\mathbb{A}_i^\infty = \left[ \mathbb{I} + \mathbb{P}_i : (\mathbf{c}_i - \mathbf{c}_m) \right]^{-1}, \quad \forall i = 1, \dots, N_i. \quad (4.4)$$

In (4.4),  $\mathbb{I}$  stands for the symmetric fourth-order identity tensor, the morphology tensor  $\mathbb{P}_i$  accounts for the shape and orientation of the inclusion, while  $\mathbf{c}_m$  and  $\mathbf{c}_i$ , respectively, are the stiffness tensors of the matrix, and of the ellipsoidal inhomogeneity. However, different from the traditional approach (Mori and Tanaka, 1973; Benveniste, 1987), we do not apply (4.3) to the matrix phase itself, i.e. we do not actively impose  $\boldsymbol{\varepsilon}_m = \mathbf{E}_\infty$ , but we introduce a general multilinear form linking  $\mathbf{E}_\infty$  and  $\mathbf{E}$ , reading as

$$\mathbf{E}_\infty = \mathbb{M} : \mathbf{E}, \quad (4.5)$$

with a fourth-order RVE-to-remote strain conversion tensor  $\mathbb{M}$ . Insertion of (4.5) into (4.3) and comparison with (4.1) yields

$$\mathbb{A}_i = \mathbb{A}_i^\infty : \mathbb{M}. \quad (4.6)$$

The format of  $\mathbb{M}$  is now derived from the required symmetry of the homogenized stiffness tensor. Standardly, the latter arises from introduction of phase elasticity tensors  $\mathbf{c}_r$  linking microscopic phase strains to microscopic phase stresses  $\boldsymbol{\sigma}_r$ ,

$$\boldsymbol{\sigma}_r = \mathbf{c}_r : \boldsymbol{\varepsilon}_r. \quad (4.7)$$

Insertion of (4.1) into (4.7), and subsequent averaging over the microscopic stresses according to the stress average rule (Hori and Nemat-Nasser, 1999; Jiménez Segura et al., 2022b),

$$\boldsymbol{\Sigma} = \sum_{r=1}^{N_r} f_r \boldsymbol{\sigma}_r, \quad (4.8)$$

leads to a macroscopic elastic law of the format

$$\boldsymbol{\Sigma} = \mathbb{C}_{hom} : \mathbf{E}, \quad (4.9)$$

with the homogenized stiffness tensor  $\mathbb{C}_{hom}$  reading as (Hill, 1963; Laws, 1973; Zaoui, 2002)

$$\mathbb{C}_{hom} = \sum_{r=1}^{N_r} f_r \mathbf{c}_r : \mathbb{A}_r. \quad (4.10)$$

In addition, the average condition for strain concentration tensors follows from (4.1) and (4.2) as

$$\sum_{r=1}^{N_r} f_r \mathbb{A}_r = \mathbb{I}. \quad (4.11)$$

Expressing, via (4.11), the matrix phase concentration tensor in terms of the concentration tensors of all other phases, and insertion of the corresponding result into (4.10), while considering the newly introduced conversion tensor  $\mathbb{M}$ , yields

$$\mathbb{C}_{hom} = \mathbf{c}_m + \sum_{i=1}^{N_i} f_i (\mathbf{c}_i - \mathbf{c}_m) : \mathbb{A}_i^\infty : \mathbb{M}, \quad (4.12)$$

whereby the second term on the right-hand side of (4.12) may be referred to as inclusion-related stiffness contribution tensor (Sevostianov and Kachanov, 2014). Symmetry of the homogenized stiffness tensor expression, in the sense of  $C_{hom,ijkl} = C_{hom,klij}$ , requires symmetry of the inclusion-related stiffness contribution tensor, which mathematically reads as

$$\sum_{i=1}^{N_i} f_i (\mathbf{c}_i - \mathbf{c}_m) : \mathbb{A}_i^\infty : \mathbb{M} = \left[ \sum_{i=1}^{N_i} f_i (\mathbf{c}_i - \mathbf{c}_m) : \mathbb{A}_i^\infty : \mathbb{M} \right]^T, \quad (4.13)$$

whereby the transpose operator  $T$  refers to the operation  $X_{ijkl}^T = X_{klij}$ . In order to identify the conversion tensor  $\mathbb{M}$ , we adopt the 2014 proposition of Sevostianov and Kachanov (2014) to straightforwardly symmetrize the results from conventional Mori-Tanaka multiphase homogenization theory. According to the latter, the homogenized stiffness tensor reads as (Benveniste et al., 1991)

$$\mathbb{C}_{hom} = \mathbf{c}_m + \left[ \sum_{i=1}^{N_i} f_i (\mathbf{c}_i - \mathbf{c}_m) : \mathbb{A}_i^\infty \right] : \left( f_m \mathbb{1} + \sum_{i=1}^{N_i} f_i \mathbb{A}_i^\infty \right)^{-1}. \quad (4.14)$$

When employing the tensor operation rules  $\mathbb{X} : \mathbb{Y}^{-1} = (\mathbb{Y} : \mathbb{X}^{-1})^{-1}$ , with  $\mathbb{X} = \sum_{i=1}^{N_i} f_i (\mathbf{c}_i - \mathbf{c}_m) : \mathbb{A}_i^\infty$  and  $\mathbb{Y}^{-1} = (f_m \mathbb{1} + \sum_{i=1}^{N_i} f_i \mathbb{A}_i^\infty)^{-1}$ , (4.14) can be transformed to

$$\mathbb{C}_{hom} = \mathbf{c}_m + \left\{ f_m \left[ \sum_{i=1}^{N_i} f_i (\mathbf{c}_i - \mathbf{c}_m) : \mathbb{A}_i^\infty \right]^{-1} + \left( \sum_{i=1}^{N_i} f_i \mathbb{A}_i^\infty \right) : \left[ \sum_{i=1}^{N_i} f_i (\mathbf{c}_i - \mathbf{c}_m) : \mathbb{A}_i^\infty \right]^{-1} \right\}^{-1}. \quad (4.15)$$

We observe that both  $\mathbf{c}_m$  and  $(\mathbf{c}_i - \mathbf{c}_m) : \mathbb{A}_i^\infty$  are symmetric; the latter term exhibits this symmetry because of

$$(\mathbf{c}_i - \mathbf{c}_m) : \mathbb{A}_i^\infty = \left[ (\mathbf{c}_i - \mathbf{c}_m)^{-1} + \mathbb{P}_i \right]^{-1}, \quad (4.16)$$

with the Hill tensor  $\mathbb{P}_i$  being symmetric. Accordingly, symmetrization  $\text{SYM}(\mathbb{X}) = \frac{1}{2}\mathbb{X} + \frac{1}{2}\mathbb{X}^T$  of the second term in the curly brackets of (4.15) yields

$$\begin{aligned} \text{SYM} \left( \left( \sum_{i=1}^{N_i} f_i \mathbb{A}_i^\infty \right) : \left[ \sum_{i=1}^{N_i} f_i (\mathbf{c}_i - \mathbf{c}_m) : \mathbb{A}_i^\infty \right]^{-1} \right) = & \quad (4.17) \\ & \frac{1}{2} \left( \sum_{i=1}^{N_i} f_i \mathbb{A}_i^\infty \right) : \left[ \sum_{i=1}^{N_i} f_i (\mathbf{c}_i - \mathbf{c}_m) : \mathbb{A}_i^\infty \right]^{-1} \\ & + \frac{1}{2} \left[ \sum_{i=1}^{N_i} f_i (\mathbf{c}_i - \mathbf{c}_m) : \mathbb{A}_i^\infty \right]^{-1} : \left( \sum_{i=1}^{N_i} f_i (\mathbb{A}_i^\infty)^T \right), \end{aligned}$$

and since the inverse of a symmetric tensor is again a symmetric tensor, the symmetrized form of (4.15) reads as

$$\begin{aligned} \mathbb{C}_{hom,sym} = & \mathbf{c}_m + \left\{ f_m \left[ \sum_{i=1}^{N_i} f_i (\mathbf{c}_i - \mathbf{c}_m) : \mathbb{A}_i^\infty \right]^{-1} + \frac{1}{2} \left( \sum_{i=1}^{N_i} f_i \mathbb{A}_i^\infty \right) : \left[ \sum_{i=1}^{N_i} f_i (\mathbf{c}_i - \mathbf{c}_m) : \mathbb{A}_i^\infty \right]^{-1} \right. \\ & \left. + \frac{1}{2} \left[ \sum_{i=1}^{N_i} f_i (\mathbf{c}_i - \mathbf{c}_m) : \mathbb{A}_i^\infty \right]^{-1} : \left( \sum_{i=1}^{N_i} f_i (\mathbb{A}_i^\infty)^T \right) \right\}^{-1}, \quad (4.18) \end{aligned}$$

whereby we have made use of (4.17). Comparing expression (4.18) with the format (4.12) yields the RVE-to-remote strain conversion tensor as

$$\mathbb{M} = \left\{ f_m \mathbb{1} + \left( \sum_{i=1}^{N_i} f_i \mathbb{A}_i^\infty \right) - \frac{1}{2} \left[ \left( \sum_{i=1}^{N_i} f_i \mathbb{A}_i^\infty \right) : \left( \sum_{i=1}^{N_i} f_i (\mathbb{c}_i - \mathbb{c}_m) : \mathbb{A}_i^\infty \right)^{-1} \right. \right. \\ \left. \left. - \left( \sum_{i=1}^{N_i} f_i (\mathbb{c}_i - \mathbb{c}_m) : \mathbb{A}_i^\infty \right)^{-1} : \left( \sum_{i=1}^{N_i} f_i (\mathbb{A}_i^\infty)^T \right) \right] : \left( \sum_{i=1}^{N_i} f_i (\mathbb{c}_i - \mathbb{c}_m) : \mathbb{A}_i^\infty \right) \right\}^{-1}, \quad (4.19)$$

while the concentration tensors for the inclusion phases follow from insertion of (4.19) into (4.6) as

$$\mathbb{A}_i = \mathbb{A}_i^\infty : \left\{ f_m \mathbb{1} + \left( \sum_{i=1}^{N_i} f_i \mathbb{A}_i^\infty \right) - \frac{1}{2} \left[ \left( \sum_{i=1}^{N_i} f_i \mathbb{A}_i^\infty \right) : \left( \sum_{i=1}^{N_i} f_i (\mathbb{c}_i - \mathbb{c}_m) : \mathbb{A}_i^\infty \right)^{-1} \right. \right. \\ \left. \left. - \left( \sum_{i=1}^{N_i} f_i (\mathbb{c}_i - \mathbb{c}_m) : \mathbb{A}_i^\infty \right)^{-1} : \left( \sum_{i=1}^{N_i} f_i (\mathbb{A}_i^\infty)^T \right) \right] : \left( \sum_{i=1}^{N_i} f_i (\mathbb{c}_i - \mathbb{c}_m) : \mathbb{A}_i^\infty \right) \right\}^{-1}. \quad (4.20)$$

Eventually, use of the average condition for strain concentration tensors (4.11) allows for deriving the concentration tensor for the matrix phase as

$$\mathbb{A}_m = \frac{1}{f_m} \left( \mathbb{1} - \sum_{i=1}^{N_i} f_i \mathbb{A}_i \right). \quad (4.21)$$

### 4.3 Benchmark example

A benchmark example is used to illustrate features of the novel concentration tensors. It refers to a matrix-inclusion composite with two types of inclusions. The specific materials of the example are a  $\text{Ti}_3\text{Al}$  matrix, one carbon spherical phase (index 1, aspect ratio  $\omega_1 = 1$ ) and one steel prolate phase (index 2, aspect ratio  $\omega_2 = 3$ , major axis aligned with the 3-direction), see Fig. 4.2 and Table 4.1 for the volume fractions and the isotropic elastic stiffness constants of the three material phases. The chosen benchmark example is problematic from the viewpoint

**Table 4.1**

Volume fractions and isotropic elastic stiffness constants of the three material phases of the benchmark material, illustrated in Fig. 4.2.

property	matrix phase	inclusion phase 1	inclusion phase 2
volume fraction	$f_m = 0.60$	$f_1 = 0.25$	$f_2 = 0.15$
bulk modulus	$k_m = 80.63 \text{ GPa}$	$k_1 = 19.29 \text{ GPa}$	$k_2 = 160.0 \text{ GPa}$
shear modulus	$\mu_m = 37.10 \text{ GPa}$	$\mu_1 = 14.30 \text{ GPa}$	$\mu_2 = 79.30 \text{ GPa}$
phase shape	–	spherical	prolate
aspect ratio	–	$\omega_1 = 1$	$\omega_2 = 3$

of the classical Mori-Tanaka scheme, because the homogenized composite is neither isotropic, nor do the inclusion phases have the same stiffness, nor do the inclusion phases have the same shape and orientation, see (Benveniste et al., 1989; Ferrari, 1991; Sevostianov and Kachanov, 2014).

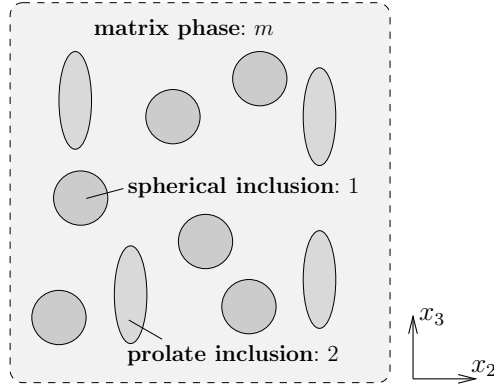


**Fig. 4.2.** Benchmark material: matrix-inclusion composite with two types of inclusions, one spherical phase (index 1, aspect ratio  $\omega_1 = 1$ ) and one prolate phase (index 2, aspect ratio  $\omega_2 = 3$ , major axis aligned with the 3-direction), see Table 4.1 for the volume fractions and the isotropic elastic stiffness constants of the three material phases; two-dimensional representation showing qualitative properties of a three-dimensional RVE.

The isotropic stiffness tensors of the phases are obtained as

$$\mathbb{C}_j = 3k_j \mathbb{I}^{vol} + 2\mu_j \mathbb{I}^{dev}, \quad (4.22)$$

where  $\mathbb{I}^{vol}$  and  $\mathbb{I}^{dev}$  denote the volumetric and deviatoric part of the symmetric fourth-order identity tensor. Their components read as  $I_{ijkl}^{vol} = \frac{1}{3} \delta_{ij} \delta_{kl}$  and  $I_{ijkl}^{dev} = \frac{1}{2} [\delta_{ik} \delta_{jl} + \delta_{il} \delta_{jk}] - \frac{1}{3} \delta_{ij} \delta_{kl}$ , with  $\delta_{ij}$  denoting the Kronecker delta which is equal to 1 for  $i = j$  and equal to 0 otherwise. The components of a tensor  $X_{ijkl}$  with so-called minor symmetries  $X_{ijkl} = X_{jikl}$  and  $X_{ijkl} = X_{ijlk}$  can be represented in Kelvin-Mandel-Walpole notation (Walpole, 1984; Rychlewski, 1984; Cowin, 2003; Helnwein, 2001) as a  $6 \times 6$  matrix:

$$\mathbb{X} = \begin{pmatrix} X_{1111} & X_{1122} & X_{1133} & \sqrt{2} X_{1123} & \sqrt{2} X_{1131} & \sqrt{2} X_{1112} \\ X_{2211} & X_{2222} & X_{2233} & \sqrt{2} X_{2223} & \sqrt{2} X_{2231} & \sqrt{2} X_{2212} \\ X_{3311} & X_{3322} & X_{3333} & \sqrt{2} X_{3323} & \sqrt{2} X_{3331} & \sqrt{2} X_{3312} \\ \sqrt{2} X_{2311} & \sqrt{2} X_{2322} & \sqrt{2} X_{2333} & 2 X_{2323} & 2 X_{2331} & 2 X_{2312} \\ \sqrt{2} X_{3111} & \sqrt{2} X_{3122} & \sqrt{2} X_{3133} & 2 X_{3123} & 2 X_{3131} & 2 X_{3112} \\ \sqrt{2} X_{1211} & \sqrt{2} X_{1222} & \sqrt{2} X_{1233} & 2 X_{1223} & 2 X_{1231} & 2 X_{1212} \end{pmatrix}. \quad (4.23)$$

The morphology tensor of a spherical inhomogeneity in an isotropic matrix with bulk modulus  $k_0$  and shear modulus  $\mu_0$  reads as (Hill, 1965a; Dvorak, 2012)

$$\mathbb{P}_{sph} = P_{vol} \mathbb{I}_{vol} + P_{dev} \mathbb{I}_{dev}, \quad (4.24)$$

with  $P_{vol} = \frac{1}{3k_0 + 4\mu_0}$  and  $P_{dev} = \frac{3(k_0 + 2\mu_0)}{5\mu_0(3k_0 + 4\mu_0)}$ . Insertion of the numerical values from Table 4.1 into (4.24) yields the morphology tensor of inclusion phase 1, reading as

$$\mathbb{P}_1 = \begin{pmatrix} +5.1312 & -1.2845 & -1.2845 & 0 & 0 & 0 \\ -1.2845 & +5.1312 & -1.2845 & 0 & 0 & 0 \\ -1.2845 & -1.2845 & +5.1312 & 0 & 0 & 0 \\ 0 & 0 & 0 & +6.4157 & 0 & 0 \\ 0 & 0 & 0 & 0 & +6.4157 & 0 \\ 0 & 0 & 0 & 0 & 0 & +6.4157 \end{pmatrix} \times 10^{-3} \text{ GPa}^{-1}. \quad (4.25)$$

The morphology tensor of a prolate inclusion with aspect ratio  $\omega > 1$  embedded in the same isotropic matrix reads, in Walpole notation, as (Ponte-Castañeda and Willis, 1995; Dvorak, 2012)

$$\mathbb{P}_{pro} = 2K_p \mathbb{W}_1 + L_p (\mathbb{W}_2 + \mathbb{W}_3) + H_p \mathbb{W}_4 + 2M_p \mathbb{W}_5 + 2P_p \mathbb{W}_6, \quad (4.26)$$

with  $K_p = \frac{\mu_0(7h-2\omega^2-4\omega^2 h)+3k_0(h-2\omega^2+2\omega^2 h)}{8\mu_0(1-\omega^2)(4\mu_0+3k_0)}$ ,  $L_p = \frac{(2\omega^2-2\omega^2 h-h)(\mu_0+3k_0)}{4\mu_0(1-\omega^2)(4\mu_0+3k_0)}$ ,  $H_p = \frac{\mu_0(6-5h-8\omega^2+8\omega^2 h)+3k_0(h-2\omega^2+2\omega^2 h)}{2\mu_0(1-\omega^2)(4\mu_0+3k_0)}$ ,  $M_p = \frac{\mu_0(15h-2\omega^2-12\omega^2 h)+3k_0(3h-2\omega^2)}{16\mu_0(1-\omega^2)(4\mu_0+3k_0)}$ , and  $P_p = \frac{2\mu_0(4-3h-2\omega^2)+3k_0(2-3h+2\omega^2-3\omega^2 h)}{8\mu_0(1-\omega^2)(4\mu_0+3k_0)}$ , where  $h = \omega \frac{\omega\sqrt{\omega^2-1}-\text{acosh}\omega}{(\omega^2-1)\sqrt{\omega^2-1}}$ . The Walpole base, in Kelvin-Mandel-Walpole notation, reads as (Walpole, 1984):

$$\begin{aligned} \mathbb{W}_1 &= \frac{1}{2} \begin{pmatrix} 1 & 1 & 0 & 0 & 0 & 0 \\ 1 & 1 & 0 & 0 & 0 & 0 \\ 0 & 0 & 0 & 0 & 0 & 0 \\ 0 & 0 & 0 & 0 & 0 & 0 \\ 0 & 0 & 0 & 0 & 0 & 0 \\ 0 & 0 & 0 & 0 & 0 & 0 \end{pmatrix}, & \mathbb{W}_2 &= \begin{pmatrix} 0 & 0 & 1 & 0 & 0 & 0 \\ 0 & 0 & 1 & 0 & 0 & 0 \\ 0 & 0 & 0 & 0 & 0 & 0 \\ 0 & 0 & 0 & 0 & 0 & 0 \\ 0 & 0 & 0 & 0 & 0 & 0 \\ 0 & 0 & 0 & 0 & 0 & 0 \end{pmatrix}, & \mathbb{W}_3 &= \begin{pmatrix} 0 & 0 & 0 & 0 & 0 & 0 \\ 0 & 0 & 0 & 0 & 0 & 0 \\ 1 & 1 & 0 & 0 & 0 & 0 \\ 0 & 0 & 0 & 0 & 0 & 0 \\ 0 & 0 & 0 & 0 & 0 & 0 \\ 0 & 0 & 0 & 0 & 0 & 0 \end{pmatrix} \\ \mathbb{W}_4 &= \begin{pmatrix} 0 & 0 & 0 & 0 & 0 & 0 \\ 0 & 0 & 0 & 0 & 0 & 0 \\ 0 & 0 & 1 & 0 & 0 & 0 \\ 0 & 0 & 0 & 0 & 0 & 0 \\ 0 & 0 & 0 & 0 & 0 & 0 \\ 0 & 0 & 0 & 0 & 0 & 0 \end{pmatrix}, & \mathbb{W}_5 &= \frac{1}{2} \begin{pmatrix} 1 & -1 & 0 & 0 & 0 & 0 \\ -1 & 1 & 0 & 0 & 0 & 0 \\ 0 & 0 & 0 & 0 & 0 & 0 \\ 0 & 0 & 0 & 0 & 0 & 0 \\ 0 & 0 & 0 & 0 & 0 & 0 \\ 0 & 0 & 0 & 0 & 0 & 2 \end{pmatrix}, & \mathbb{W}_6 &= \begin{pmatrix} 0 & 0 & 0 & 0 & 0 & 0 \\ 0 & 0 & 0 & 0 & 0 & 0 \\ 0 & 0 & 0 & 0 & 0 & 0 \\ 0 & 0 & 0 & 1 & 0 & 0 \\ 0 & 0 & 0 & 0 & 1 & 0 \\ 0 & 0 & 0 & 0 & 0 & 0 \end{pmatrix}. \end{aligned} \quad (4.27)$$

Insertion of the numerical values from Table 4.1 into (4.26), together with (4.27), yields the morphology tensor of inclusion phase 2, reading as

$$\mathbb{P}_2 = \begin{pmatrix} +6.0532 & -1.9863 & -0.6416 & 0 & 0 & 0 \\ -1.9863 & +6.0532 & -0.6416 & 0 & 0 & 0 \\ -0.6416 & -0.6416 & +2.1187 & 0 & 0 & 0 \\ 0 & 0 & 0 & +6.1880 & 0 & 0 \\ 0 & 0 & 0 & 0 & +6.1880 & 0 \\ 0 & 0 & 0 & 0 & 0 & +8.0395 \end{pmatrix} \times 10^{-3} \text{ GPa}^{-1}. \quad (4.28)$$

The Eshelby problem-related auxiliary strain concentration tensors of the inclusion phases are computed from (4.4), yielding

$$\mathbb{A}_1^\infty = \begin{pmatrix} +1.5731 & +0.1596 & +0.1596 & 0 & 0 & 0 \\ +0.1596 & +1.5731 & +0.1596 & 0 & 0 & 0 \\ +0.1596 & +0.1596 & +1.5731 & 0 & 0 & 0 \\ 0 & 0 & 0 & +1.4135 & 0 & 0 \\ 0 & 0 & 0 & 0 & +1.4135 & 0 \\ 0 & 0 & 0 & 0 & 0 & +1.4135 \end{pmatrix}, \quad (4.29)$$

$$\mathbb{A}_2^\infty = \begin{pmatrix} +5.9261 & -0.0315 & -0.5855 & 0 & 0 & 0 \\ -0.0315 & +5.9261 & -0.5855 & 0 & 0 & 0 \\ +0.0547 & +0.0547 & +8.1750 & 0 & 0 & 0 \\ 0 & 0 & 0 & +6.5692 & 0 & 0 \\ 0 & 0 & 0 & 0 & +6.5692 & 0 \\ 0 & 0 & 0 & 0 & 0 & +5.9576 \end{pmatrix} \times 10^{-1}, \quad (4.30)$$

the RVE-to-remote strain conversion tensor is computed from (4.19), yielding

$$\mathbb{M} = \begin{pmatrix} +9.3326 & -0.2574 & -0.1607 & 0 & 0 & 0 \\ -0.2574 & +9.3326 & -0.1607 & 0 & 0 & 0 \\ -0.4982 & -0.4982 & +8.8409 & 0 & 0 & 0 \\ 0 & 0 & 0 & +9.5064 & 0 & 0 \\ 0 & 0 & 0 & 0 & +9.5064 & 0 \\ 0 & 0 & 0 & 0 & 0 & +9.5900 \end{pmatrix} \times 10^{-1}, \quad (4.31)$$

and the strain concentration tensors of the inclusion and the matrix phases are computed from (4.20) and (4.21), respectively, yielding

$$\mathbb{A}_1 = \begin{pmatrix} +1.4560 & +0.1005 & +0.1132 & 0 & 0 & 0 \\ +0.1005 & +1.4560 & +0.1132 & 0 & 0 & 0 \\ +0.0664 & +0.0664 & +1.3856 & 0 & 0 & 0 \\ 0 & 0 & 0 & +1.3438 & 0 & 0 \\ 0 & 0 & 0 & 0 & +1.3438 & 0 \\ 0 & 0 & 0 & 0 & 0 & +1.3556 \end{pmatrix}, \quad (4.32)$$

$$\mathbb{A}_2 = \begin{pmatrix} +5.5605 & -0.1528 & -0.6123 & 0 & 0 & 0 \\ -0.1528 & +5.5605 & -0.6123 & 0 & 0 & 0 \\ -0.3576 & -0.3576 & +7.2257 & 0 & 0 & 0 \\ 0 & 0 & 0 & +6.2449 & 0 & 0 \\ 0 & 0 & 0 & 0 & +6.2449 & 0 \\ 0 & 0 & 0 & 0 & 0 & +5.7134 \end{pmatrix} \times 10^{-1}, \quad (4.33)$$

$$\mathbb{A}_m = \begin{pmatrix} +9.2097 & -0.3804 & -0.3187 & 0 & 0 & 0 \\ -0.3804 & +9.2097 & -0.3187 & 0 & 0 & 0 \\ -0.1874 & -0.1874 & +9.0868 & 0 & 0 & 0 \\ 0 & 0 & 0 & +9.5064 & 0 & 0 \\ 0 & 0 & 0 & 0 & +9.5064 & 0 \\ 0 & 0 & 0 & 0 & 0 & +9.5900 \end{pmatrix} \times 10^{-1}. \quad (4.34)$$

Because the chosen example is a “problematic case” where the classical Mori-Tanaka approach does not provide appropriate results,  $\mathbb{M}$  and  $\mathbb{A}_m$  are different, compare (4.31) with (4.34). Finally, the symmetric homogenized stiffness tensor is computed from (4.10), yielding

$$\mathbb{C}_{hom} = \begin{pmatrix} +1.0570 & +0.3972 & +0.3985 & 0 & 0 & 0 \\ +0.3972 & +1.0570 & +0.3985 & 0 & 0 & 0 \\ +0.3985 & +0.3985 & +1.0947 & 0 & 0 & 0 \\ 0 & 0 & 0 & +0.6679 & 0 & 0 \\ 0 & 0 & 0 & 0 & +0.6679 & 0 \\ 0 & 0 & 0 & 0 & 0 & +0.6598 \end{pmatrix} \times 10^2 \text{ GPa}. \quad (4.35)$$

Source code available in Appendix A.

## 4.4 Conclusions

Great efforts have been undertaken to clearly delineate the potentials and limitations of the multiphase Mori-Tanaka scheme when it comes to the violation of the symmetry requirements of the homogenized elasticity tensor (Benveniste et al., 1989, 1991; Ferrari, 1991) and this

violation was traditionally assigned to some type of physical deficiency of the Mori-Tanaka scheme. However, after presenting a very concise and comprehensive account of all the cases where the Mori-Tanaka scheme delivers non-symmetric homogenized stiffness tensors, Sevostianov and Kachanov (2014) take a radically different approach, by making the statement that

“the symmetry can be - in fact *must* be eliminated by imposing symmetrization: if one is interested in the linear elastic properties then the existence of the elastic potential must be enforced.”

In the present paper, we have explored the theoretical consequences of such an imposed symmetrization, by not only “correcting” homogenized stiffness estimates, but by also providing mathematical expressions for the basic physical properties from which such stiffness estimates arise: the concentration tensors linking macroscopic strains to microscopic phase strains encountered within an RVE representing a multiphase composite material. It is indeed possible to derive concentration tensors which are fully consistent with the explicit symmetrization procedure proposed by Sevostianov and Kachanov (2014), see (4.20) and (4.21).

Our novel Eshelby problem-based composite material model overcomes all the limitations of the Mori-Tanaka scheme regarding multiphase-multiform composites, while naturally reducing to the very latter scheme whenever this scheme provides physically reasonable, i.e. symmetric, homogenized stiffness estimates. This opens new avenues for exploring the mechanical effects of microstrains and microstresses, as well as the upscaling features of eigenstresses and eigenstrains, in hierarchical material systems with complex matrix-inclusion morphologies, such as wood (Bader et al., 2010), shale (Gruescu et al., 2007), fired clay (Kiefer et al., 2020), bituminous mixes (Somé et al., 2022), fiber-reinforced composites including soft biological tissues (Guilleminot et al., 2008; Morin et al., 2018, 2021), or nanoclay composites (Cauvin et al., 2007). Deeper scrutiny into the multiscale mechanics of eigenstrains would involve the extension of the present developments to the concept of transformation field analysis (Dvorak, 1992), where influence tensors linking microscopic eigenstrains and total eigenstrains are intimately related to the concentration tensors dealt with herein (Pichler and Hellmich, 2010; Franciosi, 2022). However, corresponding developments are beyond the scope of the present paper.

It is noteworthy that our novel concentration tensor estimates do not require any microstructural information which goes beyond that needed for the classical Mori-Tanaka scheme; and we regard this as particularly practically useful when compared with the probably best-known approach to overcome the symmetry-related limitations of the Mori-Tanaka scheme, namely the Ponte-Castañeda-Willis estimate (Ponte-Castañeda and Willis, 1995; Franciosi, 2022), which necessitates additional information on the spatial distribution of inclusion phases - the latter is not always accessible in real life applications. This may underline the practical relevance of the present contribution.



# Chapter 5

---

## Mix-, storage- and temperature-invariant precipitation characteristics in white cement paste, expressed through an NMR-based analytical model

**Authored by:** Nabor Jiménez Segura, Bernhard L.A. Pichler, Christian Hellmich

**Publication outlook:** At the time of finalizing the thesis, this has been submitted to *Cement and Concrete Research*, currently under review.

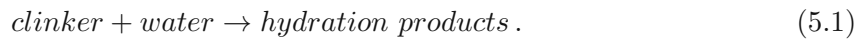
**Abstract:** Proton NMR tests on hydrating white cement paste provide access to the mix-, storage-, and temperature-dependent evolutions of the hydrogen portions found in capillary and gel pores, solid C-S-H, and calcium hydroxide, respectively. The aforementioned dependencies vanish once the hydrogen molar fractions are plotted as functions of the precipitation degree, which we have introduced here as the ratio of the amount of hydrogen bound in solids, over the total amount of hydrogen. The precipitation rate is governed by one activation energy and a linear affinity function of the current precipitation degree normalized by its maximum value. The latter decreases linearly with increasing curing temperature, being consistent with the temperature-dependent water content of solid C-S-H. The corresponding water-to-silica ratio, together with the precipitation degree and the mix and storage characteristics, provide access to the volume fractions of the hydrogen-containing phases, clinker and voids, as well as to the degree of hydration.

**Contribution:** Nabor Jiménez Segura: Investigation, Methodology, Formal analysis, Computation, Visualization, Writing – original draft, review & editing. Bernhard L.A. Pichler: Supervision, Conceptualization, Funding acquisition, Methodology, Formal analysis, Writing – original draft, Writing – review & editing. Christian Hellmich: Supervision, Conceptualization, Funding acquisition, Methodology, Formal analysis, Supervision, Writing – review & editing.

**Keywords:** Cement paste; NMR; Hydration; Kinetics; Micromechanics modeling.

## 5.1 Introduction

Cement hydration (Neville, 1995) comprises a number of chemical reactions between water and different clinker components (with the most prominent ones being tricalcium silicate or alite, with chemical formula  $(\text{CaO})_3(\text{SiO}_2)$  or, in short,  $\text{C}_3\text{S}$ , and dicalcium silicate or belite, with chemical formula  $(\text{CaO})_2(\text{SiO}_2)$  or, in short,  $\text{C}_2\text{S}$ ), leading to the formation of hydration products (with the most prominent ones being calcium-silicate-hydrate, with chemical formula  $(\text{CaO})_x(\text{SiO}_2)(\text{H}_2\text{O})_y$  or, in short, solid C-S-H, and calcium hydroxide or portlandite, with chemical formula  $\text{Ca}(\text{OH})_2$  or, in short, CH). More explicitly, when not differentiating between the individual reactants and the individual products, a single chemical equation appears as appropriate, reading as



The kinetics of this reaction is traditionally monitored by means of the degree of hydration,  $\xi$ , a standard definition of which is the following (Mouret et al., 1997; Acker, 2001; Bernard et al., 2003; Feng et al., 2004; Hellmich and Mang, 2005; Königsberger et al., 2016)

$$\xi(t) = 1 - \frac{m_{clin}(t)}{m_{clin}(t=0)} , \quad (5.2)$$

with  $m_{clin}$  standing for the mass of clinker and  $t$  denoting the age of the material.

However, Eq. (5.1) conceals that the chemical reactions between clinker and water, resulting in the formation of hydration products falls into (at least) two processes (Bullard et al., 2011; Scrivener and Nonat, 2011; Ioannidou et al., 2016; Powers, 1935; Hua et al., 1997): (i) the (exothermic) dissolution of clinker, providing an ionic solution; and (ii) the precipitation of the hydration products (mainly calcium-silicate-hydrate and calcium hydroxide) out of the aforementioned ionic solution. When focusing on the latter precipitation process, a radically simple chemical reaction equation may be adopted, namely



with H standing for the hydrogen atoms, highly mobile ( $HM$ ) in the ionic solution, and bound (and hence with low mobility -  $LM$ ) in solid C-S-H or CH. A particularly interesting feature of the precipitation equation (5.3) is that its kinetics can be followed from proton nuclear magnetic resonance relaxometry (proton NMR). This technique delivers  $T_2$  relaxation times which quantify the decay of a magnetic signal associated with the movement of hydrogen atoms. In more detail, hydrogen atoms in cement paste fall into four mobility classes associated with four typical relaxation times: (i) stronger chemical bonding in crystals such as calcium hydroxide, (ii) weaker chemical bonding in calcium-silicate-hydrate building blocks (solid C-S-H), (iii) stronger confinement in gel pores, and (iv) weaker confinement in capillary pores. As regards terminology, the composite made of solid C-S-H building blocks and gel pores is referred to as the ‘‘C-S-H gel’’ (Brough et al., 1994; Jennings et al., 2008; Jennings, 2008). In the existing literature, water bound in solid C-S-H is also referred to as ‘‘interlayer water’’ (McDonald et al., 2010), gel pores as ‘‘intra-C-S-H pores’’ (McDonald et al., 2010), and capillary pores as ‘‘inter-C-S-H pores’’ (McDonald et al., 2010) as well as ‘‘interhydrate pores’’ (Muller et al., 2013a), respectively. The essential result of one proton NMR test are four signal intensities. Their sum is referred to as the ‘‘total signal intensity’’.

The evolution of the total signal intensity depends on the storage conditions. It is constant under sealed conditions (Muller, 2014; Muller et al., 2013a), because no hydrogen enters

or leaves the tested specimen, see Fig. 5.1 for pastes with different  $w/c$  ratios. As regards cement pastes curing under water, however, the total signal intensity increases with increasing material age (Gajewicz, 2014; Gajewicz-Jaromin et al., 2019), because of uptake of water, see Fig. 5.2 for pastes cured at different temperatures. This water fills the space which emerges as the hydration products fill a smaller volume than the reactants (clinker and water) they are made of. The latter phenomenon is usually referred to as chemical shrinkage (Le Châtelier, 1900; Tazawa et al., 1995). Under sealed conditions, in turn, chemical shrinkage results in a progressively increasing hydrostatic tension of the porewater. This tension causes water to cavitate (Lura et al., 2009), which leads to the creation of voids filled by water vapor. Their volume fraction increases with increasing material maturation (Powers, 1935; Hua et al., 1997).

The experimental data illustrated in Figs. 5.1 and 5.2 are the basis for the present analysis, dealing with the quantification of the precipitation process in terms of differently mobile hydrogen fractions. As a naturally emerging quantity describing exactly this precipitation in the context of proton NMR data, we resort to the amount of solidly bound hydrogen (i.e. that with relaxation times of  $T_2 \approx 100 \mu\text{s}$  and smaller (Valori et al., 2013)), and relate it to the overall hydrogen (irrespective of its mobility). Accordingly, we here coin the term of “precipitation degree”  $\eta$  as

$$\eta = \frac{H^{LM}}{H^{HM} + H^{LM}} = \frac{a_{H,CH} + a_{H,sCSH}}{a_H}, \quad (5.4)$$

with  $a_{H,CH}$  and  $a_{H,sCSH}$  standing for the amounts of hydrogen bound into calcium hydroxide ( $CH$ ) and into solid C-S-H ( $sCSH$ ), respectively, and with  $a_H$  as the total amount of hydrogen found in the tested sample at the time of testing, including both solidly bound hydrogen and hydrogen in liquid form, the latter filling either the gel ( $gpor$ ) or the capillary pores ( $cpor$ ):  $a_H = a_{H,CH} + a_{H,sCSH} + a_{H,gpor} + a_{H,cpor}$ . As a function of this newly introduced precipitation degree, we will study paste composition, reaction kinetics, as well as the evolution of the mass density of solid C-S-H, and we will finally link all the insight gained here to the key quantity of traditional cement chemistry: the degree of hydration according to Eq. (5.2). Accordingly, the remainder of the present paper is organized as follows: Section 5.2 covers the evolution of the amounts of differently bound hydrogen portions; and then elucidates characteristics which are independent of initial composition, curing temperature, and storage conditions. The temperature-independent aspects of the precipitation kinetics are quantified in Section 5.3, in terms of an affinity function depending on a normalized precipitation degree only, while temperature intervenes through an Arrhenius-type activation term. Section 5.4 translates the molar fractions of hydrogen into masses, linking the precipitation degree to the classical hydration degree. Section 5.5 translates these masses into phase-evolution diagrams, providing volume fractions of gel and capillary porosities, calcium hydroxide, and solid C-S-H, together with the ones of clinker and vapor-filled voids as functions of the precipitation degree. Then, Section 5.6 (Conclusions) puts the novel results in context with the current state-of-the-art.

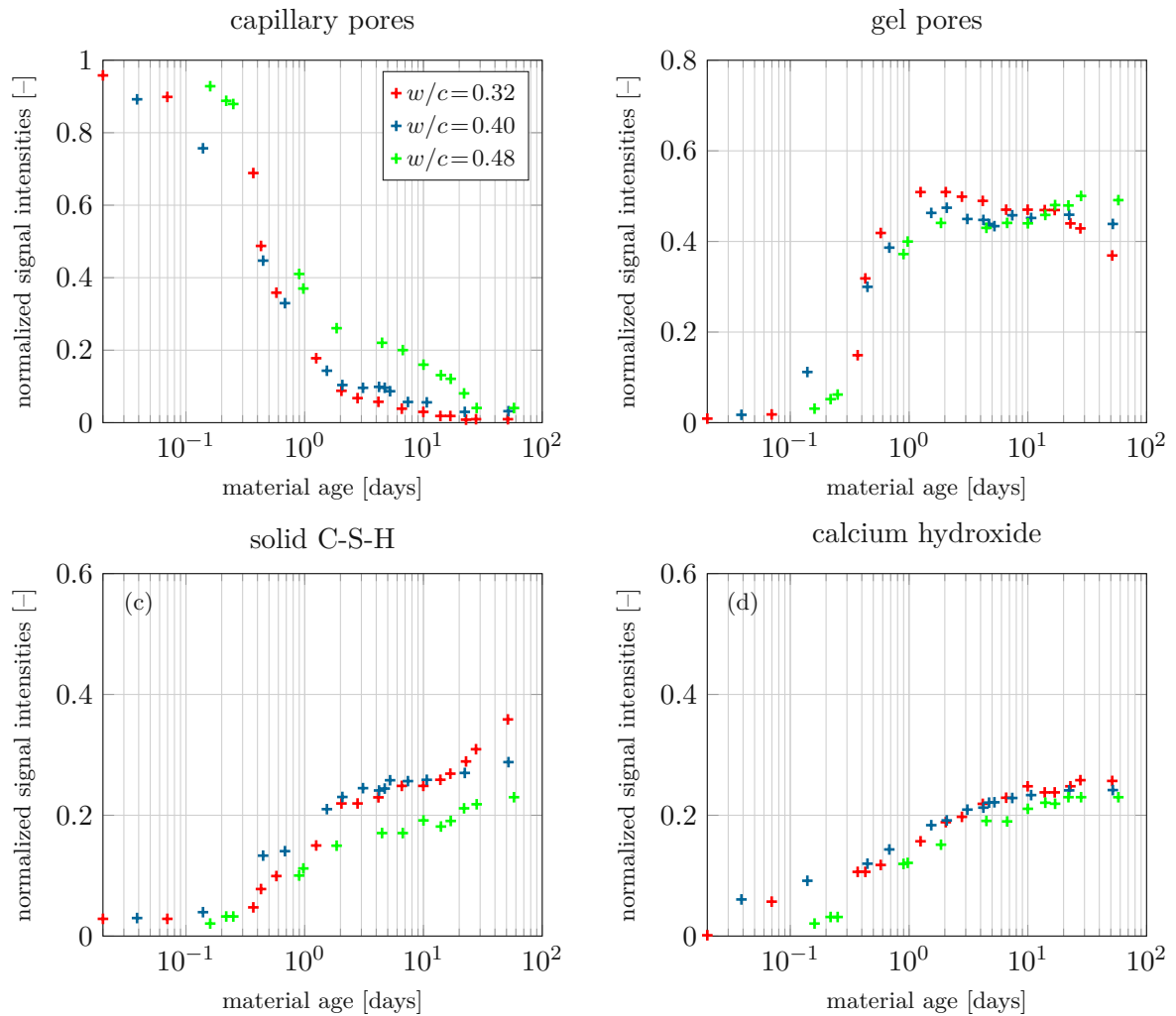


**Fig. 5.1.** Proton NMR signal fractions as function of material age, obtained from white cement paste samples of 8 mm diameter and 10 mm height, with  $w/c=0.32$  (red),  $w/c=0.40$  (blue), and  $w/c=0.48$  (green) cured under sealed conditions at  $T=20^{\circ}\text{C}$  (Muller, 2014; Muller et al., 2013a): normalized signal intensities of hydrogen (a) in capillary pores ( $cpor$ ), (b) in gel pores ( $gpor$ ), (c) in solid C-S-H ( $sC\text{SH}$ ), and (d) in calcium hydroxide ( $CH$ ).

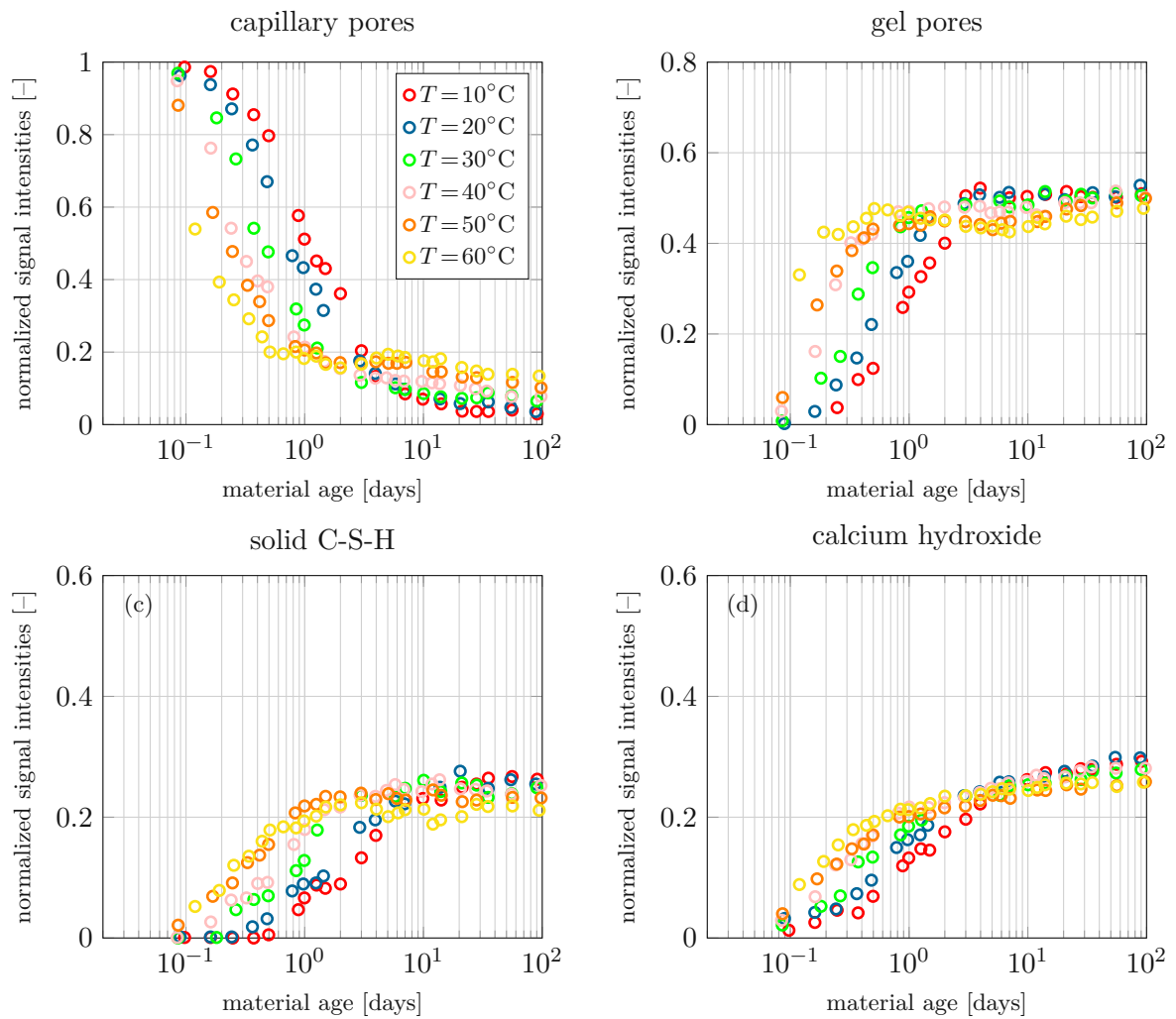


**Fig. 5.2.** Proton NMR signal fraction as function of material age, obtained from white cement paste samples of 8 mm diameter and 10 mm height, with  $w/c=0.40$  cured under water at different temperatures (Gajewicz, 2014; Gajewicz-Jaromin et al., 2019):  $T=10^\circ\text{C}$  (red),  $T=20^\circ\text{C}$  (blue),  $T=30^\circ\text{C}$  (green),  $T=40^\circ\text{C}$  (pink),  $T=50^\circ\text{C}$  (orange), and  $T=60^\circ\text{C}$  (yellow): normalized signal intensities of hydrogen in (a) capillary pores (*cpor*), (b) gel pores (*gpor*), (c) solid C-S-H (*sCSH*), and (d) calcium hydroxide (*CH*).

## 5.2 Temperature-, storage-, and mix-invariant relations between molar fractions of differently mobile hydrogen portions and the precipitation degree $\eta$

### 5.2.1 Normalized NMR signals, molar fractions of differently mobile hydrogen portions, and the precipitation degree

Muller et al. (Muller, 2014; Muller et al., 2013a) and Gajewicz et al. (Gajewicz, 2014; Gajewicz-Jaromin et al., 2019) published normalized NMR signals intensities:

$$I_j(t) := \frac{S_{H,j}(t)}{S_H(t=0)}, \quad j \in [CH, sCSH, gpor, cpor], \quad (5.5)$$

see Figs. 5.1 and 5.2.  $S_{H,j}$  stands for the signal intensity associated with hydrogen in calcium hydroxide, solid C-S-H, gel pores, and capillary pores,  $S_H$  for the total signal intensity,  $t$  for the time, and  $t=0$  for the time instant of the first NMR measurement.  $S_{H,j}$  is proportional to the amount of hydrogen in material domain  $j$ , while  $S_H$  is proportional to the total amount of hydrogen in the tested sample of cement paste. Therefore, Eq. (5.5) can be re-written in terms of amounts of hydrogen:

$$I_j(t) = \frac{a_{H,j}(t)}{a_H(t=0)}, \quad j \in [CH, sCSH, gpor, cpor]. \quad (5.6)$$

Eq. (5.6) allows for expressing  $\eta$  according to Eq. (5.4) as:

$$\eta(t) = \frac{I_{CH}(t) + I_{sCSH}(t)}{I_{CH}(t) + I_{sCSH}(t) + I_{gpor}(t) + I_{cpor}(t)}. \quad (5.7)$$

Notably, the precipitation degree according to Eq. (5.4) relates the amount of solidly bound hydrogen, at any time  $t$ , to the total amount of hydrogen which is in the system *at that time*, rather than to the initial amount of hydrogen. This provides the motivation to introduce the molar fractions of the differently bound hydrogen portions

$$\mathcal{F}_{H,j}(t) := \frac{a_{H,j}(t)}{a_H(t)}, \quad j \in [CH, sCSH, gpor, cpor], \quad (5.8)$$

where, differing from the situation encountered in Eqs. (5.5) and (5.6),  $a_H(t)$  rather than  $a_H(t=0)$  appears in the denominator. Therefore, the sum of all four different hydrogen molar fractions is, at any time  $t$ , equal to 1:

$$1 = \mathcal{F}_{H,CH}(t) + \mathcal{F}_{H,sCSH}(t) + \mathcal{F}_{H,gpor}(t) + \mathcal{F}_{H,cpor}(t). \quad (5.9)$$

The corresponding expression for the precipitation degree  $\eta$  as a function of the molar fractions of the differently mobile hydrogen portions is obtained from inserting Eq. (5.8) into Eq. (5.4), yielding

$$\eta(t) = \mathcal{F}_{H,CH}(t) + \mathcal{F}_{H,sCSH}(t). \quad (5.10)$$

Insertion of Eq. (5.10) into Eq. (5.9) allows one to express the molar fraction of hydrogen in liquid form, as function of the precipitation degree:

$$1 - \eta(t) = \mathcal{F}_{H,gpor}(t) + \mathcal{F}_{H,cpor}(t). \quad (5.11)$$

### 5.2.2 Identification of mix-invariant relations between hydrogen molar fractions and precipitation degree; obtained from NMR data of samples cured under sealed conditions

Sealed samples are closed systems. The total amount of hydrogen is constant over time, and equal to the initial amount:  $a_H(t) = a_H(t=0)$ , and the same holds for the total NMR signal intensity:  $S_H(t) = S_H(t=0)$ . Therefore, the molar fractions of the differently mobile hydrogen portions according to Eq. (5.8) are equal to the normalized NMR signals according to Eqs. (5.5) and (5.6), see Fig. 5.1 for experimental data:

$$\mathcal{F}_{H,j}(t) = I_j(t), \quad j \in [CH, sCSH, gpor, cpor]. \quad (5.12)$$

A parametric plot showing the molar fraction of hydrogen in solid C-S-H over the precipitation degree, produced from the normalized NMR signal intensities from Fig. 5.1, in combination with Eqs. (5.7) and (5.12), underlines that  $\mathcal{F}_{H,sCSH}$  increases overlinearly with increasing  $\eta$ , independently of the initial water-to-cement mass ratio, see Fig. 5.3. This overlinear trend can be quantified by means of a power law:

$$\mathcal{F}_{H,sCSH} = \pi_1 \eta^{\pi_2}, \quad (5.13)$$

with the numerical values of the constants  $\pi_1$  and  $\pi_2$  being listed in Table 5.1. The mathemati-

**Table 5.1**

Factorial, exponential, and proportionality constants quantifying mix-, storage-, and temperature-independent precipitation characteristics, identified from the NMR data of Fig. 5.1.

context	value of the constant	references
precipitation of solid C-S-H	$\pi_1 = 0.6419$	Eq. (5.13), Fig. 5.3
precipitation of solid C-S-H	$\pi_2 = 1.3000$	Eq. (5.13), Fig. 5.3
development of gel and capillary pores	$\pi_3 = 1.9095$	Eq. (5.19), Fig. 5.4

cal relation between the molar fraction of hydrogen in calcium hydroxide and the precipitation degree is obtained from inserting Eq. (5.13) into Eq. (5.10), and from solving the resulting expression for  $\mathcal{F}_{H,CH}$ :

$$\mathcal{F}_{H,CH} = \eta - \pi_1 \eta^{\pi_2}. \quad (5.14)$$

In order to differentiate, within the total water-filled pore space, between gel and capillary pores, volume fractions of gel and capillary pores with respect to the total pore volume are introduced as:

$$\varphi_{gpor}(t) = \frac{\mathcal{F}_{H,gpor}(t)}{\mathcal{F}_{H,cpor}(t) + \mathcal{F}_{H,gpor}(t)}, \quad (5.15)$$

$$\varphi_{cpor}(t) = \frac{\mathcal{F}_{H,cpor}(t)}{\mathcal{F}_{H,cpor}(t) + \mathcal{F}_{H,gpor}(t)}, \quad (5.16)$$

such that  $\varphi_{gpor}(t) + \varphi_{cpor}(t) = 1$ . Illustrating  $\varphi_{gpor}(t)$  and  $\varphi_{cpor}(t)$  according to Eqs. (5.15) and (5.16) over  $\eta(t)$ , based on NMR signals from Fig. 5.1 as well as Eqs. (5.7) and (5.12), evidences a virtually linear dependence of both  $\varphi_{cpor}$  and  $\varphi_{gpor}$ , on the precipitation degree, with decreasing and increasing trends, respectively, and independent of the initial water-to-cement



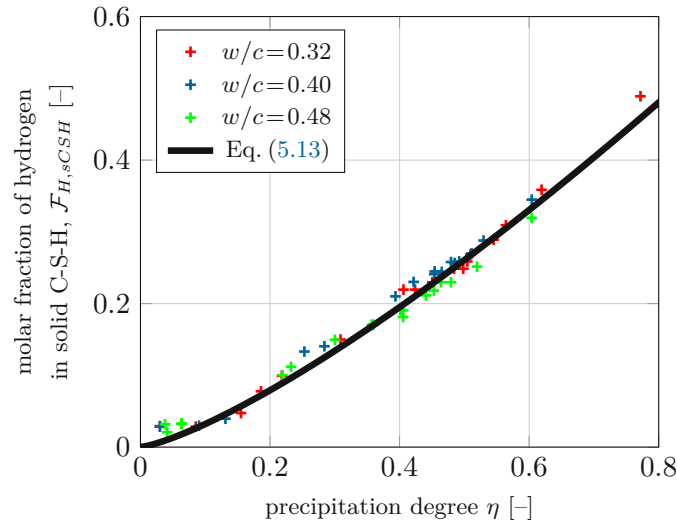


**Fig. 5.3.** Molar fraction of hydrogen in solid C-S-H,  $\mathcal{F}_{H,sCSH}$ , as function of the precipitation degree  $\eta$ : the points are derived from NMR data of Fig. 5.1, the solid line refers to the power-law of Eq. (5.13), with constants listed in Table 5.1.

mass ratio, see Fig. 5.4. The point-wisely resolved relationship is reproduced by means of the following bilinear functions:

$$\varphi_{gpor} = \begin{cases} \pi_3 \eta \dots \eta \leq 1/\pi_3, \\ 1 \dots \eta > 1/\pi_3, \end{cases} \quad (5.17)$$

$$\varphi_{cpor} = \begin{cases} 1 - \pi_3 \eta \dots \eta \leq 1/\pi_3, \\ 0 \dots \eta > 1/\pi_3, \end{cases} \quad (5.18)$$

with the numerical value of the constant  $\pi_3$  being listed in Table 5.1. The mathematical

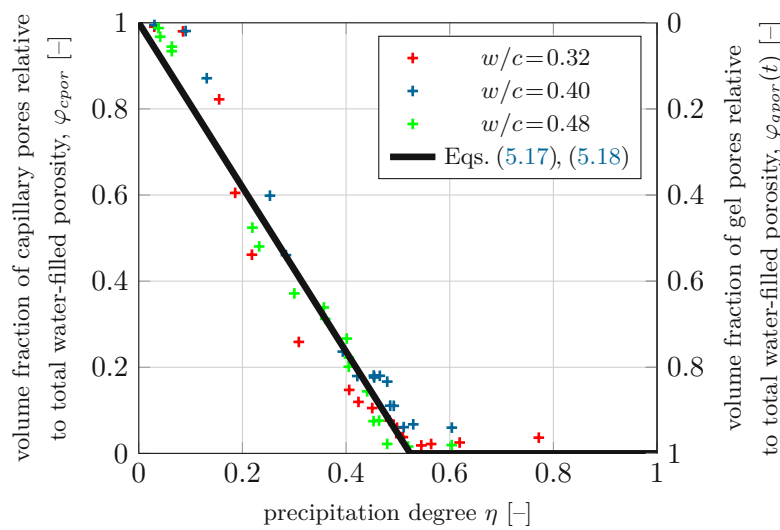


**Fig. 5.4.** Trends of gel and capillary pore fractions, with the precipitation degree: the points are derived from NMR data of Fig. 5.1, the solid line refers to the bilinear function of Eqs. (5.17) and (5.18), see also Table 5.1.

relation between  $\mathcal{F}_{H,gpor}$ , the molar fraction of hydrogen in gel pores, and  $\eta$  is obtained from solving Eq. (5.15) for  $\mathcal{F}_{H,gpor}$  and from inserting Eqs. (5.11) and (5.17) into the resulting expression, yielding

$$\mathcal{F}_{H,gpor} = \begin{cases} (1 - \eta) (\pi_3 \eta) \dots \eta \leq 1/\pi_3, \\ 1 - \eta \dots \dots \dots \eta > 1/\pi_3. \end{cases} \quad (5.19)$$

Similarly, the mathematical relation between  $\mathcal{F}_{H,cpor}$ , the molar fraction of hydrogen in capillary pores, and  $\eta$  follows as

$$\mathcal{F}_{H,cpor} = \begin{cases} (1 - \eta) (1 - \pi_3 \eta) \dots \eta > 1/\pi_3, \\ 0 \dots \dots \dots \eta > 1/\pi_3. \end{cases} \quad (5.20)$$

Eqs. (5.13), (5.14), (5.19), and (5.20) quantify the four different molar fractions of hydrogen, as functions of the precipitation degree, independently of the initial water-to-cement mass ratio, see Fig. 5.5. In order to check whether Eqs. (5.13), (5.14), (5.19), and (5.20) are also

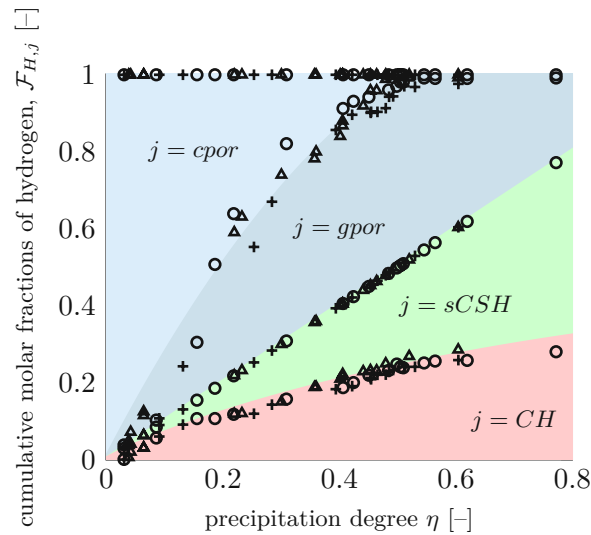


**Fig. 5.5.** Cumulative molar fractions of hydrogen found in capillary pores (*cpor*), gel pores (*gpor*), solid C-S-H (*sCSH*), and calcium hydroxide (*CH*), as functions of the precipitation degree: the data points refer to NMR data from sealed-cured cement pastes with different initial water-to-cement mass ratios (Muller, 2014; Muller et al., 2013a):  $w/c = 0.32$  (circles),  $w/c = 0.40$  (crosses), and  $w/c = 0.48$  (triangles); the shaded domains refer to hydrogen in calcium hydroxide (*CH*, pink), solid C-S-H (*sCSH*, green), gel pores (*gpor*, purple), and capillary pores (*cpor*, blue); the boundaries between the shaded domains refer to Eqs. (5.13), (5.14), (5.19), and (5.20), together with the constants of Table 5.1.

independent of curing temperature and storage conditions, the NMR data of Gajewicz et al. (Gajewicz, 2014; Gajewicz-Jaromin et al., 2019) will be analyzed next.

### 5.2.3 Testing temperature- and storage-invariance of the relations between hydrogen molar fractions and the precipitation degree: evaluation of NMR data from samples cured under water at six different temperatures

Samples cured under water are open systems. Driven by chemical shrinkage, water is sucked into the open porosity of the samples. This results in a progressive increase of the total

amount of hydrogen in the sample, as indicated by the total NMR intensity. Under these conditions, the molar fractions of hydrogen according to Eq. (5.8) are equal to normalized signal intensities according to Eqs. (5.5) and (5.6), divided by the sum of all four normalized signal intensities:

$$\mathcal{F}_{H,j}(t) = \frac{I_j(t)}{I_{CH}(t) + I_{sCSH}(t) + I_{gpor}(t) + I_{cpor}(t)}, \quad j \in [CH, sCSH, gpor, cpor]. \quad (5.21)$$

Inserting the NMR data from Fig. 5.2 into Eqs. (5.21) and (5.7) allows for illustrating the evolution of molar fractions of hydrogen as a function of the precipitation degree, see the points in Fig. 5.6. The obtained chains of data points referring to NMR data of under water

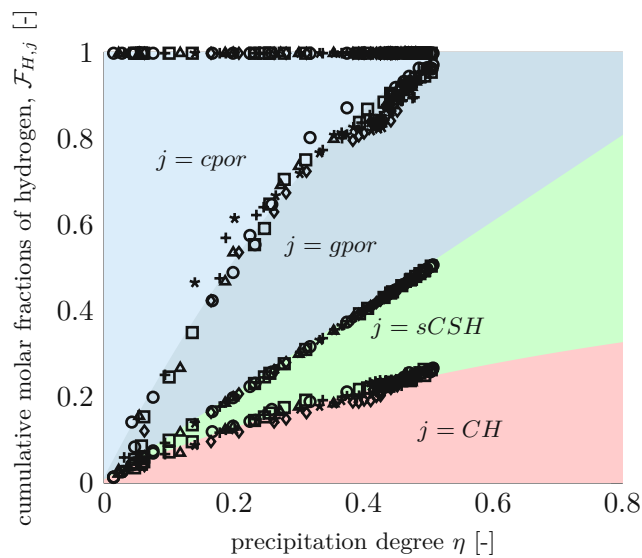


**Fig. 5.6.** Exemplary model validation: cumulative molar fractions of hydrogen as function of the precipitation degree: the data points refer to NMR data from under water cured cement pastes stored at different temperatures (Gajewicz-Jaromin et al., 2019; Gajewicz, 2014):  $T = 10^\circ\text{C}$  (circles),  $T = 20^\circ\text{C}$  (squares),  $T = 30^\circ\text{C}$  (triangles),  $T = 40^\circ\text{C}$  (crosses),  $T = 50^\circ\text{C}$  (diamonds), and  $T = 60^\circ\text{C}$  (stars); the shaded domains refer to hydrogen in calcium hydroxide ( $CH$ , pink), solid C-S-H ( $sCSH$ , green), gel pores ( $gpor$ , purple), and capillary pores ( $cpor$ , blue); the boundaries between the shaded domains are model-predictions according to Eqs. (5.13), (5.14), (5.19), and (5.20), together with the constants of Table 5.1.

cured samples agree well with the model predictions derived from samples cured under sealed conditions, according to Eqs. (5.13), (5.14), (5.19), and (5.20), together with the constants of Table 5.1; these predictions being indicated through the boundaries between the differently shaded domains in Fig. 5.6.

Notably, the boundaries between the differently shaded phase domains in Figs. 5.5 and 5.6 are the same. The data points, in turn, come from two different laboratories and refer to two different NMR testing devices, two different cements, three different values of the initial water-to-cement mass ratio, six different values of the curing temperature, and two different types of storage conditions. Thus, Figs. 5.5 and 5.6 corroborate the remarkable “universality” of the Eqs. (5.13), (5.14), (5.19), and (5.20), see also Table 5.1. These relations are independent of initial composition, curing temperature, and storage conditions.

### 5.2.4 Water and hydrogen uptake characteristics of cement pastes cured under water

Cement pastes cured under water suck in water in order to fill the space provided by chemical shrinkage (Le Châtelier contraction). It is instructive to plot the corresponding hydrogen uptake normalized by the initial hydrogen amount,  $\Delta I_H$ , which reads, under consideration of Eq. (5.6), as

$$\Delta I_H(t) = \frac{a_H(t) - a_H(t=0)}{a_H(t=0)} = \frac{I_{tot}(t) - I_{tot}(t=0)}{I_{tot}(t=0)}, \quad (5.22)$$

with  $I_{tot}(t) = I_{CH}(t) + I_{sCSH}(t) + I_{gpor}(t) + I_{cpor}(t)$ , as function of the precipitation degree, see Fig. 5.7. One observes that also the hydrogen-uptake of cement pastes cured under water turns out as a temperature-independent linear precipitation characteristic, which can be mathematically quantified as

$$\forall t : \quad \Delta I_H(t) = \pi_4 \eta(t), \quad \rightarrow \quad \Delta I_H = \pi_4 \eta = \frac{a_H(\eta) - a_H(\eta=0)}{a_H(\eta=0)}, \quad (5.23)$$

with the numerical value of the constant  $\pi_4$  being listed in Table 5.2.

**Table 5.2**

Temperature-independent binary variable  $\pi_4$  distinguishing between two types of curing conditions: (i) sealed storage (= closed system), and (ii) underwater storage (= open system), leading to the increase of the total amount of hydrogen resulting from uptake of water driven by chemical shrinkage.

curing conditions	value of the binary variable
sealed storage	$\pi_4 = 0.0000$
underwater storage	$\pi_4 = 0.1880$

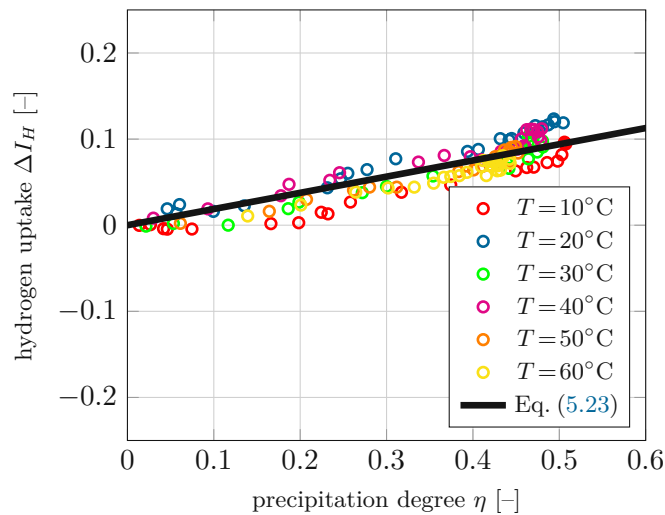


**Fig. 5.7.** Relative increase of the total NMR intensity (reflecting water uptake by cement pastes cured under water) as function of the precipitation degree; the points are derived from the NMR data of Fig. 5.2, the solid line refers to the linear function of Eq. (5.23), see also Table 5.2.

## 5.3 Precipitation kinetics

### 5.3.1 Precipitation evolutions governed by curing temperature, derived from NMR data

Translating, by means of Eq. (5.7), the NMR data of Fig. 5.2 into values of the precipitation degree, and illustrating them as a function of the age of the material, provides quantitative insight into remarkable features, as can be seen from Fig. 5.8: (i) at early age, the precipitation

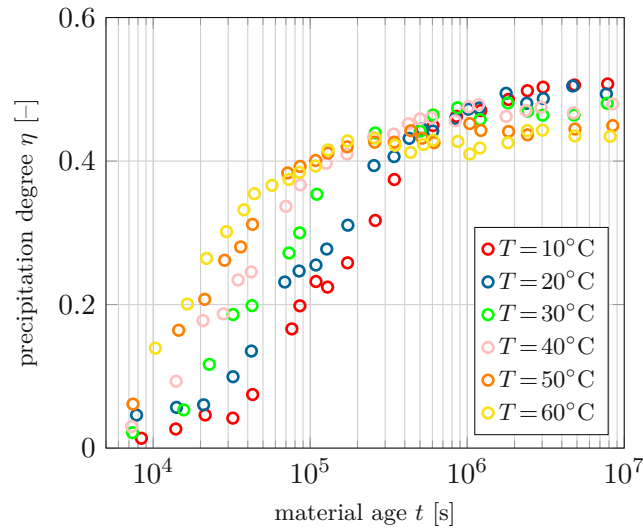


**Fig. 5.8.** Temporal evolution of the precipitation degree of cement pastes with  $w/c = 0.40$  cured under water and isothermally at:  $T = 10^\circ\text{C}$  (red),  $T = 20^\circ\text{C}$  (blue),  $T = 30^\circ\text{C}$  (green),  $T = 40^\circ\text{C}$  (pink),  $T = 50^\circ\text{C}$  (orange), and  $T = 60^\circ\text{C}$  (yellow); the points were obtained from insertion of the data of Fig. 5.2 into Eq. (5.7).

process is the faster, the higher the curing temperature, (ii) at mature material ages, the reaction kinetics decays by orders of magnitude, such that the precipitation degree reaches a virtually constant value, and (iii) the “eventually” attained “maximum” precipitation degree,  $\eta_{max}$ , decreases with increasing curing temperature, in a virtually linear fashion, see Fig. 5.9.<sup>1</sup> The corresponding best linear regression function reads as

$$\eta_{max}(T) = \pi_5 T + \pi_6, \quad (5.24)$$

with the numerical values of the constants  $\pi_5$  and  $\pi_6$  being listed in Table 5.3. The “eventually” attained “maximum” precipitation degrees of Fig. 5.9 suggests the introduction of a normalized precipitation degree,  $\tilde{\eta}$ , which increases from zero to one:

$$\tilde{\eta} = \frac{\eta}{\eta_{max}(T)}, \quad 0 \leq \tilde{\eta} \leq 1. \quad (5.25)$$

It is important to note that the termination of the precipitation degree evolution at an ever lower value for increasing temperatures does not reflect kind of a premature termination of a chemical reaction, but rather a smaller amount of water in the same amount of solid C-S-H, as was evidenced by scanning electron microscopy, X-ray diffraction, and Si<sup>29</sup> NMR

<sup>1</sup>The words “eventually” and “maximum” were put under quotation marks, because, strictly speaking, hydration does never stop completely.

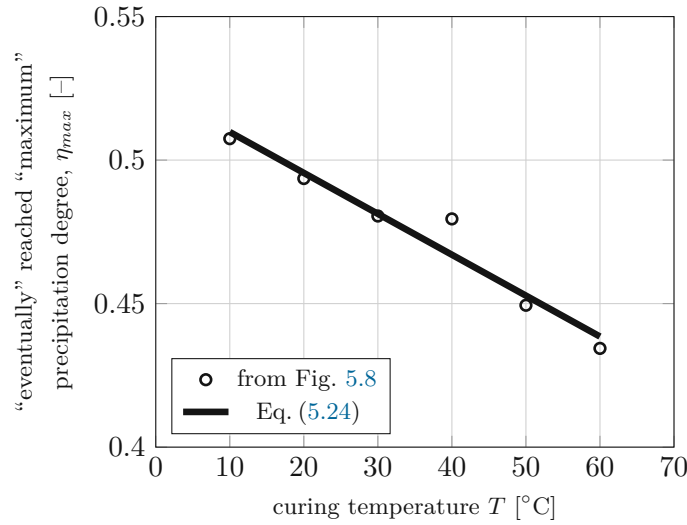


**Fig. 5.9.** “Eventually” reached “maximum” precipitation degree of cement pastes with  $w/c=0.40$  cured under water at different temperatures; the points refer to the rightmost data points in Fig. 5.8, the line refers to the best linear regression function, see Eq. (5.24) and Table 5.3.

**Table 5.3**

Constants quantifying the influence of temperature on the precipitation kinetics.

context / quantity	value of the constant	reference
slope in Fig. 5.9	$\pi_5 = -1.425 \times 10^{-3} \text{ } ^\circ\text{C}^{-1}$	Eq. (5.24)
intercept in Fig. 5.9	$\pi_6 = 0.5240$	Eq. (5.24)
reference water-to-silica ratio	$[(\text{H}_2\text{O})/(\text{SiO}_2)](T=20^\circ\text{C}) = 1.8$	(Allen et al., 2007; Muller et al., 2013a)
activation energy	$E_a = 33.260 \text{ kJ/mol}$	(Hellmich et al., 1999b; D’Aloia and
universal gas constant	$R = 8.3145 \text{ J/(mol } ^\circ\text{C)}$	
chemical affinity function	$A_0 = 6.124 \text{ s}^{-1}$	Eq. (5.28)

spectroscopy applied to cement paste samples cured at different temperatures (Gallucci et al., 2013). Considering, accordingly, a water-to-silica ratio of 1.8 at  $T = 20^\circ\text{C}$  (Allen et al., 2007; Muller et al., 2013a), the maximum precipitation degree of Eq. (5.24) proposes the former to decrease with increasing temperature in the form

$$[(\text{H}_2\text{O})/(\text{SiO}_2)](T) = [(\text{H}_2\text{O})/(\text{SiO}_2)](T=20^\circ\text{C}) \frac{\eta_{max}(T)}{\eta_{max}(T=20^\circ\text{C})} = 3.6327(\pi_5 T + \pi_6), \quad (5.26)$$

whereby we have made use of Eq. (5.24) and Table 5.3. The corresponding trend, illustrated in Fig. 5.10, agrees well with an independent testing campaign on oil-well cement, comprising X-ray diffraction with Rietveld analysis and thermogravimetry (Bahafid et al., 2017); see Fig. 5.10. An even more “perfect” match between the solid line and the series of five data points in Fig. 5.10 is not necessarily expected, since the line and the points refer to different cements (white Portland cement versus oil-well cement), different hydration periods (100 versus 28 days), and different initial composition ( $w/c = 0.40$  versus  $w/c = 0.44$ ). Still, the accordance of trends seen in Fig. 5.10 strongly motivates the development of a kinetics model on the normalized precipitation degree according to Eq. (5.25), as described next.

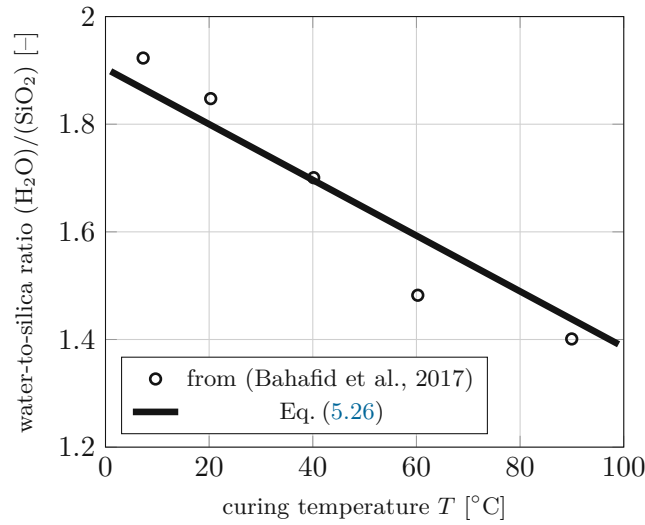


**Fig. 5.10.** Water-to-silica ratio of solid C-S-H: line computed from Eq. (5.26); data points from independent thermogravimetry (Bahafid et al., 2017).

### 5.3.2 Identification of Arrhenius-type precipitation kinetics law

In line with pertinent hydration modeling on the basis of the degree of hydration (Hellmich et al., 1999b; Ulm and Coussy, 1996; Hellmich et al., 1999a; Termkhajornkit and Barbarulo, 2012), the evolution of  $\tilde{\eta}$  is represented by an Arrhenius law (Arrhenius, 1889)

$$\frac{d\tilde{\eta}}{dt} = A(\tilde{\eta}) \exp\left(-\frac{E_a}{R[T(t) + 273.15^\circ\text{C}]}\right), \quad (5.27)$$

where  $A(\tilde{\eta})$  denotes the chemical affinity function,  $E_a = 33.260$  kJ/mol stands for the activation energy (Hellmich et al., 1999b; D'Aloia and Chanvillard, 2002), and  $R = 8.3145$  J/(mol °C) the universal constant for ideal gases.  $T(t)$  is the temporal evolution of the curing temperature in degrees centigrade. Analyzing *isothermal* NMR experiments,  $T(t)$  becomes a constant.

As regards properties of  $A(\tilde{\eta})$ , Fig. 5.8 suggests that the chemical affinity function is positive for small values of  $\tilde{\eta}$ , and that it monotonously decreases with increasing  $\tilde{\eta}$ , approaching zero as  $\tilde{\eta}$  approaches 1. From classical physical chemistry (Atkins et al., 2014), a linear function is used:

$$A(\tilde{\eta}) = A_0 (1 - \tilde{\eta}), \quad 0 \leq \tilde{\eta} \leq 1, \quad (5.28)$$

where  $A_0$  is a constant which needs to be identified from experimental data. In order to derive a closed-form-solution for the time-evolution of  $\tilde{\eta}$ , Eq. (5.28) is inserted into Eq. (5.27). This delivers (under consideration of isothermal curing:  $T = \text{const.}$ ) a linear, inhomogeneous, ordinary, first-order differential equation with constant coefficients. Its solution reads as

$$\tilde{\eta} = 1 - \exp\left(-\frac{t}{t_0}\right), \quad (5.29)$$

where  $t_0$  denotes a temperature-dependent characteristic time depending on  $A_0$  and  $T$ , reading as

$$t_0 = \frac{1}{A_0} \exp\left(\frac{E_a}{R[T + 273.15^\circ\text{C}]}\right). \quad (5.30)$$

A closed-form expression for the precipitation degree  $\eta$  as a function of the age of the material and of the curing temperature is obtained from insertion of Eq. (5.30) into Eq. (5.29), from



insertion of the resulting expression for  $\tilde{\eta}$  together with Eq. (5.24) into Eq. (5.25), and from solving the obtained equation for  $\eta$ :

$$\eta_{mod} = \left[ 1 - \exp \left( - t A_0 \exp \left( - \frac{E_a}{R [T + 273.15^\circ\text{C}]} \right) \right) \right] \times (\pi_5 T + \pi_6), \quad (5.31)$$

where the subscript *mod* stands for “modeling”.

For the identification of a value for  $A_0$ , and the subsequent checking of the significance of this value, we perform the following steps: First, we consider the NMR data associated with the experiments performed under the highest curing temperature: 60°C. The following root-mean-square error function is minimized:

$$\epsilon(T) = \sqrt{\frac{1}{n_T} \sum_{i=1}^{n_T} [\eta_{mod}(T, t_i; A_0) - \eta_{exp}(T, t_i)]^2}, \quad (5.32)$$

where  $n_T$  denotes the number of available experimental data points referring to curing temperature  $T$ , and where  $\eta_{exp}(T, t_i)$  denotes *experimental* values resulting from insertion of NMR data of Fig. 5.2 into Eq. (5.7). The smallest attainable value of  $\epsilon(60^\circ\text{C})$  amounts to 0.0182, and it is obtained for

$$A_0 = 6.124 \text{ s}^{-1}, \quad (5.33)$$

see also the yellow graph and data points in Fig. 5.11.

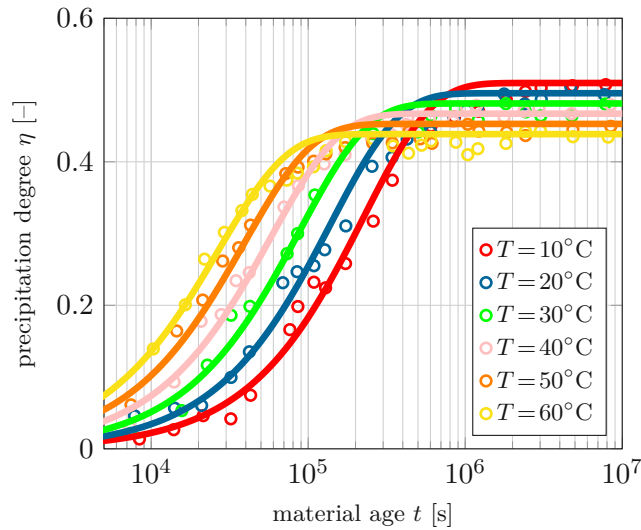


**Fig. 5.11.** Temporal evolution of the precipitation degree of cement pastes with  $w/c = 0.40$  cured under water and isothermally at:  $T = 10^\circ\text{C}$  (red),  $T = 20^\circ\text{C}$  (blue),  $T = 30^\circ\text{C}$  (green),  $T = 40^\circ\text{C}$  (pink),  $T = 50^\circ\text{C}$  (orange), and  $T = 60^\circ\text{C}$  (yellow); the points were obtained from insertion of the data of Fig. 5.2 into Eq. (5.7), the solid lines were obtained from Eq. (5.31) and constants listed in Table 5.3.

Next, we evaluate Eq. (5.31) for the affinity value given in Eq. (5.33), together with the kinetics constants of Table 5.3, for the remaining curing temperatures of 10, 20, 30, 40, and 50°C, see Fig. 5.11. The corresponding model curves agree remarkably well with the experimental data depicted in Figs. 5.8 and 5.11. Corresponding prediction errors according to Eq. (5.32) are satisfactorily small: even for the two smallest curing temperatures (10°C and 20°C, respectively) they are smaller than  $1.5 \times \epsilon(60^\circ\text{C})$ , see Table 5.4. This underlines

**Table 5.4**

Root-mean-square errors according to Eq. (5.32), referring to the differences between experimental data points and Arrhenius-type kinetics model predictions of Fig. 5.11.

$T$	10°C	20°C	30°C	40°C	50°C	60°C
$\epsilon(T)$	0.0223	0.0260	0.0185	0.0171	0.0182	0.0182

that *one* value of  $A_0$ , see Eq. (5.33), is sufficient for an appropriate description of the reaction kinetics, for curing temperatures ranging from 10°C to 60°C.

The NMR data, together with the validated kinetics model, provide a quantitative description of the following precipitation characteristics: the higher the curing temperature, the faster the reaction kinetics, but the smaller the finally attained precipitation degree (Verbeck, 1968), see Fig. 5.12. While the paste composition is solely governed by the

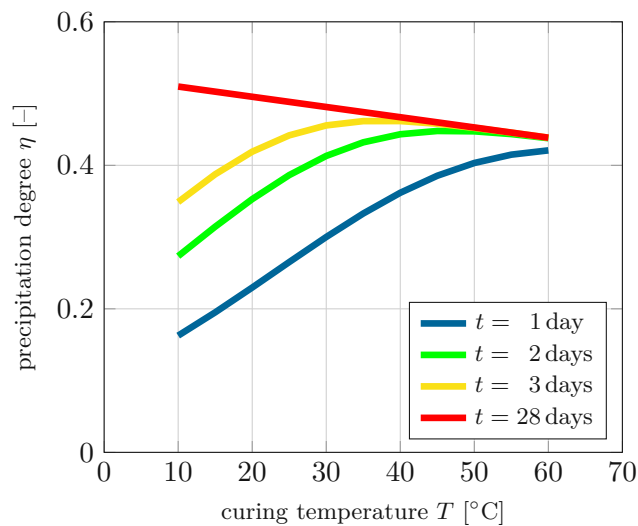


**Fig. 5.12.** Precipitation degree reached after  $t = 1$  day (blue),  $t = 2$  days (green),  $t = 3$  days (yellow), and  $t = 28$  days (red), as a function of curing temperature, according to the predictions of Eq. (5.31) and Table 5.3.

precipitation degree, see Figs. 5.5 and 5.6, and while the precipitation kinetics can be described by one temperature-invariant chemical affinity function, see Eqs. (5.28) and (5.33) as well as Fig. 5.11, the “eventually” attained “maximum” precipitation degree does depend on the curing temperature. More precisely, it decreases with increasing curing temperature, see Figs. 5.11 and 5.12.

## 5.4 Precipitation-driven constituent masses in the cement paste system, and corresponding degree of hydration

Having identified the precipitation degree as mix-, storage-, and temperature-invariant driver of all the hydrogen portions within a hydrating cement paste system, together with its temperature-dependent evolution characteristics, it is now time to relate the aforementioned hydrogen portions to all the constituents or phases which make up the investigated material system, as well as to the classical hydration degree. Starting with the hydrogen-containing phases, and denoting by  $n_{H,j}$  the number of hydrogen atoms in one molecule of phase  $j$ , the

mass of hydrogen-containing phase  $j$  amounts to

$$m_j(t) = \frac{\mathcal{F}_{H,j}(t)}{n_{H,j}} M_j a_H(t), \quad j \in [CH, sCSH, gpor, cpor], \quad (5.34)$$

with  $M_j$  as the molar mass of phase  $j$ , i.e. the mass of one mole of phase  $j$ . The number of hydrogen atoms per molecule is constant in the case of calcium hydroxide and of the water filling the gel and capillary pores (see Table 5.5), while it depends on the curing temperature in the case of solid C-S-H, with the water-to-silica ratio  $[(H_2O)/(SiO_2)](T)$  following Eq. (5.26). This leads to

$$n_{H,sCSH}(T) = n_{H,H_2O} \times 3.6327(\pi_5 T + \pi_6). \quad (5.35)$$

Accordingly, the molar mass of solid C-S-H is temperature-dependent as well, in the following way,

$$M_{sCSH}(T) = M_{CS} + M_{H_2O} \times 3.6327(\pi_5 T + \pi_6), \quad (5.36)$$

see also Table 5.5.

**Table 5.5**

Physical properties of water, calcium-silicate in C-S-H, and calcium hydroxide (Allen et al., 2007; Muller et al., 2013a; Gallucci et al., 2013).

	water	calcium-silicate in C-S-H	calcium hydroxide
chemical formula	H <sub>2</sub> O	(CaO) <sub>1.7</sub> SiO <sub>2</sub>	Ca(OH) <sub>2</sub>
hydrogen atoms per molecule [-]	$n_{H,H_2O} = 2$	-	$n_{H,CH} = 2$
molar mass [g/mol]	$M_{H_2O} = 18.01$	$M_{CS} = 155.4$	$M_{CH} = 74.09$

Turning to the only constituent which is free of hydrogen, namely clinker, we consider the beginning of the dissolution-precipitation reaction, with  $\eta=0$ , where the initial water-to-cement mass ratio,  $(w/c)$ , gives access to the mass of clinker, through

$$m_{clin}(\eta=0) = \frac{m_{H_2O}(\eta=0)}{(w/c)} = \frac{\mathcal{F}_{H,H_2O}(\eta=0)}{(w/c)} \frac{M_{H_2O}}{n_{H,H_2O}} a_H(\eta=0) = \frac{1}{(w/c)} \frac{M_{H_2O}}{n_{H,H_2O}} a_H(\eta=0), \quad (5.37)$$

whereby we have made use of Eq. (5.34) with  $j = H_2O$ , and of  $\mathcal{F}_{H,H_2O}(\eta=0) = 1$ . At  $\eta=0$ , the system consists only of water and clinker, so that the mass of overall cement paste follows as

$$m_{cp}(\eta=0) = \left(1 + \frac{1}{(w/c)}\right) m_{H_2O}(\eta=0) = \left(1 + \frac{1}{(w/c)}\right) \frac{M_{H_2O}}{n_{H,H_2O}} a_H(\eta=0). \quad (5.38)$$

Under sealed conditions,  $m_{cp}$  remains constant over time, so that Eq. (5.38) stays relevant also for any value  $\eta$  beyond zero. However, when submerged under water, the cement paste system absorbs additional water molecules, as quantified in Section 5.2.4 in terms of the normalized hydrogen increase  $\Delta I_H(\eta)$ , see Eq. (5.23). Accordingly, the mass of cement paste is composed of its initial value (at zero precipitation degree) and the mass resulting from the water uptake,

$$m_{cp}(\eta) = m_{cp}(\eta=0) + \Delta I_H(\eta) \frac{M_{H_2O}}{n_{H,H_2O}} a_H(\eta=0). \quad (5.39)$$

The initial amount of hydrogen can be expressed in terms of the mass of clinker and the initial water-to-cement mass ratio, by means of solving Eq. (5.37) for  $a_H(\eta=0)$ :

$$a_H(\eta=0) = m_{clin}(\eta=0) \times (w/c) \frac{n_{H,H_2O}}{M_{H_2O}}. \quad (5.40)$$

Insertion of Eq. (5.38) into Eq. (5.39), while considering Eq. (5.40), yields

$$m_{cp}(\eta) = \left[1 + (w/c)(1 + \Delta I_H(\eta))\right] m_{clin}(\eta=0), \quad (5.41)$$

with  $\Delta I_H(\eta)$  according to Eq. (5.23), see also Table 5.2 for values of  $\pi_4$  as a function of storage conditions. The mass of cement paste is also equal to the sum of the masses of all its constituents,

$$m_{cp}(\eta) = m_{clin}(\eta) + m_{gpor}(\eta) + m_{cpor}(\eta) + m_{sCSH}(\eta) + m_{CH}(\eta), \quad (5.42)$$

whereby the masses of hydrogen-containing phases can be readily retrieved from their specific masses according to Eq. (5.34), via

$$m_j(\eta) = \frac{\mathcal{F}_{H,j}(\eta)}{n_{H,j}} M_j \times a_H(\eta=0) \times (1 + \Delta I_H(\eta)), \quad j \in [CH, sCSH, gpor, cpor]. \quad (5.43)$$

Insertion of Eq. (5.40) into Eq. (5.43), and of the corresponding result and of Eq. (5.41), into Eq. (5.42) yields an equation for the mass of clinker, the solution of which yields

$$m_{clin}(\eta) = m_{clin}(\eta=0) \left\{ 1 - \left[ (\eta - \pi_1 \eta^{\pi_2}) \frac{M_{CH}}{n_{H,CH}} \frac{n_{H,H_2O}}{M_{H_2O}} + (\pi_1 \eta^{\pi_2}) \left( \frac{1}{3.6327(\pi_5 T + \pi_6)} \frac{M_{CS}}{M_{H_2O}} + 1 \right) - \eta \right] (w/c)(1 + \pi_4 \eta) \right\}, \quad (5.44)$$

whereby we have made use of Eqs. (5.35), (5.36), and (5.26), Table 5.5, and Eq. (5.23), see also Table 5.2 for values of  $\pi_4$  as a function of storage conditions. Insertion of Eq. (5.44) into Eq. (5.2) delivers the hydration degree as a function of the precipitation degree, in the format

$$\xi(\eta) = (w/c)(1 + \pi_4 \eta) \left[ (\eta - \pi_1 \eta^{\pi_2}) \left( \frac{M_{CH}}{M_{H_2O}} \frac{n_{H,H_2O}}{n_{H,CH}} - 1 \right) + \frac{\pi_1 \eta^{\pi_2}}{3.6327(\pi_5 T + \pi_6)} \frac{M_{CS}}{M_{H_2O}} \right], \quad (5.45)$$

with  $\pi_4 = 0$  for the sealed case and with  $\pi_4 = 0.1880$  for under water curing, according to Table 5.2. For any specific value of the precipitation degree, the associated value of the hydration degree is the larger, the larger the initial water-to-cement mass ratio and the larger the curing temperature, see Fig. 5.13 and note that  $\pi_5$  in Eq. (5.45) is negative, see Table 5.3. Also, the associated value of the hydration degree is larger in under water cured samples than in sealed-cured samples, and this difference increases with decreasing initial water-to-cement mass ratio.

## 5.5 Precipitation-driven constituent volumes of the cement paste system, and corresponding mass density of solid C-S-H

### 5.5.1 Volumes of invariably dense material constituents and of overall cement paste

Determination of volumes from masses require the knowledge of mass densities. The latter are constant for all phases except solid C-S-H, the mass density of which has been reported to

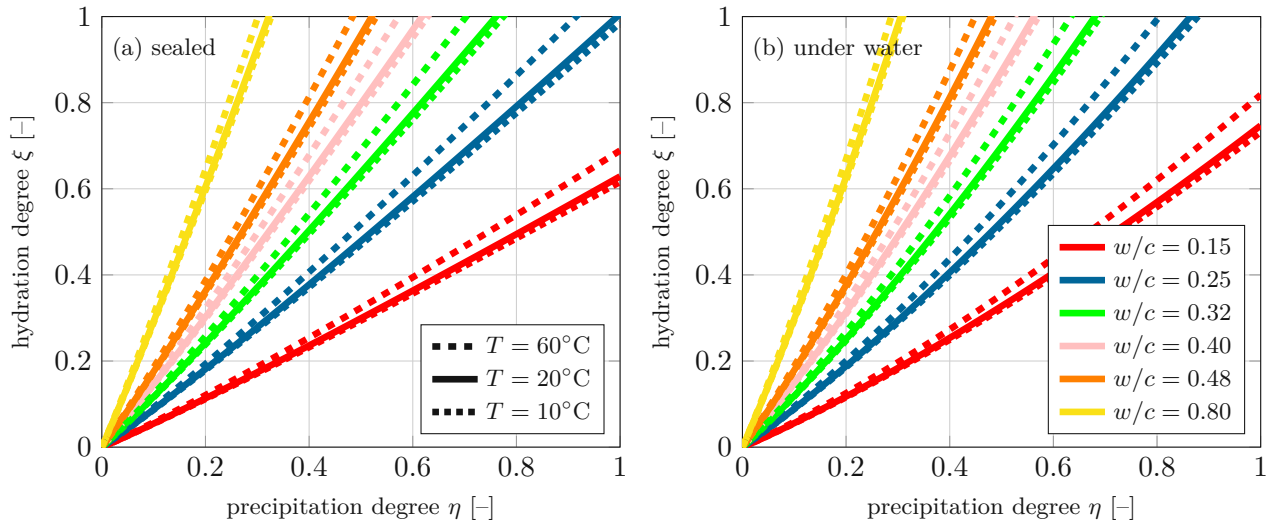


**Fig. 5.13.** Hydration degrees as functions of the precipitation degree, according to Eq. (5.45), for cement pastes with initial water-to-cement mass ratios  $w/c = 0.15$  (red),  $w/c = 0.24$  (blue),  $w/c = 0.32$  (green),  $w/c = 0.40$  (pink),  $w/c = 0.48$  (orange), and  $w/c = 0.80$  (yellow);  $T = 10^\circ\text{C}$  (dotted lines),  $T = 20^\circ\text{C}$  (solid lines), and  $T = 60^\circ\text{C}$  (dashed lines); cured (a) under sealed conditions, and (b) under water.

depend on temperature and maturity (Bahafid et al., 2017; Gajewicz-Jaromin et al., 2019). Thus, the volumes occupied by every phase except solid C-S-H are obtained from dividing their masses  $m_j(t)$ , from Eqs. (5.43) and (5.44), by their mass densities  $\rho_j$ :

$$V_j(\eta) = \frac{m_j(\eta)}{\rho_j}, \quad j \in [clin, CH, gpor, cpor], \quad (5.46)$$

where  $\rho_{gpor} = \rho_{cpor} = \rho_{H_2O}$ , see Table 5.6 for numerical values.

**Table 5.6**

Mass densities of water, calcium hydroxide, and clinker (Muller et al., 2013a).

	water	calcium hydroxide	clinker
mass density [g/cm <sup>3</sup> ]	$\rho_{H_2O} = 1.00$	$\rho_{CH} = 2.24$	$\rho_{clin} = 3.15$

In cement pastes stored both under water and sealed, the total volume of cement paste  $V_{cp}$  may be treated as being virtually constant throughout hardening, because bulk volume changes at the macroscopic scale of cement paste are by two orders of magnitude smaller than chemical shrinkage (Lura et al., 2003; Abuhaikal et al., 2018). Thus,  $V_{cp}$  is set equal to the initial volume of cement paste, i.e. to the sum of the initial volumes of water and clinker. Under consideration of Eqs. (5.46) and  $(w/c) = m_{H_2O}(\eta=0)/m_{clin}(\eta=0)$ , this yields

$$V_{cp} = V_{cp}(\eta=0) = V_{H_2O}(\eta=0) + V_{clin}(\eta=0) = m_{clin}(\eta=0) \left[ \frac{(w/c)}{\rho_{H_2O}} + \frac{1}{\rho_{clin}} \right]. \quad (5.47)$$

The constituent volumes according to Eq. (5.46), together with Eqs. (5.44) and (5.43), and the volume of cement paste according to Eq. (5.47) give access to the volume fractions of the

phases with invariable mass density,  $f_j = V_j/V_{cp}$ , in the form

$$f_{clin} = \left\{ 1 + (w/c)(1 + \pi_4 \eta) - \left[ (\eta - \pi_1 \eta^{\pi_2}) \frac{M_{CH}}{n_{H,CH}} \frac{n_{H,H_2O}}{M_{H_2O}} + (1 - \eta) + \right. \right. \quad (5.48)$$

$$\left. \left. (\pi_1 \eta^{\pi_2}) \left( \frac{1}{3.6327(\pi_5 T + \pi_6)} \frac{M_{CS}}{M_{H_2O}} + 1 \right) \right] (w/c)(1 + \pi_4 \eta) \right\} \left[ \frac{(w/c)\rho_{clin}}{\rho_{H_2O}} + 1 \right]^{-1},$$

$$f_{CH} = \frac{n_{H,H_2O}}{M_{H_2O}} \frac{M_{CH}}{n_{H,CH}} (\eta - \pi_1 \eta^{\pi_2}) (1 + \pi_4 \eta) \left[ \frac{\rho_{CH}}{\rho_{H_2O}} + \frac{\rho_{CH}}{(w/c)\rho_{clin}} \right]^{-1}, \quad (5.49)$$

$$f_{gpor} = \begin{cases} (1 - \eta)(\pi_3 \eta)(1 + \pi_4 \eta) \left[ 1 + \frac{\rho_{H_2O}}{(w/c)\rho_{clin}} \right]^{-1} \dots \eta \leq 1/\pi_3, \\ (1 - \eta)(1 + \pi_4 \eta) \left[ 1 + \frac{\rho_{H_2O}}{(w/c)\rho_{clin}} \right]^{-1} \dots \eta > 1/\pi_3, \end{cases} \quad (5.50)$$

$$f_{cpor} = \begin{cases} (1 - \eta)(1 - \pi_3 \eta)(1 + \pi_4 \eta) \left[ 1 + \frac{\rho_{H_2O}}{(w/c)\rho_{clin}} \right]^{-1} \dots \eta \leq 1/\pi_3, \\ 0 \dots \eta > 1/\pi_3. \end{cases} \quad (5.51)$$

The remaining volume fraction, complementing the sum of Eqs. (5.48) to (5.51) to one, is associated to solid C-S-H and vapor-filled voids in the case of sealed curing, and by solid C-S-H only in the case of under water curing.

### 5.5.2 Determination of mass density of solid C-S-H, from under water cured samples

For under water cured samples, the total volume of cement paste is made up of the volumes of clinker, of calcium hydroxide, of gel pores and capillary pores, and of solid C-S-H. Hence, the latter volume can be computed from

$$V_{sCSH}(\eta, T) = V_{cp} - \left[ V_{clin}(\eta, T) + V_{CH}(\eta) + V_{gpor}(\eta) + V_{cpor}(\eta) \right]. \quad (5.52)$$

This volume allows for determination of both the volume fraction of solid C-S-H in under water cured samples, as

$$f_{sCSH} = \frac{V_{sCSH}}{V_{cp}} = 1 - \left[ f_{clin} + f_{CH} + f_{gpor} + f_{cpor} \right], \quad (5.53)$$

see Fig. 5.15, and of the mass density of solid C-S-H,  $\rho_{sCSH} = \frac{m_{sCSH}}{V_{sCSH}}$ , as

$$\rho_{sCSH} = \left( \frac{M_{sCSH}(T)}{n_{H,sCSH}(T)} \pi_1 \eta^{\pi_2} \right) \left\{ \frac{M_{H_2O}}{n_{H,H_2O}} \left[ \frac{1}{\rho_{H_2O}} \left( \frac{1}{1 + 0.188 \eta} + \eta - 1 \right) - \frac{\eta}{\rho_{clin}} \right] \right.$$

$$\left. + \left( \frac{1}{\rho_{clin}} - \frac{1}{\rho_{CH}} \right) \frac{M_{CH}}{n_{H,CH}} (\eta - \pi_1 \eta^{\pi_2}) + \frac{1}{\rho_{clin}} \frac{M_{sCSH}(T)}{n_{H,sCSH}(T)} \pi_1 \eta^{\pi_2} \right\}^{-1}, \quad (5.54)$$

where  $\pi_4$  was set equal to 0.188, and whereby we have made use of Eqs. (5.52), (5.47), (5.46), (5.44), (5.43), (5.13), (5.14), (5.19), and (5.20), see Fig. 5.14. We note that the mass density of solid C-S-H decreases with increasing precipitation degree and with decreasing temperature, while being independent of the initial water-to-cement mass ratio; and the corresponding range of values agrees very well with the range of values reported in the open literature (Muller et al., 2013a; Gajewicz-Jaromin et al., 2019; Gallucci et al., 2013; Allen et al., 2007; Bahafid et al., 2017; Taylor, 1986; Constantinides and Ulm, 2004).

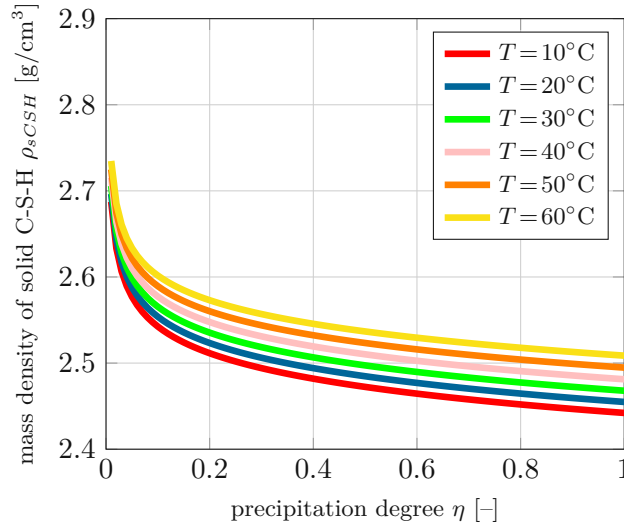


**Fig. 5.14.** Density of solid C-S-H in cement pastes cured under water and isothermally at:  $T = 10^\circ\text{C}$  (red),  $T = 20^\circ\text{C}$  (blue),  $T = 30^\circ\text{C}$  (green),  $T = 40^\circ\text{C}$  (pink),  $T = 50^\circ\text{C}$  (orange), and  $T = 60^\circ\text{C}$  (yellow); from Eq. (5.54).

### 5.5.3 Volume fractions in cement paste precipitating under sealed conditions

When considering that the precipitation- and temperature-dependence of the mass density of solid C-S-H according to Fig. 5.14 and Eq. (5.54) holds also for sealed curing conditions, the volume occupied by solid C-S-H is obtained as

$$V_{sCSH}(\eta, T) = \frac{m_{sCSH}(\eta, T)}{\rho_{sCSH}(\eta, T)}, \quad (5.55)$$

with the mass of solid C-S-H following Eq. (5.43), with  $\pi_4 = 0$ , expressing sealed conditions, see Table 5.2; and with the mass density of solid C-S-H following Eq. (5.54), expressing that the mass density of solid C-S-H does not depend on storage conditions. This yields

$$\begin{aligned} V_{sCSH}(\eta, T) = & m_{clin}(\eta=0)(w/c) \left[ \frac{1}{\rho_{H_2O}} \left( \frac{1}{1 + 0.188\eta} + \eta - 1 \right) - \frac{\eta}{\rho_{clin}} \right. \\ & + \left( \frac{1}{\rho_{clin}} - \frac{1}{\rho_{CH}} \right) \frac{M_{CH}}{n_{H,CH}} \frac{n_{H,H_2O}}{M_{H_2O}} (\eta - \pi_1 \eta^{\pi_2}) \\ & \left. + \frac{1}{\rho_{clin}} \left( \frac{1}{3.6327(\pi_5 T + \pi_6)} \frac{M_{CS}}{M_{H_2O}} + 1 \right) \pi_1 \eta^{\pi_2} \right]. \end{aligned} \quad (5.56)$$

We are left with the determination of the volume filled by voids resulting from chemical shrinkage under sealed conditions, based on representing the overall cement paste volume as the sum of the volumes of all phases, and solving this volume balance equation for  $V_{void}$ . Mathematically, this reads as

$$V_{void}(\eta) = V_{cp} - \left[ V_{clin}(\eta, T) + V_{CH}(\eta) + V_{sCSH}(\eta, T) + V_{gpor}(\eta) + V_{cpor}(\eta) \right], \quad (5.57)$$

whereby the volume expressions on the right-hand side of Eq. (5.57) follow from Eqs. (5.47), (5.46), (5.56), (5.44), (5.43), (5.13), (5.14), (5.19), and (5.20), and the temperature dependence



vanishes. Thus, the volume fractions of calcium hydroxide, gel and capillary pores, and clinker in sealed samples follow from Eqs. (5.48)–(5.51), for  $\pi_4 = 0$ , see Table 5.2. The volume fraction of solid C-S-H, in turn, follows from diving Eq. (5.56) by Eq. (5.47) as

$$f_{sCSH}^{seal} = \left[ \frac{1}{\rho_{H_2O}} \left( \frac{1}{1 + 0.188\eta} + \eta - 1 \right) - \frac{\eta}{\rho_{clin}} + \left( \frac{1}{\rho_{clin}} - \frac{1}{\rho_{CH}} \right) \frac{M_{CH}}{n_{H,CH}} \frac{n_{H,H_2O}}{M_{H_2O}} (\eta - \pi_1 \eta^{\pi_2}) + \frac{1}{\rho_{clin}} \left( \frac{1}{3.6327(\pi_5 T + \pi_6)} \frac{M_{CS}}{M_{H_2O}} + 1 \right) \pi_1 \eta^{\pi_2} \right] \left[ \frac{1}{\rho_{H_2O}} + \frac{1}{(w/c)\rho_{clin}} \right]^{-1}, \quad (5.58)$$

where  $\rho_{sCSH}(\eta, T)$  was taken from Eq. (5.54). Lastly, the volume fraction of voids reads as

$$f_{void} = 1 - [f_{clin} + f_{CH} + f_{gpor} + f_{cpor} + f_{sCSH}^{seal}], \quad (5.59)$$

see Fig. 5.15.

## 5.6 Conclusions

We have presented a new cement hydration model which explicitly accounts for the increasing evidence that hydration is a combined dissolution-precipitation process (Bullard et al., 2011; Scrivener and Nonat, 2011; Ioannidou et al., 2016; Powers, 1935; Hua et al., 1997). Accordingly, the formation of calcium hydroxide and C-S-H is quantified through a precipitation degree quantified, from proton NMR data (Muller et al., 2013a; Gajewicz-Jaromin et al., 2019), as the amount of bound hydrogen over the total amount of hydrogen found in a hydrating cement paste sample. As the only functional argument, fully independent of mix proportions, storage characteristics (sealed versus under water curing), and curing temperature, the precipitation degree governs the hydrogen molar fractions associated with the gel and capillary porosities, as well as with calcium hydroxide and solid C-S-H. Moreover, the precipitation degree provides temperature-independent linear water uptake characteristics, as driven by chemical shrinkage of cement pastes.

Apart from these mix-, storage-, and temperature-invariances, the precipitation degree also provides an interesting complement to pertinent hydration degree-based kinetics modeling (De Schutter and Taerwe, 1995; Ulm and Coussy, 1995; Hellmich et al., 1999a); namely through consideration of the temperature-driven stoichiometry of solid C-S-H, a characteristic which has become more and more evident in recent years (Gallucci et al., 2013; Bahafid et al., 2017): Hydration products arising in pastes cured isothermally under different temperature exhibit a water-to-silica ratio which decreases with increasing temperature; and such a loss of water bound to calcium-silicate is even recorded when changing the temperature of cement pastes at a constant maturation state, resulting in water redistributions towards the gel and capillary porosities (Wyrzykowski et al., 2017), as well as to the vapor-filled voids in the context of hygrothermal effects (Wang et al., 2018). Accordingly, we have normalized the precipitation degree by its temperature-dependent maximum, and this normalized quantity turns out to be governed by thermally activated Arrhenius-type reaction. The latter is characterized by a simple, linear affinity function, as normally expected in standard physical chemistry application. We note that pertinent kinetics modeling approaches based on the degree of hydration required the introduction of a more complex, non-linear affinity function (Ulm and Coussy, 1996; Hellmich et al., 1999b,a), indicating the presence of quite distinct chemical processes having been, somewhat arbitrarily, lumped together.

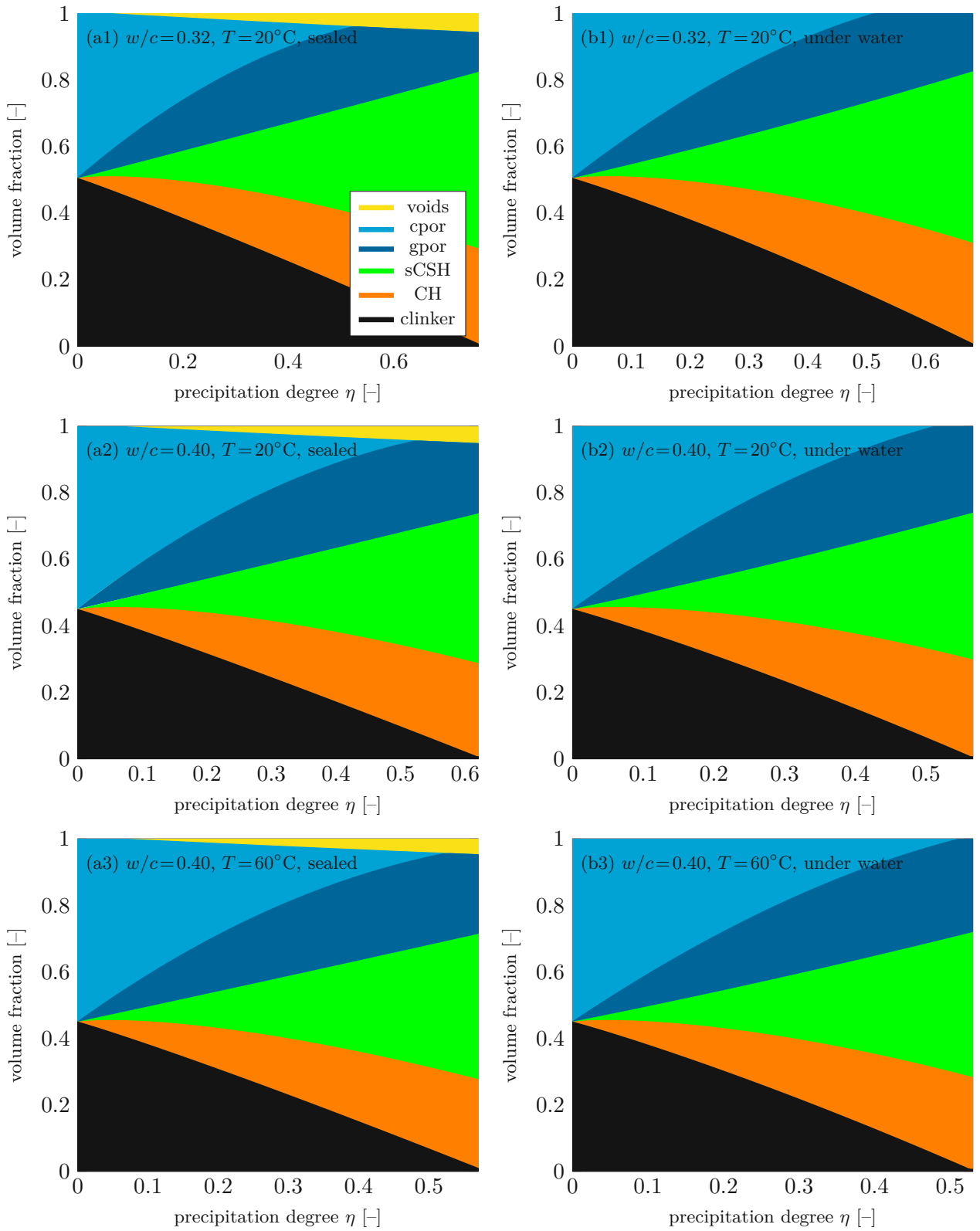


**Fig. 5.15.** Evolution of phase assemblage of cement pastes with (1)  $w/c = 0.32$  and (2,3)  $w/c = 0.40$ ; cured at (1,2)  $T = 20^{\circ}\text{C}$  and (3)  $T = 60^{\circ}\text{C}$ ; stored (a) under sealed conditions and (b) under water, as functions of the precipitation degree.

Finally, mass and volume balancing shows that the mass density of solid C-S-H is dependent on both the precipitation degree and the curing temperature, spanning over a range of numerical values which is fully consistent with the variations known between earlier estimations provided in the open literature, encompassing values from 2.5 g/cm<sup>3</sup> (Bahafid et al., 2017; Constantinides and Ulm, 2004), via 2.6 g/cm<sup>3</sup> (Allen et al., 2007; Taylor, 1986) to 2.7 g/cm<sup>3</sup> (Muller et al., 2013a; Gajewicz-Jaromin et al., 2019); and similar balancing considerations provide also links between the precipitation degree introduced in the present paper, and the classical hydration degree, as well as the volume fractions of material constituents. The latter allow for linking the novel developments presented herein with the rich world of micromechanical modeling (Bernard et al., 2003; Hellmich and Mang, 2005; Sanahuja et al., 2007; Pichler and Hellmich, 2011; Königsberger et al., 2018); especially to models accounting for different pore structures and hydrate densification (Bahafid et al., 2018; Königsberger et al., 2020). Over the last two decades, such models have become major theoretical and computational tools for innovative concrete design.

# Chapter 6

---

## Swelling of nanoscopic solid C-S-H governs macroscopic expansion of mature cement paste during isothermal adsorption

**Authored by:** Nabor Jiménez Segura, Hui Wang, Christian Hellmich, Bernhard L.A. Pichler

**Publication outlook:** At the time of finalizing the thesis, this is to be submitted soon to *Cement and Concrete Research*.

**Abstract:** The macroscopic volumetric expansion of mature cement paste, resulting from an isothermal stepwise increase of the relative humidity, is modeled using a multiscale poromechanical approach. The evolution of the water content, measured during an adsorption experiment, is used to identify the pore-size distribution of two samples of mature cement paste with different initial water-to-cement mass ratios ( $w/c$ ). This is the basis for a poromechanical analysis. At first, changes of the effective pore pressures resulting from changes of the relative humidity are upscaled. It is found that the effective pore pressures explain the measured macroscopic swelling of the samples only partly. Thus, adsorption-induced swelling of microscopic solid C-S-H is introduced as a second microstructural effect. A top-down identification procedure is used to quantify the microscopic eigenstrain of the solid C-S-H as a function of the relative humidity. The changes of effective pore pressures and the microscopic eigenstrain of the solid C-S-H are upscaled in order to predict the macroscopic expansion of mature cement paste during isothermal adsorption with satisfactory result.

**Contribution:** Nabor Jiménez Segura: Investigation, Methodology, Formal analysis, Computation, Visualization, Writing – original draft, review & editing. Hui Wang: Conceptualization, Methodology. Christian Hellmich: Supervision, Conceptualization, Funding acquisition, Methodology, Formal analysis, Supervision, Writing – review & editing. Bernhard L.A. Pichler: Supervision, Conceptualization, Funding acquisition, Methodology, Formal analysis, Writing – review & editing.

**Keywords:** Cement paste; NMR; Hydration; Kinetics; Micromechanics modeling.

## 6.1 Introduction

In the existing literature, “C-S-H” is used in many different contexts. This provides the motivation to explain the terminology used in the present paper. Calcium-silicate-hydrates (C-S-H) with chemical formula  $(\text{CaO})_x(\text{SiO}_2)(\text{H}_2\text{O})_y$ , also referred to as poorly crystalline “solid C-S-H” (MacTavish et al., 1985) and calcium hydroxide (CH) with chemical formula  $(\text{CaO})(\text{H}_2\text{O})$ , are the main products resulting from the hydration of ordinary Portland clinkers including tricalcium silicate or alite, with chemical formula  $(\text{CaO})_3(\text{SiO}_2)$ , and dicalcium silicate or belite, with chemical formula  $(\text{CaO})_2(\text{SiO}_2)$ , (Richardson, 1999). Water which is part of the molecular structure of solid C-S-H is referred to as “interlayer water” (McDonald et al., 2010). Solid C-S-H interacts with two types of pore families: gel and capillary pores. Gel pores are also referred to as “intra-C-S-H pores” (McDonald et al., 2010). Together with solid C-S-H and they form a composite called “C-S-H gel” (Brough et al., 1994; Jennings et al., 2008; Jennings, 2008). The next larger type of pores, the capillary pores, are also referred to as “inter-C-S-H pores” (McDonald et al., 2010) as well as “interhydrate pores” (Muller et al., 2013a), respectively. Together with hydration products they form a composite called “hydrate foam” (Pichler and Hellmich, 2011).

The water content of solid C-S-H (see  $y$  in the chemical formula) is variable rather than a universal constant.

- Curing cement paste isothermally results in the precipitation of solid C-S-H with a temperature-specific water-to-silica ratio which is the larger, the smaller the curing temperature (Bahafid et al., 2017; Jiménez Segura et al., 2022a).
- Increasing the temperature of mature cement paste results in a release of water by solid C-S-H. This phenomenon was found in molecular dynamics simulations coupled with a Grand Canonical Monte-Carlo approach (Bonnaud et al., 2013). Experimental evidence was provided by proton nuclear magnetic resonance relaxometry (Wyrzykowski et al., 2017), clarifying that solid C-S-H releases water upon heating and takes up water upon cooling in a quasi instantaneous and reversible manner. This water migration phenomenon results in changes of (i) the internal relative humidity ( $RH$ ), as well as (ii) effective porewater underpressures acting on the solid skeleton, and the latter mechanism provides a microporomechanical explanation for the anomalous macroscopic thermal expansion of mature cement paste (Wang et al., 2018). Returning to molecular simulations, water release by solid C-S-H upon heating was described for different calcium-to-silica ratios using a reactive molecular simulation model (Zhang et al., 2021).
- Isothermal drying and re-wetting of cementitious materials have the potential to change the water content of solid C-S-H. Desorption-induced drying of solid C-S-H, however, requires internal relative humidities lowered to values smaller than 20% (Feldman, 1968; Muller et al., 2013b; Pinson et al., 2015). Provided that such an advanced desorption (= drying) is followed by adsorption (= re-wetting), the interlayer spaces are considered to be progressively re-filled by water along the entire  $RH$  range back to full saturation (Feldman, 1968; Muller et al., 2013b; Pinson et al., 2015).

The present paper refers to yet another interesting feature of solid C-S-H: volume changes under isothermal conditions and constant water content.

The porosity in cement pastes ranges from the micrometer scale down to pores in the order of the nanometer. As in other porous materials, changes in relative humidity ( $RH$ ) produce

changes in water content and volume in mature cement paste (Powers and Brownyard, 1946; Feldman, 1968). These changes are produced by the following time-dependent effects:

- water transport from the ambient environment to the open porosity of the sample due to capillary condensation, or vice versa, (Camuffo, 1984)
- water transport from the solid C-S-H to the porosity of the sample, or vice versa, (Wang et al., 2018; Wyrzykowski et al., 2017)
- creep resulting from change of mechanical stress acting on the solid skeleton.

The porosity of a material sample can be characterized based on measurements of the water content as a function of  $RH$  (Hagymassy et al., 1972; Baroghel-Bouny, 2007; Jennings et al., 2015). However, the following issues need to be considered when calculating the pore-size distribution from sorption water content:

- (a) Pore-blockage/ bottle-necks/ pore-network effects, i.e. pores which would be expected to be empty are full because they are not in contact with the vapor phase due to pore connectivity (Brunauer et al., 1967).
- (b) Around  $RH = 30 - 40\%$ , a sudden drop in water content results from the evaporation of water in pores larger than a threshold radius (even behind the bottle-necks) (Feldman, 1968; Maruyama et al., 2018).
- (c) In desorption, water content in the interlayer spaces of C-S-H and/or in very small spaces is considered to remain mainly unchanged until very low  $RH$  (typically  $RH < 20\%$ ) (Feldman, 1968; Muller et al., 2013b; Pinson et al., 2015).
- (d) In adsorption, emptied interlayer spaces and/or small spaces are considered to be filled along the entire  $RH$  range (Feldman, 1968; Muller et al., 2013b; Pinson et al., 2015).

Calculating the pore-size distribution from the desorption branch would not be affected by (c) but it would produce misleading results because of (a). Calculating the pore-size distribution from the (classical) adsorption branch after severe drying (oven-drying/  $RH$  0%) would not be affected by (a) but the effects of (d) must be considered. This is not an easy task as the mechanisms behind this behavior are not fully understood. Therefore, a less common practice is here proposed considering all (a)(b)(c)(d): the pore-size distribution can be then calculated from isothermal adsorption starting at  $RH = 20\%$ . Because of (b), studying samples dried to  $RH = 20\%$  would avoid (a). Moreover, as the samples have not been dried severely (below  $RH = 20\%$ ), the interlayer water will not be altered (c), hence avoiding (d).

Successfully validated multiscale models of mature cement paste (Ulm et al., 2004; Pichler et al., 2008; Koichi et al., 2009; Pichler and Dormieux, 2010; Pichler and Hellmich, 2011) brought the motivation to study volume changes induced by changes in relative humidity ( $RH$ ) under a multiscale framework. The present study is focused on the swelling of mature cement pastes observed during isothermal adsorption experiments by Maruyama (Maruyama, 2010). The increase in water content is used to characterize the porosity of the sample. The test data refer to a sequence of equilibrium states, i.e. to the final water content and to the final macroscopic deformation, which are both reached once the time-dependent effects such as water transport and creep have decayed to insignificant intensities.

## 6.2 Model development

### 6.2.1 Experimental measurements: water content and uniaxial swelling during isothermal adsorption

The experimental measurements from (Maruyama, 2010) are analyzed. Ordinary Portland cement was mixed as a paste with initial water-to-cement mass ratios of  $w/c = 0.40$  and  $w/c = 0.55$  (notation N40 and N55 respectively). The specimens were cured under water at a temperature of  $T = 293.15$  K for 91 days before the tests commenced. The dimensions of the specimens were  $V = 3 \times 13 \times 300$  mm<sup>3</sup>.

The specimens were stored in a chamber with controlled relative humidity ( $RH$ ) for 56 days at each targeted relative humidity at  $T = 293.15$  K in order to get reasonably close to equilibrium. It is important to emphasize that a sequence of equilibrium states is analyzed, i.e. temperature and  $RH$  are prescribed around an unsealed specimen and kept constant, targeting the 'final' deformation which is reached as late as all time-dependent effects have come to an end (or have decayed to insignificant intensities). The specimens were stored at  $RH = 98\%$ ,  $95\%$ ,  $90\%$ ,  $80\%$ ,  $70\%$ ,  $60\%$ ,  $50\%$ ,  $40\%$ , and  $30\%$ , then dried to  $RH = 20\%$ , and after that they were stored under higher relative humidities  $RH = 30\%$ ,  $40\%$ ,  $50\%$ ,  $60\%$ ,  $70\%$ ,  $80\%$ ,  $90\%$ , and  $95\%$ . The current study is focused on the isothermal adsorption in the range of capillary condensation, from  $RH = 20\%$  to  $RH = 90\%$ .

The water content of each sample was measured and normalized using the mass of a different oven-dried sample,  $m_{exp}^{dry}$ , as

$$w_{exp}(RH) = \frac{m_{exp}(RH) - m_{exp}^{dry}}{m_{exp}^{dry}}, \quad (6.1)$$

where  $m_{exp}(RH)$  is the mass of the sample at a  $RH$ , see Fig. 6.1. The uniaxial volume change  $E_{uni}$  during the isothermal re-wetting was measured with a contact displacement meter, see Fig. 6.2. Then, the macroscopic strain tensor of the sample is  $\mathbf{E}_{cp} = E_{uni} \mathbf{1}$ , where  $\mathbf{1}$  is the second-order unity tensor with the Kronecker delta  $\delta_{ij}$  as its components.

In order to interpret the experimental data, the mass of the oven-dried sample  $m_{exp}^{dry}$  must be calculated. The normalized value of the mass of water in the saturated sample  $w_{exp}^{sat}$  and the density of cement paste  $\rho_{cp}$  provided in Table 6.1 yield

$$m_{dry} = \frac{\rho_{cp}}{w_{exp}^{sat} + 1} V. \quad (6.2)$$

The resulting masses of the oven-dried samples with initial water-to-cement mass ratios of  $w/c = 0.40$  and  $w/c = 0.55$  are  $m_{exp}^{dry}(w/c = 0.40) = 26.30$  g and  $m_{exp}^{dry}(w/c = 0.55) = 23.70$  g.

**Table 6.1**

Densities and water contents of saturated mature cement pastes (Maruyama, 2010).

	$w/c = 0.40$	$w/c = 0.55$
density ( $\rho_{cp}$ ) [g/cm <sup>3</sup> ]	2.67	2.56
water content in saturated sample ( $w_{exp}^{sat}$ ) [g/g-dry]	0.188	0.264

The poromechanical model will be developed using the data obtained from the samples with initial water-to-cement mass ratio of  $w/c = 0.40$ . Afterwards, the model will be used to predict the macroscopic expansion of the samples of mature cement paste with  $w/c = 0.55$ .



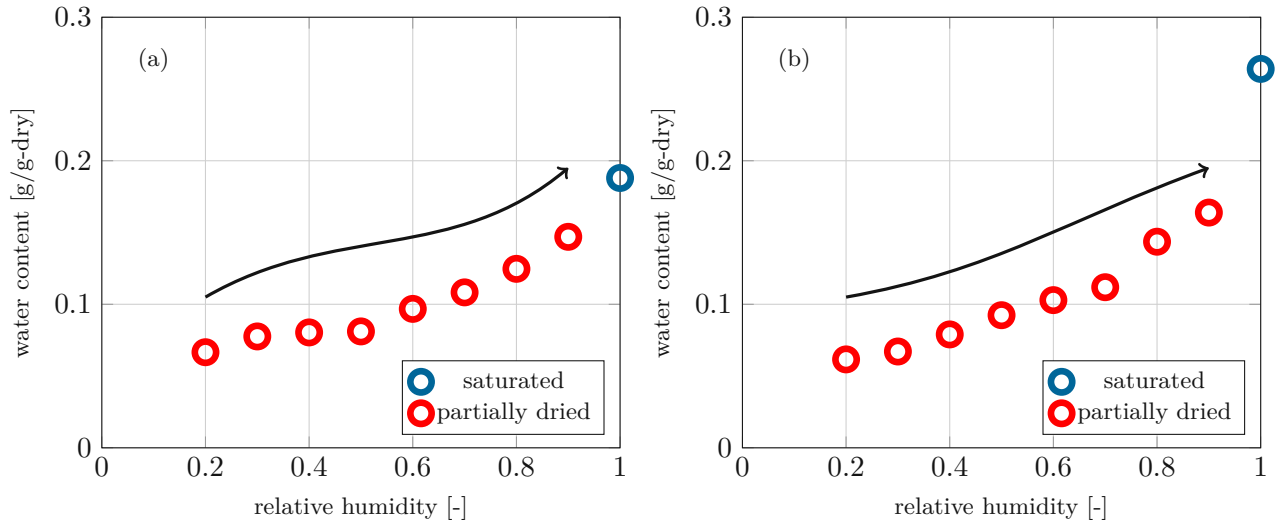


**Fig. 6.1.** Experimentally measured water content  $w_{exp}(RH)$  during isothermal adsorption (Maruyama, 2010) of partially-dried (red) mature cement pastes with (a)  $w/c = 0.40$  and (b)  $w/c = 0.55$ . The values are normalized using the mass of the dried sample, see Eq. (6.1). The water content of the (initial) saturated sample, in blue.

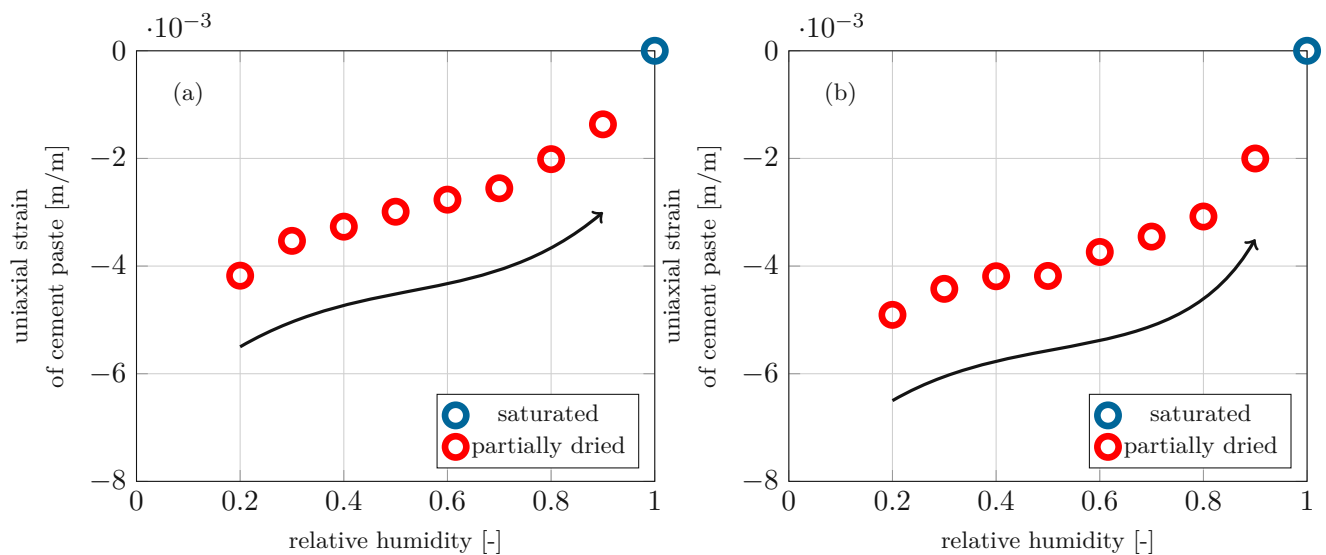


**Fig. 6.2.** Experimentally measured isothermal swelling (Maruyama, 2010) of partially-dried (red) mature cement pastes with (a)  $w/c = 0.40$  and (b)  $w/c = 0.55$ . The reference is the (initial) saturated sample, in blue.

## 6.2.2 Hierarchical organization of mature cement paste

Mature cement paste consists of unhydrated clinker grains, calcium hydroxide, solid C-S-H, and pores with different sizes (Wang et al., 2018; Pichler et al., 2008; Pichler and Hellmich, 2011). Cement paste ( $cp$ ) is modeled by means of four matrix-inclusion composites at different scales, see Fig. 6.3:

1. The microstructure of cement paste consists of spherical clinker grains ( $uc$ ) embedded in a hydrate foam ( $hf$ ) matrix.
2. The microstructure of the hydrate foam consists of spherical calcium hydroxide ( $CH$ ) embedded in a C-S-H foam ( $CSHf$ ) matrix.
3. The microstructure of the C-S-H foam consists of spherical capillary pores ( $cpor$ ) embedded in a C-S-H gel ( $CSHg$ ) matrix.
4. The microstructure of the C-S-H gel consists of spherical gel pores ( $gpor$ ) embedded in a solid C-S-H ( $sCSH$ ) matrix.

The pores are considered to be interconnected. The pore-size distributions of the pore families are described mathematically as exponential distributions (Koichi et al., 2009), i.e. the pore-size probability distribution function reads as

$$\phi_k^{pdf}(r) = \frac{1}{R_k} \exp\left(-\frac{r}{R_k}\right), \quad k \in \{gpor, cpor\}, \quad (6.3)$$

where  $R_{gpor}$  and  $R_{cpor}$  are the characteristic radii which describe the gel and capillary porosities, respectively.  $\phi_k^{pdf} dr$  represents the fraction of pores with radii ranging from  $r$  to  $r + dr$ .

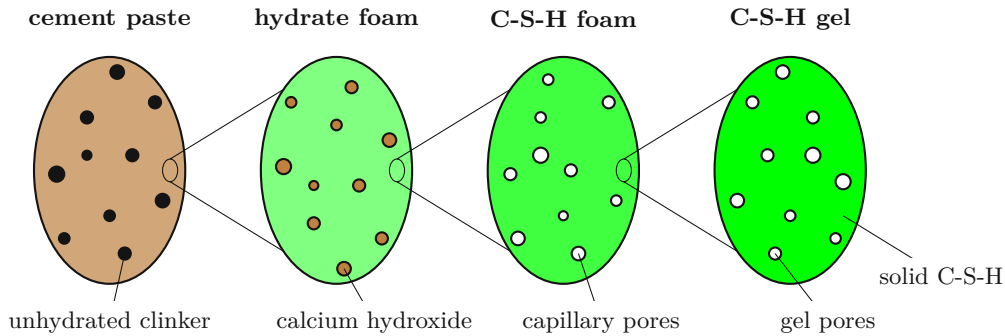


**Fig. 6.3.** Hierarchical representation of mature cement pastes. Two-dimensional sketches of three-dimensional representative volume elements.

The volume fractions of the constituents of the cement paste are defined by the precipitation model developed in (Jiménez Segura et al., 2022a), as a function of the initial water-to-cement mass ratio ( $w/c$ ) and the precipitation degree ( $\eta$ ), associated to a hydration degree ( $\xi$ ). The volume fractions of the different material phases relative to cement paste are calculated considering the hydration degree associated to the precipitation degree reached after 90 days (Jiménez Segura et al., 2022a), i.e.  $\xi = 0.86$ , see Table 6.2.

The pore-size distribution of the total porosity of cement paste can be expressed from the gel and capillary pore-size distributions, see Eq. (6.3) as

$$\phi^{pdf}(r) = f_{gpor}^{por} \phi_{gpor}^{pdf}(r) + f_{cpor}^{por} \phi_{cpor}^{pdf}(r). \quad (6.4)$$

**Table 6.2**

Volume fractions of material phases relative to cement paste derived from precipitation model (for  $\xi = 0.86$ ).

material phase	$w/c = 0.40$	$w/c = 0.55$
unhydrated clinker ( $f_{uc}^{cp}$ )	0.06	0.05
calcium hydroxide ( $f_{CH}^{cp}$ )	0.27	0.24
capillary pores ( $f_{cpor}^{cp}$ )	0.02	0.12
gel pores ( $f_{gpor}^{cp}$ )	0.29	0.30
solid C-S-H ( $f_{CSH}^{cp}$ )	0.37	0.28

Therefore, it is also interesting to get the volume relations of the porosity. The volume of pores per unit volume of cement paste is

$$f_{por}^{cp} = f_{gpor}^{cp} + f_{cpor}^{cp}. \quad (6.5)$$

The volume fractions of the capillary pores and the gel pores relative to the entire porosity read as

$$f_{cpor}^{por} = \frac{f_{cpor}^{cp}}{f_{por}^{cp}}, \quad f_{gpor}^{por} = 1 - f_{cpor}^{por}, \quad (6.6)$$

see Table 6.2.

### 6.2.3 Status of individual pores of partially saturated cement paste

Pores are either filled by air or by water. In both cases there is a layer of water physically adsorbed at the electrostatically charged pore surface, see Fig. 6.4. The thickness of the

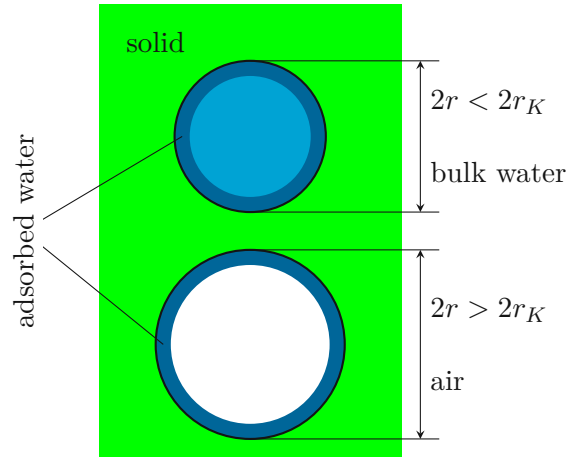


**Fig. 6.4.** Representation of pore status under partial saturation. The Kelvin radius  $r_K$  distinguishes air-filled and water-filled pores, see Eq. (6.10). A layer of water is adsorbed on the pore surface. Two-dimensional sketch of three-dimensional configurations.

adsorbed layer of water is quantified empirically as (Badmann et al., 1981)

$$t = 0.388 \text{ nm} - \ln[-\ln(RH)] \times 0.191 \text{ nm}. \quad (6.7)$$

The difference between gas and liquid pressures is defined as the capillary pressure  $p_c$ . The Young-Laplace equation describe the capillary pressure, from hydrostatic force balance between

liquid and vapor phases, in terms of the curvature of the meniscus  $\mathbf{b}$ , and for hemispherical meniscus ( $|\text{tr } \mathbf{b}| = \frac{2 \cos \theta}{r_m}$ ) it reads as (Laplace, 1805; Young, 1805)

$$p_c = p_g - p_l = \gamma^{lg} \frac{2 \cos \theta}{r_m}, \quad (6.8)$$

where  $\gamma^{lg}$  stands for the surface tension of interfaces between liquid and gas,  $\theta$  is the contact angle between the liquid and the solid, and  $r_m$  is the radius of the meniscus, see Fig. 6.5.

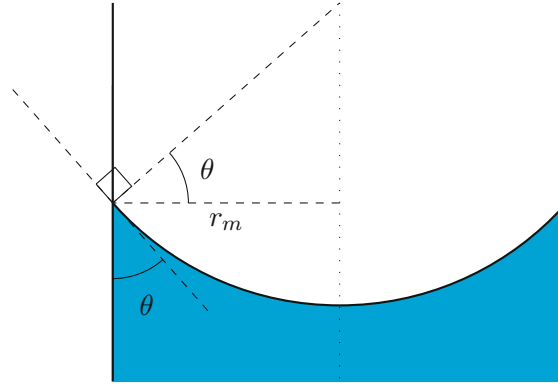


**Fig. 6.5.** Representation of a spherical meniscus in a cylinder. Two-dimensional sketch of three-dimensional configuration.

Assuming the vapor phase is an ideal gas and the liquid is incompressible (bulk modulus several orders of magnitude larger than shear modulus), the Kelvin equation results from thermodynamic equilibrium: (Thomson, 1871; Rowlinson and Widom, 1982)

$$\ln(RH) = -\frac{v_m}{RT} p_c, \quad (6.9)$$

where  $R = 8.21446 \text{ J mol}^{-1} \text{ K}^{-1}$  denotes the universal gas constant, and  $v_m$  is the molar volume. Note the  $-$  sign for concave radius curvature.

The Kelvin radius,  $r_K = r_m + t$ , is a threshold which determines whether a pore is filled by air or water. Combining Eqs. (6.8) and (6.9), the Kelvin radius depends on the ambient conditions according to

$$r_K = -\frac{2\gamma^{lg} v_m \cos \theta}{\ln(RH) RT} + t. \quad (6.10)$$

For water  $\gamma^{lg} = 0.073 \text{ N m}^{-1}$  (Vargaftik et al., 1983),  $v_m = 1.805 \times 10^{-5} \text{ m}^3 \text{ mol}^{-1}$ , and  $\theta$  is so small for cement-based materials that it is set equal to zero (Hua et al., 1995). Both the Kelvin radius and the thickness of the adsorbed layer monotonically increase with increasing relative humidity, see Fig. 6.6.

#### 6.2.4 Characterization of porosity: identification of characteristic radii

$R_{gpor}$  and  $R_{cpor}$

The mass of pore water at a certain relative humidity  $m_{H_2O}(RH)$  is obtained by subdividing the volume of the total porosity  $f_{por}^{cp}$  into water-filled  $f_{H_2O}^{por}$  and air-filled  $f_{air}^{por}$  subvolumes, such that  $f_{H_2O}^{por} + f_{air}^{por} = 1$ . The water-filled subvolume accounts for the water-filled pores and the water layers adsorbed on the surface of air-filled pores. The air-filled fraction is related to

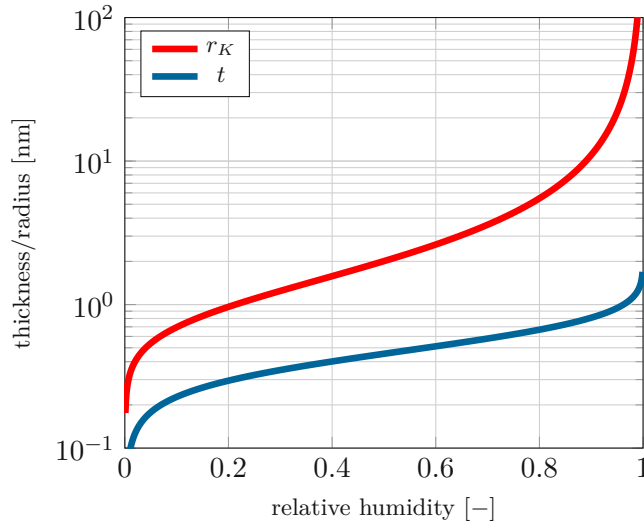


**Fig. 6.6.** Kelvin radius, see Eq. (6.10), and thickness of adsorbed layer, see Eq. (6.7), for different values of internal relative humidity.

the pore-size distribution  $\phi^{pdf}(r)$ , see Eq. (6.4), by means of the following integral over the air-filled pores

$$f_{air}^{por}(RH) = \int_{r_K(RH)}^{\infty} \left[ \frac{r - t(RH)}{r} \right]^3 \phi^{pdf}(r) dr. \quad (6.11)$$

The mass of water at any specific relative humidity can be calculated as

$$m_{mod}^{H_2O}(RH) = \rho_{H_2O} f_{por}^{cp} f_{H_2O}^{por}(RH) V = \rho_{H_2O} f_{por}^{cp} [1 - f_{air}^{por}(RH)] V. \quad (6.12)$$

The increase of water content during isothermal adsorption is associated with an increase of both adsorbed and bulk water in the pores, i.e. the changes in interlayer water content is negligible compared to it. This assumption is supported by the fact that the samples were dried only partially (down to  $RH = 20\%$ ), and therefore the interlayer water content remains almost unchanged (Feldman, 1968; Muller et al., 2013b; de Burgh et al., 2016).

The modeled content of water at a certain  $RH$  can be compared with the experimental, see Eq. (6.1), for a given pair  $R_{gpor}$  and  $R_{cpor}$  defining

$$w_{mod}(RH) = w_{exp}(RH = 20\%) + \frac{m_{mod}^{H_2O}(RH) - m_{mod}^{H_2O}(RH = 20\%)}{m_{exp}^{dry}}. \quad (6.13)$$

Then, a function which quantifies the difference between the modeled adsorption curve for certain  $R_{gpor}$  and  $R_{cpor}$ ,  $w_{mod}(R_{gpor}, R_{cpor})$ , and the experimental curve,  $w_{exp}$ , is developed.

$$\epsilon(R_{gpor}, R_{cpor}) = \sum_{RH=20\%}^{90\%} [w_{mod}(RH, R_{gpor}, R_{cpor}) - w_{exp}(RH)]^2. \quad (6.14)$$

The optimal combination of  $R_{gpor}$  and  $R_{cpor}$  are found numerically with a shift-and-shrink algorithm, as detailed in (Irfan-ul Hassan et al., 2016).

The characteristic radii obtained for the sample with  $w/c = 0.55$  are  $R_{gpor} = 3$  nm and  $R_{cpor} = 9$  nm, and the characteristic radius of the gel porosity obtained for the sample with  $w/c = 0.40$  is  $R_{gpor} = 4$  nm. The amount of capillary pores in the sample with  $w/c = 0.40$

is not large enough to quantify the characteristic radius of the capillary porosity with the available data. As a remedy, the proportion between the gel and the capillary characteristic radii is assumed to be similar in both samples, i.e. the capillary characteristic radius in the sample with  $w/c = 0.40$  is  $R_{cpor} = 11$  nm. The modeled water contents for these pairs of characteristic radii are in good agreement with the experimental measurements, see Fig. 6.7. The values of the characteristic radii are comparable to the ones reported in similar analyses (Huang et al., 2015; Wang et al., 2018).

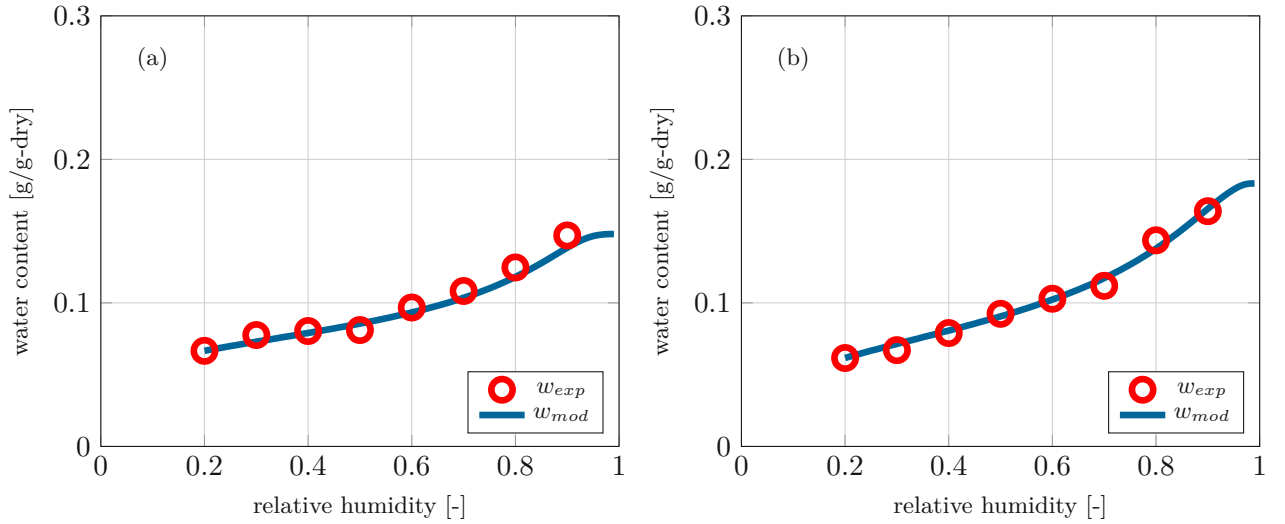


**Fig. 6.7.** Experimentally measured water content  $w_{exp}(RH)$  (Maruyama, 2010) and modeled water content  $w_{mod}(RH)$  during isothermal adsorption of partially-dried mature cement pastes with (a)  $w/c = 0.40$  (for identified  $R_{gpor} = 4$  nm and  $R_{cpor} = 11$  nm) and (b)  $w/c = 0.55$  (for identified  $R_{gpor} = 3$  nm and  $R_{cpor} = 9$  nm). The values are normalized using the mass of the dried sample, see Eqs. (6.1) and (6.13).

## 6.3 Multiscale homogenization of mature cement paste

### 6.3.1 Microscopic input

Homogenization techniques are used to calculate the macroscopic properties of a representative volume element (RVE) given the microscopic properties of the subvolumes in which the RVE is divided. In matrix-inclusion composites, such as mature cement paste, see Fig. 6.3, the RVE consists of a matrix phase and an inclusion phase, occupying the subvolumes  $V_m$  and  $V_i$ , respectively. The material phases are characterized by an elastic stiffness tensor  $\mathbb{C}_k$ , an eigenstress  $\sigma_k^E$ , and a volume fraction  $f_k = V_k/V_{RVE}$ , such that

$$\forall \underline{x} \in V_k : \begin{cases} \mathbb{C}(\underline{x}) = \mathbb{C}_k \\ \sigma^E(\underline{x}) = \sigma_k^E, \end{cases} \quad k \in \{m, i\}. \quad (6.15)$$

The stiffness tensors of the solid constituents are considered to be isotropic. They are expressed in terms of their bulk moduli  $k$  and shear moduli  $\mu$ , see Table 6.3:

$$\mathbb{C}_k = 3k_k \mathbb{1}_{vol} + 2\mu_k \mathbb{1}_{dev}, \quad k \in \{uc, sCSH\}, \quad (6.16)$$

where  $\mathbb{I}_{vol}$  and  $\mathbb{I}_{dev}$  stand for the volumetric and the deviatoric parts of the symmetric fourth-order unity tensor  $\mathbb{I}$  ( $I_{ijrs} = 1/2(\delta_{ir}\delta_{js} + \delta_{is}\delta_{jr})$ ), respectively.  $\mathbb{I}_{vol} = 1/3(\mathbf{1} \otimes \mathbf{1})$  and  $\mathbb{I}_{dev} = \mathbb{I} - \mathbb{I}_{vol}$ . Air and pore water are fluids. Their solid stiffness is equal to zero  $\mathbb{C}_{cpor} = \mathbb{C}_{gpor} = 0$ .

**Table 6.3**

Elastic constants of solid constituents of mature cement paste (Ulm et al., 2004).

material phase	bulk modulus $k_k$	shear modulus $\mu_k$
clinker ( $k = uc$ )	116.7 GPa	53.8 GPa
calcium hydroxide ( $k = CH$ )	33.3 GPa	14.5 GPa
solid C-S-H ( $k = sCSH$ )	31.8 GPa	19.1 GPa

The solid skeleton of cement paste is subjected to effective pore pressures  $p$ . These effective pore pressures account for the pressure of the fluid filling the pore, see Fig. 6.4, and for the surface tension, which depends on the pore radius. The effective pressure in a pore of radius  $r$  with liquid pressure  $p_l$  and gas pressure  $p_g$  reads as (Pichler and Dormieux, 2010)

$$p(r) = \begin{cases} p_l - \frac{2\gamma^{sl}}{r-t} & \text{if } r < r_K, \\ p_g - \frac{2\gamma^{sg}}{r-t} & \text{if } r \geq r_K, \end{cases} \quad (6.17)$$

where  $\gamma^{sl}$  and  $\gamma^{sg}$  stand for surface tension at solid-liquid and solid-gas interfaces, respectively. The surface tensions  $\gamma^{sl}$  and  $\gamma^{sg}$  can be related by means of Young's equation, see Appendix 6.A,

$$\gamma^{sl} + \gamma^{lg} \cos \theta - \gamma^{sg} = 0, \quad (6.18)$$

and the equation of state obtained through Berthelot's averaging rule, see Appendix 6.B,

$$\gamma^{lg} + \gamma^{sg} - \gamma^{sl} = 2\sqrt{\gamma^{sg}\gamma^{lg}}, \quad (6.19)$$

and therefore expressed in terms of  $\gamma^{lg}$ , considering  $\theta \approx 0$ . As the difference between gas and liquid pressures is defined as the capillary pressure, see Eq. (6.8), and gas pressure is set as a reference pressure  $p_g \equiv 0$ , the effective pressure in a pore of radius  $r$  can be expressed as follows:

$$p(r) = \begin{cases} \ln(RH) \frac{RT}{v_m} & \text{if } r < r_K, \\ -\frac{2\gamma^{lg}}{r-t} & \text{if } r \geq r_K. \end{cases} \quad (6.20)$$

In order to upscale these pressures to the macroscopic scale, the average effective pressures over the pore families  $p_{gpor}$  and  $p_{cpor}$  are meaningful. The average effective pressure of a pore family is calculated through an integral over its pore-size distribution, see Eq. (6.3),

$$p_k = \int_0^\infty p(r) \phi_k^{pdf}(r) dr, \quad k \in \{gpor, cpor\}. \quad (6.21)$$

### 6.3.2 Bottom-up homogenization of pore pressures

The homogenization of matrix-inclusion composites is usually implemented by means of the Mori-Tanaka-Benveniste scheme (Mori and Tanaka, 1973; Benveniste, 1987). The Mori-Tanaka-Benveniste scheme provides analytic expressions for the strain concentration tensors (Benveniste, 1987)

$$\mathbb{A}_k = [\mathbb{I} + \mathbb{P} : (\mathbb{C}_k - \mathbb{C}_m)]^{-1} : \left\{ \sum_{j=m,i} f_j [\mathbb{I} + \mathbb{P} : (\mathbb{C}_k - \mathbb{C}_m)]^{-1} \right\}^{-1}, \quad k \in \{m, i\}, \quad (6.22)$$



where  $\mathbb{P}$  is the morphology tensor, or Hill tensor, which accounts for the shape and orientation of the inclusion (Hill, 1963). In the particular case of spherical inclusions in an isotropic matrix,  $\mathbb{P}$  reads as (Eshelby, 1957)

$$\mathbb{P} = (S_{vol}\mathbb{1}_{vol} + S_{dev}\mathbb{1}_{dev}) : \mathbb{C}_m^{-1}, \quad (6.23)$$

$$S_{vol} = \frac{3k_m}{3k_m + 4\mu_m}, \quad (6.24)$$

$$S_{dev} = \frac{6(k_m + 2\mu_m)}{5(3k_m + 4\mu_m)}. \quad (6.25)$$

The strain concentration tensors  $\mathbb{A}_k$  are used as link between the microscopic and the macroscopic properties.

The homogenized macroscopic stiffness  $\mathbb{C}_{hom}$  and the homogenized eigenstress  $\Sigma_{hom}^E$  are calculated as follows (Zaoui, 2002; Levin, 1967)

$$\mathbb{C}_{hom} = f_m \mathbb{C}_m : \mathbb{A}_m + f_i \mathbb{C}_i : \mathbb{A}_i, \quad (6.26)$$

$$\Sigma_{hom}^E = f_m \sigma_m^E : \mathbb{A}_m + f_i \sigma_i^E : \mathbb{A}_i. \quad (6.27)$$

Thus, the generalized Hooke's law of the homogenized macroscopic material reads as

$$\Sigma = \mathbb{C}_{hom} : \mathbf{E} + \Sigma_{hom}^E, \quad (6.28)$$

where  $\Sigma$  is the macroscopic stress, and  $\mathbf{E}$  the macroscopic strain.

The macroscopic swelling due to changes in effective pore pressures induced by changes in relative humidity is homogenized from the smallest scale up to the macroscopic level, see Table 6.4. The outcome of one homogenization step is used as an input in the following step. The volume fractions are obtained from Table 6.2 (Jiménez Segura et al., 2022a). The eigenstresses assigned to the pore families come from the average effective pore pressures, see Eq. (6.21),  $\sigma_{gpor}^E = p_{gpor} \mathbf{1}$  and  $\sigma_{cpor}^E = p_{cpor} \mathbf{1}$ . In order to study the effect of changes in effective pore pressures, no eigenstress in the solid C-S-H is considered  $\sigma_{sCSH}^E = 0$ .

**Table 6.4**

Step-by-step homogenization of mature cement paste from the smallest scale to the macroscopic application scale (cement paste).

homogenization scale	constituents	volume fraction	stiffness	eigenstress	homogenized stiffness	homogenized eigenstress
C-S-H gel	solid C-S-H	$f_{sCSH}^{hg}$	$\mathbb{C}_{sCSH}$	$\sigma_{sCSH}^E$	$\mathbb{C}_{CSHg}$	$\Sigma_{CSHg}^E$
	gel pores	$f_{gpor}^{CSHg}$	$\mathbb{C}_{gpor} = 0$	$\sigma_{gpor}^E = p_{gpor} \mathbf{1}$		
C-S-H foam	C-S-H gel	$f_{CSHf}^{CSHg}$	$\mathbb{C}_{CSHg}$	$\sigma_{CSHf}^E = \Sigma_{CSHg}^E$	$\mathbb{C}_{CSHf}$	$\Sigma_{CSHf}^E$
	capillary pores	$f_{cpor}^{CSHf}$	$\mathbb{C}_{cpor} = 0$	$\sigma_{cpor}^E = p_{cpor} \mathbf{1}$		
hydrate foam	C-S-H foam	$f_{CSHf}^{hf}$	$\mathbb{C}_{CSHf}$	$\sigma_{CSHf}^E = \Sigma_{CSHf}^E$	$\mathbb{C}_{hf}$	$\Sigma_{hf}^E$
	calcium hydroxide	$f_{CH}^{hf}$	$\mathbb{C}_{CH}$	$\sigma_{CH}^E = 0$		
cement paste	hydrate foam	$f_{hf}^{cp}$	$\mathbb{C}_{hf}$	$\sigma_{hf}^E = \Sigma_{hf}^E$	$\mathbb{C}_{cp}$	$\Sigma_{cp}^E$
	unhydrated clinker	$f_{uc}^{cp}$	$\mathbb{C}_{uc}$	$\sigma_{uc}^E = 0$		

The volume change of cement paste occurred under stress-free conditions ( $\Sigma_{cp} = 0$ ), which means that the macroscopic deformation is a result of an eigenstress

$$\mathbf{E}_{cp} = -\mathbb{C}_{cp}^{-1} : \Sigma_{cp}^E. \quad (6.29)$$

The modeled deformation produced by changes in effective pore pressures explains the experimental measurements only partially, see Fig. 6.8. Consequently, there is another source of deformation. A  $RH$ -dependent volume change of the solid C-S-H, i.e. an eigenstrain, is proposed here.

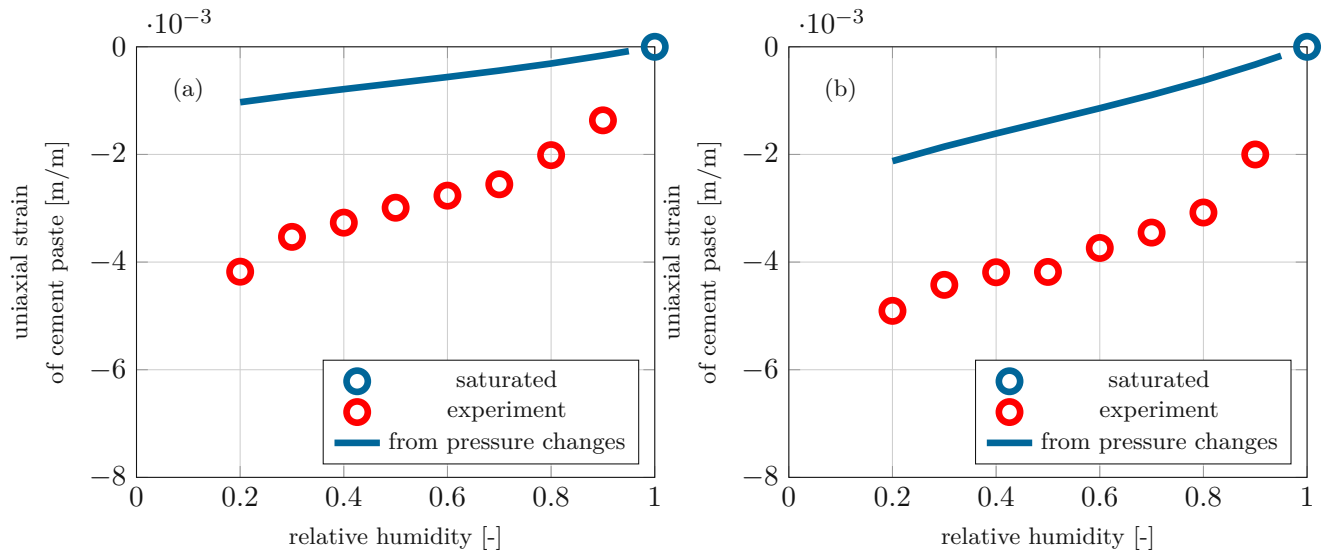


**Fig. 6.8.** Modeled volume deformation in mature cement pastes with (a)  $w/c = 0.40$  and (b)  $w/c = 0.55$  produced due to changes in effective pore pressures induced by changes of relative humidity (blue) and macroscopic measured deformation (Maruyama, 2010) (red).

### 6.3.3 Top-down identification of eigenstrain of solid C-S-H

In order to identify the volume change of the solid C-S-H, the sample with  $w/c = 0.40$  is used as a benchmark. The deformation of the solid C-S-H is identified in a way that for each  $RH$ , the modeled macroscopic deformation equals the measured deformation.

The top-down identified microscopic eigenstrain  $\epsilon_{sCSH}^E$  increases with increasing  $RH$ , see Fig. 6.9. The values obtained are fitted by a linear and a third order polynomials, resulting in  $\epsilon_{sCSH}^E = 0.004(RH) - 0.006$  and  $\epsilon_{sCSH}^E = 0.027(RH)^3 - 0.043(RH)^2 + 0.025(RH) - 0.009$ , respectively. The eigenstrain can be transformed into an eigenstress using the stiffness tensor

$$\sigma_{sCSH}^E = -\mathbb{C}_{sCSH} : \epsilon_{sCSH}^E. \quad (6.30)$$

### 6.3.4 Bottom-up prediction of macroscopic swelling

In order to test the universality of the identified microscopic swelling of the solid C-S-H, the sample with  $w/c = 0.55$  is studied. Thus, the macroscopic swelling of the sample is predicted considering the volume change produced due to changes in effective pore pressures *and* the identified microscopic swelling of solid C-S-H. Therefore, the macroscopic deformation of cement paste is calculated according to Table 6.4, where the  $RH$ -dependent microscopic

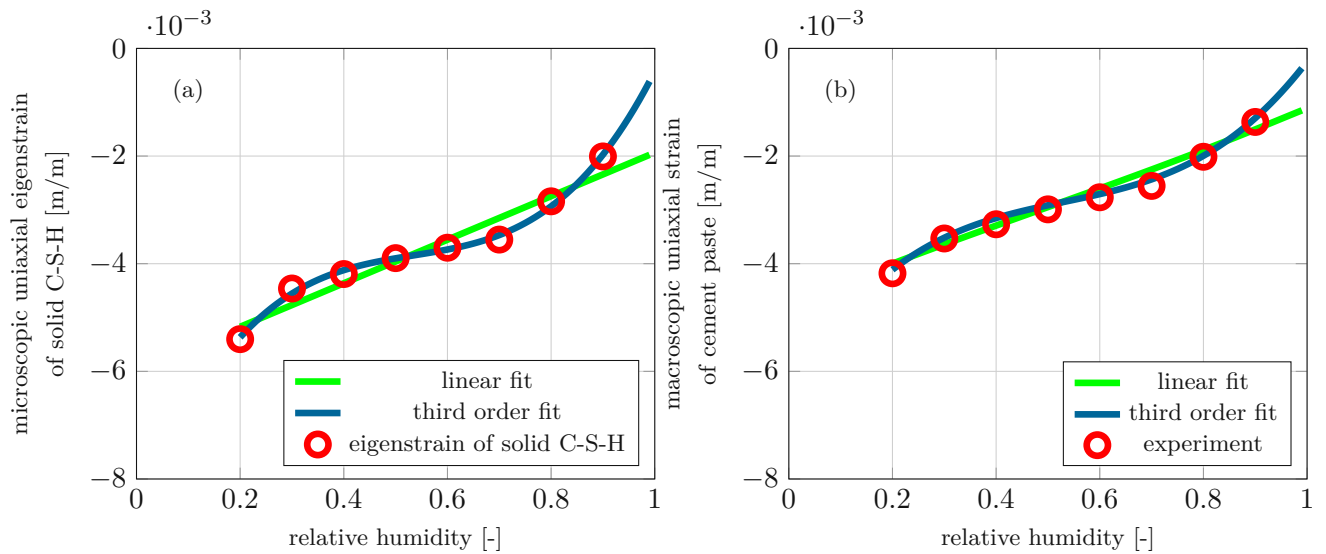


**Fig. 6.9.** (a) Top-down identified eigenstrain of the solid C-S-H as a function of relative humidity. (b) The value of the eigenstrain was calculated based on the sample with  $w/c = 0.40$ .

swelling of the solid C-S-H identified in the sample with  $w/c = 0.40$  is introduced (as an eigenstress) in the smallest scale .

The prediction of macroscopic strain is in good agreement with the experimental measurements, see Fig. 6.10. This suggests that the microscopic eigenstrain of the solid C-S-H is a material property of solid C-S-H, see Fig. 6.9.

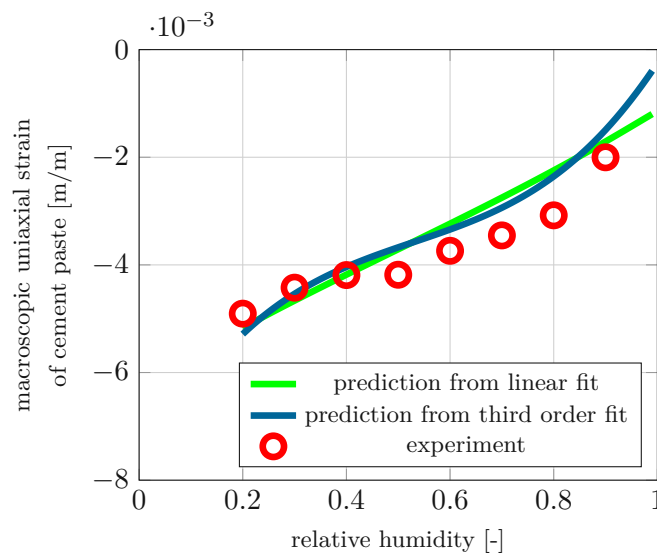


**Fig. 6.10.** Sample with  $w/c = 0.55$ . Prediction of macroscopic expansion produced due to changes in effective pore pressures *and* microscopic swelling of solid C-S-H (linear fit in green, third order fit in blue). Macroscopic measured deformation (Maruyama, 2010) in red.

## 6.4 Conclusions

A new material property is quantified at the nanoscale in cement pastes: the microscopic swelling of solid C-S-H induced by increasing RH. This swelling is introduced as a RH-dependent eigenstrain at the smallest scale and quantified through a top-down analysis. The macroscopic volume change of cement paste with different  $w/c$  during isothermal adsorption was predicted considering the changes in effective pore pressures induced by changes in RH and the microscopic swelling of solid C-S-H with satisfactory result.

The identification of these microscopic volume changes of solid C-S-H leads to an interesting discussion: what are the mechanisms behind them? A possible source of swelling could be the uptake of small amounts of water by the solid C-S-H with increasing RH. Another source of deformation could be the disjoining pressure caused by adsorbed water within the microstructure of the solid C-S-H. The decrease (in magnitude) of the capillary pressure (due to the increase of  $RH$ ) may influence the water within the solid C-S-H, producing swelling. The presented eigenstrain of solid C-S-H accounts for all the effects occurring in a smaller within their microstructure.

### Appendix 6.A Young's equation

Young's equation is a result of static equilibrium between the three phases: solid, liquid, and gas. The equilibrium of the surface tensions in a plane parallel to the pore surface yields, see Fig. 6.11,

$$\gamma^{sl} + \gamma^{lg} \cos \theta - \gamma^{sg} = 0. \quad (6.A.1)$$

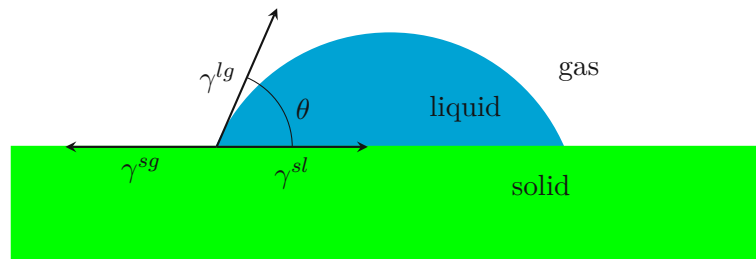


**Fig. 6.11.** Representation of a liquid droplet wetting a plain surface. Two-dimensional sketch of three-dimensional configuration.

### Appendix 6.B The equation of state through Berthelot rule

The free energy of adhesion of a pair liquid-solid is calculated as the energy required to separate the gas from the interface and create a solid-liquid interface, i.e.

$$W_{sl} = \gamma^{lg} + \gamma^{sg} - \gamma^{sl}. \quad (6.B.1)$$

The value of  $W_{sl}$  can be calculated by analogy with Berthelot average rule for admixture of gases (Berthelot, 1898; Li and Neumann, 1992) through a geometric mean combining the free energy of adhesion of pairs solid-solid and liquid-liquid

$$W_{sl} = \sqrt{W_{ss} W_{ll}}, \quad (6.B.2)$$

where the free energy of adhesion of a pair solid-solid and a pair liquid-liquid are  $W_{ss} = 2\gamma^{sg}$  and  $W_{ll} = 2\gamma^{lg}$ , respectively. Thus, the following relation for the surface tensions can be obtained

$$\gamma^{lg} + \gamma^{sg} - \gamma^{sl} = 2\sqrt{\gamma^{sg} \gamma^{lg}}. \quad (6.B.3)$$

Berthelot average rule is reliable if  $W_{ss} \approx W_{ll}$ , i.e.  $\gamma^{sg} \approx \gamma^{lg}$ . As the contact angle in cementitious materials is close to zero, such that  $\cos \theta \approx 1$ , Eq. (6.B.3) can be used as a state equation.

## Summary, conclusions, and outlook

### 7.1 Summary of the micromechanics modeling

One of the pillars of micromechanics modeling is the stress average rule. The fundamentals of the stress average rule are revisited in Chapter 2. While this well-known average rule was typically introduced as a definition, a different approach is here taken to obtain it as a *derivation*. The mechanical equilibrium of microheterogeneous representative volume elements subjected to homogeneous (macroscopic) kinematic boundary conditions was reviewed and re-evaluated in the framework of the principle of virtual power, leading to the stress average rule, and to a less frequently discussed volume force average rule.

Thereafter, the stress average rule and the equilibrium conditions, together with other fundamental relations such as the geometrical boundary conditions and the micro- and macroscopic elasticity laws allows to develop a novel scheme to study complex microstructures, see Chapter 3. To this end, the effects of elastic behavior at the microscale are represented by means of the Green's function formalism in an infinite medium, leading to Fredholm integral equations which provide novel, series-type integral expressions for the auxiliary concentration tensor field. The latter are related to the RVE-related concentration tensor field by comparing the auxiliary strain to the average strain in the RVE. In special cases, such as a microstructure with harmonically fluctuating bulk moduli, it is possible to solve these expressions analytically, which yields explicit macro-to-micro relations.

The case of materials with a microstructure consisting of several inclusion phases embedded in a matrix phase is faced in Chapter 4. The traditional Mori-Tanaka-Benveniste scheme (Mori and Tanaka, 1973; Benveniste, 1987) exhibits well-known limitations. Namely, when applied to composites with multiple inclusion phases of different shapes, the corresponding homogenized stiffness estimates remain symmetric only if at least one of the following conditions is fulfilled (Benveniste et al., 1989; Ferrari, 1991; Sevostianov and Kachanov, 2014):

1. all material constituents and the homogenized composite are isotropic,
2. all the inclusion phases have the same stiffness, and
3. all the inclusion phases have the same shape and the same orientation.

For all other cases, Sevostianov and Kachanov (2014) proposed to symmetrize the unsymmetric result delivered by the Mori-Tanaka-Benveniste scheme. In the present thesis, the general consequences of such a symmetrization are explored. The symmetrization process implies mathematical expressions for the concentration tensors in the case of elastic composites

different than those derived in the classical Mori-Tanaka-Benveniste scheme. The aforementioned concentration tensors overcome all the limitations of the Mori-Tanaka-Benveniste scheme, yielding symmetric homogenized stiffness estimates in multiphase-multiform composites.

These developments open new avenues for exploring the mechanical deformations in hierarchical material systems with complex morphologies, such as shale (Gruescu et al., 2007), wood (Bader et al., 2010), or fired clay (Kiefer et al., 2020).

## 7.2 Summary of their application to cementitious materials

### 7.2.1 Conclusions drawn from the study of precipitation in cement paste

The hydration degree is focused on cement clinker. Defined as the mass of dissolved clinker divided by its initial mass, it is the most popular variable used for the description of the microstructural phase evolution of hydrating cementitious materials. This way, it is one essential prerequisite for quantitative upscaling of microstructural properties to corresponding macroscopic homogenized material properties. Related “hydration models” (Powers and Brownyard, 1946; Powers, 1958; Hansen, 1986; Acker, 2001) provide closed-form expressions for the volume fractions of the microstructural constituents (clinker, hydration products, and pores) as functions of the initial water-to-cement mass ratio and the hydration degree. These models were derived mainly from studies on water vapour sorption isotherms and chemically bound water in hydrating cement pastes. Water was classified into free capillary water, physically bound gel water (0.19 g water per gram of clinker consumed), and chemically bound “nonevaporable” water (0.23 g water per gram of clinker consumed). Because of the proportionality between the two types of bound water and the consumed clinker, related phase volume fractions evolve linearly with increasing hydration degree. Another interesting property described by the hydration models is that the *ratios of the volume fractions* of capillary pores and gel pores as well as of capillary pores and solid hydrates *depend* on the initial water-to-cement mass ratio. This dependence is challenged by the results of the present study, developed in Chapter 5.

The newly introduced precipitation degree is focused on the hydrogen-containing material phases. It is defined as the sum of hydrogen bound solidly into calcium hydroxide and solid C-S-H, divided by the total amount of hydrogen in the two solids as well as in water-filled gel and capillary pores. In other words, the precipitation degree refers to the subsystem of cement paste, which is equal to the total material *minus* the clinker and the air-filled voids. This hydrogen-containing subsystem was comprehensively characterized by means of proton NMR testing, see (Muller et al., 2013a; Muller, 2014) and (Gajewicz-Jaromin et al., 2019; Gajewicz, 2014), respectively. The presented analysis was based on measurements taken from these two studies:

1. 51 measurements by Muller (2014) who characterized sealed samples, cured at 20°C, with initial water-to-cement mass ratios,  $w/c$ , ranging from 0.32 to 0.48, and
2. 131 measurements by Gajewicz (2014) who characterized samples stored under water, with  $w/c=0.40$ , cured at constant temperatures ranging from 10 to 60°C.

Using this proton NMR database for studying the evolution of the relative amounts of the four hydrogen-containing material phases as functions of the precipitation degree, it was demonstrated that these functions are independent of the initial composition of cement paste,



the curing temperature, and the the storage conditions (sealed or underwater), see Eqs. (5.13), (5.14), (5.19), and (5.20), Table 5.1, and Figs. 5.5 and 5.6. This underlines the significance of the precipitation degree as a new variable for the description of the microstructural phase evolution. Notably, also the *ratios of volume fractions* of capillary pores and gel pores as well as of capillary pores and solid hydrates are *independent* of the initial water-to-cement mass ratio. This sheds an interesting light on the role of clinker. It dissolves provided that it is in contact with undersaturated porewater, but this dissolution merely represents the supply for the continued formation of hydrates, while precipitation of calcium hydroxide and solid C-S-H as well as the subdivision of the total water-filled porosity into gel and capillary pores follow universal laws *inside* the system of the four hydrogen-containing material phases.

As regards the influence of the curing temperature on the precipitation-induced maturing of cement paste, the following conclusions are drawn:

- The influence of curing temperature on the precipitation kinetics can be modeled based on the Arrhenius equation, see Eq. (5.27), and a chemical affinity function which decreases *linearly* with increasing precipitation degree, as expected in classical physical chemistry, see Eq. (5.28).
- One value of the chemical affinity constant and one value of the activation energy allow for reproducing the precipitation kinetics in the studied range of temperatures from 10 to 60°C, see Eq. (5.31), as well as Table 5.3 and Fig. 5.12.
- The “finally” reached precipitation degree decreases linearly with increasing curing temperature, see Eq. (5.24) and Fig. 5.9. This is related to the temperature-dependent water-to-silica ratio, see Fig. 5.10.

The masses and volumes of clinker, solid C-S-H, and chemical-shrinkage-related voids (= phases that do not contain hydrogen), can be determined by means of mass and volume balance. This allows to calculate the mass density of solid C-S-H, which depends on the curing temperature and the precipitation degree, see Fig. 5.14. Results obtained from modeling of the phase volume fractions as a function of the initial water-to-cement mass ratio  $w/c$  and the precipitation degree  $\eta$  yields the following conclusions:

- The uptake of water in samples cured underwater is virtually proportional to the precipitation degree. It counteracts the creation of air-filled voids, which is driven by chemical shrinkage and e.g. in sealed samples.
- One set of formulae, see Eqs. (5.48)–(5.51), (5.53), (5.58), and (5.59), is sufficient to describe the evolution of phase assemblage for both types of curing conditions: sealed curing and underwater storage, respectively, see Fig. 5.15. This is possible because of a binary variable  $\pi_4$ , see Table 5.2.
- The relation between the precipitation degree  $\eta$  and the hydration degree  $\xi$  depends on the initial water-to-cement mass ratio  $w/c$  and the curing conditions, see Eq. (5.45) and Fig. 5.13.

The here reported results become directly applicable in the context of multiscale modeling. As an example, they were applied in the context of adsorption-induced swelling of cement paste.

### 7.2.2 Conclusions drawn from the study of swelling C-S-H

Chapter 6 studies a set of experiments by Maruyama (2010). In these experiments, the deformation of cement paste samples with different initial compositions is measured while they are subjected to isothermal adsorption.

The precipitation model developed in Chapter 5 was used to obtain the phase assemblage of the samples. Then, the Mori-Tanaka scheme was applied to calculate the expected deformation resulting from changes in pore pressures. These changes in effective pore pressures explained the measured deformation only partially. Therefore, the microscopic swelling of solid C-S-H induced by increasing  $RH$  was considered as an additional source of macroscopic deformation. This swelling is introduced as a material property, described as a  $RH$ -dependent eigenstrain at the smallest scale and quantified through a top-down analysis. The changes in effective pore pressures, together with the microscopic swelling of solid C-S-H, were upscaled to predict the macroscopic volume change of cement pastes with different  $w/c$  during isothermal adsorption. The result was satisfactory.

## 7.3 Perspectives

The present thesis included fundamental theoretical developments regarding homogenization methods of continuum micromechanics and selected applications of such methods to the hierarchically organized microstructures of cementitious materials at early and mature ages. The presented research results open the door to the following future perspectives:

- The novel scheme of Chapter 3 was applied to a complex microstructure with harmonically fluctuating bulk moduli. In the future, it will be interesting to study also microstructures with harmonically fluctuating shear moduli. This will complete a new toolbox of fundamental solutions. It will open the door to homogenization of general complex microstructures with any distribution of isotropic microstiffnesses, noting that the latter can be developed into trigonometric Fourier series.
- In Chapter 4, the investigation of multiform multiphase matrix-inclusion microstructures was focused on strain concentration tensors. In the future, it will be interesting to extend these developments towards eigenstressed media by means of the transformation field analysis. This extension will also include influence tensors which relate the eigenstress in one phase to the microstrain that it induces in another phase. This will open the door to stress and strain downscaling also in the context of poromicromechanics, temperature changes, and elasto-plastic phase behavior.
- The NRM study of Chapter 5 was focused on white cement paste. In the future it will be interesting to develop similar models also for other cementitious binders, noting that the cement and concrete industry addresses the urgent pressure to reduce  $\text{CO}_2$  emissions by the development of binder systems in which significant amounts of Portland cement clinker are replaced by supplementary cementitious materials.
- In the context of sorption-induced volume changes of solid C-S-H, Chapter 6 is focused on adsorption-induced nanoscopic swelling of solid C-S-H. In the future, it will be interesting to study also desorption problems. This will make it necessary to tackle the challenge of the bottle-neck-effect also known from Mercury Intrusion Porosimetry. Additional open research questions regard irreversible microstructural processes associated with the first drying process as well as sequences of drying and rewetting including severe

drying to relative humidities significantly lower than 20%, such that the water content of solid C-S-H is also significantly decreased.

- The physical mechanisms standing behind the nanoscopic deformation of solid C-S-H also deserve future exploration. It will be interesting to study the interaction between capillary underpressure in the porewater and the “effective pressure” experienced by water inside solid C-S-H. In addition, also disjoining pressure which is caused by adsorbed water within the microstructure of the solid C-S-H and which may also result in nanoscopic volume changes deserves future attention.

# Bibliography

- Abuhaikal, M., Ioannidou, K., Petersen, T., Pellenq, R. J. M., and Ulm, F.-J. (2018). Le Châtelier's conjecture: Measurement of colloidal eigenstresses in chemically reactive materials. *Journal of the Mechanics and Physics of Solids*, 112:334–344.
- Acker, P. (2001). Micromechanical analysis of creep and shrinkage mechanisms. In *Creep, Shrinkage and Durability Mechanics of Concrete and Other Quasi-brittle Materials (Proceedings of ConCreep-6@ MIT)*, pages 15–26. Elsevier, Amsterdam.
- Allen, A. J., Thomas, J. J., and Jennings, H. M. (2007). Composition and density of nanoscale calcium–silicate–hydrate in cement. *Nature Materials*, 6(4):311–316.
- Arrhenius, S. (1889). Über die Reaktionsgeschwindigkeit bei der Inversion von Rohrzucker durch Säuren. *Zeitschrift für Physikalische Chemie*, 4U(1):226–248.
- Atkins, P., Atkins, P. W., and Paula, J. d. (2014). *Atkins' physical chemistry*. OUP Oxford.
- Auriault, J.-L., Boutin, C., and Geindreau, C. (2010). *Homogenization of coupled phenomena in heterogenous media*. John Wiley & Sons
- Bader, T., Hofstetter, K., Hellmich, C., and Eberhardsteiner, J. (2010). Poromechanical scale transitions of failure stresses in wood: from the lignin to the spruce level. *ZAMM - Journal of Applied Mathematics and Mechanics / Zeitschrift für Angewandte Mathematik und Mechanik*, 90(10-11):750–767.
- Badmann, R., Stockhausen, N., and Setzer, M. J. (1981). The statistical thickness and the chemical potential of adsorbed water films. *Journal of Colloid and Interface Science*, 82(2):534–542.
- Bahafid, S., Ghabezloo, S., Duc, M., Faure, P., and Sulem, J. (2017). Effect of the hydration temperature on the microstructure of Class G cement: C-S-H composition and density. *Cement and Concrete Research*, 95:270–281.
- Bahafid, S., Ghabezloo, S., Faure, P., Duc, M., and Sulem, J. (2018). Effect of the hydration temperature on the pore structure of cement paste: Experimental investigation and micromechanical modelling. *Cement and Concrete Research*, 111:1–14.
- Baroghel-Bouny, V. (2007). Water vapour sorption experiments on hardened cementitious materials: Part I: Essential tool for analysis of hygral behaviour and its relation to pore structure. *Cement and Concrete Research*, 37(3):414–437.
- Bažant, Z. P. (1972). Thermodynamics of hindered adsorption and its implications for hardened cement paste and concrete. *Cement and Concrete Research*, 2(1):1–16.

- Benveniste, Y. (1987). A new approach to the application of Mori-Tanaka's theory in composite materials. *Mechanics of Materials*, 6(2):147–157.
- Benveniste, Y., Dvorak, G. J., and Chen, T. (1989). Stress fields in composites with coated inclusions. *Mechanics of Materials*, 7(4):305–317.
- Benveniste, Y., Dvorak, G. J., and Chen, T. (1991). On diagonal and elastic symmetry of the approximate effective stiffness tensor of heterogeneous media. *Journal of the Mechanics and Physics of Solids*, 39(7):927–946.
- Bernard, O., Ulm, F.-J., and Lemarchand, E. (2003). A multiscale micromechanics-hydration model for the early-age elastic properties of cement-based materials. *Cement and Concrete Research*, 33(9):1293–1309.
- Berthelot, D. (1898). Sur le mélange des gaz [Mixture of gases]. *Comptes Rendus*, 126:1703–1706.
- Bonnaud, P. A., Ji, Q., and Vliet, K. J. V. (2013). Effects of elevated temperature on the structure and properties of calcium–silicate–hydrate gels: the role of confined water. *Soft Matter*, 9(28):6418–6429.
- Brisard, S. and Dormieux, L. (2010). FFT-based methods for the mechanics of composites: A general variational framework. *Computational Materials Science*, 49(3):663–671.
- Brough, A. R., Dobson, C. M., Richardson, I. G., and Groves, G. W. (1994). Application of selective <sup>29</sup>Si isotopic enrichment to studies of the structure of calcium silicate hydrate (C-S-H) gels. *Journal of the American Ceramic Society*, 77(2):593–596.
- Brunauer, S., Mikhail, R. S., and Bodor, E. E. (1967). Some remarks about capillary condensation and pore structure analysis. *Journal of Colloid and Interface Science*, 25(3):353–358.
- Bullard, J. W., Jennings, H. M., Livingston, R. A., Nonat, A., Scherer, G. W., Schweitzer, J. S., Scrivener, K. L., and Thomas, J. J. (2011). Mechanisms of cement hydration. *Cement and Concrete Research*, 41(12):1208–1223.
- Buryachenko, V. (2007). *Micromechanics of heterogeneous materials*. Springer Science & Business Media.
- Cai, X., Brenner, R., Peralta, L., Olivier, C., Gouttenoire, P.-J., Chappard, C., Peyrin, F., Cassereau, D., Laugier, P., and Grimal, Q. (2019). Homogenization of cortical bone reveals that the organization and shape of pores marginally affect elasticity. *Journal of The Royal Society Interface*, 16(151):20180911.
- Camuffo, D. (1984). Condensation-evaporation cycles in pore and capillary systems according to the Kelvin model. *Water, Air, and Soil Pollution*, 21(1):151–159.
- Cauvin, L., Bhatnagar, N., Brieu, M., and Kondo, D. (2007). Experimental study and micromechanical modeling of MMT platelet-reinforced PP nanocomposites. *Comptes Rendus Mécanique*, 335(11):702–707.
- Chen, W. and Fish, J. (2006). A mathematical homogenization perspective of virial stress. *International Journal for Numerical Methods in Engineering*, 67(2):189–207.

- Clausius, R. (1870). Xvi. on a mechanical theorem applicable to heat. *The London, Edinburgh, and Dublin Philosophical Magazine and Journal of Science*, 40(265):122–127.
- Constantinides, G. and Ulm, F.-J. (2004). The effect of two types of C-S-H on the elasticity of cement-based materials: Results from nanoindentation and micromechanical modeling. *Cement and Concrete Research*, 34(1):67–80.
- Cormier, J., Rickman, J. M., and Delph, T. J. (2001). Stress calculation in atomistic simulations of perfect and imperfect solids. *Journal of Applied Physics*, 89(1):99–104.
- Cowin, S. C. (2003). A recasting of anisotropic poroelasticity in matrices of tensor components. *Transport in Porous Media*, 50(1):35–56.
- D'Aloia, L. and Chanvillard, G. (2002). Determining the “apparent” activation energy of concrete:  $E_a$ —numerical simulations of the heat of hydration of cement. *Cement and Concrete Research*, 32(8):1277–1289.
- de Burgh, J. M., Foster, S. J., and Valipour, H. R. (2016). Prediction of water vapour sorption isotherms and microstructure of hardened Portland cement pastes. *Cement and Concrete Research*, 81:134–150.
- De Schutter, G. and Taerwe, L. (1995). General hydration model for Portland cement and blast furnace slag cement. *Cement and Concrete Research*, 25(3):593–604.
- Diamond, S. (2004). The microstructure of cement paste and concrete—a visual primer. *Cement and Concrete Composites*, 26(8):919–933. Scanning electron microscopy of cements and concretes.
- Drugan, W. J. and Willis, J. R. (1996). A micromechanics-based nonlocal constitutive equation and estimates of representative volume element size for elastic composites. *Journal of the Mechanics and Physics of Solids*, 44(4):497–524.
- Dvorak, G. J. (1992). Transformation field analysis of inelastic composite materials. *Proceedings of the Royal Society of London. Series A: Mathematical and Physical Sciences*, 437(1900):311–327.
- Dvorak, G. J. (2012). *Micromechanics of composite materials*. Springer Science & Business Media.
- Eremeyev, V. A. and Altenbach, H. (2014). Equilibrium of a second-gradient fluid and an elastic solid with surface stresses. *Meccanica*, 49(11):2635–2643.
- Eshelby, J. D. (1957). The determination of the elastic field of an ellipsoidal inclusion, and related problems. *Proceedings of the Royal Society of London. Series A: Mathematical and Physical Sciences*, 241(1226):376–396.
- Feldman, R. and Sereda, P. (1964a). Sorption of water on compacts of bottle-hydrated cement. I. The sorption and length-change isotherms. *Journal of applied Chemistry*, 14(2):87–93.
- Feldman, R. and Sereda, P. (1964b). Sorption of water on compacts of bottle-hydrated cement. II. Thermodynamic considerations and theory of volume change. *Journal of Applied Chemistry*, 14(2):93–104.



- Feldman, R. F. (1968). Sorption and length-change scanning isotherms of methanol and water on hydrated portland cement. *Proceedings of Fifth International Symposium on the Chemistry of Cement, Tokyo*.
- Feng, X., Garboczi, E. J., Bentz, D. P., Stutzman, P. E., and Mason, T. O. (2004). Estimation of the degree of hydration of blended cement pastes by a scanning electron microscope point-counting procedure. *Cement and Concrete Research*, 34(10):1787–1793.
- Ferrari, M. (1991). Asymmetry and the high concentration limit of the Mori-Tanaka effective medium theory. *Mechanics of Materials*, 11(3):251–256.
- Finger, J. (1897). Über das innere Virial eines elastischen Körpers [On the internal virial of an elastic body]. *Kaiserliche Akademie der Wissenschaften in Wien (Proceedings of the Imperial Academy of Sciences in Vienna)*, 106:722–738.
- Franciosi, P. (2022). Phase mean strain and stress estimates in possibly multi-continuous composites under affine elastic-like behavior. *European Journal of Mechanics - A/Solids*, 91:104385.
- Fredholm, I. (1900). Sur les équations de l'équilibre d'un corps solide élastique [On the equations of equilibrium of an elastic solid body]. *Acta Mathematica*, 23(1):1–42.
- Fritsch, A., Dormieux, L., Hellmich, C., and Sanahuja, J. (2009). Mechanical behavior of hydroxyapatite biomaterials: An experimentally validated micromechanical model for elasticity and strength. *Journal of Biomedical Materials Research Part A*, 88A(1):149–161.
- Fritsch, A. and Hellmich, C. (2007). 'Universal' microstructural patterns in cortical and trabecular, extracellular and extravascular bone materials: Micromechanics-based prediction of anisotropic elasticity. *Journal of Theoretical Biology*, 244(4):597–620.
- Fritsch, A., Hellmich, C., and Young, P. (2013). Micromechanics-derived scaling relations for poroelasticity and strength of brittle porous polycrystals. *Journal of Applied Mechanics*, 80(2):020905 (12 pages).
- Gajewicz, A. M. (2014). Characterisation of cement microstructure and pore-water interaction by  $^1\text{H}$  Nuclear Magnetic Resonance Relaxometry (Ph.D. thesis).
- Gajewicz-Jaromin, A. M., McDonald, P. J., Muller, A. C. A., and Scrivener, K. L. (2019). Influence of curing temperature on cement paste microstructure measured by  $^1\text{H}$  NMR relaxometry. *Cement and Concrete Research*, 122:147–156.
- Gallucci, E., Zhang, X., and Scrivener, K. L. (2013). Effect of temperature on the microstructure of calcium silicate hydrate (C-S-H). *Cement and Concrete Research*, 53:185–195.
- Germain, P. (1972). Sur l'application de la méthode des puissances virtuelles en mécanique des milieux continus [On the application of the method of virtual power in mechanics of continuous media]. *Comptes Rendus - Académie des Sciences*, 274:1051–1055.
- Germain, P. (1973). The method of virtual power in continuum mechanics. Part 2: Microstructure. *SIAM Journal of Applied Mathematics*, 25(3):556–575.
- Grasley, Z. C., Lange, D. A., and D'Ambrosia, M. D. (2006). Internal relative humidity and drying stress gradients in concrete. *Materials and Structures*, 39(9):901–909.



- Grimal, Q., Raum, K., Gerisch, A., and Laugier, P. (2011). A determination of the minimum sizes of representative volume elements for the prediction of cortical bone elastic properties. *Biomechanics and Modeling in Mechanobiology*, 10(6):925–937.
- Gruescu, C., Giraud, A., Homand, F., Kondo, D., and Do, D. P. (2007). Effective thermal conductivity of partially saturated porous rocks. *International Journal of Solids and Structures*, 44(3):811–833.
- Grédiac, M., Pierron, F., Avril, S., and Toussaint, E. (2006). The virtual fields method for extracting constitutive parameters from full-field measurements: A review. *Strain*, 42(4):233–253.
- Guilleminot, J., Soize, C., Kondo, D., and Binetruy, C. (2008). Theoretical framework and experimental procedure for modelling mesoscopic volume fraction stochastic fluctuations in fiber reinforced composites. *International Journal of Solids and Structures*, 45(21):5567–5583.
- Gusev, A. A. (1997). Representative volume element size for elastic composites: A numerical study. *Journal of the Mechanics and Physics of Solids*, 45(9):1449–1459.
- Hagymassy, J., Odler, I., Yudenfreund, M., Skalny, J., and Brunauer, S. (1972). Pore structure analysis by water vapor adsorption. III. Analysis of hydrated calcium silicates and portland cements. *Journal of Colloid and Interface Science*, 38(1):20–34.
- Hansen, T. C. (1986). Physical structure of hardened cement paste. A classical approach. *Materials and Structures*, 19(6):423–436.
- Hansson, T., Oostenbrink, C., and van Gunsteren, W. (2002). Molecular dynamics simulations. *Current opinion in structural biology*, 12(2):190–196.
- Hashin, Z. (1963). *Theory of mechanical behavior of heterogeneous media*. Towne School of Civil and Mechanical Engineering, University of Pennsylvania, Philadelphia, Pa.
- Hashin, Z. (1965). Viscoelastic Behavior of Heterogeneous Media. *Journal of Applied Mechanics*, 32(3):630–636.
- Hashin, Z. (1983). Analysis of composite materials—A survey. *Journal of Applied Mechanics*, 50(3):481–505.
- Hellmich, C., Barthélémy, J.-F., and Dormieux, L. (2004). Mineral–collagen interactions in elasticity of bone ultrastructure – a continuum micromechanics approach. *European Journal of Mechanics - A/Solids*, 23(5):783–810.
- Hellmich, C. and Mang, H. (2005). Shotcrete elasticity revisited in the framework of continuum micromechanics: From submicron to meter level. *Journal of Materials in Civil Engineering*, 17(3):246–256.
- Hellmich, C. and Ulm, F.-J. (2002). Micromechanical model for ultrastructural stiffness of mineralized tissues. *Journal of Engineering Mechanics*, 128(8):898–908. Publisher: American Society of Civil Engineers.
- Hellmich, C., Ulm, F.-J., and Mang, H. A. (1999a). Consistent linearization in Finite Element analysis of coupled chemo-thermal problems with exo- or endothermal reactions. *Computational Mechanics*, 24(4):238–244.

- Hellmich, C., Ulm, F.-J., and Mang, H. A. (1999b). Multisurface chemoplasticity. I: Material model for shotcrete. *Journal of Engineering Mechanics*, 125(6):692–701.
- Helnwein, P. (2001). Some remarks on the compressed matrix representation of symmetric second-order and fourth-order tensors. *Computer Methods in Applied Mechanics and Engineering*, 190(22):2753–2770.
- Hill, R. (1963). Elastic properties of reinforced solids: Some theoretical principles. *Journal of the Mechanics and Physics of Solids*, 11(5):357–372.
- Hill, R. (1965a). Continuum micro-mechanics of elastoplastic polycrystals. *Journal of the Mechanics and Physics of Solids*, 13(2):89–101.
- Hill, R. (1965b). A self-consistent mechanics of composite materials. *Journal of the Mechanics and Physics of Solids*, 13(4):213–222.
- Hofstetter, K., Hellmich, C., and Eberhardsteiner, J. (2005). Development and experimental validation of a continuum micromechanics model for the elasticity of wood. *European Journal of Mechanics - A/Solids*, 24(6):1030–1053.
- Hori, M. and Nemat-Nasser, S. (1999). On two micromechanics theories for determining micro–macro relations in heterogeneous solids. *Mechanics of Materials*, 31(10):667–682.
- Horwitz, A. (2001). A version of Simpson’s rule for multiple integrals. *Journal of Computational and Applied Mathematics*, 134(1-2):1–11.
- Hua, C., Acker, P., and Ehrlacher, A. (1995). Analyses and models of the autogenous shrinkage of hardening cement paste: I. Modelling at macroscopic scale. *Cement and Concrete Research*, 25(7):1457–1468.
- Hua, C., Ehrlacher, A., and Acker, P. (1997). Analyses and models of the autogenous shrinkage of hardening cement paste II. Modelling at scale of hydrating grains. *Cement and Concrete Research*, 27(2):245–258.
- Huang, Q., Jiang, Z., Gu, X., Zhang, W., and Guo, B. (2015). Numerical simulation of moisture transport in concrete based on a pore size distribution model. *Cement and Concrete Research*, 67:31–43.
- Höller, R., Aminbaghai, M., Eberhardsteiner, L., Eberhardsteiner, J., Blab, R., Pichler, B., and Hellmich, C. (2019). Rigorous amendment of Vlasov’s theory for thin elastic plates on elastic Winkler foundations, based on the Principle of Virtual Power. *European Journal of Mechanics - A/Solids*, 73:449–482.
- Ioannidou, K., Krakowiak, K. J., Bauchy, M., Hoover, C. G., Masoero, E., Yip, S., Ulm, F.-J., Levitz, P., Pellenq, R. J.-M., and Del Gado, E. (2016). Mesoscale texture of cement hydrates. *Proceedings of the National Academy of Sciences*, 113(8):2029–2034.
- Irfan-ul Hassan, M., Pichler, B., Reihnsner, R., and Hellmich, C. (2016). Elastic and creep properties of young cement paste, as determined from hourly repeated minute-long quasi-static tests. *Cement and Concrete Research*, 82:36–49.
- Jennings, H. M. (2008). Refinements to colloid model of C-S-H in cement: CM-II. *Cement and Concrete Research*, 38(3):275–289.

- Jennings, H. M., Bullard, J. W., Thomas, J. J., Andrade, J. E., Chen, J. J., and Scherer, G. W. (2008). Characterization and modeling of pores and surfaces in cement paste. *Journal of Advanced Concrete Technology*, 6(1):5–29.
- Jennings, H. M., Kumar, A., and Sant, G. (2015). Quantitative discrimination of the nanopore-structure of cement paste during drying: New insights from water sorption isotherms. *Cement and Concrete Research*, 76:27–36.
- Jiménez Segura, N., Pichler, B. L., and Hellmich, C. (2022a). Mix-, storage- and temperature-invariant precipitation characteristics in white cement paste, expressed through an NMR-based analytical model (*under revision*). *Cement and Concrete Research*.
- Jiménez Segura, N., Pichler, B. L., and Hellmich, C. (2022b). Stress average rule derived through the principle of virtual power. *ZAMM - Journal of Applied Mathematics and Mechanics / Zeitschrift für Angewandte Mathematik und Mechanik*, [Online before inclusion in an issue](n/a):e202200091.
- Kalliauer, J., Kahl, G., Scheiner, S., and Hellmich, C. (2020). A new approach to the mechanics of DNA: Atoms-to-beam homogenization. *Journal of the Mechanics and Physics of Solids*, 143:104040.
- Kiefer, T., Füssl, J., Kariem, H., Konnerth, J., Gaggli, W., and Hellmich, C. (2020). A multi-scale material model for the estimation of the transversely isotropic thermal conductivity tensor of fired clay bricks. *Journal of the European Ceramic Society*, 40(15):6200–6217.
- Kohlhauser, C. and Hellmich, C. (2013). Ultrasonic contact pulse transmission for elastic wave velocity and stiffness determination: Influence of specimen geometry and porosity. *Engineering Structures*, 47:115–133.
- Koichi, M., Tetsuya, I., and Toshiharu, K. (2009). Multi-scale modeling of structural concrete. *London and New York: Taylor & Francis*.
- Korringa, J. (1973). Theory of elastic constants of heterogeneous media. *Journal of mathematical physics*, 14(4):509–513.
- Krasny, W., Morin, C., Magoariec, H., and Avril, S. (2017). A comprehensive study of layer-specific morphological changes in the microstructure of carotid arteries under uniaxial load. *Acta Biomaterialia*, 57:342–351.
- Kröner, E. (1977). Bounds for effective elastic moduli of disordered materials. *Journal of the Mechanics and Physics of Solids*, 25(2):137–155.
- Kröner, E. (1958). Berechnung der elastischen Konstanten des Vielkristalls aus den Konstanten des Einkristalls [Calculation of the elastic constant of the multi-crystal from the constants of the single crystals]. *Zeitschrift für Physik*, 151(4):504–518.
- Königsberger, M., Hellmich, C., and Pichler, B. (2016). Densification of C-S-H is mainly driven by available precipitation space, as quantified through an analytical cement hydration model based on NMR data. *Cement and Concrete Research*, 88:170–183.
- Königsberger, M., Hlobil, M., Delsaute, B., Staquet, S., Hellmich, C., and Pichler, B. (2018). Hydrate failure in ITZ governs concrete strength: A micro-to-macro validated engineering mechanics model. *Cement and Concrete Research*, 103:77–94.

- Königsberger, M., Pichler, B., and Hellmich, C. (2020). Multiscale poro-elasticity of densifying calcium-silicate hydrates in cement paste: An experimentally validated continuum micromechanics approach. *International Journal of Engineering Science*, 147:103196.
- Laplace, P. S. (1805). *Traité de mécanique céleste*, volume 4. Paris, Duprat.
- Laws, N. (1973). On the thermostatics of composite materials. *Journal of the Mechanics and Physics of Solids*, 21(1):9–17.
- Laws, N. (1977). The determination of stress and strain concentrations at an ellipsoidal inclusion in an anisotropic material. *Journal of Elasticity*, 7(1):91–97.
- Le Châtelier, H. (1900). Sur les changements de volume qui accompagnent le durcissement des ciments [On the changes in volume which accompany the hardening of cement]. *Bulletin de la Société de l'Encouragement pour l'Industrie Nationale*, 5 (5):54–57.
- Levin, V. M. (1967). Thermal expansion coefficient of heterogeneous materials. *Mekhanika Tverdogo Tela*, 2(1):83–94.
- Li, D. and Neumann, A. W. (1992). Equation of state for interfacial tensions of solid-liquid systems. *Advances in Colloid and Interface Science*, 39:299–345.
- Lippmann, B. A. and Schwinger, J. (1950). Variational principles for scattering processes. I. *Physical Review*, 79(3):469–480.
- Lura, P., Couch, J., Jensen, O. M., and Weiss, J. (2009). Early-age acoustic emission measurements in hydrating cement paste: Evidence for cavitation during solidification due to self-desiccation. *Cement and Concrete Research*, 39(10):861–867.
- Lura, P., Jensen, O. M., and Van Breugel, K. (2003). Autogenous shrinkage in high-performance cement paste: An evaluation of basic mechanisms. *Cement and Concrete Research*, 33(2):223–232.
- MacTavish, J. C., Miljkovic, L., Pintar, M. M., Blinc, R., and Lahajnar, G. (1985). Hydration of white cement by spin grouping NMR. *Cement and Concrete Research*, 15(2):367–377.
- Maruyama, I. (2010). Origin of drying shrinkage of hardened cement paste: Hydration pressure. *Journal of Advanced Concrete Technology*, 8(2):187–200.
- Maruyama, I., Rymeš, J., Vandamme, M., and Coasne, B. (2018). Cavitation of water in hardened cement paste under short-term desorption measurements. *Materials and Structures*, 51(6):159.
- McDonald, P. J., Rodin, V., and Valori, A. (2010). Characterisation of intra- and inter-C-S-H gel pore water in white cement based on an analysis of NMR signal amplitudes as a function of water content. *Cement and Concrete Research*, 40(12):1656–1663.
- Molinari, A. and El Mouden, M. (1996). The problem of elastic inclusions at finite concentration. *International journal of solids and structures*, 33(20-22):3131–3150.
- Mori, T. and Tanaka, K. (1973). Average stress in matrix and average elastic energy of materials with misfitting inclusions. *Acta Metallurgica*, 21(5):571–574.

- Morin, C., Avril, S., and Hellmich, C. (2015). The fiber reorientation problem revisited in the context of Eshelbian micromechanics: theory and computations. *PAMM - Proceedings in Applied Mathematics and Mechanics*, 15(1):39–42.
- Morin, C., Avril, S., and Hellmich, C. (2018). Non-affine fiber kinematics in arterial mechanics: a continuum micromechanical investigation. *ZAMM - Journal of Applied Mathematics and Mechanics / Zeitschrift für Angewandte Mathematik und Mechanik*, 98(12):2101–2121.
- Morin, C., Hellmich, C., Nejm, Z., and Avril, S. (2021). Fiber rearrangement and matrix compression in soft tissues: Multiscale hypoelasticity and application to tendon. *Frontiers in Bioengineering and Biotechnology*, 9.
- Moulinec, H. and Suquet, P. (1994). A fast numerical method for computing the linear and nonlinear mechanical properties of composites. *Comptes Rendus de l'Académie des sciences. Série II. Mécanique, physique, chimie, astronomie*.
- Moulinec, H. and Suquet, P. (1998). A numerical method for computing the overall response of nonlinear composites with complex microstructure. *Computer Methods in Applied Mechanics and Engineering*, 157(1):69–94.
- Mouret, M., Bascoul, A., and Escadeillas, G. (1997). Study of the degree of hydration of concrete by means of image analysis and chemically bound water. *Advanced Cement Based Materials*, 6(3):109–115.
- Moës, N., Cloirec, M., Cartraud, P., and Remacle, J. F. (2003). A computational approach to handle complex microstructure geometries. *Computer Methods in Applied Mechanics and Engineering*, 192(28):3163–3177.
- Muller, A. C. A. (2014). Characterization of porosity & C-S-H in cement pastes by 1H NMR (Ph.D. thesis).
- Muller, A. C. A., Scrivener, K. L., Gajewicz, A. M., and McDonald, P. J. (2013a). Densification of C-S-H measured by 1H NMR relaxometry. *The Journal of Physical Chemistry C*, 117(1):403–412.
- Muller, A. C. A., Scrivener, K. L., Gajewicz, A. M., and McDonald, P. J. (2013b). Use of bench-top NMR to measure the density, composition and desorption isotherm of C-S-H in cement paste. *Microporous and Mesoporous Materials*, 178:99–103.
- Neville, A. M. (1995). *Properties of concrete*. Longman, London, 4 edition.
- Newton, I. (1687). *Philosophiæ Naturalis Principia Mathematica [Mathematical Principles of Natural Philosophy]*
- Nicot, F., Kruyt, N. P., and Millet, O. (2017). On Hill's lemma in continuum mechanics. *Acta Mechanica*, 228(5):1581–1596.
- Pahr, D. H. and Zysset, P. K. (2008). Influence of boundary conditions on computed apparent elastic properties of cancellous bone. *Biomechanics and Modeling in Mechanobiology*, 7(6):463–476.
- Pichler, B. and Dormieux, L. (2010). Cracking risk of partially saturated porous media—Part I: Microporoelasticity model. *International Journal for Numerical and Analytical Methods in Geomechanics*, 34(2):135–157.



- Pichler, B. and Hellmich, C. (2010). Estimation of influence tensors for eigenstressed multiphase elastic media with nonaligned inclusion phases of arbitrary ellipsoidal shape. *Journal of Engineering Mechanics*, 136(8):1043–1053.
- Pichler, B. and Hellmich, C. (2011). Upscaling quasi-brittle strength of cement paste and mortar: A multi-scale engineering mechanics model. *Cement and Concrete Research*, 41(5):467–476.
- Pichler, B., Hellmich, C., and Eberhardsteiner, J. (2008). Spherical and acicular representation of hydrates in a micromechanical model for cement paste: prediction of early-age elasticity and strength. *Acta Mechanica*, 203(3):137.
- Pinson, M. B., Masoero, E., Bonnaud, P. A., Manzano, H., Ji, Q., Yip, S., Thomas, J. J., Bazant, M. Z., Van Vliet, K. J., and Jennings, H. M. (2015). Hysteresis from multiscale porosity: Modeling water sorption and shrinkage in cement paste. *Physical Review Applied*, 3(6):064009.
- Ponte-Castañeda, P. and Willis, J. R. (1995). The effect of spatial distribution on the effective behavior of composite materials and cracked media. *Journal of the Mechanics and Physics of Solids*, 43(12):1919–1951.
- Powers, T. (1935). Absorption of water by Portland cement paste during the hardening process. *Industrial & Engineering Chemistry*, 27(7):790–794.
- Powers, T. (1968). The thermodynamics of volume change and creep. *Matériaux et construction*, 1(6):487–507.
- Powers, T. C. (1958). Structure and physical properties of hardened Portland cement paste. *Journal of the American Ceramic Society*, 41(1):1–6.
- Powers, T. C. and Brownyard, T. L. (1946). Studies of the physical properties of hardened Portland cement paste. *Journal Proceedings*, 43(9):101–132.
- Rajagopal, K. and Srinivasa, A. (2009). On a class of non-dissipative materials that are not hyperelastic. *Proceedings of the Royal Society A: Mathematical, Physical and Engineering Sciences*, 465(2102):493–500.
- Richardson, I. G. (1999). The nature of C-S-H in hardened cements. *Cement and Concrete Research*, 29(8):1131–1147.
- Rosen, B. W. and Hashin, Z. (1970). Effective thermal expansion coefficients and specific heats of composite materials. *International Journal of Engineering Science*, 8(2):157–173.
- Rowlinson, J. S. and Widom, B. (1982). *Molecular Theory of Capillarity*. Oxford: Clarendon.
- Rychlewski, J. (1984). On Hooke's law. *Journal of Applied Mathematics and Mechanics*, 48(3):303–314.
- Saeb, S., Steinmann, P., and Javili, A. (2016). Aspects of computational homogenization at finite deformations: A unifying review from Reuss' to Voigt's bound. *Applied Mechanics Reviews*, 68(050801).
- Salençon, J. (2018). *Virtual Work Approach to Mechanical Modeling*. John Wiley & Sons

- Sanahuja, J., Dormieux, L., and Chanvillard, G. (2007). Modelling elasticity of a hydrating cement paste. *Cement and Concrete Research*, 37(10):1427–1439.
- Sanahuja, J., Dormieux, L., Meille, S., Hellmich, C., and Fritsch, A. (2010). Micromechanical explanation of elasticity and strength of gypsum: From elongated anisotropic crystals to isotropic porous polycrystals. *Journal of Engineering Mechanics*, 136(2):239–253.
- Scheiner, S., Sinibaldi, R., Pichler, B., Komlev, V., Renghini, C., Vitale-Brovarone, C., Rustichelli, F., and Hellmich, C. (2009). Micromechanics of bone tissue-engineering scaffolds, based on resolution error-cleared computer tomography. *Biomaterials*, 30(12):2411–2419.
- Sciarra, G., dell’Isola, F., and Coussy, O. (2007). Second gradient poromechanics. *International Journal of Solids and Structures*, 44(20):6607–6629.
- Scrivener, K. L. and Nonat, A. (2011). Hydration of cementitious materials, present and future. *Cement and Concrete Research*, 41(7):651–665.
- Sevostianov, I. and Kachanov, M. (2014). On some controversial issues in effective field approaches to the problem of the overall elastic properties. *Mechanics of Materials*, 69(1):93–105.
- Somé, S. C., Barthélémy, J.-F., Mouillet, V., Hammoum, F., and Liu, G. (2022). Effect of thermo-oxidative ageing on the rheological properties of bituminous binders and mixes: Experimental study and multi-scale modeling. *Construction and Building Materials*, 344:128260.
- Taylor, H. F. (1986). Proposed structure for calcium silicate hydrate gel. *Journal of the American Ceramic Society*, 69(6):464–467.
- Tazawa, E.-I., Miyazawa, S., and Kasai, T. (1995). Chemical shrinkage and autogenous shrinkage of hydrating cement paste. *Cement and Concrete Research*, 25(2):288–292.
- Termkhajornkit, P. and Barbarulo, R. (2012). Modeling the coupled effects of temperature and fineness of Portland cement on the hydration kinetics in cement paste. *Cement and Concrete Research*, 42(3):526–538.
- Thomson, W. (1871). On the equilibrium of vapour at a curved surface of liquid. *The London, Edinburgh, and Dublin Philosophical Magazine and Journal of Science*, 42(282):448–452.
- Ting, T. C. T. and Lee, V.-G. (1997). The three-dimensional elastostatic Green’s function for general anisotropic linear elastic solids. *The Quarterly Journal of Mechanics and Applied Mathematics*, 50(3):407–426.
- Torquato, S. (1997). Effective stiffness tensor of composite media—i. exact series expansions. *Journal of the Mechanics and Physics of Solids*, 45(9):1421–1448.
- Touratier, M. (1991). An efficient standard plate theory. *International Journal of Engineering Science*, 29(8):901–916.
- Truesdell, C. (1955). Hypo-elasticity. *Journal of Rational Mechanical Analysis*, 4:83–133.
- Ulm, F. J., Constantinides, G., and Heukamp, F. H. (2004). Is concrete a poromechanics materials?—A multiscale investigation of poroelastic properties. *Materials and Structures*, 37(1):43–58.



- Ulm, F.-J. and Coussy, O. (1995). Modeling of thermochemomechanical couplings of concrete at early ages. *Journal of Engineering Mechanics*, 121(7):785–794.
- Ulm, F.-J. and Coussy, O. (1996). Strength growth as chemo-plastic hardening in early age concrete. *Journal of Engineering Mechanics*, 122(12):1123–1132.
- Valori, A., McDonald, P. J., and Scrivener, K. L. (2013). The morphology of C–S–H: Lessons from 1H nuclear magnetic resonance relaxometry. *Cement and Concrete Research*, 49:65–81.
- Vargaftik, N. B., Volkov, B. N., and Voljak, L. D. (1983). International Tables of the Surface Tension of Water. *Journal of Physical and Chemical Reference Data*, 12(3):817–820.
- Verbeck, G. J. (1968). Structures and physical properties of cement paste. In *5th International Congress on the Chemistry of Cement, 1968*, volume 3, pages 1–37.
- Voigt, W. (1889). Über die Beziehung zwischen den beiden Elasticitätsconstanten isotroper Körper [On the relation between the elasticity constants of isotropic bodies]. *Annalen der Physik*, 274(12):573–587.
- Walpole, L. J. (1984). Fourth-rank tensors of the thirty-two crystal classes: multiplication tables. *Proceedings of the Royal Society of London. A. Mathematical and Physical Sciences*, 391(1800):149–179.
- Wang, H., Hellmich, C., Yuan, Y., Mang, H., and Pichler, B. (2018). May reversible water uptake/release by hydrates explain the thermal expansion of cement paste? — Arguments from an inverse multiscale analysis. *Cement and Concrete Research*, 113:13–26.
- Whittaker, E. and Robinson, G. (1967). The trapezoidal and parabolic rules. *The Calculus of Observations: a Treatise on Numerical Mathematics*, pages 156–158.
- Willis, J. R. (1977). Bounds and self-consistent estimates for the overall properties of anisotropic composites. *Journal of the Mechanics and Physics of Solids*, 25(3):185–202.
- Wolfram, U., Peña Fernández, M., McPhee, S., Smith, E., Beck, R. J., Shephard, J. D., Ozel, A., Erskine, C. S., Büscher, J., Titschack, J., Roberts, J. M., and Hennige, S. J. (2022). Multiscale mechanical consequences of ocean acidification for cold-water corals. *Scientific Reports*, 12(1):8052.
- Wyrzykowski, M., McDonald, P. J., Scrivener, K. L., and Lura, P. (2017). Water redistribution within the microstructure of cementitious materials due to temperature changes studied with 1H NMR. *The Journal of Physical Chemistry C*, 121(50):27950–27962.
- Young, T. (1805). An essay on the cohesion of fluids. *Philosophical Transactions of the Royal Society of London*, 95:65–87.
- Zaoui, A. (2002). Continuum micromechanics: survey. *Journal of Engineering Mechanics*, 128(8):808–816.
- Zeller, R. and Dederichs, P. (1973). Elastic constants of polycrystals. *Physica status solidi (b)*, 55(2):831–842.
- Zhang, J.-L., Vida, C., Yuan, Y., Hellmich, C., Mang, H. A., and Pichler, B. (2017). A hybrid analysis method for displacement-monitored segmented circular tunnel rings. *Engineering Structures*, 148:839–856.

- Zhang, Y., Zhou, Q., Ju, J. W., and Bauchy, M. (2021). New insights into the mechanism governing the elasticity of calcium silicate hydrate gels exposed to high temperature: a molecular dynamics study. *Cement and Concrete Research*, 141:106333.
- Zhou, M. (2003). A new look at the atomic level virial stress: on continuum-molecular system equivalence. *Proceedings of the Royal Society of London. Series A: Mathematical, Physical and Engineering Sciences*, 459(2037):2347–2392.
- Zienkiewicz, O. C., Taylor, R. L., and Zhu, J. Z. (2005). *The finite element method: Its basis and fundamentals*. Elsevier.

# Appendix **A**

---

## Numerical computation of strain concentration and homogenized stiffness tensor of multiphase matrix-inclusion composites

### Computer routine for MATLAB

```
%  
%1matrix phase +(1 spherical inclusion, 1 prolate inclusion)  
%volume fractions and elastic constants (k=bulk modulus; mu=shear modulus)  
fm=.6; km=80.634e9; mum=37.1e9;  
f1=.25; k1=19.29e9; mu1=14.3e9;  
f2=.15; k2=160e9; mu2=79.3e9;  
  
% stiffness tensors  
Cm=stiffness_tensor_kmu(km,mum);  
C1=stiffness_tensor_kmu(k1,mu1);  
C2=stiffness_tensor_kmu(k2,mu2);  
  
% Hill tensors  
Pm=Hill_tensor_sphere(km,mum);  
P1=Hill_tensor_sphere(k1,mu1);  
P2=Hill_tensor_prolate(km,mum,3);  
  
% AUXILIARY strain concentration tensors  
Aminf=aux_strain_concentration(Cm,Cm,Pm); %=I  
A1inf=aux_strain_concentration(Cm,C1,P1);  
A2inf=aux_strain_concentration(Cm,C2,P2);  
  
% corrected RVE-TO-AUXILIARY STRAIN LINK  
M_sym=real_to_aux_macrostrain_sym_2(Cm, 1-fm,  
    f1/(1-fm), C1, A1inf, f2/(1-fm), C2, A2inf);
```

```

% STRAIN CONCENTRATION TENSORS INCLUSION PHASES
A1_sym=A1inf*M_sym;
A2_sym=A2inf*M_sym;

% STRAIN CONCENTRATION TENSOR MATRIX PHASE
Am_sym=(eye(6)-(f1*A1_sym+f2*A2_sym))/fm;

% HOMOGENIZED STIFFNESS TENSOR
Chom_sym=fm*Cm*Am_sym+f1*C1*A1_sym+f2*C2*A2_sym;

```

## Functions used in this computer routine

### Computation of isotropic stiffness tensor

```

function [C] = stiffness_tensor_kmu(k, mu)

%k,mu    bulk, shear moduli of the phase

%volumetric and deviatoric identity tensors
Ivol=zeros(6,6);
Ivol(1:3,1:3)=ones(3,3)/3;
Idev=eye(6)-Ivol;

C=3*k*Ivol+2*mu*Idev;

end

```

### Computation of Hill tensors for spherical and prolate inclusions

```

function [P] = Hill_tensor_sphere(k0, mu0)

%Hill tensor of sphere in Isotropic matrix
%k,mu    bulk, shear moduli of the Eshelby matrix

alpha=1/(3*k0+4*mu0);
beta=3*(k0+2*mu0)/5/mu0/(3*k0+4*mu0);

Ivol=zeros(6,6);
Ivol(1:3,1:3)=ones(3,3)/3;
Idev=eye(6)-Ivol;

P=alpha*Ivol+beta*Idev;

end

function [P] = Hill_tensor_prolate(k0,mu0,omega)

```

```

%Hill tensor of prolate in Isotropic matrix
%k,mu    bulk, shear moduli of the Eshelby matrix
%omega: aspect ratio (>1)

h=omega*(omega*sqrt(omega*omega-1)-acosh(omega))/(sqrt(omega*omega-1)*(omega*omega-1));

%P=(2kp,lp,lp,np,2mp,2pp) Walpole notation
kp=((7*h-2*omega*omega-4*omega*omega*h)*mu0+
    3*(h-2*omega*omega+2*omega*omega*h)*k0)/(8*(1-omega*omega)*mu0*(4*mu0+3*k0));
lp=((mu0+3*k0)*(2*omega*omega-h-2*omega*omega*h)
    /(4*(1-omega*omega)*mu0*(4*mu0+3*k0)));
np=((6-5*h-8*omega*omega+8*omega*omega*h)*mu0+
    3*(h-2*omega*omega+2*omega*omega*h)*k0)/(2*(1-omega*omega)*mu0*(4*mu0+3*k0));
mp=((15*h-2*omega*omega-12*omega*omega*h)*mu0+3*(3*h-2*omega*omega)*k0
    /(16*(1-omega*omega)*mu0*(4*mu0+3*k0)));
pp=(2*(4-3*h-2*omega*omega)*mu0+3*(2-3*h+2*omega*omega-3*omega*omega*h)*k0
    /(8*(1-omega*omega)*mu0*(4*mu0+3*k0)));

%Walpole basis
W1=zeros(6);W1(1:2,1:2)=ones(2); W1=W1/2;
W2=zeros(6);W2(1,3)=1;W2(2,3)=1;
W3=zeros(6);W3(3,1)=1;W3(3,2)=1;
W4=zeros(6);W4(3,3)=1;
W5=zeros(6);W5(1,1)=1;W5(2,2)=1;W5(1,2)=-1;W5(2,1)=-1;W5(6,6)=2;W5=W5/2;
W6=zeros(6);W6(4,4)=1;W6(5,5)=1;

P=2*kp*W1+lp*W2+lp*W3+np*W4+2*mp*W5+2*pp*W6;

end

```

### Computation of auxiliary concentration tensors

```

function [A_inf_i] = aux_strain_concentration(C0, C_i,P_i)

%Calculate strain concentration tensor for auxiliar macrostrain
%(infinite matrix Eshelby problem)
%0=matrix phase;i=inclusion phase

A_inf_i=eye(6)+P_i*(C_i-C0);
A_inf_i=inv(A_inf_i);

end

```

### Computation of the RVE-to-auxiliary macrostrain link (for composites with 2 inclusion phases)

```

function [M] = real_to_aux_macrostrain_sym_2(C_0, c, f_1, C_1, A_inf_1,

```

```
f_2, C_2, A_inf_2)

%E0=M*(E)
%c volume fraction of inclusions
%f_i normalized volume fraction of inclusion i (/c)
%A_inf_i auxiliar strain concentration tensor for inclusion i
%C_0 stiffness tensor of matrix
%C_i stiffness tensor of inclusion i

N_1=(C_1-C_0)*A_inf_1;
N_2=(C_2-C_0)*A_inf_2;

sum_N=f_1*N_1+f_2*N_2;

M=(1-c)*eye(6)+c*( (f_1*A_inf_1) + (f_2*A_inf_2) ) - c/2*( (f_1*inv(C_1-C_0)*N_1) +
    (f_2*inv(C_2-C_0)*N_2) ) + c/2*( inv(sum_N)*( (f_1*N_1*inv(C_1-C_0)) +
    (f_2*N_2*inv(C_2-C_0)) )*sum_N);
M=inv(M);

end
```

# Personal information

## Curriculum Vitae

### Personal Data

Name: **Nabor Jiménez Segura**  
Academic Degree: **Mag. Inž.**  
Date of Birth: [REDACTED]  
Place of Birth: [REDACTED]  
Nationality: [REDACTED]  
Current address: [REDACTED]

### Education

11/2017 – 09/2022 Doctoral studies in Civil Engineering at Vienna University of Technology (TU-Wien), Vienna (Austria)  
06/2016 – 10/2017 Master's studies in Technical Physics at Cracow University of Technology, AGH (Poland)  
09/2011 – 08/2015 Bachelor's studies in Physics at University of Zaragoza (Spain)

### Work Experience

11/2017 – 09/2022 Project Assistant, Institute for Mechanics of Materials and Structures, Vienna University of Technology (Austria)  
06/2016 – 12/2016 Master Researcher, Empa, Thun (Switzerland)  
09/2015 – 12/2015 Assistant Researcher, Computer Science Faculty, Dublin City University (Ireland)

### Activities Abroad

10/2018 – 10/2018 Visit Research Center of St. Gobain (France)  
03/2020 – 03/2020 Research stay at Heidelberg Technology Center (Germany)  
04/2019 – 04/2019 NMR training at University of Surrey, Guildford (United Kingdom)  
09/2014 – 07/2015 Erasmus+ program at Cracow University of Technology (Poland)

### Awards and Scholarships

2019 Best presentation in China-Austria Forum for post-graduates of Civil Engineering  
2011 Silver medal in Spanish Physics Olympiad and Bronze medal in Spanish Chemistry Olympiad



## Scientific Dissemination

### Publications

- N. Jiménez Segura, B. L. A. Pichler, and C. Hellmich. Stress average rule derived through the principle of virtual power. *ZAMM: Journal of Applied Mathematics and Mechanics / Zeitschrift für Angewandte Mathematik und Mechanik*, [Online before inclusion in an issue](n/a):e202200091.
- N. Jiménez Segura, B. L. A. Pichler, and C. Hellmich. A Green's function-based approach to the concentration tensor fields in complex elastic microstructures. *submitted to European Journal of Mechanics - A/Solids*.
- N. Jiménez Segura, B. L. A. Pichler, and C. Hellmich. Concentration tensors preserving elastic symmetry of multiphase composites. *submitted to Mechanics of Materials*.
- N. Jiménez Segura, B. L. A. Pichler, and C. Hellmich. Mix-, storage- and temperature-invariant precipitation characteristics in white cement paste, expressed through an NMR-based analytical model. *submitted to Cement and Concrete Research*.
- N. Jiménez Segura, H. Wang, C. Hellmich, and B. L. A. Pichler. Swelling of nanoscopic solid C-S-H governs macroscopic expansion of mature cement paste during isothermal adsorption. *soon to be submitted to Cement and Concrete Research*.

### Conference Papers

- N. Jiménez Segura, H. Wang, C. Hellmich, and B. L. A. Pichler. Poromechanical modelling of swelling of cement paste during isothermal adsorption. In: *Programme & Proceedings of the China-Austria Forum for Postgraduates of Civil Engineering, Vienna University of Technology, Institute for Mechanics of Materials and Structures*, pages 66–68, 2019.

### Conference Presentations and Posters

- N. Jiménez Segura, B. L. A. Pichler, and C. Hellmich. Homogenization of stiffness and eigenstresses/eigenstrains of matrix-inclusion composites. Oral presentation at the “90th Annual Meeting of the International Association of Applied Mathematics and Mechanics (GAMM 2019)”, Vienna, Austria, 2019.
- N. Jiménez Segura, H. Wang, C. Hellmich, and B. L. A. Pichler. Poromechanical modelling of swelling of cement paste during isothermal adsorption. Oral presentation at the “China-Austria Forum for Postgraduates of Civil Engineering”, Vienna, Austria, 2019.
- N. Jiménez Segura, H. Wang, C. Hellmich, and B. L. A. Pichler. Expansion of cement paste during isothermal adsorption: a multiscale poromechanical model. Oral presentation at the “ERICA CASH II Final Conference”, 2021.
- N. Jiménez Segura, H. Wang, C. Hellmich, and B. L. A. Pichler. Multiscale poromechanics of mature cement pastes: Volume changes during isothermal drying and re-wetting. Oral presentation at the conference “Engineering Mechanics Institute Conference and Probabilistic Mechanics & Reliability Conference (EMI/PMC 2021)”, New York, USA, 2021.

- N. Jiménez Segura, B. L. A. Pichler, and C. Hellmich. NMR-derived precipitation degree governs composition and kinetics of white cement paste. Oral presentation at the conference “Engineering Mechanics Institute Conference (EMI 2022)”, Baltimore, USA, 2022.
- N. Jiménez Segura, B. L. A. Pichler, and C. Hellmich. Concentration tensor fields in micromechanical systems, derived from Green’s functions. Oral presentation at the conference on “Computer Methods in Mechanics and Solid Mechanics (CMM/SolMech 2022)”, Swinoujście, Poland, 2022.